UNIVERSITY
OF OSLO

Thea Josefine Ellevold

Numerical investigations of internal solitary waves: the evolution of instability in the bottom boundary layer and the wave-vortex-induced particle motion

Thesis submitted for the degree of Philosophiae Doctor

Department of Mathematics
Faculty of Mathematics and Natural Sciences

University of Oslo

2023

Series of dissertations submitted to the
Faculty of Mathematics and Natural Sciences, University of Oslo
No. 2685

ISSN 1501-7710

Cover: UiO.
Print production: Graphic center, University of Oslo.

To family

Preface

This thesis is submitted in partial fulfillment of the requirements for the degree of *Philosophiae Doctor* at the University of Oslo. The research presented here was conducted at the University of Oslo, under the supervision of Professor John Grue and Dr. Johannes Röhrs. This work was supported by the Norwegian Research Council under the "ECOPULSE" project, grant number 300329.

The thesis is a collection of three papers presented in practical order. The first two papers are related to internal waves and tracer particle motion induced by these waves, and the last paper concerns a study regarding air bubbles as tracers in the ocean to measure the two-dimensional velocity field of water. The common theme is the investigation of fluid dynamics, wave characteristics, and the evaluation of wave-induced vertical and horizontal particle motion.

The papers are preceded by five chapters that provide relevant background information, motivation for the work, and a perspective on future directions. Chapter one introduces the topic *Internal Waves* and briefly reviews the internal wave field. Chapter two provides the background information and motivation for the work conducted in Papers I and 2. The third chapter introduces internal waves on the Norwegian continental shelf. It highlights the importance of conducting in-situ measurements along the coast to measure internal waves. The new methodology, field work, and laboratory work conducted in Paper III are presented at the end of the third chapter. Chapter four summarizes each paper's main findings, and chapter five provides a summary and perspectives on future directions. Two Appendices follow after the papers. I am the first author of the two first papers and the second author of the third paper. The third paper is a collaboration with Dr. Trygve Løken and colleagues, where I have conducted the fieldwork and been involved in all stages of the experimental work and analysis.

Thea Josefine Ellevold
Oslo, October 2023

Acknowledgements

I would like to thank my main supervisor, Professor John Grue, who has provided great guidance through my doctoral studies and for always having time to explain and discuss the field of internal waves. I am grateful for all the knowledge you have shared with me.

I am grateful for the help and support I have gotten from my co-supervisor, Dr. Johannes Röhrs, at the Norwegian Meteorological Institute (MET). Thank you for introducing me to the science group at MET and including me in the PhD/PD group. Those meetings have been of great value.

I want to thank the whole team within my research project, Ecopulse. Thanks to Trygve Halsne, Øystein Skagseth, Henrik Søiland, Tina Kutti, and all the other scientists and researchers making fieldwork a reality.

I want to express my gratitude to Olav Gundersen, our lab Senior Engineer, for his invaluable help, regardless of what it should be, the countless cups of coffee, and the long conversations that kept me sane, grounded, and motivated during my PhD journey.

I want to acknowledge our IT staff, Terje Kvernes and Lucy Karpen, for their tremendous service. It would not have been without the IT help that Terje has provided through my journey with Basilisk that this thesis would have come to an end.

I want to express my gratitude to all of my exceptional colleagues in the Mechanics Section for making my past three years very enjoyable. A special thanks to Jarle, my office mate (in my office?), for tolerating my personality. Also, a big thank you to Stephane, Jarle, and Vanessa for valuable feedback on my thesis. Thanks to Lars Olsen for all the strolls in the hallways, with needed conversations, reading articles aloud, and boosting my motivation.

I would also like to thank all the co-authors on the articles created during my master's and the beginning of my PhD journey.

Last but most importantly, I want to thank my partner Morten for always supporting me the way you know best. I cannot wait to start the post-PhD life with you! To my family for always having my back and cheering me on. Thank you Mom for all the things you have done for me during my years at the University; they have been invaluable. Immense gratitude to my closest friend, trusted confidant, and companion on every remarkable journey in life, Linda Johansen.

Thea Josefine Ellevold
Oslo, October 2023

You are not where you want to be.
You feel like you are supposed to be somewhere else.
Well, say you could snap your fingers and be wherever you wanted it to be.
I bet you would still feel this way.
Not in the right place.
Point is, you cannot get so hung up on where you would rather be that you forget how to make the most of where you are.
Take a break from worrying about what you cannot control.
Live a little.
–Passengers, the movie

Abstract

English

Internal waves are a phenomenon present inside the stratified ocean. They are commonly observed, e.g., over continental shelves where stratification, strong currents, and tides coexist over various topography. When internal waves interact with other physical processes and/or move through a varying background environment, they may alter their form and possibly become unstable. Nonlinear internal solitary waves owe their existence due to a delicate balance between the nonlinear wave-steepening and the linear dispersion. This balance sustains the wave shape and velocity while propagating with amplitudes varying from a few to tens of meters. Understanding the behavior and dynamics of internal solitary waves is essential for comprehending their role in the oceanic ecosystem. This phenomenon has also proven essential in the oceans by causing vertical exchange and transport of particles and sediments. On the other hand, internal waves can be dangerous and pose numerous threats to, for instance, offshore installations.

Research on internal waves has been conducted for decades through field observations, numerical simulations, and laboratory experiments. Numerous studies have examined internal solitary waves of depression propagation over a flat bottom through laboratory experiments and numerical simulations. Despite the long-standing study of these waves, there are still some qualitative discrepancies between the results of these two methods.

In this thesis, we investigate internal solitary waves of depression propagating over flat bottom through high-resolution direct numerical simulations. Utilizing a two-dimensional laminar numerical model, we replicate and reproduce well-known laboratory experiments conducted in a three-dimensional wave tank. Throughout the study, we have addressed three central objectives: ascertain how well a laminar numerical model can reproduce laboratory measurements, gain further insight into the instabilities induced by the internal solitary waves in the bottom boundary layer, and ascertain an understanding of how Lagrangian tracer particles behave in scenarios where vortices in the bottom boundary layer arise. In addition, the effect of scale is systematically investigated throughout the study, where the kinematic viscosity of the water is varied. Hence, our calculations are presented for the wave Reynolds number Re_w in the range $Re_w = 1.9 \times 10^4 - 6.5 \times 10^5$, where the wave Reynolds number is a function of the linear long wave speed, the kinematic viscosity of the water, and the total water depth H. The non-dimensional amplitude of the internal waves is in the range of $a/H \sim 0.19 - 0.33$.

When the internal solitary waves propagate, they create a wave-induced velocity field that can cause instability and vortex shedding in the bottom boundary layer. An essential part of this thesis regards the threshold when the separation bubbles formed due to flow separation in the bottom boundary layer are experiencing instability. The stability border is investigated as a function of the wave amplitude and the wave Reynolds number and as a function of the adverse pressure gradient and the momentum-thickness Reynolds number estimated at the flow separation point. With a strong emphasis on convergence, including the resolution of the bottom boundary layer, we obtained a very good agreement with laboratory experiments for the transition to instability. We find that the threshold from the stable to unstable regime depends on the depth of the pycnocline. The same outcome was also observed in previous laboratory experiments. The present calculations of the transition to instability, fitting with the laboratory experiments, imply that previous numerical simulations have overestimated the instability border. Hence, the instability occurs much earlier for internal waves of considerably smaller amplitude than previously suggested. When examining the created vortex formation in the bottom boundary, the numerical calculation matched the vortices generated in the three-dimensional laboratory experiment. The results indicate that the instability observed in the laboratory experiments was predominantly two-dimensional up to a certain distance behind the wave trough. The results contribute to the ongoing debate about whether laboratory-observed instabilities are primarily three-dimensional.

The interchange between the internal wave-induced velocity field, vortex formation, and Lagrangian tracer particle motion in the bottom boundary layer is also investigated. A cloud of tracer particles is implemented in the bottom boundary upstream of the internal solitary wave. The internal solitary wave intercepts the tracer particle cloud twice: first, during propagation along the undisturbed fluid and second, as a reflected wave from the right end of the tank. The tracer particles' displacement and trajectories are computed and seen to be affected by both the wave and the vortices. The tracer particles' vertical height reached up to approximately 23% of the total water depth after the second interception, independent of the wave Reynolds number.

In this thesis, most of the work involves performing direct numerical simulations of internal solitary waves. However, in addition to this, fieldwork has been conducted outside Lofoten, Vesterålen, Norway, to measure this phenomenon. A train of internal waves was measured, where the leading wave had a nondimensional amplitude of $0.4H$.

Leaving the internal wave topic, a different study regarding measuring water motion has been conducted. A new methodology is presented to measure the two-dimensional velocity field of water near a heaving ice floe in the marginal ice zone in the Barents Sea. The new system consists of an open-source remotely operated vehicle (ROV) functioning as an optical instrument to record the two-dimensional velocity field by tracking seeded air bubbles. The methodology was successfully tested in the Barents Sea and validated under controlled settings in the laboratory.

Norsk

Indre bølger er et fenomen tilstede inne i det lagdelte havet. De er ofte observert for eksempel over Norges kontinentalsokkel hvor lagdeling, sterke strømmer og tidevann eksisterer side om side over forskjellige topografier. Når indre bølger interagerer med andre fysiske prosesser og/eller beveger seg gjennom et varierende bakgrunnsmiljø, kan de endre form og muligens bli ustabile. Store havgående indre bølger, solitoner, kan forplante seg over store avstander hvor bølgeformen og bølgens hastighet opprettsholdes, med bølgeamplituder som varierer fra noen få til titalls meter. Å forstå atferden og dynamikken til indre solitære bølger er en viktig faktor for å skjønne deres rolle i økosystemet i havet og hva dem kan forårsake. Indre bølger har vist seg å yte en viktig mekansisme i havene ved for eksempel å forårsake vertikal utveksling og transport av partikler og sedimenter. På den annen side kan indre bølger være farlige og utgjøre en rekke trusler mot for eksempel offshoreinstallasjoner.

Forskning på indre bølger har blitt utført i flere tiår gjennom feltobservasjoner, numeriske simuleringer og laboratorieeksperimenter. Atskillige studier har undersøkt indre solitære bølger av depresjon over en flat bunn gjennom laboratorie eksperimenter og numeriske simuleringer. Til tross for den langvarige studien av disse bølgene, er det fortsatt noen kvalitative avvik mellom resultatene av disse to metodene.

I denne oppgaven undersøker vi indre solitære bølger av depresjon som forplanter seg over flat bunn gjennom høyoppløselige direkte numeriske simuleringer. Ved å bruke en todimensjonal laminær numerisk modell, replikerer og reproduserer vi velkjente laboratorie eksperimenter utført i en tredimensjonal bølgetank. Gjennom hele studien har vi adressert tre sentrale mål: forstå hvor godt en laminær numerisk modell kan reprodusere laboratoriemålinger, få ytterligere innsikt i ustabilitetene indusert av de indre solitære bølgene i det nederste grenselaget, og forstå hvordan Lagranske sporpartikler oppføre seg i scenarier der virvler i det nederste grensesjiktet oppstår. I tillegg er effekten av skala systematisk undersøkt gjennom hele studien, hvor den kinematiske viskositeten til vannet varieres. Derfor er våre beregninger presentert for bølge Reynolds tallet Re_w i området $Re_w = 1.9 \times 10^4 - 6.5 \times 10^5$, hvor bølgens Reynolds tall er en funksjon av den lineære langbølgehastigheten, den kinematiske viskositeten til vannet, og den totale vanndybden H. Den ikke-dimensjonale amplituden til de indre bølgene er i området $a/H \sim 0.19 - 0.33$.

Når de indre solitære bølgene forplanter seg, skaper de et bølgeindusert hastighetsfelt som kan forårsake ustabilitet og virvelavgivelse i det nederste grensesjiktet. En vesentlig del av denne oppgaven omhandler grensen når separasjonsboblene som dannes på grunn av strømningsseparasjon i det nederste grensesjiktet opplever ustabilitet. Stabilitetsgrensen undersøkes som en funksjon av bølgeamplituden og bølge Reynolds tallet og som en funksjon av trykkgradienten og momentum-tykkelsen Reynolds tallet estimert ved strømningsseparasjonspunktet. Med sterk vekt på konvergens, inkludert oppløsningen av bunngrensesjiktet, oppnådde vi en meget god overensstemmelse med de fysiske eksperimentene for overgang til ustabilitet. Grensen fra stabilt til ustabilt regime avhenger av pyknoklindybden, og samme utfall ble også observert i laboratorieundersøkelsene. De nåværende beregningene av overgangen til ustabilitet, i samsvar med laboratorieeksperimentene, antyder at tidligere numeriske simuleringer har overestimert denne grensen. Ustabiliteten oppstår mye tidligere for indre bølger med betydelig mindre amplitude enn tidligere antatt. I undersøkelsen rundt virvelformasjonen i bunngrensesjiktet, samsvarer den numeriske beregningen med virvlene generert i det tredimensjonale laboratorie eksperimentet. Resultatene indikerer at ustabiliteten som ble observert i laboratorieforsøkene var hovedsakelig todimensjonale opp til en viss avstand bak bølgebuken. Resultatene bidrar til den pågående debatten om hvorvidt laboratorieobserverte ustabiliteter primært er tredimensjonale.

Samhandlingen mellom det indre bølgeinduserte hastighetsfeltet, virveldannelse og Lagranske sporpartikkelbevegelser i det nederste grensesjiktet er også undersøkt. En sky av sporpartikler er implementert i bunngrensesjiktet oppstrøms for den indre solitære bølgen. Den indre solitære bølgen passerer sporpartiklene to ganger: Den interne ensomme bølgen fanger opp sporpartikkelskyen to ganger: første gangen når den forplanter seg i det uforstyrrede fluidet og andre gang som en reflektert bølge. Sporpartiklenes forflytning og baner er beregnet og ses å bli påvirket av både bølgen og virvlene. Sporpartiklenes vertikale høyde nådde opp til omtrent 23% av den totale vanndybden etter at den reflekterte bølgen hadde passert, uavhengig av bølgens Reynolds tall.

I denne oppgaven innebærer det meste av arbeidet å utføre direkte numeriske simuleringer av interne solitære bølger. Men i tillegg til dette er det utført feltarbeid utenfor Lofoten, Vesterålen, Norge, for å måle dette fenomenet. Et tog av interne bølger ble målt i 2021, hvor den ledende bølgen hadde en dimensjonsløs amplitude på $0.4H$.

En annen studie angående måling av vannbevegelse er utført, hvor vi nå også forlater indre bølger emnet. En ny metodikk er presentert for å måle et todimensjonalt hastighetsfelt av vannet nær et isflak i den marginale issonen i Barentshavet. Det nye systemet består av et fjernstyrt kjøretøy (ROV) som fungerer som et optisk instrument for å registrere det todimensjonale hastighetsfeltet ved å spore luftbobler som sporpartikler. Metodikken ble vellykket testet i Barentshavet og validert under kontrollerte omgivelser i et laboratorium.

List of Papers

Paper I

Ellevold, T. and Grue, J. “Calculation of internal-wave-driven instability and vortex shedding along a flat bottom”. In: *Journal of Fluid Mechanics*. Volume 966 (2023), Pages A40. DOI: doi:10.1017/jfm.2023.476.

Paper II

Ellevold, T. , Grue, J. and Sletten, J. “Tracer particle motion driven by vortex formation in the bottom boundary layer underneath internal solitary waves”. In: *Frontiers in Marine Science*. Volume 10 (2023), Pages 1155270. DOI: doi:10.3389/fmars.2023.1155270.

Paper III

Løken, T. Ellevold, T., de la Torre, R., Rabault, J. and Jensen, A. “Bringing optical fluid motion analysis to the field: a methodology using an open source ROV as a camera system and rising bubbles as tracers”. In: *Measurement Science and Technology*. Volume 32 (2021), No. 9, Pages 095302. DOI: doi:10.1088/1361-6501/abf09d.

Relevant paper not included

In addition to the selected works mentioned above, one publication is not included in this thesis. This paper continues and extend the work conducted in Paper III.

Paper IV

Løken, T., Marchenko, A., Ellevold, T., Rabault, J., and Jensen, A. “Experiments on turbulence from colliding ice floes”. In: *Physics of Fluids*. Volume 34 (2022), No. 6, Pages 065133. DOI: 10.1063/5.0088953.

Contents

Chapter 1

Introduction

1.1 Internal waves and the present thesis

1.1.1 Internal waves as a phenomenon

The movement of waves in the ocean is truly remarkable and can be a gorgeous sight, but they can also be quite dangerous. When people think of ocean waves, they generally only consider those moving on the surface of the ocean. Nevertheless, underwater waves exist beneath the surface, called internal waves. Internal waves are a spectacular phenomenon and can grow significantly larger than surface waves. They can reach amplitudes of up to hundreds of meters, compared to less than twenty meters for surface waves, and can travel long distances without breaking up (Helfrich and Melville 2006).

Internal waves appear in stratified waters which arise, e.g., in the ocean basin (Holligan, Pingree, and Mardell 1985; Zhao and Alford 2009), the coastal ocean (Bogucki, Dickey, and Redekopp 1997; Dokken et al. 2001; C. Jackson 2007; Klymak and Moum 2003), in fjords, riverbeds, and in lakes (Boegman, Imberger, et al. 2003; D. M. Farmer 1978; Thorpe 1971). Internal waves can also occur in the atmosphere (Christie 1989; Christie and White 1992) (not discussed in this thesis).

The stratification occurs due to differences in density (ρ) within the water column. The density of the water depends on a combination of the local water temperature and the salinity content. A pycnocline describes the localized change in the density of the water column and provides the waveguide. The density variation along the vertical is sometimes abrupt and other times gradual. The density jump across the pycnocline ($\Delta\rho/\rho$) is typically one in one thousand (10^{-3}), which applies to both deep and coastal oceans. Occasionally, instead of the term pycnocline, this is referred to as a thermocline or a halocline in the case of temperature gradients or salinity gradients, respectively.

The pycnocline separates an upper layer of light water from the denser water below. The upper layer is usually thin, while the lower layer is deep. There are several types of wave motion created on the pycnocline. One type is a train of periodic sine waves, whereas another is pulse-like waves, termed solitary waves. The waves may appear in groups. The sine- and pulse-waves are shown in Figure 1.1. The pulses described are depression waves that occur when the upper layer is thinner than the lower layer (Figure 1.1b). Conversely, they are waves of elevation when the lower layer is thinner than the upper (Figure 1.1c). The waves propagating along the pycnocline have a spectrum of modes. In this thesis, we only discuss internal waves of mode 1. Internal waves in the continuously stratified oceans may also propagate in the form of beams (Mathur and Peacock 2009). Such propagation is not discussed here.

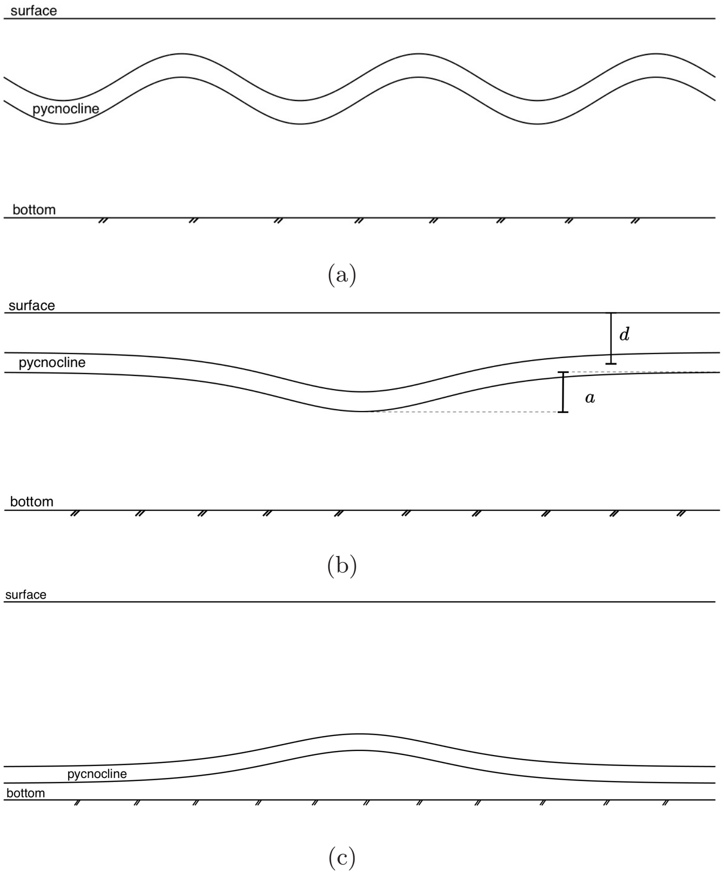

Figure 1.1: Schematics of (a) periodic sine waves, (b) an internal solitary wave of depression, (c) an internal solitary wave of elevation. The vertical excursion (the amplitude a) and the middle depth d of the pycnocline are visualized in (b).

Internal waves typically have a large vertical excursion of the pycnocline, the amplitude a, for depression and elevation waves. The kinetic energy of the wave-induced velocity field is in balance with the potential energy. This implies that a large amplitude is required to compensate for the small density differences across the pycnocline. Internal solitary waves are finite-amplitude waves due to the delicate dynamic balance between nonlinear wave-steepening (ratio between wave amplitude and water depth) and linear dispersion. They can propagate without any temporal evolution in shape or size when the reference frame is moving with the wave (Stanton and Ostrovsky 1998).

1.1.2 Typical internal wave speed

The internal waves we consider in this thesis are driven by gravity (characterized by the gravitational acceleration g) and are termed internal gravity waves. The propagation speed of the waves is roughly proportional to the square root of the relative density jump across the pycnocline, times the acceleration of gravity, times the middle depth d of the pycnocline (more elaborate estimates of the wave speed are given below Section 1.2). Accordingly, the wave speed is estimated by $c_0 = \sqrt{(\Delta\rho/\rho)gd}$. Here $d = h_1 + h_2/2$ where h_1 is the thickness of the thinner layer, and h_2 is the thickness of the pycnocline (see Figure 1.2 for a schematic representation (three-layer model)). The middle depth of the pycnocline may be at $d = 200$ m in the deep oceanic waters. In the coastal sea, for instance, along the Norwegian continental shelf, the seasonal pycnocline is approximately at a middle depth of $d = 25$ m. The pycnocline in the Norwegian fjords, where the density jump separates fresh river water from salty sea water, is typically found at a middle depth of $d = 5$ m (unpublished computations). The speed in the different cases becomes $c_0 = 1.5$ m s^{-1} with $d = 200$ m, $c_0 = 0.5$ m s^{-1} with $d = 25$ m, and $c_0 = 0.22$ m s^{-1} with $d = 5$ m, where $\Delta\rho/\rho$ is in the range $1 - 2 \times 10^{-3}$ in all cases.

In this context, it is worth mentioning that the Norwegian Atlantic Current flows along the Norwegian shelf northward. With a temperature of approximately 8 degrees Celcius, this current flows on top of the cold, dense Arctic water of temperature -0.5 degrees Celcius on the shelf/slope. The pycnocline is located at approximately 550 m depth with a relative density jump across the pycnocline of $\Delta\rho/\rho \simeq 0.5 \times 10^{-3}$. The corresponding local internal wave speed becomes 1.6 m s^{-1}. The motion of the pycnocline caused strong currents at the Ormen Lange gas field development of Equinor, a complete sub-sea development in the deep water on the Norwegian shelf/slope (Grue and Sveen 2010). Concerns regarding large amplitude internal waves and their potentially damaging effects were communicated by the offshore industry on the Norwegian Continental Shelf, and elsewhere worldwide, during the 1990s and onwards (Grue, Friis, et al. 1997).

1.1.3 Generation mechanisms

The primary generation source of internal waves is wind or tide (Helfrich and Melville 2006). See further the review by C. R. Jackson, Da Silva, and Jeans 2012 regarding internal solitary wave generation mechanisms in the ocean.

When wind is acting on the ocean surface, it pushes (lifts) the pycnocline downwards (upwards), inducing internal waves of depression (elevation) (Boegman and Stastna 2019). When tidal disturbances travel over topography, underwater mountains, or along the continental shelf, the blockage will lower (rise) the pycnocline and induce internal waves of depression (elevation) (Alford et al. 2012; Grue 2015; Maxworthy 1979).

Internal waves commonly occur in wave groups, where the tidal period regulates the distance between the groups. The period of the waves within a group is typically 10-30 minutes (Alford et al. 2012; Dokken et al. 2001; Stanton and Ostrovsky 1998).

1.1.4 The present thesis

The main part of this thesis represents an effort to conduct detailed numerical simulations of internal solitary waves of depression propagating over a flat bottom to gain further insight into the physical mechanisms these waves govern. While most of the work considers direct numerical simulations of internal solitary waves (Papers I and II), fieldwork has been conducted outside Lofoten, Vesterålen, Norway, to measure this phenomenon (Chapter 3). The project is a part of the Ecosystem structuring by pulses of internal wave breaking ("ECOPULSE" 2020-2023), where the goals are to quantify the impact of tidally forced (breaking) internal waves on marine productivity, plankton distribution, and on cold-water coral reefs, in addition to enable a mechanistic understanding of how internal waves can increase the vertical mixing locally. Accordingly, internal waves can significantly impact the marine ecosystem as a driver of sediment movement on continental margins (R. Bøe et al. 2009; Sandstrom and Elliott 1984).

Another study regarding measuring water motion has also been conducted. In this study, internal waves were not investigated, but the two-dimensional velocity field of water next to a heaving ice floe in the Barents Sea. To conduct the investigation, a new methodology is presented, which utilizes a remotely operated vehicle and air bubbles seeded in the water as tracers.

The present thesis aims to achieve several key objectives:

(i) Conduct numerical simulations of fully nonlinear internal waves by replicating the laboratory experiments by Carr, Davies, and Shivaram 2008. Additionally, to provide a (until now lacking) comparison between simulations and lab experiments (Boegman and Stastna 2019).

(ii) Gain further insight into the bottom boundary layer instability border/threshold induced by internal solitary waves of depression propagating over a flat bottom.

(iii) Examine the behavior of Lagrangian tracer particles in the bottom boundary layer vorticity field induced by the wave.

(iv) Use the improved understanding of internal waves from the numerical calculations for theoretical background, reference model, and a tool for interpreting field measurements undertaken at the Hola Reef in Vesterålen, Norway (unpublished results are in progress).

(v) Obtain the water's two-dimensional velocity field next to an ice floe.

Throughout the numerical work, the following questions have been asked:

(vi) How well can a two-dimensional laminar numerical model reproduce laboratory measurements conducted in a three-dimensional wave tank?

(*vii*) How can the numerical model be used to evaluate quantities which have not been measured in the laboratory?

As described above, the main work conducted in this thesis analyzes internal solitary waves of depression propagating over a flat bottom and the instabilities emerging in the bottom boundary layer. However, it is important to note that this particular research only covers a small portion of the broader field of internal waves and the diverse instability mechanisms that they may exhibit.

The rest of this chapter will give a short but broader overview of the internal wave field and different instability mechanisms (Section 1.3). Before all else, a section of some mathematical model descriptions of internal wave motion is provided (Section 1.2).

Subsequently, Chapter 2 outlines the main research conducted in this thesis and our contribution to the field. The first part of Chapter 3 will provide insight into internal waves on the Norwegian continental shelf and why Vesterålen, Norway, was chosen as the fieldwork site to measure this phenomenon. The last part of Chapter 3 regards the new methodology and a validation of the method. A summary of the articles, their main findings, author contribution, and an integrated view of the articles are presented in Chapter 4. Summary and future perspectives can be found in Chapter 5

1.2 Mathematical models of internal wave motion

Internal waves are *i*) long compared to the depth of the pycnocline and *ii*) nonlinear with amplitudes comparable to the pycnocline depth. Long internal waves are weakly dispersive. Initially, weakly nonlinear and dispersive wave theories were developed, with the weakly nonlinear Korteweg-de Vries (KdV) equation being the most frequently referenced example. This equation demonstrates that a balance can be achieved between nonlinearity and dispersion, enabling the existence of solitary wave solutions. A review written by Grue 2006 is further followed regarding the calcualtions presented in Section 1.2.1.

1.2.1 KdV theory

In 1847, Stokes derived the linear theory of internal waves in the form of the motion of two fluids. In the 1870s, Boussinesq expanded the theory with a nonlinear extension. The equations for nonlinear motion in a stratified fluid were derived by Dubreil-Jacotin in 1932. Subsequently, Keulegan 1953 and Long 1956 provided differenciations of the KdV equation for the motion in two-layer fluids.

The development of weakly nonlinear theory of internal waves in continuous stratified fluids was derived by Benney 1966. Later, it was extended to the KdV equation and its higher-order extension, see the review by Grue 2006. The KdV theory arises from the assumption that nonlinearity ($\epsilon = a/H$) and nonhydrostatic dispersion ($\mu = H^2/\lambda^2$) are small and of same order of magnitude $\mu = O(\epsilon) \ll 1$. Here, λ is the wavelength and H is the total water depth. A step-by-step calculation outline is provided in the Appendix A. The KdV equation is a simple two-layer model, where at a certain depth, the density undergoes a stepwise variation, while the density above and below this depth is constant, as visualized in Figure 1.2. The KdV equation describes then a long wave propagating along the horizontal x-axis as follows:

$$A_t + c_0 A_x + \epsilon \alpha_0 A A_x + \mu \beta_0 A_{xxx} = 0. \tag{1.1}$$

Here, $A(x,t)$ is the amplitude function, the constants α_0 (nonlinear coefficient) and β_0 (measure of dispersion) are given in equations A.72 and A.74, respectively, and c_0 is the linear wave speed corresponding to the lowest mode. The notation $_x$ and $_t$ denotes derivation with respect to the horizontal direction and time, respectively.

When having a sharp pycnocline separating an upper layer of depth h_1 and density ρ_1 from a lower layer of depth h_2 ($h_2 > h_1$) and density ρ_2 ($\rho_2 > \rho_1$) (two-layer interfacial case), the coefficients in equation 1.1 ($\epsilon = \mu = 1$) become

$$\alpha_0 = -\frac{3}{2}\frac{c_0(\rho_1 h_2^2 - \rho_2 h_1^2)}{h_2 h_1(\rho_1 h_2 + \rho_2 h_1)} \approx -\frac{3}{2}\frac{c_0(h_2 - h_1)}{h_2 h_1}, \tag{1.2}$$

$$\beta_0 = \frac{1}{6}\frac{c_0 h_2 h_1(\rho_2 h_2 + \rho_1 h_1)}{\rho_1 h_2 + \rho_2 h_1} \approx \frac{1}{6} c_0 h_2 h_1, \tag{1.3}$$

$$c_0^2 = \frac{g h_2 h_1(\rho_2 - \rho_1)}{\rho_1 h_2 + \rho_2 h_1} \approx \frac{g' h_2 h_1}{h_2 + h_1}, \tag{1.4}$$

where $g' = g(\rho_2 - \rho_1)/\rho_1$ is the reduced gravity, and the approximations on the right hand sides are valid for $(\rho_2 - \rho_1)/\rho_2 \ll 1$. Equation 1.4 is the two-layer approximation of the linear long wave speed and is often used as the reference speed in calculations, e.g., Carr and Davies 2006; Carr, Davies, and Shivaram 2008.

Equation 1.1 has a solitary wave solution of permanent shape when there is a balance between the effects of nonlinearity and dispersion. Hence, we obtain

$$A_0 = a_0 \operatorname{sech}^2[(x - c_{nl} t)/\lambda] \tag{1.5}$$

as a solution for the longest wave mode, where $c_{nl} = c_0 + \Delta c$ is the nonlinear wave speed and Δc denotes the nonlinear excess speed. For an interfacial soliton in a two-layer case, the coefficients Δc and λ are related by

$$\Delta c = -\frac{a_0 c_0(\rho_1 h_2^2 - \rho_2 h_1^2)}{2 h_1 h_2(\rho_1 h_2 + \rho_2 h_1)} \approx -\frac{1}{2} a_0 c_0 \frac{h_2 - h_1}{h_2 h_1}, \tag{1.6}$$

$$\frac{1}{\lambda^2} = -\frac{3 a_0[1 - \rho_2 h_1^2/(\rho_1 h_2^2)]}{4 h_1^2 h_2(\rho_2/\rho_1 + h_1/h_2)} \approx -\frac{3 a_0}{4}\frac{h_2 - h_1}{h_2^2 h_1^2}, \tag{1.7}$$

with c_0 in equation 1.4 and the approximation $(\rho_2 - \rho_1)\rho_2 \ll 1$.

Interfacial solitary waves have an upper theoretical limit on the wave speed and amplitude when h_1 and h_2 are finite (Grue, Jensen, et al. 1999):

$$c_{max}^2 = \frac{g(h_2 + h_1)(\rho_2 - \rho_1)}{(\rho_2^{1/2} + \rho_1^{1/2})^2} \qquad a_{max} = \frac{h_2 \rho_1^{1/2} - h_1 \rho_2^{1/2}}{\rho_2^{1/2} + \rho_1^{1/2}}. \tag{1.8}$$

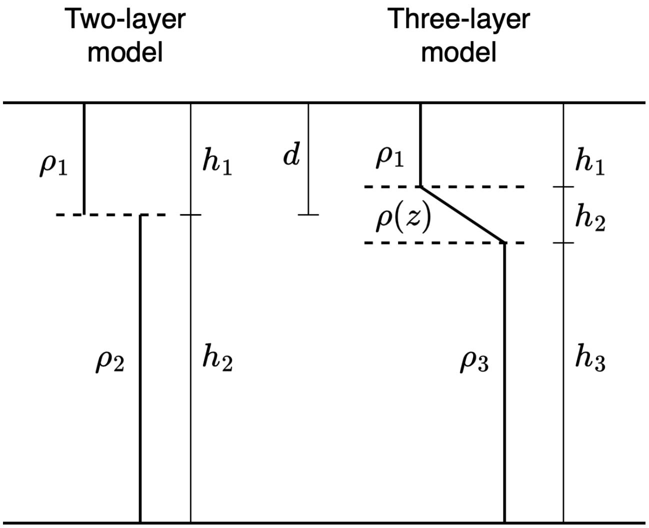

Figure 1.2: The figure presents a schematic of the two- and three-layer model setups. The two-layer model has an upper layer thickness h_1 and density ρ_1 and a lower layer thickness h_2 and density ρ_2, separated by a sharp pycnocline visualized by a dotted line. The three-layer model has an upper layer thickness h_1 and density ρ_1 and a lower layer thickness h_3 and density ρ_3. The layers are separated by a pycnocline (visualized by dotted lines) of thickness h_2 and density $\rho(z)$ that varies linearly within the pycnocline. The variable d visualizes the middle depth of the pycnocline in each case.

Alternatively, c_{max} can be expressed on the form $c_{max}^2 = gh_2'h_1'(\rho_2 - \rho_1)/(\rho_2 h_1' + \rho_1 h_2')$, with $h_1' = h_1 - a_{max}$ and $h_2' = h_2' + a_{max}$ $(h_1 < h_2)$.

Experimental and numerical studies show that the KdV theory provides a valid description of solitary waves with small amplitude (Diamessis and Redekopp 2006; Grue, Jensen, et al. 2000). An extended variant of the KdV equation, the eKdV equation, is a useful variant which includes cubic nonlinearity. See e.g., Fructus and Grue 2004; Grimshaw, Pelinovsky, and Poloukhina 2002; Lee and Beardsley 1974; Miles 1981; Stanton and Ostrovsky 1998.

1.2.2 KdV theory versus fully nonlinear theory

Models based on weakly nonlinear and weakly dispersive theories are useful for describing the motion of internal waves when the lines of constant density do not deviate too much from their resting level and the waves are long compared to the water depth. However, based on field observations, it was found that the waves were (highly) nonlinear and remained coherent with a finite amplitude for long distances. The waves possess characteristics that can only be explained through fully nonlinear models. Nevertheless, KdV-type theories, even in their weakly nonlinear form, have played an essential role in exposing fundamental properties of internal waves, despite falling short of exact quantitative outcomes.

Fully nonlinear two-layer models, where an interface separates two homogeneous fluid layers of constant depth, have had the most extensive development theoretically (Amick and Turner 1986; Grue, Friis, et al. 1997), experimentally (Koop and Butler 1981; Michallet and Barthelémy 1998), and numerically (Camassa et al. 2006; Fructus and Grue 2004; Grue, Friis, et al. 1997; Grue, Jensen, et al. 2000).

Grue, Friis, et al. 1997 derived a time-stepping method for a two-layer fluid fully nonlinear two-dimensional motion. They found good agreement when comparing their fully nonlinear interface model to available experiments. Further, in comparison with weakly nonlinear theories like KdV, Benjamin-Ono, and finite-depth theories (see e.g., Grue 2006 for definitions), their results indicated that in many cases, weakly nonlinear theories have a limited application. They showed that these theories could lead to inaccurate wave shapes when the maximum elevation of the wave becomes comparable to the thinner layer's thickness. Consequently, weakly nonlinear theories have a limited range of validity. This was further explored by Grue, Jensen, et al. 1999. They conducted laboratory experiments of large-amplitude internal waves over various depth layers and wave amplitudes. The laboratory results were compared against the fully nonlinear interface model presented by Grue, Friis, et al. 1997 with good agreement. In addition, a comparison to the weakly nonlinear KdV theory was conducted, where their results show that the KdV theory deviates systematically when the waves' amplitude exceeds approximately 0.4 times the thinner layer's thickness, as seen in Figure 1.3. Please be advised that in the figures, the upper layer is labeled h_2 from their experiment, which is h_1 described here. Figure 1.3a illustrates the wave profile as the non-dimensional wave amplitude increases, and Figure 1.3b displays the evolution of the excess speed computed from Equation (1.6). Nevertheless, the KdV theory was found valuable for all the different depth ratios experimented with as long as the wave amplitude was small.

1.2.3 Linear long wave speed of a three-layer model

Following Fructus and Grue 2004, linear (lin.) internal waves (waves of small amplitude) can be described by the stream function on the form $\psi(x - c_{lin}t, z) = a_0\phi(z)\exp(ik(x - c_{lin}t))$, where a_0 denotes the amplitude, z denotes the vertical axis, and c_{lin} is the linear long-wave speed. The wave train is assumed periodic with a wavenumber k, propagating with a linear wave speed. The vertical structure function $\phi(z)$ satisfies the Taylor-Goldenstein equation

$$(d^2/dz^2 + N^2/c_{lin}^2 - k^2)\phi = 0, \tag{1.9}$$

with the boundary conditions $\phi(0) = \phi(H) = 0$, and at the two interfaces the functions ϕ and $d\phi/dz$ are continuous. The solution takes the form

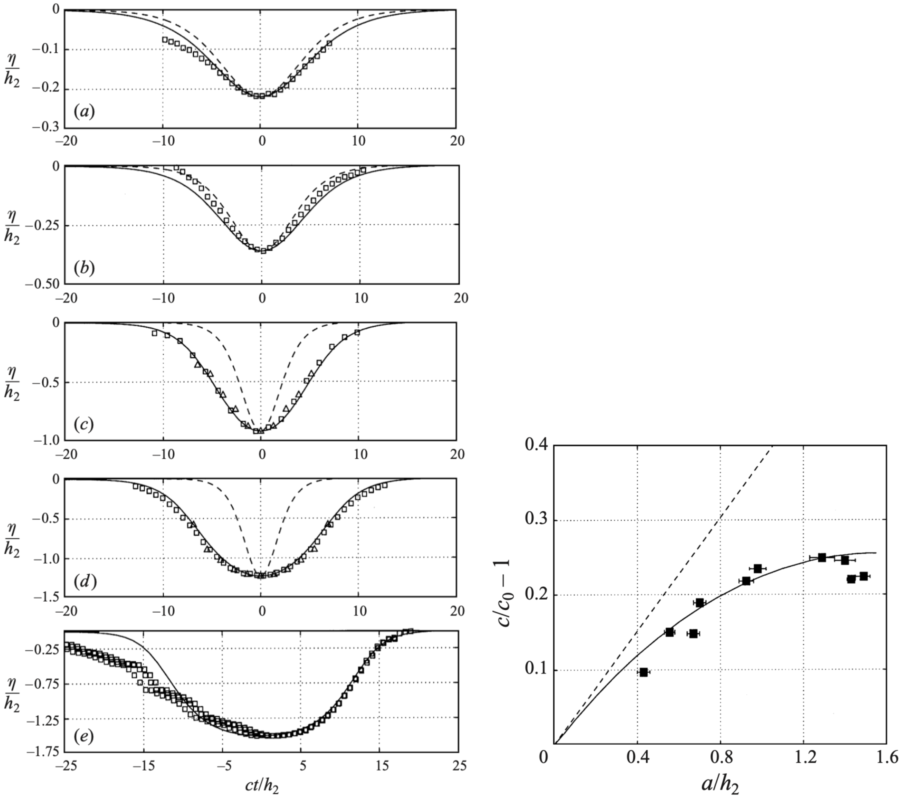

(a) (b)

Figure 1.3: a) Comparisons of experimental wave profiles (squares) to fully nonlinear theory (solid lines) and KdV theory (dashed lines). The subfigures in a) have non-dimensionless wave amplitudes of (a) $a/h_1 = 0.22$, (b) $a/h_1 = 0.36$, (c) $a/h_1 = 0.91$, (d) $a/h_1 = 1.23$, and (e) $a/h_1 = 1.51$. b) Comparison of the excess speed $\Delta c = c/c_0 - 1$ versus non-dimensionless wave amplitude of the measured waves (square) to fully nonlinear theory (solid lines) and KdV theory (dashed lines). Please be advised that in the figures, the upper layer is labeled h_2 from their experiment, which is h_1 described here. Images adapted from Grue, Jensen, et al. 1999.

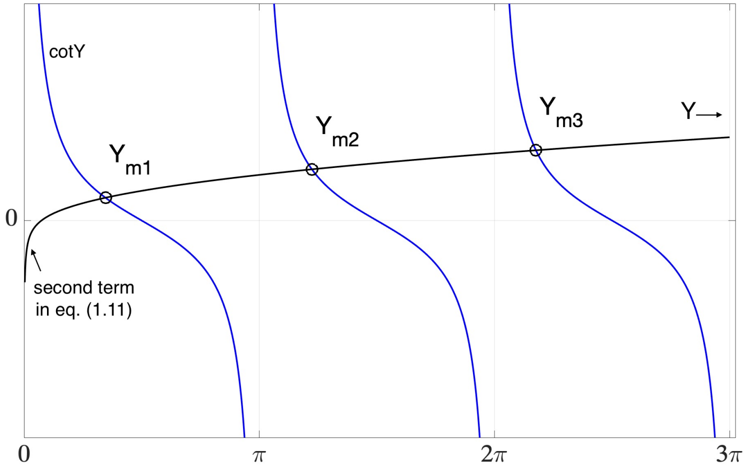

Figure 1.4: The solution of the three first modes, Y_{m1}, Y_{m2}, and Y_{m3}, respectively, from Equation (1.11). The blue lines represent the first term in the equation, and the black line is the second term. The circles mark the intersections.

$A_j \cos(\hat{K}_j z) + B_j \sin(\hat{K}_j z)$ in each layer ($j = 1, 2, 3$). Here, $\hat{K}_j = \sqrt{N_j^2/c_{lin}^2 - k^2}$, A_j and B_j are constants, and $N_j^2 = -(g\Delta\rho_j)/(\rho h_j)$ is the Brünt-Väisälä frequency. By using the boundary conditions at $z = h_1 + h_2 + h_3$, $z = h_1 + h_2$, $z = h_1$, and $z = 0$, the dispersion relation $c_{lin}(k)$ can be obtained, providing

$$\hat{K}_2^2 - T_1T_2 - T_1T_3 - T_2T_3 = 0, \quad T_j = \hat{K}_j \cot(\hat{K}_j h_j). \tag{1.10}$$

By letting $k \to 0$ in Equation (1.10), the linear long wave speed c_{lin} is obtained. The three-layer model presented here is a case where $N_1 = N_3 = 0$ (see Fructus and Grue 2004 regarding other cases). Then Equation (1.10) simplifies to

$$\cot(Y) - [(Yh_1)/h_2 - h_2/(h_3 Y)] \,/\, [1 + (h_1/h_3)] = 0, \tag{1.11}$$

where $Y = (N_2/c_{lin})h_2$. The Brünt-Väisälä frequency in the pycnocline is constant (at rest) and given by $N_\infty^2 = g(\rho_3 - \rho_1)/h_2\rho_3$, where $(\rho_3 - \rho_1)/\rho_3 \ll 1$. The longest wave mode (m1) is obtained for $Y = N_\infty h_2/c_{lin}$ in the interval $(0, \pi)$. The speed of the mode 2 (m2) wave is found in the interval $(\pi, 2\pi)$. See Figure 1.4.

1.3 Internal waves - a brief review

1.3.1 Early observations

There is an old phenomenon related to internal waves known as dead-water. In the Arctic Ocean during Nansen's Polar expedition (1893-96), with the boat

Fram, Nansen encountered internal tides (Nansen 1897). At the time, he did not know it was the internal tide he had measured but described this as the dead-water phenomenon. When the ship entered the water with a thermocline close to the surface, internal waves were generated by the ship, and they experienced a considerable reduction in the ship's speed, hence the term dead-water. This phenomenon was first known amongst the seamen. Ekman 1904 presented the findings of Nansen with more details, in addition to carrying out theoretical and experimental work. In 1909, the Swedish oceanographer Otto Pettersson discovered internal tides in Gullmarfjorden and described the phenomenon (Grue 2006). It is important to mention that proper credit by Otto Pettersson was given to Nansen for being the first to describe internal tides in this field.

Internal solitary waves and wave trains in marginal seas, straits, and coastal waters are undoubtedly present, as confirmed by numerous in-situ and remote-sensing observations (for a short review, see, for instance, Ostrovsky and Stepanyants 1989 and references therein). In the 1960s, the development of oceanography equipment, e.g., fast internally recording vertical arrays of thermistors, led to observations of large ocean-going internal pulse waves (Helfrich and Melville 2006). In 1965, Perry and Schimke (Perry and Schimke 1965) recorded groups of internal waves with amplitudes reaching 80 m and with wavelengths of 2000 m, propagating on a thermocline at 500 m where the local water depth was 1500 m. Other early observations were conducted in the Strait of Gibraltar (Ziegenbein 1969; Ziegenbein 1970), in the Massachusetts Bay (Halpern 1971; Haury, Briscoe, and Orr 1979), in Lock Ness (Thorpe 1971), and in the Seneca Lake in New York (Hunkins and Fliegel 1973). From field observation, Ziegenbein 1969; Ziegenbein 1970 measured short-period internal waves, propagating in the pycnocline as groups, with steepness (the amplitude-length ratio) occasionally reaching considerable large values implying that these waves may be significantly nonlinear. Even though internal solitary waves may become highly nonlinear, they may remain stable at the same time, as measured by Duda et al. 2004 in the South China Sea.

1.3.2 Observing internal waves from above

Even though internal waves cannot be seen with the naked eye, Ziegenbein 1969 demonstrated that the scattering of short surface waves observed by marine radars could be inferred as internal waves. Internal waves strongly modulate the surface wave spectrum on the ocean's surface. They can be seen as alternating bands of smooth and rough water appearing as dark and light stripes on images taken by, e.g., synthetic aperture radar (SAR). Apel, Proni, et al. 1975 successfully combined and correlated images from the ERTS-1 spacecraft and measurement from ship. However, it was first in 1978, with the launch of SEASAT, SAR images of the coastal ocean showing packets of internal waves propagating shoreward, separated by tidal periods, were taken (Apel, Holbrook, et al. 1985). The images proved that internal waves are a common phenomenon in the oceans. Dokken et al. 2001 studied 2600 SAR images taken over nine years along the Norwegian

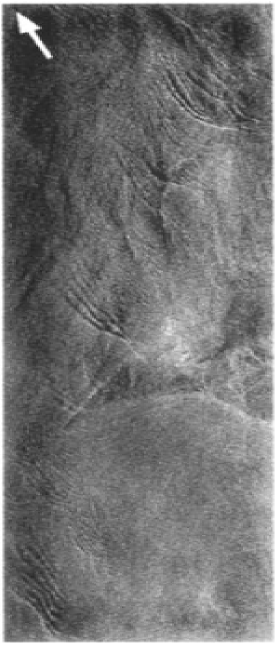

Figure 1.5: ERS-1 SAR image (30 × 100 km) of internal waves outside Andøya, Norway, where the white arrow indicates the North direction. A total of 8 wave trains, with an average distance of 10.8 km between the trains, can be seen propagating against the coastal current. Image adapted from Dokken et al. 2001, with permission from Wiley.

continental shelf. Figure 1.5 presents one SAR image showing eight internal wave trains outside Andøya, Norway.

Consequently, SAR images, sunlight images, and Moderate Resolution Imaging Spectroradiometer have been used to study internal wave behavior and properties (Hsu, A. K. Liu, and C. Liu 2000; C. Jackson 2007; Nash and Moum 2005). Remote imaging has accelerated our understanding and mapping of internal waves. We now have a much bigger picture and a better idea of how widespread internal waves are in our oceans (C. Jackson 2007). Identifying such internal wave patterns also holds great significance in oceanography and has implications for various industries, such as marine transportation and offshore engineering.

1.3.3 Evolution scenarios of internal waves

Internal waves can evolve in various manners. The following sections will touch upon three different scenarios before introducing various instability mechanisms the waves experience and or induce (Section 1.3.4) and how these instability mechanisms affect sediment motion in the bottom boundary layer (Section 1.3.5).

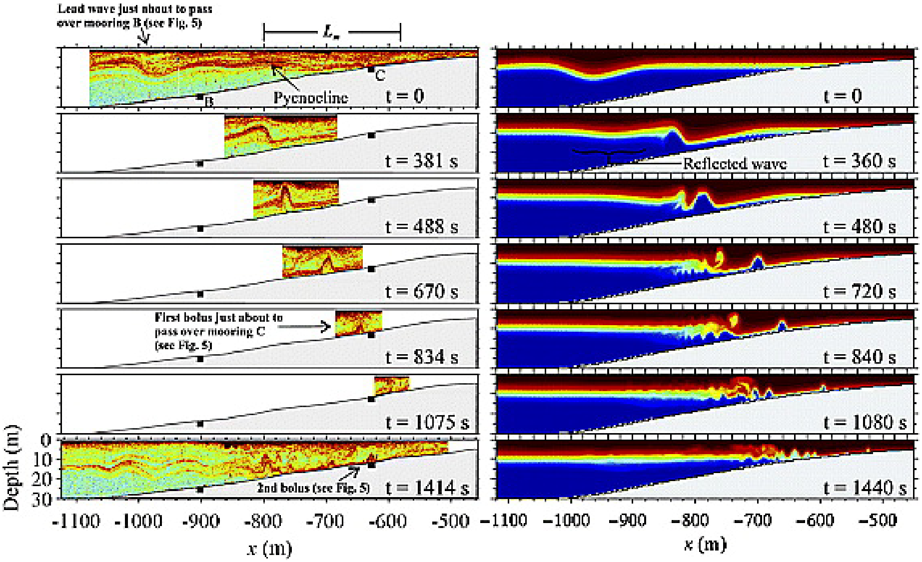

Figure 1.6: The left figure shows the evolution of an observed internal solitary wave of depression propagating up a slope moving past the turning point, evolving into waves of elevation, measured by Bourgault et al. 2007. The right figure displays the results of a numerical simulation showing the density field variations of an internal solitary wave exhibiting similar characteristics as the observed wave in the left figure. Image adapted from Bourgault et al. 2007, with permission from Wiley.

1.3.3.1 Depression to elevation waves during shoaling

The highly nonlinear wave structure, characteristics, and behavior of internal solitary waves from deep-depth sites propagating towards the shore are still poorly understood (Lamb 2014; Vlasenko and Hutter 2002). On the Continental slope in the Northern South China Sea, Duda et al. 2004 conducted field measurements observing both transbasin waves and waves at or near tidal frequencies. Transbasin waves are large-amplitude solitary waves of depression and may be considered the largest internal gravity waves in terms of their amplitude (Duda et al. 2004). Duda et al. 2004 measured stable waves of nearly permanent form with amplitude a up to 165 m ($a/d \sim 3.7$, mid-depth of the pycnocline $d \sim 45$ m) at a 350 m depth site propagating with a nonlinear speed of $c \sim 1.27$ m s^{-1}. When the waves encountered the slope, they were seen to undergo rapid changes when propagating from 350 m to 80 m depth. Nevertheless, the waves appeared to be stable.

When waves of depression propagate up weak slopes, where at a particular position the upper and lower layer may be of equal height (known as a turning point (Knickerbocker and Newell 1980)), the waves may go from a single depression wave to break up into one or a series of dispersive elevation waves due to a steepening of the rear part of the depression wave (see Figure 1.6). Bourgault et al. 2007 conducted field measurements in the St. Lawrence Estuary, measuring shoaling internal wave trains to quantify the evolution of waves from depression to elevation (change of polarity). Figure 1.6 presents their results of the evolution of the internal solitary wave as it propagates up the slope. The left figure illustrates the results from their field observation, whereas the right figure shows the results from a numerical simulation of the field observations. They observed waves of elevation (note: they term these waves for boluses) generated from shoaling waves of depression where the properties amplitude, nonlinear wave speed, and wavelength (L) remained almost constant prior to the polarity change but started to decrease rapidly and linearly afterward. However, they showed that the boluses aspect ratio $a/L = 0.4 \pm 01$ remained constant during the run-up.

Numerous studies have examined the breaking process of shoaling internal solitary waves of depression, both in laboratory experiments (Boegman and G. N Ivey 2009; Boegman, G. N. Ivey, and Imberger 2005; Helfrich 1992; Helfrich and Melville 1986; Michallet and G. N. Ivey 1999; B. R. Sutherland, Barrett, and G. N. Ivey 2013) and numerical simulations (Aghsaee, Boegman, and Lamb 2010; Arthur and Fringer 2014; Nakayama et al. 2019; Vlasenko and Hutter 2002; Xu and Stastna 2020). When waves of depression travel over steeper slopes, the waves will break instead of fission into packets of elevation waves (Xu and Stastna 2020). Waves with large enough amplitude propagating over slopes where there is no turning point will also break (e.g. Kao, Pan, and Renouard 1985). Hartharn-Evans et al. 2022 conducted a combined study of numerical simulations and laboratory experiments of internal solitary waves of depression propagating up a linear slope. They investigated how the effect of stratification would have on the shoaling characteristics of the wave. The studies were conducted with three different stratifications, where they found that the form of stratifications affects the breaking type associated with the shoaling wave.

1.3.3.2 Depression waves

The majority of the published field studies are on waves of depression. Waves of depression propagating over near-flat topography have been observed by, e.g., Stanton and Ostrovsky 1998 over the Continental Shelf offshore from Oregon. Quaresma et al. 2007 conducted in-situ observations at the northern shelf of Portugal, over the Nasaré sub-marine canyon rim, where the semi-diurnal tide drives the waves. Nonlinear internal waves of depression with amplitude in the range $a \sim 10-30$ m ($a/d \sim 0.68-1.98$, $d \sim 15$ m) with periods of $8-25$ minutes were propagating where the local water depth was 80 m (see Figure 1.7).

Field observations of nonlinear internal waves of depression over a low-gradient topography on Australia's Northwest Shelf have been conducted by Zulberti, N. L. Jones, and G. N. Ivey 2020. The semi-diurnal tide drove the measured internal waves, and the wave groups had amplitude in the range of $a \sim 37$ m ($a/d \sim 0.75$, $d \sim 50$ m) up to 70 m ($a/d \sim 1.4$, $d \sim 50$ m) where the local

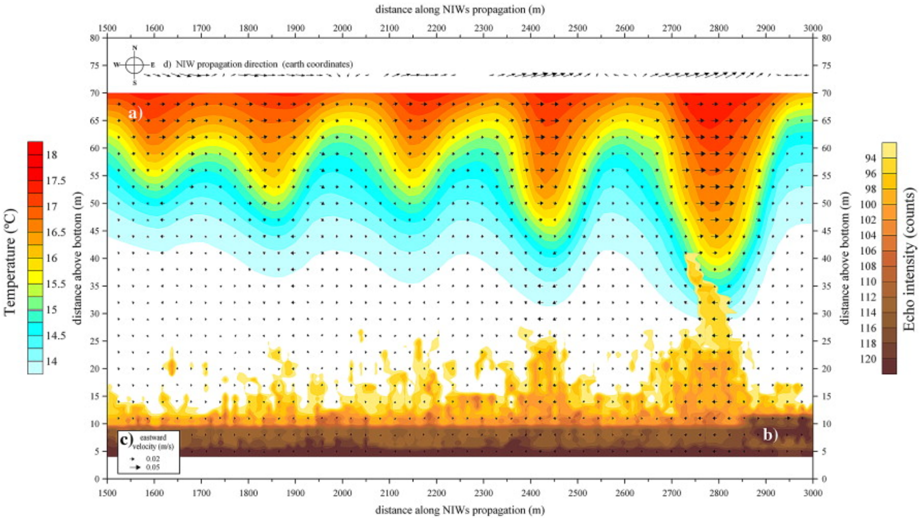

Figure 1.7: a) Isotherms contoured for five nonlinear internal solitary waves propagating from left to right observed by Quaresma et al. 2007. b) The echo intensity displays the motion of sediments. c) Vector plot of the measured eastward velocity. d) Velocity vectors of the near-surface short-period current showing. Image adapted from Quaresma et al. 2007, with permission from Elsevier.

water depth was 250 m. The waves had periods of 20 minutes and a measured propagation speed of $c = 0.95\ \mathrm{ms}^{-1}$.

Numerous laboratory investigations, such as those carried out by Carr and Davies 2006; Carr, Davies, and Shivaram 2008; Grue, Jensen, et al. 1999 and Aghsaee and Boegman 2015, along with several numerical simulations conducted by Aghsaee, Boegman, Diamessis, et al. 2012; Diamessis and Redekopp 2006; Ellevold and Grue 2023; Fructus, Carr, et al. 2009; Grue, Friis, et al. 1997; Thiem et al. 2011; Zahedi, Aghsaee, and Boegman 2021, have been undertaken.

We will examine internal solitary waves of depression in detail in Chapter 2.

1.3.3.3 Elevation waves

Research on internal solitary waves of elevation has been carried out both in laboratory settings (Carr and Davies 2010) and through the use of numerical simulations (Bogucki and Redekopp 1999; Diamessis and Redekopp 2006; Stastna and Lamb 2002; Stastna and Lamb 2008; Wang and Redekopp 2001). Due to the difficulties of measuring and observing them in nature, these studies aim to gain a deeper understanding of the nature of these waves and their effects.

Waves of elevation propagating over near-flat topography have been observed, e.g., on the Continental Shelf by Ostrovsky and Stepanyants 1989. Ostrovsky and Stepanyants 1989 provide additionally a review of various field observations. On the shelf of Palos Verdes (California, LA), Bogucki, Dickey, and Redekopp 1997 observed packets of internal solitary waves propagating in a bottom stratified layer, with a well-mixed upper layer, against a shear current of speed O(1cm s^{-1}) at the bottom. They observed waves with leading amplitude up to 4 m ($a/d \sim 0.2$, $d \sim 20$ m) with a length of 90 m, where the total water depth was approximately 60 m. In Massachusetts Bay, Scotti and Pineda 2004 observed trains of large-amplitude, high-frequency internal waves of elevation with trapped turbulent cores. The waves had amplitudes nearly half the water depth (H = 25 m).

1.3.4 Instability

As seen above, various internal waves may develop, and they all evolve differently when propagating through or encountering varying environments such as current, topography, and stratification. Consequently, internal waves can induce and or experience various instability mechanisms. For instance, internal waves may induce bottom boundary layer instability (Aghsaee, Boegman, Diamessis, et al. 2012; Diamessis and Redekopp 2006; Ellevold and Grue 2023; Stastna and Lamb 2008), experience shear instability and dissipation in the interior of the water column (Carr, Franklin, et al. 2017; Fructus, Carr, et al. 2009; Moum et al. 2003), or overturning as they shoal (Boegman, G. N. Ivey, and Imberger 2005; Helfrich 1992; Helfrich and Melville 1986; Lamb 2014). Internal waves that break can be highly effective in mixing water that is rich in nutrients from the lower depths up to the more biologically active upper layer (Sandstrom and Elliott 1984).

1.3.4.1 Bottom boundary interaction

Propagating internal waves induce a velocity field that may interact with the bottom boundary layer. This interaction can lead to the onset of several different instability mechanisms, where the induced instability depends on whether the wave is of depression or elevation (Boegman and Stastna 2019). However, the velocity field along the bathymetry (relative to a frame of reference following the wave) will, regardless of the vertical direction of the pycnocline, experience a spatially varying acceleration (Bogucki and Redekopp 1999). The basic instability scenarios for the different waves can be seen in Boegman and Stastna 2019 their Figure 6. An overview of the different bottom boundary layer instability mechanisms can be found in the review by Boegman and Stastna 2019.

The internal wave-induced pressure gradient is not precisely balanced in the bottom boundary layer (due to no-slip boundary). Hence, there is always an adverse pressure gradient region beneath the wave trough, regardless of whether the wave is of depression or elevation (Aghsaee, Boegman, Diamessis, et al. 2012; Boegman and Stastna 2019; Diamessis and Redekopp 2006; Stastna and Lamb 2008). For waves of depression, the adverse pressure gradient region occurs underneath the rear half of the wave. When the adverse pressure gradient increases, an (unstable) reversed flow boundary jet in the same direction as the wave propagation is formed above the bottom (Aghsaee, Boegman, Diamessis, et al. 2012; Carr and Davies 2006; Diamessis and Redekopp 2006; Ellevold and Grue 2023). This jet is labeled *separation bubble*, an enclosed region of flow (Gaster 1967; Pauley, Moin, and Reynolds 1990). Carr and Davies 2006 found that flow separation will always occur, having laminar boundary layers under waves of depression. When the wave amplitude is above a certain threshold, instabilities will develop in the separation bubble (Aghsaee, Boegman, Diamessis, et al. 2012; Carr, Davies, and Shivaram 2008; Diamessis and Redekopp 2006; Ellevold and Grue 2023). Vortices may then form, grow, and shed into the water column. The majority of the work conducted in this thesis regards this type of instability and how it evolves, which is elaborated in Chapter 2.

For waves of elevation, the adverse pressure gradient region and separation bubble develop now ahead of the wave crest (Bogucki and Redekopp 1999; Stastna and Lamb 2002; Stastna and Lamb 2008). Nonlinear internal solitary waves of elevation and their boundary layer have been investigated numerically (Bogucki and Redekopp 1999; Stastna and Lamb 2002; Stastna and Lamb 2008) and by experiments (Carr and Davies 2010). Stastna and Lamb 2002 performed fully nonlinear simulations of the scenario described in Bogucki and Redekopp 1999, where waves of elevation propagate against an opposing current. Bogucki and Redekopp 1999 discusses that the bottom layer separates when the wave amplitude is above a certain threshold, and vorticity forms and becomes advected with the flow. However, Stastna and Lamb 2002 showed that the vortex instability arising was not due to a boundary layer separation but due to the interaction between the wave's velocity field and the boundary layer vorticity of the opposite background current. Stastna and Lamb 2008 showed further that no instability would arise if the current was too weak or the wave amplitude was too low. In addition, they showed that the current-driven vorticity was advected into the footprint of the wave. In the laboratory experiments by Carr and Davies 2010, an internal solitary wave of elevation propagated in an unsheared two-layer, stably-stratified fluid. They found conversely that the flow reversal occurred under the wave's rear part, in the deceleration phase where the pressure gradient is favorable. They observed no instability in the experiments despite having waves with amplitudes up to the theoretical maximum.

During shoaling, the waves focus wave energy and create a strong near-bottom velocity field and adverse pressure gradient (Aghsaee, Boegman, Diamessis, et al. 2012; Aghsaee, Boegman, and Lamb 2010; Boegman and Stastna 2019). Xu and Stastna 2020 performed a high-resolution numerical simulation of internal solitary waves of depression, where their domain represented a tilted wave tank. They found that boundary layer instability consistently occurred during the shoaling process, presented as a separation bubble. As the wave turns into packets of elevation waves, the separation bubble breaks down into two parts.

1.3.4.2 Breaking and mixing in the pycnocline

Internal wave motion, especially the breaking of internal waves, is a topic of great importance and interest to physical oceanographers and climate modelers. They are particularly interested in the wave-driven turbulent mixing that occurs

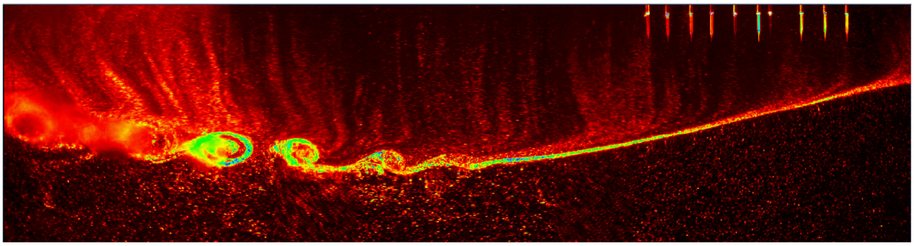

Figure 1.8: Side view image of an internal solitary wave of depression from a laboratory experiment conducted by Carr, Franklin, et al. 2017, presented in a false color image showing light intensity. It is a composite image (see their Figure 4 for the sequential development of the overturning billows) providing a qualitative view of the observed breaking dynamics. Uneven seeding caused the vertical streaks in the upper layer and are not artifacts of the flow dynamics. The horizontal and vertical extent of the image are $\Delta x = 1.81$ m and $\Delta z = 0.42$ m, respectively. Image adapted from Carr, Franklin, et al. 2017.

in the ocean. The study conducted by MacKinnon, Zhao, et al. 2017 provides a summary of recent developments in the understanding of internal wave-driven turbulent mixing in the ocean interior. The study presents new parameterizations for global climate and ocean models and discusses their climate impacts.

Breaking of internal waves often occurs due to either shear-driven instability across the pycnocline or convective instability, or, in some cases, a combination (Carr, Fructus, et al. 2008). The occurrence of internal waves that result in breaking can profoundly impact the surrounding environment. Their effect on mixing is of particular significance, which can significantly alter the composition and distribution of particles. Many different breaking criteria have been outlined and discussed over the past decades, and we will present some of these below.

Shear instability:

When having a thin, continuously linear stratified interface in a two/three-layer system, a shear flow characterized by the velocity gradient $\partial u/\partial z$ may occur at the interface. Here, u is the horizontal velocity and z is the vertical coordinate. The shear flow may become unstable, and the growth of the perturbation typically presents as Kelvin-Helmholtz billows, which will begin to grow at the wave's maximum depression, hence at the trough (Lamb and D. Farmer 2011; Moum et al. 2003). Figure 1.8 visualize an internal solitary wave of depression experiencing Kelvin-Helmholtz instability in the pycnocline from the experiments conducted by Carr, Franklin, et al. 2017. The front of the internal wave will always be stable when propagating between homogeneous layers in a pycnocline that was initially linear stratified (three-layer stratification) (Fructus, Carr, et al. 2009).

A sufficient condition for the internal waves to be stable, according to Miles 1961 when having steady shear flows, the Richardson number should exceed a value of 1/4 everywhere. The Richardson number provides an estimate of the inverse ratio between the stable density profile and the unstable velocity profile

(Grue, Jensen, et al. 1999): $Ri = -\frac{g}{\rho}\frac{\partial \rho}{\partial z}/(\frac{\partial u}{\partial z})^2$.

Grue, Jensen, et al. 1999 investigated the properties of internal waves of large amplitude and documented the breaking of internal solitary waves through laboratory experiments. They estimated the Richardson number given by Miles 1961 for different experiments and found that for a breaking wave $Ri = 0.07$ and $Ri = 0.23$ or larger for stable waves.

Further analysis and studies under different conditions (Almgren, Camassa, and Tiron 2012; Barad and Fringer 2010; Fructus, Carr, et al. 2009; Lamb and D. Farmer 2011; Troy and Koseff 2005) show that the criterion for the formation of Kelvin Helmholtz billows cannot solely be based upon the Richardson number alone. Having $Ri < 1/4$ is a necessary condition for shear instabilities but insufficient (Lamb 2014). For a comprehensive investigation of the shear-induced billows generated, see e.g. Carr, Franklin, et al. 2017.

Fructus, Carr, et al. 2009 conducted laboratory experiments to examine this stability threshold when having internal solitary waves of large amplitude and $Ri < 1/4$. In addition, they compared their results with fully nonlinear calculations in a three-layer fluid with good agreement. Based on the derivation conducted by Bogucki and Garrett 1993, a novel stability criterion was obtained for the shear instability of the Richardson number in the form of $Ri_{min} = -0.23L_{x,p}/\lambda + 0.298 \pm 0.016$, in the $(L_{x,p}/\lambda, Ri_{min})$-plane. Here λ is the wave's half-width, and $L_{x,p}$ is the horizontal length of a small region, a pocket, of a finite lateral extent present in the wave (see Fructus, Carr, et al. 2009 their Figure 9). In addition, they presented an even sharper breaking threshold than Ri_{min}: $L_{x,p}/\lambda > 0.86$ (breaking) and $L_{x,p}/\lambda < 0.86$ (stable). Accordingly, $L_{x,p}/\lambda = 0.86$ provides a more suitable threshold. This threshold also takes the minimum values of the Ri_{min} into account since it is viewed in a fixed frame of reference; thus, the pocket will have a Ri_{min} less than 1/4 within its horizontal domain.

When internal solitary waves of depression propagate on a slope, the wave may break in its rear face. If breaking, it results in mixing the pycnocline and generating multiple boluses (i.e., a turning point is present). The boluses will continue propagating up the slope, past the pycnocline-slope intersection. The boluses transport denser water and enhance the mixing of the pycnocline. Laboratory experiments (Boegman, G. N. Ivey, and Imberger 2005; Helfrich 1992; Helfrich and Melville 1986) have been performed on internal solitary waves of depression incident on a uniform slope to measure and describe the kinematics and conversion into boluses and to find a breaking criterion. Three different types of wave breaking were identified: when the rear face of the wave overturns, it is identified as plunging breakers, whereas when the rear face begins to overturn but collapses on itself, it is labeled collapsing breakers, and the third type of wave breaking is spilling (Boegman, G. N. Ivey, and Imberger 2005). Aghsaee, Boegman, and Lamb 2010 expanded this classification to four different types: surging, collapsing, plunging, and fission breaker. Studies have explored a coherent classification scheme of the four given different types of key-breaking processes (Aghsaee, Boegman, and Lamb 2010; Hartharn-Evans et al. 2022; Nakayama et al. 2019; B. R. Sutherland, Barrett, and G. N. Ivey

2013). There has been an interest in classifying the breaking mechanisms based on the full range of incoming wave and slope conditions. Boegman, G. N. Ivey, and Imberger 2005 introduced a classification system based on the internal Iribarren number, a function of the bathymetric slope, wave amplitude, and the wavelength of the solitary wave. Studies have further shown that only having the internal Iribarren number is insufficient to classify the different types of breakers, and different alternative classifications for these breakers have been proposed (e.g., Aghsaee, Boegman, and Lamb 2010; Hartharn-Evans et al. 2022; Nakayama et al. 2019; B. R. Sutherland, Barrett, and G. N. Ivey 2013)

From the fieldwork of Duda et al. 2004, the aspect ratio (amplitude-wavelength) of the induced boluses remained constant during the run-up and was concluded to prevent the attainment of the kinematic instability-breaking criterion given by Vlasenko and Hutter 2002. Vlasenko and Hutter 2002 conducted numerical research on the transformation of large amplitude internal solitary waves over a slope-shelf topography. They documented the changes and development of the waves as they moved up the slope. Their calculations indicate that the wave breaking is mainly caused by the kinematic overturning of the wave's trailing face.

Convective instability:
Convective instability occurs when the local fluid velocity exceeds the wave velocity. Grue, Jensen, et al. 2000 conducted laboratory experiments on internal solitary waves of depression in a two-layer configuration with a thin linear stratified layer above a thicker homogeneous layer and having a free surface as the upper boundary (note: this two-layer configuration differs from the one presented in Figure 1.2. See Figure 2a in Grue, Jensen, et al. 2000 for a visualization of their configuration). From their experiments, convective breaking was seen to occur in trapped cores in the waves, where the instability arose in the leading part of the wave as small vortices. Carr, Fructus, et al. 2008 also conducted laboratory experiments on internal solitary waves of depression for the same two-layer configuration. From the experiments, they observed a combination of shear and convective instability, which had never been seen before. However, they conducted their experiments with different upper boundaries (free surface, a rigid lid, and a wetting agent added to the free surface). They showed that the type of upper boundary chosen directly affects convective instability and wave amplitude (but does not affect the shear instability). Hence, they pointed out that the rigid lid approximation is the cause of the discrepancy between the laboratory experiments by Grue, Jensen, et al. 2000 and the fully nonlinear theoretical predictions by Fructus and Grue 2004.

1.3.5 Sediment motion

As briefly presented above, internal waves may feel and interact with the bottom boundary, creating complex instabilities. These instability mechanisms provide potential for significant mixing and transport of sediments across the bottom boundary layer (Boegman and Stastna 2019).

The primary goal of the fieldwork conducted by Bogucki, Dickey, and Redekopp 1997 was to understand the function of the present internal solitary wave of elevation regarding resuspension and mixing of sediments. During their fieldwork, they observed enriched concentrations of particles, resuspension, and transport. Based on their data, they proposed a two-reason resuspension mechanism hypothesis; due to the adverse pressure gradient on the leading edge of the wave, a reverse flow - separation bubble - is present, and the resulting sediment resuspension and transport are a result of instabilities destabilizing the separation bubble. They measured a flow reversal up to $\sim 13\%$ of the total water column above the sea bottom and discussed that by having sufficiently large waves, the wave train would behave as a pump by lifting and mixing sediments.

Quaresma et al. 2007 investigated the ability of the internal waves of depression to resuspend particles. Their results showed that only the strongest measured waves could resuspend sediments. One of the most substantial local sediment concentrations measured was as high up as 56% of the total water column below the leading wave. This interaction can be seen in Figure 1.7, showing a nonlinear internal wave group of five nonlinear waves, where the echo intensity visualizes the sediments. A vertical pumping mechanism was associated with the compression underneath the wave trough that was immediately followed by a subsequent layer expansion and was seen as one of the factors driving the resuspension mechanism observed by Zulberti, N. L. Jones, and G. N. Ivey 2020.

Comparison between laboratory experiments/simulations and the ocean still has a long way to go (Boegman and Stastna 2019; Stastna and Lamb 2008). However, numerical simulations and laboratory experiments of internal solitary waves-sediment interaction are beneficial for visualization and idealized investigations (Aghsaee and Boegman 2015; Aghsaee, Boegman, Diamessis, et al. 2012; Boegman and G. N Ivey 2009; Stastna and Lamb 2008). Aghsaee and Boegman 2015 conducted laboratory experiments of internal solitary waves of depression propagating over a flat bottom, investigating sediment transport and resuspension. Their results showed that the primary resuspension mechanism was the induced instabilities in the separation bubble, i.e., the generated vortices (bursts of vertical velocities). The work conducted in this thesis regarding the displacement of particles under the influence of internal waves of depression is further discussed in Paper II and Section 2.4.

Chapter 2

Internal solitary waves of depression

In this thesis, we investigate nonlinear internal solitary waves of depression propagating over a flat bottom. Our study focuses on the impact these waves have on the bottom boundary layer, inducing instabilities and vortex formations.

We examine internal solitary waves using high-resolution direct numerical simulations in two dimensions. The simulations are performed on a laboratory scale, while variations of the wave Reynolds number (defined below) provide insight for upscaling the results to the field scale. The work conducted in Paper I is directed towards the points (i), (ii) and (vi), (vii) stated in Section 1.1.4. Hence, regarding point (i), we numerically simulate and follow the setup and wave-generation procedure as conducted in the laboratory experiments by Carr, Davies, and Shivaram 2008, and provide answers to point (vi), in addition towards point (ii) where we have scrutinized the stability border in terms of different parameters, where as well point (vii) comes into play. Paper II considers point (iii) where the focus is on the internal wave-vortex-induced motion of Lagrangian tracer particles, in addition to points (vi) and (vii).

Papers I and II provide additional details on the method and procedure used in this thesis. The following overview will complement the Papers and present additional information and results.

The chapter is structured as follow: firstly, Section 2.1 will shortly present some motivation. Section 2.2 will briefly explain the solver used, the numerical wave tank, and wave characteristics. Then, we will continue with the wave-induced instability and stability borders in Section 2.3 where we also touch upon the generated vortices (Section 2.3.3) and the shear stress (Section 2.3.5) in the bottom boundary layer. Particle motion is examined in Section 2.4.

2.1 Motivation

Internal solitary waves of depression propagating over a flat bottom have been investigated through experiments performed in laboratory settings (Aghsaee and Boegman 2015; Carr and Davies 2006; Carr, Davies, and Shivaram 2008; Carr, Fructus, et al. 2008; Grue, Jensen, et al. 1999), numerical computations (Aghsaee, Boegman, Diamessis, et al. 2012; Camassa et al. 2006; Diamessis and Redekopp 2006; Fructus, Carr, et al. 2009; Fructus and Grue 2004; Grue, Friis, et al. 1997; Thiem et al. 2011; Zahedi, Aghsaee, and Boegman 2021), and field observations (Quaresma et al. 2007; Stanton and Ostrovsky 1998; Zulberti, N. L. Jones, and G. N. Ivey 2020).

To perform numerical simulations of non-hydrostatic features as internal solitary waves, one requires high-resolution and small time steps to produce accurate simulations, making it a challenging task (Boegman and Stastna 2019). Various methods and solvers have been used in numerous studies to simulate internal solitary waves. Diamessis and Redekopp 2006 conducted two-dimensional direct numerical simulations using the Navier-Stokes equations combined with weakly nonlinear Korteweg-de Vries (KdV) theory. Whereas Aghsaee, Boegman, Diamessis, et al. 2012 solved the Navier-Stokes equations in combinations with fully nonlinear wave formulations. Their simulations were initialized with a single mode-1 internal solitary wave by solving the eigenvalue problem Dubreil-Jacotin-Long (DJL) equation in terms of streamline displacement.

The numerical model used in this thesis is the second-order finite-volume solver Basilisk (Popinet and collaborators 2013–2023), which solves the two-phase incompressible Navier-Stokes equations. Instead of providing a background density profile as a tanh-profile to approximate a laboratory-generated two-layer stratified fluid, as implemented by, e.g., Aghsaee, Boegman, Diamessis, et al. 2012, we follow the same setup of the wave tank and wave generation procedure as conducted in the laboratory experiments of Carr, Davies, and Shivaram 2008. The choice to utilize this specific configuration and wave generation mechanism in the numerical model was influenced by the following statement by Boegman and Stastna 2019: *"While DNS provide much richer flow field data relative to experiments, to finally allow meaningful comparisons, one needs to address numerical simulations' long-standing inability (since Carr, Davies, and Shivaram 2008) to directly reproduce experimental observations"*.

Carr, Davies, and Shivaram 2008 conducted laboratory experiments of internal solitary waves of depression moving along a flat bottom, investigating the flow separation and vortex formation induced in the bottom boundary layer having the wave Reynolds number in the range $Re_w = 5.8 \times 10^4 - 6.6 \times 10^4$. The wave Reynolds number is determined by the total water depth H, the linear long-wave speed c_0, and the kinematic viscosity ν, obtaining $Re_w = c_0 H/\nu$ (Aghsaee, Boegman, Diamessis, et al. 2012; Carr, Davies, and Shivaram 2008; Diamessis and Redekopp 2006). Carr, Davies, and Shivaram 2008 studied and measured the threshold of when instability in form of vortices emerged in the bottom boundary layer by varying the wave amplitude from small amplitudes where no instability was present to large amplitudes where instability occurred.

In the two-dimensional numerical study by Aghsaee, Boegman, Diamessis, et al. 2012, they investigated the wave-driven instability over flat and sloping bottoms. Regarding their flat bottom cases, having $Re_w = 1.2 \times 10^4 - 4.9 \times 10^5$, they were not able to reproduce the threshold of instability found by Carr, Davies, and Shivaram 2008, which occurred much earlier than what was found in the simulations. Aghsaee, Boegman, Diamessis, et al. 2012 suggested possible reasons for this discrepancy, which was also repeated in the review by Boegman and Stastna 2019. Two of the reasons proposed were that the laboratory-observed instabilities are primarily three-dimensional and that the wave-generation method causes a flow that may influence the vortex generation. The conflicting results are addressed in Papers I and II, where we respond to the ongoing discussion.

2.2 Model setup in this thesis

The studies carried out in Papers I and II are described in each paper. Below, we briefly describe the finite volume solver, the creation of the numerical wave tank in Basilisk, and the various grid methods utilized in this thesis. We then explain and define the setup of the numerical wave tank, wave generation, wave characteristics and parameters, followed by an introduction to the parameter range of the numerical simulations.

2.2.1 Finite volume solver

2.2.1.1 The numerical solver

Fluid dynamics research is ever-evolving, focusing on creating faster and more precise numerical modeling algorithms. The numerical solver used in this thesis is Basilisk, the successor of Gerris (Popinet 2003; Popinet and collaborators 2013–2023). Basilisk is an open-source program for solving partial differential equations on adaptive Cartesian meshes. Accordingly, Basilisk is a second-order finite-volume solver where we can solve the two-phase incompressible Navier-Stokes equations (Popinet 2009). The field equations are solved by means of a multilevel Poisson solver, a second-order upwind scheme (Bell-Colella-Glaz Bell, Colella, and Glaz 1989) integrates the momentum equation, a geometric volume-of-fluid (VOF) method is used to describe the variable-density two-phase flow where the interfaces are immiscible, and the viscous terms are treated implicitly. The spatial discretization of the domain utilizes a quadtree-grid discretization scheme. The crucial part of the calculations is to resolve the wave-driven viscous boundary layer effect at the bottom of the fluid domain. We refer the reader to Paper II for a description of the time integration and spatial discretization used in this thesis. Some complementary descriptions of the discretization of the wave tank, the different grid structures, and the resolutions used in this thesis will be briefly described below. The solver has been widely documented in, e.g., López-Herrera, Popinet, and Castrejón-Pita 2019; Popinet 2003; Popinet 2009; Popinet 2011; Popinet 2015; van Hooft et al. 2018. See also references in Paper I.

The Basilisk framework includes OpenMP/MPI parallelism capability. The simulations conducted in this thesis were run in parallel (except for parts of the convergence study in Paper II) using shared memory (OpenMP). The computations were conducted on the Norwegian Research and Education Cloud (NREC) (http://nrec.no).

2.2.1.2 Spatial discretization - creating the numerical wave tank

Basilisk defines a spatial, quadratic domain of size $L \times L$ (Figure 2.1a) by default. The numerical wave tank is defined as a part of this domain, with the horizontal length L and a vertical height H $(< L)$ as seen in Figure 2.1b. Hence, the region above $L = H$ is masked out (marked by slanted lines). At $L = H$ we implement a rigid lid (see Section 2.2.2).

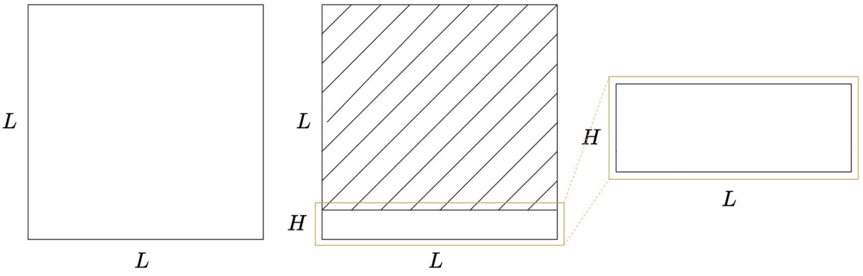

(a) (b) (c)

Figure 2.1: Schematic of (*a*) the default quadratic domain generated in Basilisk, (*b*) the domain where the shaded area visualizes the area masked out, and the non-shaded area becomes the numerical wave tank, (*c*) the numerical wave tank (further visualized in Figure 2.3).

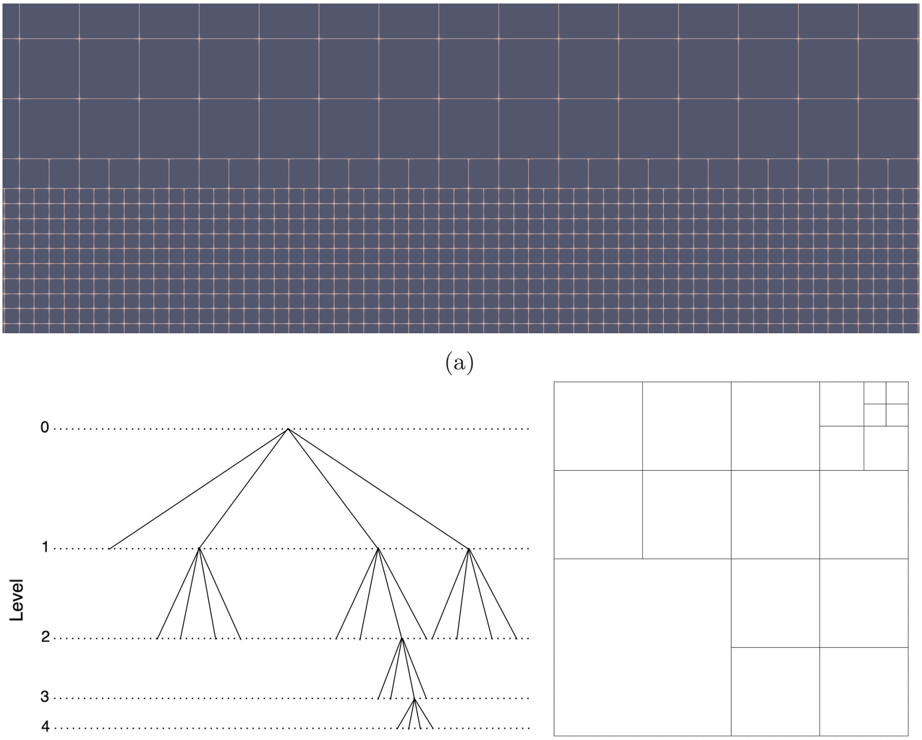

(a)

(b) (c)

Figure 2.2: Example of a quadtree discretization and structure: (a) visualization of a non-uniform grid with high resolution in the bottom transitioning over to a coarser resolution, (b) a logical tree representation, with the grid cells' respective spatial structure with varying refinement levels in (c).

2.2.1.3 Grid

In Basilisk, three different mesh/grid methods are available. These are Uniform Grid, Non-Uniform Grid, and Adaptive Grid, where each method will give rise to different grid structures. For uniform grids, the grid spacing in the whole domain is uniform, meaning that the grid level N is constant throughout. For a non-uniform grid, the grid spacing can vary throughout the domain. Hence, there can be regions of higher or lower grid refinement. An example is shown in Figure 2.2a where smaller squares indicate a finer grid. The adaptive grid aims to efficiently allocate computational resources by dynamically refining and coarsening the computation grid in space and time.

Basilisk uses a tree-based grid, i.e., a quadtree (in two dimensions), to maintain a Cartesian grid structure while facilitating local (adaptive) refinement and coarsening. The quadtree configuration establishes a hierarchy between cells at integer levels of refinement. Illustrations are displayed in Figure 2.2, where 2.2b shows a quadtree representation where the respective spatial structure of the grid cells with varying levels of refinement is seen in 2.2c.

The grid is composed of finite-volume cells, where each cell is identified with a grid-level N that is related to the size of the cell. Accordingly, the size of the cell, at a given level, is $\Delta_N = L/2^N$. The grid resolution in Papers I and II are discussed relative to the boundary layer thickness (defined in Section 2.2.5 below), i.e., Δ_N/δ. Near the bottom of the numerical wave tank, parts of the computational domain may have a finer discretization (higher N) than the rest, with a transition between the finest grid and a coarser grid (quadtree configuration) as visualized in Figure 2.2a showing part of the domain with three different resolutions. The combined grid in this thesis is presented as $N = N_1 - N_2$ where $N_2 > N_1$. The highest/finest resolution (N_2) developed near the bottom is enforced up to a vertical height $0.015H$ in runs with $\nu = 10^{-6}$, $10^{-6.5}$ and 10^{-7} m^2 s^{-1}, and up to $0.02H$ having $\nu = 10^{-5.5}$ m^2 s^{-1}. Thus, $N = 12 - 14$ when having $\nu = 10^{-5.5}$ and $\nu = 10^{-6}$ m^2 s^{-1}, $N = 12 - 15$ when having $\nu = 10^{-6.5}$ m^2 s^{-1}, and $N = 11 - 16$ when having $\nu = 10^{-7}$ m^2 s^{-1}. See further Section 2.2.6 for the parameter range used in this thesis.

In Papers I and II, the non-uniform grid is applied, as visualized in Figure 2.2a, where a finer discretization is applied in the bottom boundary layer. However, in Paper II, the uniform and adaptive grid structures are tested out in the convergence study, where the uniform grid and the adaptive grid are referred to as "refine" and "adapt", respectively. In the study, it was not a priori clear if using the adaptive grid algorithm would have improved the representation of the flow field, even though the adaptive grid is an essential algorithm since the computational resources can be focused on the regions that require them the most (lowering the computational costs) (van Hooft et al. 2018).

2.2.2 Numerical wave tank

The numerical wave tank is filled with a stratified fluid. A pycnocline of thickness h_2 and density $\rho(z)$ that varies as a linear function within the pycnocline, is

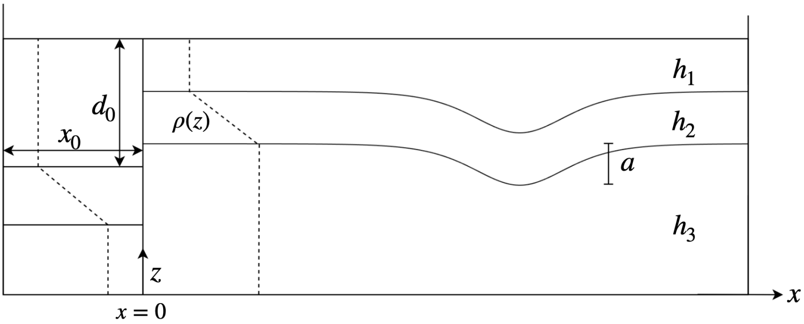

Figure 2.3: Sketch of the numerical wave tank. Image from Ellevold and Grue 2023

sandwiched between an upper layer of thickness h_1 and density ρ_1 and a lower layer of thickness h_3 with density ρ_3. The density is continuous throughout the vertical. A schematic of the wave tank is visualized in Figure 2.3.

The two-dimensional wave tank has length L and depth H, where the physical length of 6.4 m and depth of 0.38 m provide a non-dimensional length of $L/H = 16.84$. The total water depth is provided as $H = h_1 + h_2 + h_3$. The physical depth provides the dimensional length scale, characteristic velocity $\sqrt{gH}$, and the ratio $\sqrt{H/g}$ the characteristic time, where g denotes the acceleration due to gravity.

The horizontal $x-$axis is along the bottom of the wave tank, where the horizontal position of the gate defines $x = 0$. The vertical coordinate is $z = 0$ at the bottom, and at z=H, a rigid lid is placed. Free-slip condition is used at the upper boundary, vertical end walls, and gate for wave generation. A no-slip condition is applied at the lower horizontal boundary.

2.2.3 Wave generation

A gate is located $\Delta x_0 = 0.6$ m from the left tank wall, where a volume V $(= x_0 \times (d_0 - h_1))$ of density ρ_1 is added behind the gate. Upon release of the added volume, the fluid motion is locally rather violent. However, the initial disturbance develops into a leading nonlinear solitary wave of mode 1 after a short time. The amplitude a of the wave is defined as the maximum excursion of the interface separating the pycnocline and the lower layer. Variations of the depth d_0 provide waves with different amplitudes. In physical experiments, the gate is lifted vertically out of the wave tank as quickly as possible. In our numerical simulations, the gate is imposed before time zero, and we assume it is instantaneously removed after time zero.

2.2.4 Wave characteristics

The linear long-wave speed for the two-layer approximation (introduced in Section 1.2.1) is used as reference speed. Hence, $c_0 = (g'd(H-d)/H)^{1/2}$, where $g' = g(\rho_3 - \rho_1)/\rho_3$ and $\Delta\rho/\rho_3 \ll 1$. This definition is as well utilized in the calculations by Aghsaee, Boegman, Diamessis, et al. 2012; Carr, Davies, and Shivaram 2008; Diamessis and Redekopp 2006. The fully nonlinear speed c of the wave is used to connect the time and wave propagation, both in experiments and simulations.

The wave frequency is estimated by $\omega_0 = c_0/L_w$, where the wavelength of the internal solitary wave is defined by

$$L_w = (1/a)\int_{-\infty}^{\infty} \eta(x)dx. \tag{2.1}$$

Here, η is the vertical excursion of the isoline separating the pycnocline and the lower layer.

2.2.5 Boundary layer thickness

The Stokes boundary layer thickness δ at the bottom beneath the wave phase is characterized by the viscosity of the water ν and the wave frequency ω_0, providing

$$\delta = (2\nu/\omega_0)^{1/2}. \tag{2.2}$$

Evidently, as the wave Reynolds number increases, the thickness of the boundary layer decreases.

The Stokes boundary layer thickness provides a length scale. A boundary layer thickness-based Reynolds number can then be defined as

$$Re_\delta = \frac{\delta U_\infty}{\nu}, \tag{2.3}$$

where the free-stream velocity U_∞ underneath the trough, above the bottom, is used as the velocity scale.

2.2.6 Parameter range

The numerical simulations are conducted with non-dimensional amplitude in the range $a/H \sim 0.19 - 0.33$ and wave Reynolds number $Re_w = c_0H/\nu \sim 1.9 \times 10^4 - 6.5 \times 10^5$. A small side note: in Paper I, the Reynolds number is referred to as the stratification Reynolds number, whereas in Paper II, it is referred to as the wave Reynolds number. The variation of the Re_w is obtained by varying the kinematic viscosity by $\nu = 10^{-n}$, with $5.5 < n < 7$. The main simulation parameters are summarized in Tables 2.1 to 2.4, and whether the simulations are experiencing instability or not. The simulations with $n = 6$ are provided in Tables 2.1 and 2.3 and with $n = 5.5, 6.5$ and 7 are provided Tables 2.2 and 2.4. In addition, the simulations provided in Table 1 in Paper I are listed in the Tables here with the same numbers in parentheses, and the simulations provided in Table 1 in Paper II are marked with (**).

Date	$h_3/h_2/h_1$ (cm)	a (cm)	L_w (m)	x_{sep}/L_w	$\theta_{sep}\times10^{-4}$ (m)	$\delta\times10^{-3}$ (m)	Re_w	Inst.
050207 (1a)	30.2/2.7/5.2	10.17	0.977	-0.264	3.831	3.51	60579	Y
140207 (1b)	30.8/2.5/4.7	10.02	0.884	-0.268	3.667	3.40	58140	Y
(1c)	30.8/2.5/4.7	9.41	0.817	-0.284	3.656	3.27	58140	Y
(1d)	30.8/2.5/4.7	9.14	0.823	-0.277	3.649	3.28	58140	Y
(1e)	30.8/2.5/4.7	8.63	0.801	-0.276	3.655	3.24	58140	N
080207	29.3/5.2/3.5	12.51	1.459	-0.235	4.334	4.34	58900	Y
(2*) (**)	29.3/5.2/3.5	11.36	1.043	-0.261	3.970	3.68	58900	Y
(2c)	29.3/5.2/3.5	8.94	0.791	-0.273	3.633	3.19	58900	Y
(2d)	29.3/5.2/3.5	8.47	0.770	-0.286	3.670	3.15	58900	N
060307 (2a)	29.0/5.2/3.8	9.41	0.881	-0.256	3.694	3.30	61560	Y
090207 (2b)	29.2/5.3/3.7	9.24	0.838	-0.275	3.726	3.27	59974	Y
	29.2/5.3/3.7	8.47	0.801	-0.282	3.736	3.19	59974	N
	29.2/5.3/3.7	7.99	0.774	-0.291	3.766	3.14	59974	N
210207	27.6/5.3/5.0	10.02	1.189	-0.222	4.010	3.75	64051	Y
(3a)	27.6/5.3/5.0	8.59	0.988	-0.241	3.897	3.42	64051	Y
230207 (3b)	28.0/4.7/5.5	8.29	0.950	-0.266	3.945	3.33	65322	Y
(3c)	28.0/4.7/5.5	7.81	0.917	-0.273	3.960	3.27	65322	N
	28.0/4.7/5.5	7.29	0.890	-0.279	3.972	3.23	65322	N

Table 2.1: Numerical simulation number and date in Carr, Davies, and Shivaram 2008 (their Table 1), stratification, and amplitude. Numerical values of L_w, x_{sep}/L_w, θ_{sep}, δ, and Re_w defined in the text. Instability (Inst.). The simulations are conducted with $\nu = 10^{-6}$ m^2 s^{-1} and resolution $N = 12 - 14$ (see Section 2.2.1.3).

2.3 Wave-induced instability

2.3.1 Wave-induced velocity field

Figure 2.4 presents an internal solitary wave of depression traveling from left to right with a propagation speed c. The internal wave visualized is labeled in Table 2.1 as (2c). The stratification is visualized in Figure 2.4a. Figure 2.4b shows the horizontal velocity field, whereas the vertical velocity w is presented in Figure 2.4c. The horizontal velocity u above the pycnocline moves in the same direction as the wave ($u > 0$). The induced horizontal velocity field beneath the trough, outside the bottom boundary layer, moves in the opposite direction ($u < 0$). The velocity field varies from a maximum underneath the wave trough, decreasing to zero horizontal velocity behind the wave.

In the deceleration phase behind the trough, the pressure gradient is adverse ($-p_x > 0$), and the horizontal acceleration is positive ($Du/Dt > 0$). Due to a

Date	$h_3/h_2/h_1$ (cm)	a (cm)	L_w (m)	x_{sep}/L_w	$\theta_{sep}\times10^{-4}$ (m)	$\delta\times10^{-3}$ (m)	Re_w	Inst.
140207	30.8/2.5/4.7	11.42	1.053	-0.265	6.766	6.60	18385	Y
	30.8/2.5/4.7	10.94	0.968	-0.262	6.577	6.33	18385	N
080207	29.3/5.2/3.5	11.27	1.048	-0.260	6.295	6.54	18626	Y
	29.3/5.2/3.5	10.88	0.968	-0.255	6.172	6.28	18626	N
230207	28.0/4.7/5.5	10.95	1.469	-0.209	7.424	7.37	20657	Y
	28.0/4.7/5.5	10.80	1.388	-0.217	7.330	7.16	20657	N
	28.0/4.7/5.5	10.64	1.330	-0.223	7.267	7.01	20657	N
	28.0/4.7/5.5	10.17	1.220	-0.225	7.046	6.72	20657	N
140207	30.8/2.5/4.7	9.15	0.824	-0.259	1.985	1.85	183855	Y
	30.8/2.5/4.7	8.63	0.798	-0.274	1.984	1.82	183855	N
	30.8/2.5/4.7	8.14	0.760	-0.294	2.039	1.77	183855	N
080207	29.3/5.2/3.5	8.46	0.760	-0.262	2.002	1.76	186258	Y
	29.3/5.2/3.5	8.11	0.784	-0.255	2.024	1.79	186258	N
230207	28.0/4.7/5.5	8.00	0.944	-0.240	2.114	1.87	206566	Y
	28.0/4.7/5.5	7.04	0.876	-0.257	2.135	1.80	206566	N
140207	30.8/2.5/4.7	8.73	0.783	-0.282	1.150	1.01	581400	Y
	30.8/2.5/4.7	7.22	0.733	-0.305	1.173	0.98	581400	N
	30.8/2.5/4.7	6.28	0.711	-0.315	1.194	0.94	581400	N
080207 (**)	29.3/5.2/3.5	11.29	1.147	-0.236	1.211	1.22	589000	Y
	29.3/5.2/3.5	7.15	0.711	-0.300	1.171	0.96	589000	Y
	29.3/5.2/3.5	6.27	0.686	-0.321	1.201	0.94	589000	N
	29.3/5.2/3.5	5.00	0.653	-0.347	1.257	0.92	589000	N
230207	28.0/4.7/5.5	5.34	0.816	-0.296	1.274	0.98	653220	Y
	28.0/4.7/5.5	4.09	0.799	-0.326	1.356	0.97	653220	N

Table 2.2: Numerical simulation number and date in Carr, Davies, and Shivaram 2008 (their Table 1), stratification, and amplitude. Numerical values of L_w, x_{sep}/L_w, θ_{sep}, δ, and Re_w defined in the text. Instability (Inst.). The first eight rows are conducted with $\nu = 10^{-5.5}$ m^2 s^{-1} and resolution $N = 12 - 14$ (see Section 2.2.1.3). The next seven rows are conducted with $\nu = 10^{-6.5}$ m^2 s^{-1} and resolution $N = 12 - 15$. The last nine rows are conducted with $\nu = 10^{-7}$ m^2 s^{-1} and resolution $N = 11 - 16$.

no-slip boundary at the bottom, the wave-induced adverse pressure gradient is not precisely balanced in the bottom boundary layer and velocity reversal in the viscous bottom boundary layer where the horizontal velocity is positive ($u_{bottom} > 0$ as shown in the inset of Figure 2.4b) occurs (Aghsaee, Boegman, Diamessis, et al. 2012; Carr, Davies, and Shivaram 2008). Thus, the adverse pressure gradient established in the deceleration phase after the passing wave results in flow reversal and gives rise to an inflection point in the velocity profile. This is shown in Figure 2.5, where the Figure displays the velocity profiles in the bottom boundary layer at different wave phase positions $\xi = (x - x_{trough})/H$ for one case that starts to show signs of being unstable (Figure 2.5a, corresponding to Figure 2.4, and see Figure 4a in Paper I) and two unstable cases (Figures 2.5b and 2.5c). The flow reversal occurs close to the bottom and decreases in strength when Re_w increases. The colors in the Figure are used solely for visualization purposes.

In the laboratory experiments by Carr and Davies 2006, they observed that an unsteady boundary jet-like flow was always generated at a fixed reference location shortly after the internal solitary wave had passed. This indicated that the generation of a boundary jet is associated with the induced adverse pressure gradient and was found to always occur having a laminar boundary layer under internal solitary waves of depression. The wave-induced boundary layer separation in the adverse pressure gradient region aft of the wave was shown theoretically by Diamessis and Redekopp 2006 (note that their work is based on weakly nonlinear theory). In all the experiments by Carr, Davies, and Shivaram 2008, a reverse flow along the bottom boundary aft of the wave in the adverse pressure gradient region was also observed.

2.3.2 Separation bubbles

The separated flow (shear layer) may curve back (reattachment point) to the bottom further downstream to form a shallow reverse flow region. This region is known as the separation bubble (Gaster 1967; Pauley, Moin, and Reynolds 1990). Hence, a separation bubble evolves in the pressure-driven bottom layer, commencing from the separation point ($\partial u/\partial z = 0$) beneath the wave trough and is an instability attached to the moving wave (Chomaz 2005). Aghsaee, Boegman, Diamessis, et al. 2012 found that the separation point is located a certain distance behind the wave trough, specifically, between $0.24L_w$ and $0.4L_w$ in their simulations for $Re_w \sim 1.2 \times 10^4 - 4.93 \times 10^5$ for the flat bottom case. In our numerical results for $Re_w \sim 1.9 \times 10^4 - 6.5 \times 10^5$, we found that the separation point is located between $0.209L_w$ and $0.347L_w$ (Paper I), matching the range presented in Aghsaee, Boegman, Diamessis, et al. 2012.

Carr and Davies 2006; Carr, Davies, and Shivaram 2008 measured the boundary layer separation in their laboratory experiments. However, neither managed to visualize the separation bubble(s) directly.

Aghsaee, Boegman, Diamessis, et al. 2012 described the separation bubble as two contiguous parallel vortex sheets with opposite signs. The reverse flow represents the lower sheet, while the flow above defines the upper sheet (see their

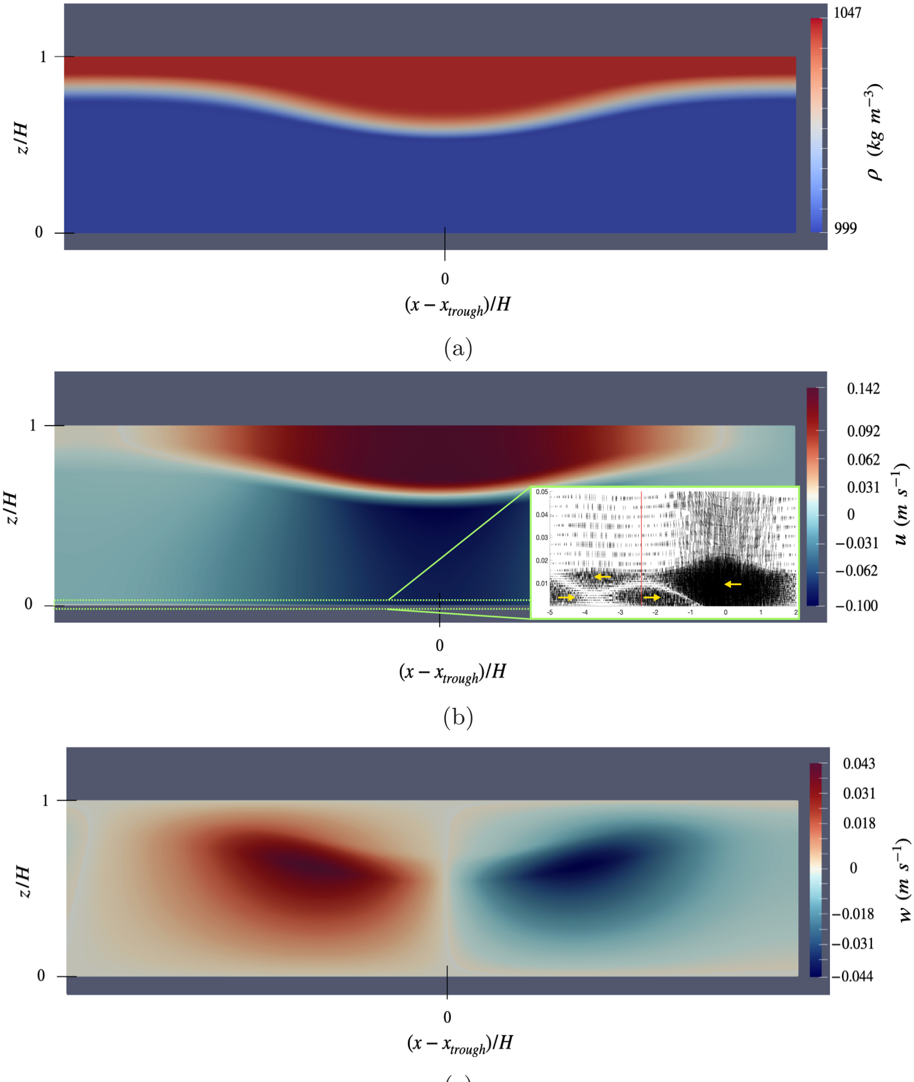

(a)

(b)

(c)

Figure 2.4: The figure displays a section of an internal solitary wave propagating from left to right in the numerical wave tank. Wave amplitude of $a/H = 0.235$. From Table 2.1, run (2c) 080207. (a) Visualizes the stratification in terms of the density of the water. The wave-induced velocity field is visualized, showing the horizontal velocity field (b) and the vertical velocity field (c). The inset in (a) visualizes the flow reversal close to the bottom as a quiver plot of the velocity field (black arrows) (note: only a certain number of velocity arrows are displayed). The yellow arrows are purely for better visualization of the direction of the flow. The red line indicates the left horizontal position of Figure 2.4 (this is the same for all three subfigures).

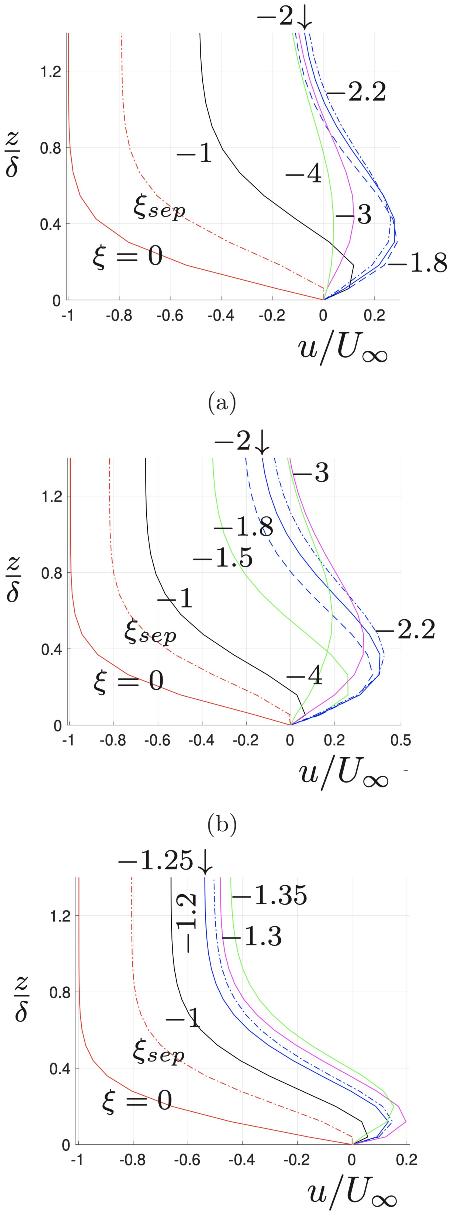

(a)

(b)

(c)

Figure 2.5: Velocity profiles in the bottom boundary layer at different wave phase positions, $\xi = (x - x_{trough})/H$. a) $a/H = 0.235$, right above threshold for instability, run (2c), $Re_w = 5.9 \cdot 10^4$. b) same as a) but $a/H \sim 0.30$, run (2^*). c) same as b) but $Re_w = 5.9 \cdot 10^5$.

Figure 2). The separation bubble grows gradually having a stable boundary layer until the vortex sheets achieve a steady state or become unstable, leading to vortex shedding. The description provided by Diamessis and Redekopp 2006 is quite similar, thus, they described that the separation bubble consisted, of what they called a "tongue", where a thin region of positive vorticity was seen close to the bottom with an overlying region of negative vorticity.

Paper I presents two separation bubbles of anticlockwise vorticity formed in the boundary layer behind the wave trough. While in previous numerical computations (Aghsaee, Boegman, Diamessis, et al. 2012; Diamessis and Redekopp 2006; Sakai, Diamessis, and Jacobs 2020), only one separation bubble has been documented. In the present results, the first bubble evolves from the separation point and is located in the wave phase. The second bubble develops further downstream, outside the wave phase. The bubbles are seen to separate for the larger Reynolds number, e.g., $Re_w = 5.9 \times 10^5$, and for smaller Reynolds number, e.g., $Re_w = 5.9 \times 10^4$, they partially overlap. See Figure 4 in Paper I for a visual representation of the cases. For $Re_w = 2 \times 10^4$, they coalesce (Diamessis and Redekopp 2006). The computed estimates regarding the separation bubbles presented in Paper I are calculated at the onset of instability.

2.3.3 Instability growth and vortex formation

The instability starts to emerge in the back of the bubble located in the wave phase and then moves towards the front (Aghsaee, Boegman, Diamessis, et al. 2012; Diamessis and Redekopp 2006; Ellevold and Grue 2023). Within the separation bubble, a characteristic wavelength λ_0 of the dominant unstable mode manifests. The growth rate, visualized by the red lines in Figure 5 in Paper I displaying the vertical velocity non-dimensionalized by c_0, increases approximately exponentially, where the growth distance is seen to be independent of the scale (see Table 5 in Paper I). The stronger vertical velocities are mainly confined to the wave phase when the scale increases. A series of vortex rolls then forms (see Figures 2.6a and 2.7a) with a wavelength similar to the initial wavelength before the growth slows down and the instability saturates (Figures 2.6b, 2.6c, 2.7b and 2.7c). Figures 2.6a and 2.7a are Figure 6a and 6b in Paper I, respectively, however, displayed here in a different color scheme. Diamessis and Redekopp 2006 discusses that the induced instability is global, which imposes its own manifested length scale on the separation bubble by creating distinct, coherent vortices within the bubble and weaker fine-scale waves emitting away behind the bubble.

The instability in the two cases shown in Figures 2.6a and 2.7a evolves similarly, where the dimensionless wavelength λ_0/δ and the intermediate wavelength immediately afterward, $\lambda_{v,0}/\delta$, are of the same order (before the vortices are emitted). Nevertheless, some noticeable differences stand out when comparing the higher Reynolds number with the lower Reynolds number: i) the boundary layer thickness is much thinner, as expected, and ii) the shed vortices are smaller and weaker and emitted at higher frequencies into the water column

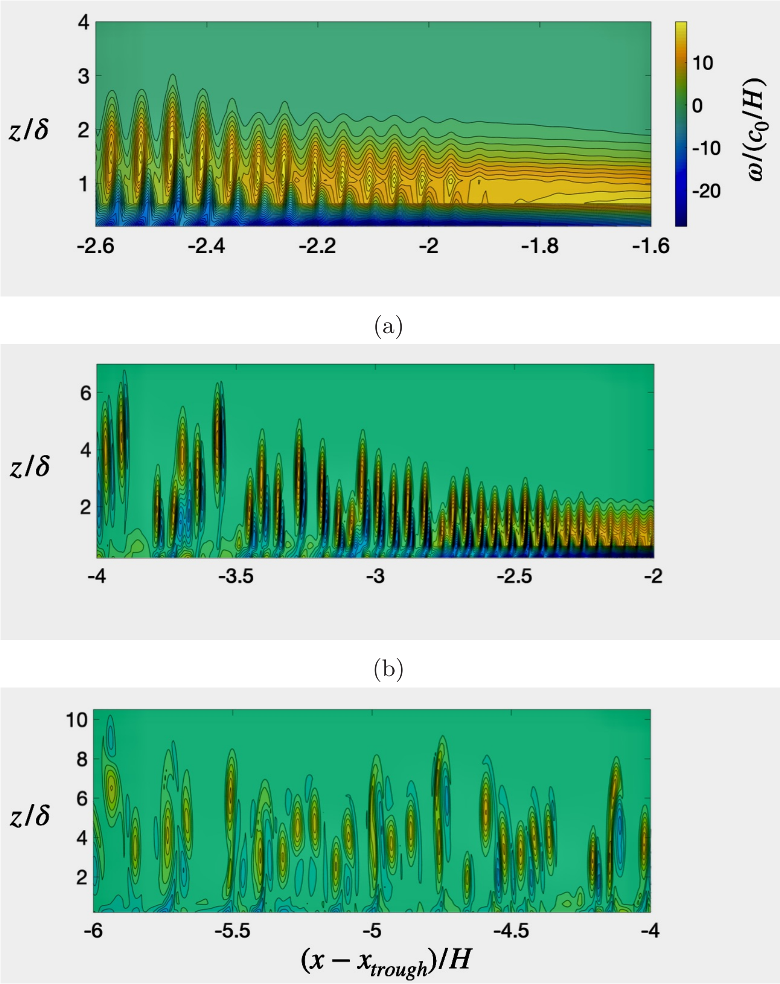

(a)

(b)

(c)

Figure 2.6: Vorticity $\omega/(c_0/H)$ in color scale (contour lines (black) of $\omega/(c_0/H)$). $Re_w = 5.9 \times 10^4$, run (2*) 080207, illustrating the vortex roll-up (a)-(c).

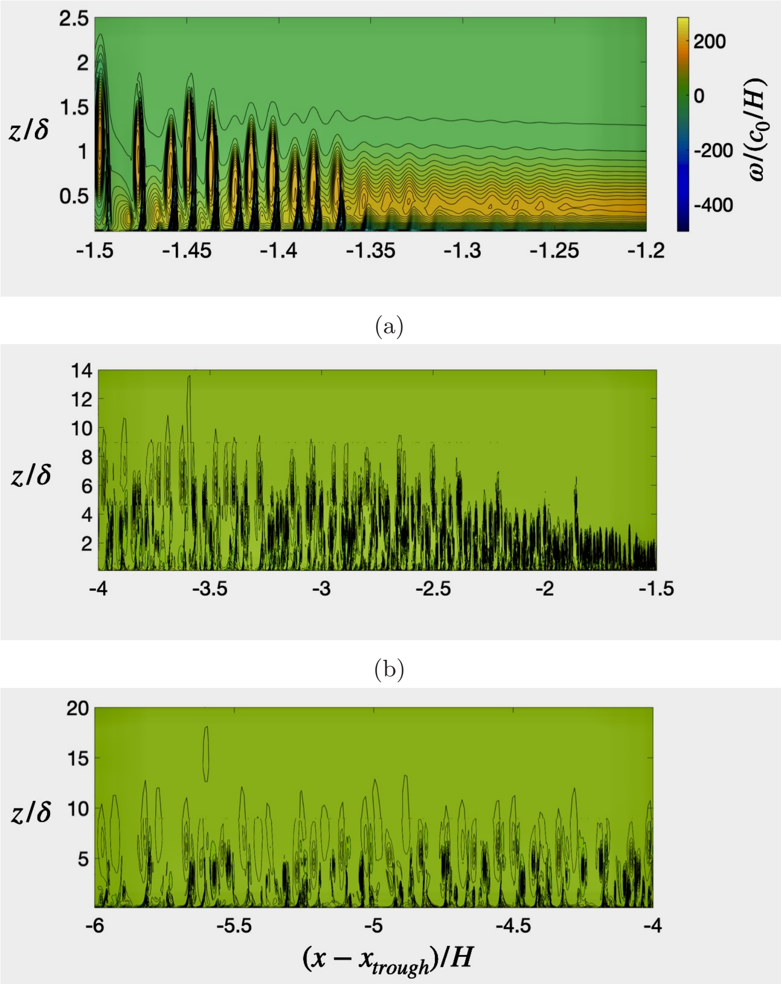

(a)

(b)

(c)

Figure 2.7: Vorticity $\omega/(c_0/H)$ in color scale (contour lines (black) of $\omega/(c_0/H)$). $Re_w = 5.9 \times 10^5$, 080207 (**) Table 2.2, illustrating the vortex roll-up (a)-(c).

for the higher Re_w. However, the vertical ascended height of the vortices out of the boundary layer is of the same magnitude.

In Papers I and II, we perform convergence tests, e.g., on the resolution of the bottom boundary layer, vortex formation, and other wave parameters. In Paper I, we also investigates the transition from stable to unstable separation bubbles (the stability border, presented below in Section 2.3.4). In Paper II, a convergence study was conducted on the vortices formed in Figures 2.6a to 2.6c. Accordingly, the study replicated the experiment labeled 080207 in Table 1 in Carr, Davies, and Shivaram 2008 (Run 2$*$ in Table 2.1 here and in Paper I, whereas it is denoted Run 1 in Paper II). The numerical calculations agree very well with the laboratory measurements, and convergence of the vortex formation is documented. The results are presented in Figure 2.8. See Paper II for more information regarding the Figures and label descriptions. The results presented in both Papers obtain a very good agreement with the laboratory experiments by Carr, Davies, and Shivaram 2008, where previous long-standing computational attempts have been unsuccessful, as communicated in Aghsaee, Boegman, Diamessis, et al. 2012 and in the conclusion by Boegman and Stastna 2019. They argued that the experiments by Carr, Davies, and Shivaram 2008 did not represent the transition to instability, implying conflicting results.

2.3.4 Stability border

During the past decades, one essential question has been regarding the stability border for when the trailing jet in the bottom boundary layer, i.e., the separation bubble, experiences instability. Over the years, several discrepancies have occurred between numerical simulations (e.g., Aghsaee, Boegman, Diamessis, et al. 2012; Diamessis and Redekopp 2006) and laboratory experiments (e.g., Carr and Davies 2006; Carr, Davies, and Shivaram 2008; Zahedi, Aghsaee, and Boegman 2021). The parameters presented in the different stability borders below are computed for the numerical experiments presented in this thesis and provided in Tables 2.3 and 2.4.

The stability border has been discussed in terms of different parameters, creating various criteriums. We will present three stability border thresholds below, where Paper I addresses the first two cases, whereas the third one is mentioned briefly here.

The first threshold is based on the wave amplitude and the wave Reynolds number (Carr, Davies, and Shivaram 2008; Diamessis and Redekopp 2006) and is presented here as Stability border *i*). The second one regards the momentum thickness Reynolds number and the non-dimensional pressure gradient taken at the separation point (Aghsaee, Boegman, Diamessis, et al. 2012) and is presented as Stability border *ii*). In Stability border *iii*), the parameters in Stability border *ii*) are parameterized to only be functions of wave parameters (Aghsaee, Boegman, Diamessis, et al. 2012).

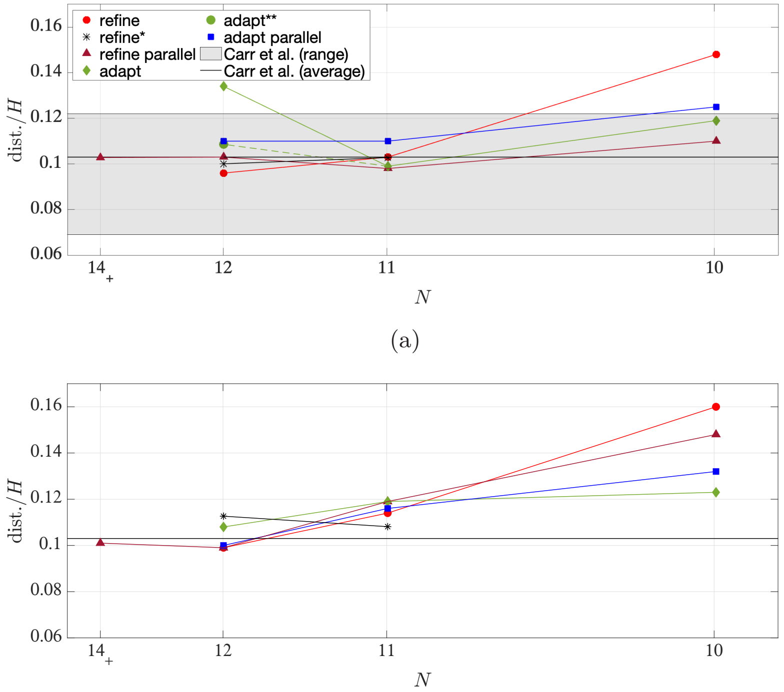

(a)

(b)

Figure 2.8: Vortex separation distance (dist.) vs. the resolution level N. The result from the simulation with $N = 12$, $N_+ = 14$ ($N = 12 - 14$) is marked by $N = 14_+$. (a) Distance over the local area. (b) Distance over the range $-13.3 < (x - x_{trough})/H < -4.3$. The black lines illustrate the experimental average local dist. and the grey-shaded area corresponds to the measured individual separation distance in the laboratory experiment in Carr, Davies, and Shivaram 2008 (their Figure 13, Figure 2c in Paper II). Simulations without parallelization: refine ○, refine* $*$, adapt ◇ and adapt** ○. Simulations with parallelization: refine △ and adapt □. Figure (a) is Figure 3 in Paper II. See further Paper II for more descriptions.

2.3.4.1 Stability border i)

Carr, Davies, and Shivaram 2008 investigated the transition to instability for wave Reynolds number in the range $Re_w = 5.8 \times 10^4 - 6.6 \times 10^4$, with non-dimensional wave amplitudes of $a/H \sim 0.216 - 0.296$. The laboratory experiments provide a qualitative comparison to the theoretical and numerical work by Diamessis and Redekopp 2006. Diamessis and Redekopp 2006 conducted numerical simulations with wave Rynolds number $Re_w = 1 \times 10^4 - 1 \times 10^5$ with wave amplitudes of $a/H \sim 0.30 - 0.55$. However, when investigating the stability border, in the sense of wave amplitude and wave Reynolds number, a quantitative comparison revealed significant differences between the laboratory experiments and the simulations.

The internal solitary waves generated in the simulations by Diamessis and Redekopp 2006 were based on weakly nonlinear KdV theory. In contrast, the internal waves generated in the laboratory grow to be nonlinear, partly explaining the disparity (see, e.g., Section 1.2.2). In addition, the parameters in both works were also outside the range of validity of the KdV theory. Nonlinear internal solitary waves with large amplitudes also possess different fronts and flatter troughs than waves defined by KdV theory with the same amplitude. An example can be seen in Figure 1.3a. This affects the onset of instability in the bottom boundary layer. In any case, the study by Diamessis and Redekopp 2006 was expected to capture the qualitative dynamics under consideration rather than providing a quantitative description. They also stated that if they had higher-order theories, they would expect instability at lower amplitudes than what they predicted. The proposed threshold by Diamessis and Redekopp 2006 is given as $a_{cr} = 0.5(Re_w/10^4)^{-0.12}$, where a_{cr} is the critical amplitude for instability. Carr, Davies, and Shivaram 2008 combined their results with Diamessis and Redekopp 2006, presenting a power law by $a_{cr} = 0.5(Re_w/10^4)^{-0.12} - 0.15$.

The numerical simulations by Aghsaee, Boegman, Diamessis, et al. 2012 for wave Reynolds number in the range $Re_w = 1.2 \times 10^4 - 4.9 \times 10^5$ provide the same qualitative descriptions. However, they were not able to reproduce the threshold of instability as measured in Carr, Davies, and Shivaram 2008 nor the threshold proposed by Diamessis and Redekopp 2006. See Figure 9 in Aghsaee, Boegman, Diamessis, et al. 2012 for a comparison between those three works. Aghsaee, Boegman, Diamessis, et al. 2012 proposed several reasons for the discrepancy between their numerical results and the experimental results by Carr, Davies, and Shivaram 2008. Boegman and Stastna 2019 later reiterated those same arguments. Paper I considers the main arguments proposed by Aghsaee, Boegman, Diamessis, et al. 2012 and responds to the possible reasons questioned.

The calculations presented in Paper I, regarding the threshold based on the wave amplitude versus wave Reynolds number, match the experiments by Carr, Davies, and Shivaram 2008 with good agreement. In addition, the computations in Paper I are conducted for a wider wave Reynolds number than in the laboratory experiments. The instability is seen to depend on the depth of the pycnocline and decays faster with increasing Re_w for a deeper than for a

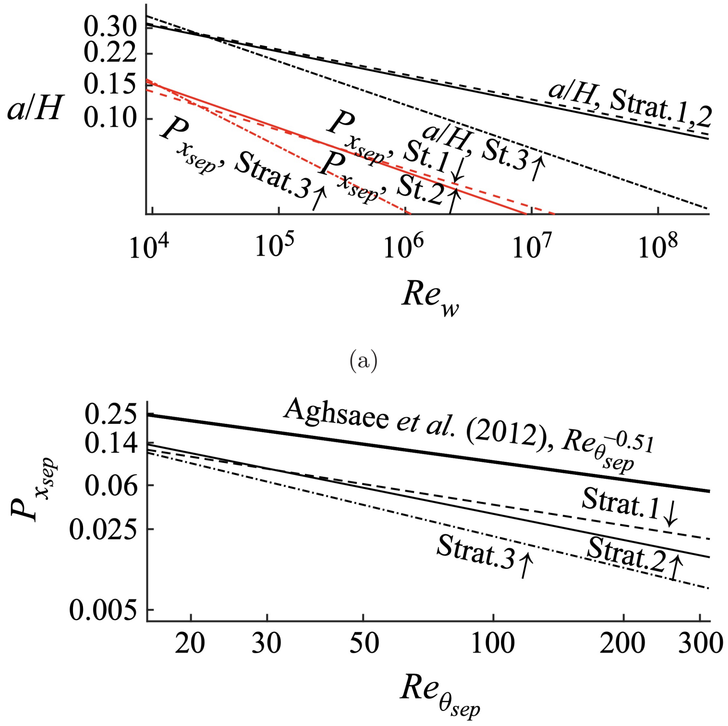

(a)

(b)

Figure 2.9: Threshold of instability, displayed in log scale. The individual stability borders (Paper I) in the Re_w vs. a/H plane (a) and the $Re_{\theta_{sep}}$ vs. $P_{x_{sep}}$ plane (b) for the different stratifications (strat.), including the threshold proposed by Aghsaee, Boegman, Diamessis, et al. 2012 in (b). The red lines in (a) present the adverse pressure gradient as a function of the wave Reynolds number – parameters defined in the text. Figures from Paper I.

shallower pycnocline. For further calculations of the stability border, see Paper I. The results are presented in Figure 2.9a, where Stratification (Strat.) 1, 2, and 3 are referred to the three different stratifications the stability border is computed from. Hence, Strat. 1 is the stratification provided in run (1c), Strat. 2 corresponds to the. stratification in run (2^*), and Strat. 3 is the stratification in run (3b) in, e.g., Table 2.1.

2.3.4.2 Stability border ii)

Aghsaee, Boegman, Diamessis, et al. 2012 discusses the instability threshold by drawing an analogy with the procedures studied in aerodynamic flows (e.g., Gaster 1967; Pauley, Moin, and Reynolds 1990). They point out that two main parameters will contribute to the stability characteristic of the separation bubble. The first parameter addresses the strength of the flow separation. This is measured by the pressure gradient $(\partial P/\partial x)$, non-dimensionalized by $(1/\rho_0 g')$, providing

$$P_{x_{sep}} = (1/\rho_o g')(\partial P/\partial x)_{x_{sep}}. \tag{2.4}$$

Here, $(\partial P/dx)_{x_{sep}} = -\rho_0(U_\infty + c)(\partial U_\infty/\partial x)_{x_{sep}}$ and ρ_0 is a reference density. The second parameter is the momentum thickness Reynolds number

$$Re_{\theta_{sep}} = \frac{U_\infty \theta_{sep}}{\nu}. \tag{2.5}$$

The momentum thickness θ_{sep} of the boundary layer is assessed by

$$\theta_{sep} = \int_0^{Z_\infty} \frac{u}{U_\infty}(1 - \frac{u}{U_\infty})dz, \tag{2.6}$$

where the vertical coordinate Z_∞ is outside of the boundary layer at the separation point. All the quantities evaluated at the separation point at the bottom are denoted by the subscripts x_{sep} or $_{sep}$. In our study, the separation point x_{sep} refers to the separation point of the bubble in the wave phase.

Aghsaee, Boegman, Diamessis, et al. 2012 presented a unified criteria for vortex shedding, in an arbitrary two-layer continuous stratification, based on their numerical results. Hence, they proposed the function $P_{x_{sep}} = (Re_{\theta_{sep}})^{-0.51}$ as the threshold for instability.

In Paper I, we compute the variables x_{sep}, u/U_∞, θ_{sep}, $Re_{\theta_{sep}}$ and $P_{x_{sep}}$. See Tables 2.3 and 2.4. Throughout the calculations of these parameters, we found that the separation point was very sensitive to the resolution in the bottom boundary layer. Consequently, the separation evolved further downstream when running with poor resolution. All the parameters are calculated from this location, providing incorrect results if the resolution is too low. This gave rise to the convergence study visualized through the momentum thickness θ_{sep} (discussed in Paper I). Consequently, the proposed stability threshold by Aghsaee, Boegman, Diamessis, et al. 2012 is sensitive to the numerical resolution in the bottom boundary layer (and thereby requires high computation resources).

From the numerical simulations where the threshold lines in Figure 2.9a are computed, the corresponding pressure versus momentum thickness Reynolds number are visualized in Figure 2.9b with the threshold proposed by Aghsaee, Boegman, Diamessis, et al. 2012. In addition, the non-dimensional pressure, as a function of the wave Reynolds number instead (see Paper I for the corresponding computations) is visualized in Figure 2.9a.

As discussed under stability border i), the threshold is found to be a function of the relative depth of the pycnocline. Our results for stability border ii) also illustrate this. Note also that the momentum thickness Reynolds number is a function with parameters (U_∞ and ω_0) that depend upon the relative depth of the pycnocline. A discussion of this is provided in Paper I.

The parameters $P_{x_{sep}}$ and $Re_{\theta_{sep}}$ are variables that are challenging to measure in the field. Consequently, Aghsaee, Boegman, Diamessis, et al. 2012 proposed a more applicable criterion to predict instability from field observations. This is introduced here as stability border *iii*).

2.3.4.3 Stability border *iii*)

Aghsaee, Boegman, Diamessis, et al. 2012 generalized their threshold criterion to be a threshold that is more readily computed by measurement obtained from field observation. The parameterization of the momentum thickness Reynolds number is conducted by parameterizing the momentum thickness by balancing the friction with inertia in a steady flow, providing

$$Re_{\theta_{sep}} \approx Re_{ISW} = |U_2|\sqrt{\frac{L_W}{\nu(|U_2|+c)}}, \tag{2.7}$$

where $U_2 = ca/(h_2 - a)$ is the wave-induced velocity beneath the trough. The non-dimensional pressure gradient is correlated by

$$P_{x_{sep}} \approx P_{ISW} = (|U_2|+c)\frac{U_2}{L_w g'}, \tag{2.8}$$

where the relation $U_2/L_w \sim -(dU_\infty/dx)_{x_{sep}}$ is implemented (Aghsaee, Boegman, Diamessis, et al. 2012). Hence, the parameters are now only functions of wave variables.

From their numerical results, they found a best-fit power law of

$$P_{ISW} = \frac{50}{Re_{ISW}^{1.1}}, \tag{2.9}$$

to be the new vortex shedding criteria.

The proposed vortex shedding criterion is only valid up to $Re_{ISW} \sim 1200$, for where the laminar boundary layer is discussed to transition over to a turbulent regime and the criteria breaks down (Aghsaee, Boegman, Diamessis, et al. 2012). Consequently, in-situ measurements are needed to investigate further stability in the regime above $Re_{ISW} > 1200$.

Zahedi, Aghsaee, and Boegman 2021 conducted laboratory experiments of internal solitary waves propagating over a flat bottom, studying the dissipation of turbulent kinetic energy in the bottom boundary layer. In their research, their calculations adopt the parameterization of Re_{ISW} and P_{ISW}. During their study, they compared their results to the laboratory experiments by Carr, Davies, and Shivaram 2008, the stability criterion proposed by Diamessis and Redekopp 2006 in the Re_w vs. a/H space, and the numerical results from Aghsaee, Boegman, Diamessis, et al. 2012 in addition to the proposed criterion by Aghsaee, Boegman, Diamessis, et al. 2012 in the Re_{ISW} vs. P_{ISW} space. The results are visualized in Figure 5 in Zahedi, Aghsaee, and Boegman 2021. The comparison between the laboratory experiments of Zahedi, Aghsaee, and Boegman 2021 and Carr, Davies, and Shivaram 2008 indicates agreement in the Re_{ISW} vs. P_{ISW} space. A shift from stable to unstable waves was seen to occur at $Re_{ISW} \sim 200$. Their results contradict the stability criterion proposed by Aghsaee, Boegman, Diamessis, et al. 2012.

Date	$h_3/h_2/h_1$ (cm)	a (cm)	$Re_{\theta_{sep}}$	$-P_{x_{sep}}$	Re_{ISW}	P_{ISW}	Re_w	Inst.
050207 (1a)	30.2/2.7/5.2	10.17	29.10	0.109	177.7	0.102	60579	Y
140207 (1b)	30.8/2.5/4.7	10.02	25.9	0.109	164.6	0.103	58140	Y
(1c)	30.8/2.5/4.7	9.41	23.8	0.102	150.8	0.104	58140	Y
(1d)	30.8/2.5/4.7	9.14	21.7	0.094	143.7	0.095	58140	Y
(1e)	30.8/2.5/4.7	8.63	19.8	0.087	146.5	0.090	58140	N
080207	29.3/5.2/3.5	12.51	53.3	0.113	286.7	0.091	58900	Y
(2*) (**)	29.3/5.2/3.5	11.36	39.2	0.129	214.9	0.110	58900	Y
(2c)	29.3/5.2/3.5	8.94	22.9	0.098	144.3	0.100	58900	Y
(2d)	29.3/5.2/3.5	8.47	20.6	0.091	134.1	0.099	58900	N
060307 (2a)	29.0/5.2/3.8	9.41	25.7	0.104	159.4	0.096	61560	Y
090207 (2b)	29.2/5.3/3.7	9.24	24.2	0.102	152.3	0.097	59974	Y
	29.2/5.3/3.7	8.47	20.8	0.089	135.6	0.089	59974	N
	29.2/5.3/3.7	7.99	18.7	0.080	124.6	0.083	59974	N
	27.6/5.3/5.0	10.02	35.3	0.107	206.5	0.081	64051	Y
210207 (3a)	27.6/5.3/5.0	8.59	25.7	0.090	155.7	0.075	64051	Y
230207 (3b)	28.0/4.7/5.5	8.29	23.8	0.087	147.9	0.075	65322	Y
(3c)	28.0/4.7/5.5	7.81	21.5	0.079	135.9	0.070	65322	N
	28.0/4.7/5.5	7.29	19.34	0.071	123.6	0.065	65322	N

Table 2.3: Numerical simulation number and date in Carr, Davies, and Shivaram 2008 (their Table 1), stratification, and amplitude. Numerical values of $Re_{\theta_{sep}}$, $P_{x_{sep}}$, Re_{ISW}, P_{ISW}, and Re_w defined in the text. Instability (Inst.). The simulations are conducted with $\nu = 10^{-6}$ m^2 s^{-1} and resolution $N = 12 - 14$ (see Section 2.2.1.3).

2.3.5 Bottom shear stress

The vortices in the bottom boundary layer give rise to strong oscillating bed shear stress τ. In the present calculations (Paper I), the bed shear stress is non-dimensionalized by $\rho c_0^2/2$. The shear stress visualized in Figure 7 in Paper I is presented here in Figure 2.10. However, the results are visualized over a broader range. The strong oscillations in each simulation are visually highlighted in the inset figures. By evaluating the bottom shear stress (Figure 2.10), the stress amplitude is seen to confine to the wave phase mainly and relaxes to smaller values afterward (Aghsaee, Boegman, Diamessis, et al. 2012; Diamessis and Redekopp 2006). Diamessis and Redekopp 2006 also documented this sudden growth of shear stress and vertical velocity associated with the initial formation of the vortices. However, in their calculations, only the shear stress shared similar increase/decrease tendencies as our results, whereas the vertical velocity remained significantly high. The strong shear stress occurring in the wave phase is also measured in the field (Quaresma et al. 2007; Zulberti, N. L. Jones, and

Date	$h_3/h_2/h_1$ (cm)	a (cm)	$Re_{\theta_{sep}}$	$-P_{x_{sep}}$	Re_{ISW}	P_{ISW}	Re_w	Inst.
140207	30.8/2.5/4.7	11.42	20.11	0.127	118.0	0.108	18385	Y
	30.8/2.5/4.7	10.94	18.01	0.120	107.5	0.109	18385	N
080207	29.3/5.2/3.5	11.27	19.20	0.139	120.7	0.110	18626	Y
	29.3/5.2/3.5	10.88	17.58	0.132	110.2	0.111	18626	N
230207	28.0/4.7/5.5	10.95	24.42	0.112	143.4	0.083	20657	Y
	28.0/4.7/5.5	10.80	23.27	0.113	136.7	0.087	20657	N
	28.0/4.7/5.5	10.64	22.35	0.114	131.4	0.079	20657	N
	28.0/4.7/5.5	10.17	20.18	0.109	119.3	0.080	20657	N
140207	30.8/2.5/4.7	9.15	38.32	0.093	255.6	0.111	183855	Y
	30.8/2.5/4.7	8.63	34.29	0.087	238.7	0.091	183855	N
	30.8/2.5/4.7	8.14	30.97	0.078	218.6	0.087	183855	N
080207	29.3/5.2/3.5	8.46	37.16	0.088	237.3	0.095	186258	Y
	29.3/5.2/3.5	8.11	33.11	0.080	223.8	0.082	186258	N
230207	28.0/4.7/5.5	8.00	39.68	0.080	251.2	0.071	206566	Y
	28.0/4.7/5.5	7.04	31.95	0.065	208.8	0.062	206566	N
140207	30.8/2.5/4.7	8.73	62.71	0.087	418.5	0.107	581400	Y
	30.8/2.5/4.7	7.22	46.65	0.065	337.0	0.075	581400	N
	30.8/2.5/4.7	6.28	38.07	0.050	287.9	0.062	581400	N
080207 (**)	29.3/5.2/3.5	11.29	118.70	0.126	713.9	0.101	589000	Y
	29.3/5.2/3.5	7.15	48.93	0.063	333.4	0.075	589000	Y
	29.3/5.2/3.5	6.27	40.03	0.053	283.0	0.062	589000	N
	29.3/5.2/3.5	5.00	29.91	0.034	214.5	0.045	589000	N
230207	28.0/4.7/5.5	5.34	38.54	0.040	263.3	0.046	653220	Y
	28.0/4.7/5.5	4.09	27.76	0.026	193.7	0.031	653220	N

Table 2.4: Numerical simulation number and date in Carr, Davies, and Shivaram 2008 (their Table 1), stratification, and amplitude. Numerical values of $Re_{\theta_{sep}}$, $P_{x_{sep}}$, Re_{ISW}, P_{ISW}, and Re_w defined in the text. Instability (Inst.). The first eight rows are conducted with $\nu = 10^{-5.5}$ m^2 s^{-1} and resolution $N = 12 - 14$ (see Section 2.2.1.3). The next seven rows are conducted with $\nu = 10^{-6.5}$ m^2 s^{-1} and resolution $N = 12 - 15$. The last nine rows are conducted with $\nu = 10^{-7}$ m^2 s^{-1} and resolution $N = 11 - 16$.

G. N. Ivey 2020).

Diamessis and Redekopp 2006 reported an increase in the shear stress up to a factor of 5 independent of the scale, whereas Aghsaee, Boegman, Diamessis, et al. 2012 observed an increase of 2.4 in their study. The increased shear amplitudes seen in Figure 2.10 are 1.5 and 5 for the lowest and highest Reynolds numbers, respectively. In addition, the strength and frequencies are seen to increase with scale. The strong variations of bed shear stress can contribute to sediment resuspension and transport across the bottom boundary layer (Boegman and Stastna 2019; Quaresma et al. 2007). The two-dimensional studies by Diamessis and Redekopp 2006 and Aghsaee, Boegman, Diamessis, et al. 2012 showed that the induced vortices in the wave phase would increase the instantaneous bed stress, thus providing a potential mechanism for resuspension, although neither of them directly simulated sediment resuspension.

2.4 Particle motion

2.4.1 Sediment resuspension

Field observations (Quaresma et al. 2007; Zulberti, N. L. Jones, and G. N. Ivey 2020) have shown evidence of resuspension of particles in the adverse pressure gradient region where bed shear stress intensification is one of the driving mechanisms. Zulberti, N. L. Jones, and G. N. Ivey 2020 also noticed that the sediment-layer growth occurred when the bed stress rapidly declined (see their Figure 3). In the laboratory experiments by Aghsaee and Boegman 2015, the resuspension of particles was also seen to not occur during the maximum bed stress but in the phase afterward, where vortices are created, lifting the sediments.

When estimating sediment resuspension, calculations of the mobility Shields parameter θ are usually computed (Boegman and Stastna 2019; Quaresma et al. 2007). The parameter is described by the ratio of the force exerted by bed shear stress to the submerged weight of the grain, which counteracts this force (Soulsby1997), providing

$$\theta = \frac{\tau}{(\rho_s - \rho_w)gd}. \tag{2.10}$$

Here, d is the particle diameter and ρ_s and ρ_w are the density of the grain and bottom water, respectively.

A threshold for when the seabed grains begin to move (Quaresma et al. 2007) is then obtained by

$$\theta_{cr} = \frac{0.3}{1+1.2D_*} + 0.055[1 - exp(-0.02D_*)]. \tag{2.11}$$

Here D_* is the dimensionless grain size given by

$$D_* = [\frac{g(s-1)}{\nu}]^{1/3}d, \tag{2.12}$$

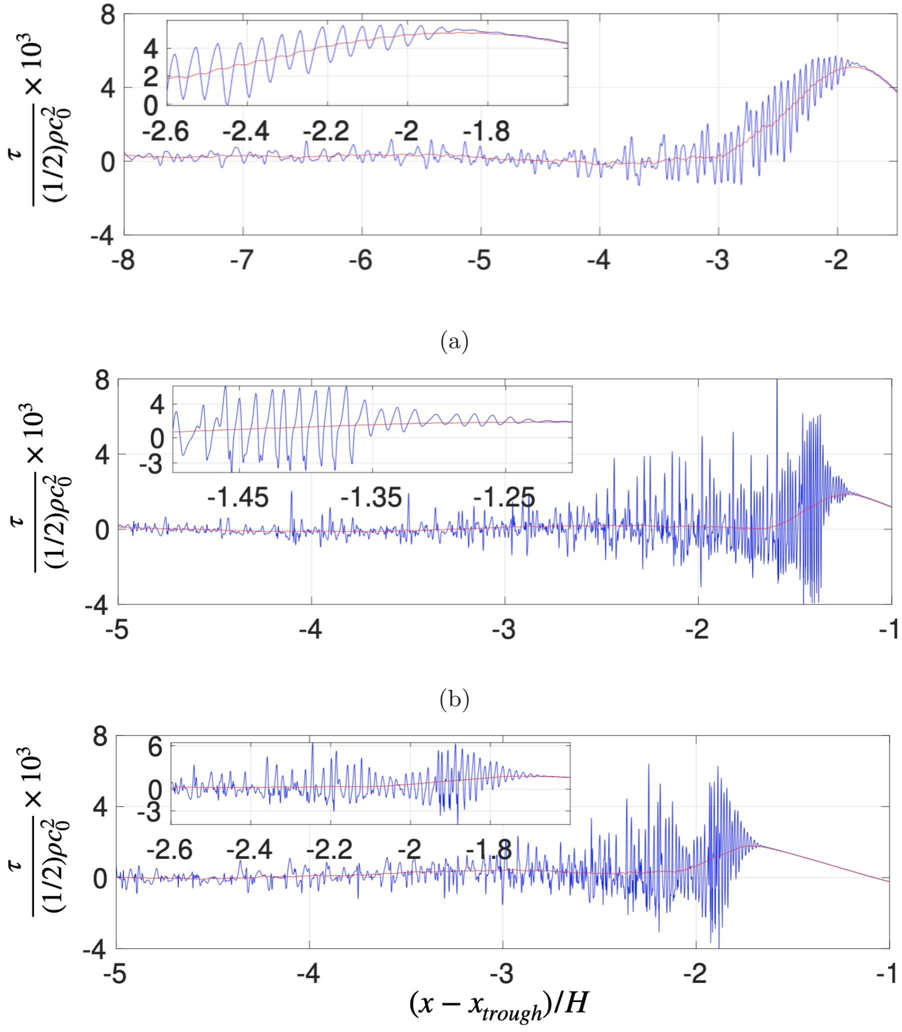

(a)

(b)

(c)

Figure 2.10: Non-dimensionalized bottom shear stress τ (blue line) vs. horizontal position and the red line is average τ. $a/H \sim 0.30$ and (a) $Re_w = 5.0 \times 10^4$, run (2*), (b) $Re_w = 5.9 \times 10^5$, 080207 (**), (c) $Re_w = 6.5 \times 10^5$. The insets provide a more detailed view of the respective non-dimensionalized shear.

where $s = \rho_s/\rho_w$. Reaching this threshold has shown that the incipient sediment motion is possible, leading to bed-load transport; however, sediment re-suspension is not guaranteed.

From the field observations by Quaresma et al. 2007, only the strongest internal waves were seen capable of sediment resuspension. This resuspension contributed to a measured summer bottom nepheloid layer reaching $10-15$ m, which corresponds to a thickness of $0.13H - 0.19H$. The local measured sediments showed a concentration of 93% sandy elements. However, the median grain size was $d \sim 214$ μm (quarts). Having $d = 214$ μm, $\rho_s = 2650$ kg m^{-3}, and $\rho_w = 1027$ kg m^{-3}, the threshold parameter θ_{cr} was calculated to be $\theta_{cr} \sim 0.049$, where at this value, Quaresma et al. 2007 documented "frequent particle movement at all locations".

In Paper II, we utilize Lagrangian tracer particles to study how particles are affected by the velocity field and vortices induced by internal waves. Since we utilize Lagrangian tracer particles, we cannot compute the Shields parameter for comparisons towards field observations. However, after the second passage of the internal wave in our simulations, the tracer particles' vertical position is located up to a vertical level of approximately 0.23H. Our computer-generated findings are consistent with the observed results by Quaresma et al. 2007. However, we note that the processes involved in moderate-scale computations and field-scale measurements may not be directly comparable.

2.4.2 Lagrangian tracer particles

As mentioned, we implement a cloud of Lagrangian tracer particles roughly in the middle of the wave tank near the bottom (Paper II). In order to effectively track the Lagrangian tracer particles, a two-stage Runge-Kutta (RK2) scheme is enforced (Sanderse and Veldman 2019). This method involves a numerical integration technique that computes the position and velocity of the particles at each time step. Hence, the Lagrangian dynamic of the flow is described by the kinematic equation $\frac{d\mathbf{x}}{dt} = \mathbf{u}$. By utilizing this approach, we can obtain reliable data on the movement and behavior of the tracer particles.

The results computed in Paper II are presented in a frame of reference following the wave and a fixed frame of reference. The Paper investigates the tracer particles' trajectories and displacements for four different wave Reynolds numbers, $Re_w = 5.9 \times 10^4,\ 5.9 \times 10^5$, and $Re_w =\ 6.5 \times 10^4,\ 6.5 \times 10^5$, with non-dimensional wave amplitude of $a/H \sim 0.3$. The corresponding boundary layer Reynolds number is in the range $Re_\delta = 490 - 2080$ (see Tables in Paper II).

The tracer particles trajectories for $Re_w = 6.5 \times 10^4$ and 6.5×10^5, labeled Runs 3 and 4 in Paper II, are not visualized in the Paper; thus they are shown here in Figures 2.11 and 2.12. The Figures display 12 random tracer particles where the colors are constant according to their initial vertical location. See Paper II for more details and explanations.

In Paper II, the terminal vertical position is discussed in terms of the 50th and 90th percentile of the vertical position of the particles in a fixed frame

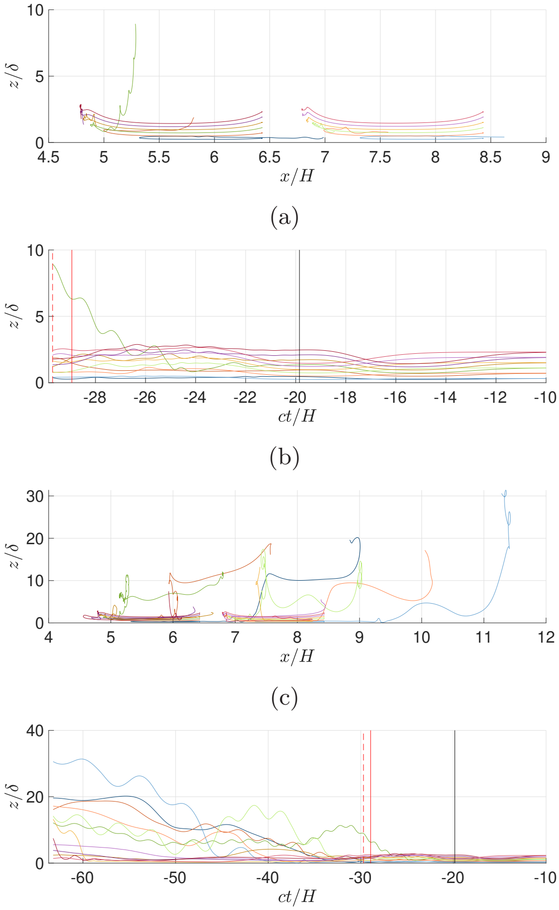

(a)

(b)

(c)

(d)

Figure 2.11: Tracer particles trajectories for $Re_w = 6.5 \cdot 10^4$. (a) and (c) fixed frame of reference. (b) and (d) frame of reference following the wave. In (a)-(b) wave passage one, $tc_0/H = 0 - 21.0$. In (c)-(d) wave passage two, $tc_0/H = 0 - 44.7$.

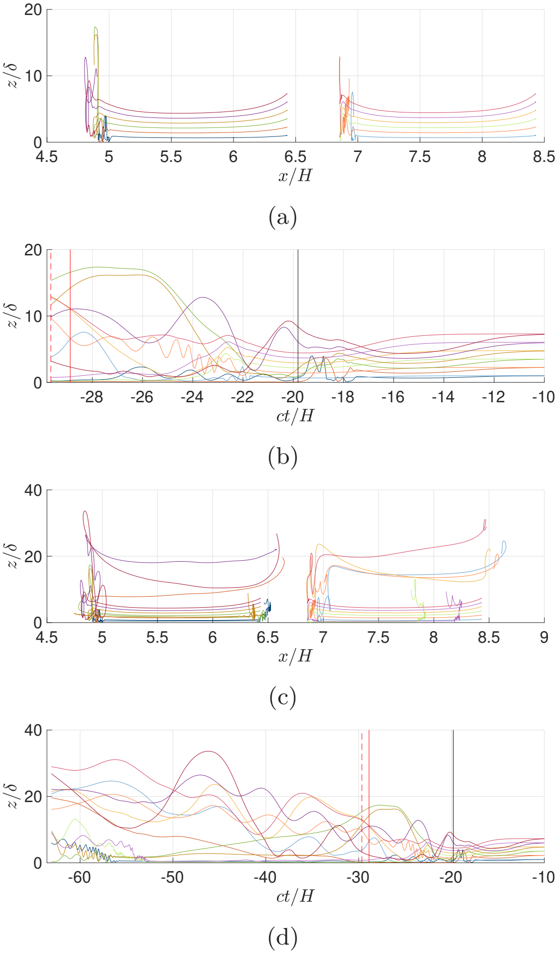

(a)

(b)

(c)

(d)

Figure 2.12: Same as figure 2.11 but $Re_w = 6.5 \cdot 10^5$.

of reference. However, the evolution of the 90th percentile of the particle's vertical position in a reference frame that follows the wave is computed. We refer to this as the mixed layer thickness (MLT), where Figure 2.13 visualize the evolution of the MLT for all four simulations. The MLT exhibits the same trend in the beginning as seen in the trajectory Figures for the same frame of reference, in addition to the two vertical negative displacements of the MLT (a feature provoked by the location of the particles before time zero) due to the wave-induced velocity field right below the wave trough.

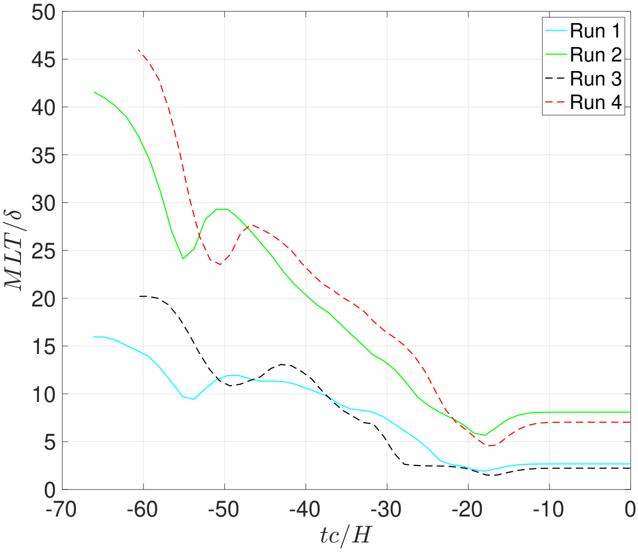

Figure 2.13: Following the wave, the 90th percentile (MLT) evolution in a frame of reference. Run 1−4 corresponds to the four runs in Paper II. Run 3 corresponds also to the simulation presented Figure 2.11, whereas run 4 corresponds to the simulation presented Figure 2.12.

Chapter 3

The Norwegian continental shelf

In this chapter, two different studies will be presented. The first study will concern internal solitary waves along the Norwegian coast. Four places along the coast have been characterized as hot spots for high internal wave activity (Dokken et al. 2001). One of these locations is near Egga and the Hola trough in Vesterålen (see Figures 3.1a and 3.2b). Strong coastal currents and tides flow over the shallow banks and deep valleys there (see Figures 3.1b and 3.1c). In addition, a cold-water coral reef is located in the Hola trough (Fosså, Kutti, et al. 2015) (see Figure 3.2). Internal waves can transport nutrients, and breaking internal waves provide vertical mixing in the water column. Thus, internal waves might contribute to the nutrient supply for primary production in the euphotic zone in the Hola area and supply the cold-water coral reef with food.

The second study considers the new methodology presented in Paper III. A new methodology is introduced to measure the two-dimensional velocity field of water near a heaving ice floe. The system is tested in the Barents Sea and validated in the laboratory.

This chapter is presented as follow: Section 3.1 introduces the Norwegian continental shelf, the location of interest regarding the first study, and the dominating currents and tides. Sections 3.2 and 3.3 present some characteristics of the marine ecosystem and observations of internal waves at the Norwegian continental shelf. Section 3.4 describes the field campaign conducted as part of the Ecopulse project to observe internal wave trains. What regards the second study (Paper III) is presented in Section 3.5.

3.1 The Norwegian continental shelf

The Norwegian continental shelf is a region extending from the coastline to the margin of the shelf break. The shelf break is a narrow zone that separates the continental shelf from the deeper ocean. It is characterized by a steep drop in depth and a sharp change in the water properties, such as temperature and salinity (L. Buhl-Mortensen et al. 2012). In northern Norway, the continental shelf is uneven with shallow banks separated by deeper troughs that were formed during the last glaciations. Part of northern Norway is the Lofoten-Vesterålen-Troms area. The continental shelf in this area is relatively narrow, measuring only a width of 10 to 90 km.

In the Lofoten-Vesterålen area (the red box displayed in Figure 3.1a is within this area), the banks and troughs slope gently in an offshore direction with water depths varying from 40 to 270 m. One of the troughs in this area is known as the Hola trough and is located between the bank Vesterålgrunnen to the north and Eggagrunnen to the south, with water depths of 150 to 270 m. See

Figure 3.2b for a visual overview. Vesterålgrunnen has a water depth of 70 to 90 m and is sloping toward the Hola trough at angles between 4 and 10 degrees. Eggagrunnen has a water depth of 70 to 80 m and slopes towards the Hola trough at angles of 2 to 4 degrees (R. Bøe et al. 2009).

3.1.1 Currents

The dominating currents along the Norwegian continental shelf are the Norwegian Atlantic Current (NwAC) and the Norwegian Coastal Current (NCC). Figure 3.1b shows these two currents and their main circulation patterns. Red arrows display the NwAC, and green arrows show the NCC. The circulation patterns of the NwAC and the NCC in the Lofoten-Vesterålen area are shown in greater detail in Figure 3.1c.

Close to the coast, the NCC flows northward and comprises the coastal water of low salinity (< 35 ppt) and variable temperature. In addition, the NCC consists of seasonally stratified water caused by river runoff and surface heating (Sætre 2007) and has a variable velocity along the coast (R. Bøe et al. 2009). The speed of the current in the northern part of Norway is typically of order $0.2 - 0.5$ m s^{-1} (Sperrevik, Christensen, and Röhrs 2015).

Parallel to the edge of the continental slope and to the NCC, the NwAC flows northwards, consisting of relatively warmer water and higher salinity (> 35 ppt). The NwAC propagates in areas below and along the seaside of the NCC (see Figure 4.8 in Sætre 2007). While propagating side by side, dynamic interactions exist in addition to transporting, e.g., salt, heat, and nutrients from the NwAC to the NCC (Sætre 2007).

3.1.2 Tides

Gravitational forces from the moon and the sun cause tides in the ocean. On the Norwegian coast, tides originate from the Atlantic Ocean and propagate as a tidal wave into the Norwegian Sea and along the coast northward (Sætre 2007). The tidal motion along the coastline can sometimes be seen as a Kelvin wave (Weber and Isachsen 2023).

Several harmonic tidal components cause temporal variation in the sea level. Some of these are, for instance, the semi-diurnal components M2 (principal lunar) and S2 (principal solar) and the diurnal components K1 (lunar-solar) and O1 (principal lunar). The components M2 and S2 have periods of 12.42 and 12 hours, respectively, whereas K1 and O1 have periods of 24 and 25.82 hours, respectively.

Different tides around the Lofoten Island were simulated with a high-resolution tidal model by Moe, Ommundsen, and Gjevik 2002. Specifically, the tidal components M2, S2, and K1, in addition to the semi-diurnal component N2, were simulated, where the dominant tide was found to be the diurnal K1 current component in the Lofoten-Vesterålen area.

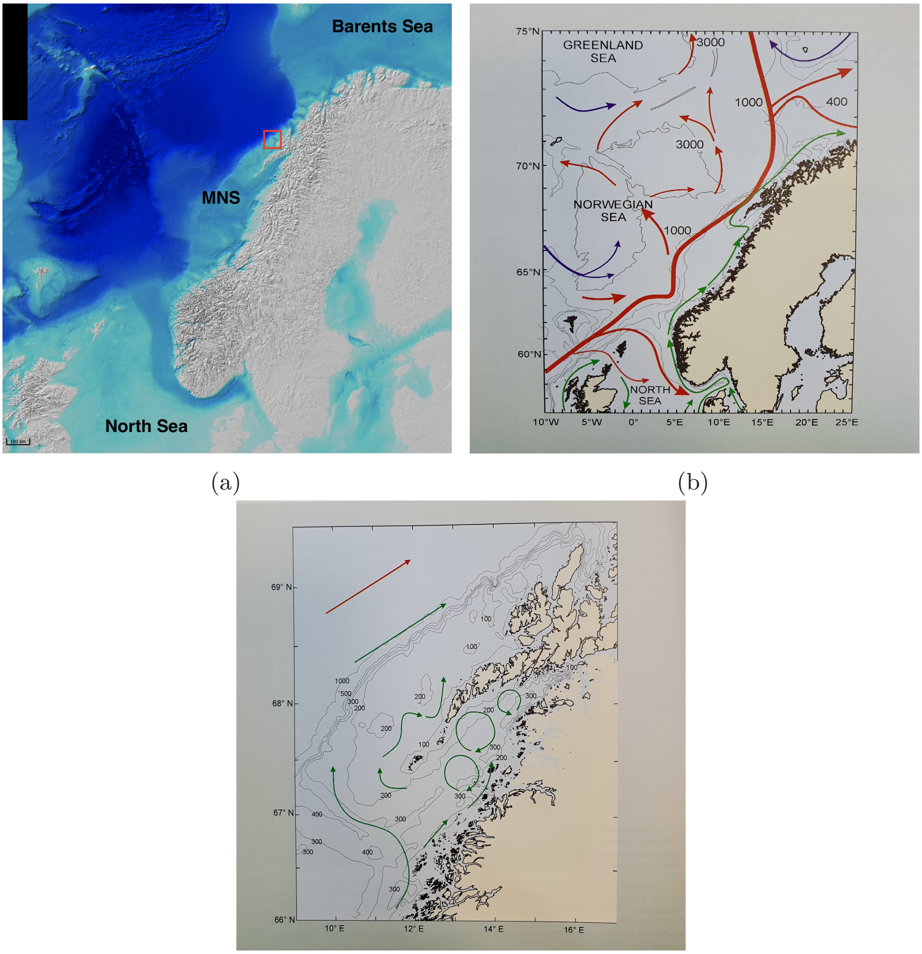

(a)

(b)

(c)

Figure 3.1: An overview of Northern Europe and the maritime areas of Norway, from the Barents Sea (up north) down to the North Sea. MNS: Mid-Norway Shelf. The red box marks the area of interest in the Lofoten-Vesterålen region, further displayed in Figure 3.2b. Images is created in Mareano (www.mareano.no, publicly available). The scale in the lower left corner is 100 km. Visualization of the main circulation pattern of the Nordic Seas (b) and a schematic of the circulation in the Vesterålen-Lofoten area (c). The blue arrows indicate the Arctic water, the red arrows display the Atlantic Water, and the green arrow illustrates the coastal water. Image (b) and (c) are adapted from Sætre 2007, with permission from Fagbokforlaget.

3.2 Characteristics of the marine ecosystem

3.2.1 Spring bloom

On the Norwegian continental shelf, there are regions where spring blooms are prevalent. The site for primary production of nutrients is in the well-mixed upper layer of the water column, penetrated by sunlight (the euphotic zone). The production of phytoplankton is controlled by light availability and nutrients to maintain a net growth (Sverdrup 1953). Estimating the quantity of phytoplankton biomass in water can be accomplished by measuring the concentration of chlorophyll-a. All photosynthetic organisms that produce oxygen use chlorophyll-a, and as a result, increased chlorophyll-a concentrations indicate a rise in nutrient loads (Silva et al. 2021).

The spring bloom usually starts in early April/May, and by the end of the summer the upper part of the water column is partly or fully depleted of nutrients (Osterloff et al. 2019; Silva et al. 2021). For a new bloom to take place, it is essential to have mechanisms that bring nutrients into the euphotic zone. To understand the transport, dispersion, and growth of plankton and nutrients, it is necessary to comprehend the dynamics that occur throughout the water column.

Silva et al. 2021 conducted a 21-year study of phytoplankton bloom phenology in the Barents, Norwegian, and North Seas. From their analysis corresponding to the Lofoten-Vesterålen region, the climatology results show that the spring bloom phenology typically starts towards the end of March and lasts approximately 40 days. Additionally, a summer bloom phenology usually begins in mid-July and lasts approximately 41 days. Note that our data collection timeline from 2021 (see Section 3.4) was from the last day of June to early September. Hence, it contains the whole summer bloom duration time measured by Silva et al. 2021.

3.2.2 Cold-water coral reefs

The movement of water and internal waves play a vital role in shaping the environment on the continental shelf. They affect sediment resuspension and deposition (R. Bøe et al. 2009). Additionally, internal waves transport nutrients from deeper depths to the euphotic zone. This movement is believed to significantly impact the ecosystem's supply by facilitating the movement of essential components and organisms, helping to maintain the delicate balance of marine life.

Cold-water coral reefs are a threatened and fragile ecosystem in deep, dark, colder waters. A reef is a complex structure supporting a diversity of life. One of the cold-water corals is the *Lophelia pertusa*, a stony coral (Scleractinia) (Fosså, Mortensen, and Furevik 2002). Over 1300 animal species have been recorded to live on or near the *Lophelia pertusa* reefs in the northeast Atlantic (Roberts and Hirshfield 2004).

Along the Norwegian shelf and coast, numerous deep-water coral reefs are formed by *Lophelia pertusa* (Fosså, P. Buhl-Mortensen, and Furevik 2000). *Lophelia pertusa* is present in the Skagerak and Oslo fjord in the south, along the Norwegian coastline, and up to Finnmark in northern Norway. Available radiocarbon dating of *Lophelia pertusa* has yielded ages up to 8700 years (Freiwald et al. 2002).

Most of the living *Lophelia pertusa* reefs are found along the continental break and shelves at depths between 200 and 400 m (Fosså, Mortensen, and Furevik 2002). Nevertheless, in Trondheimsfjorden, a living reef is recorded at 39 m. One of the best-known areas is the Sula Ridge Complex off Mid-Norway. Here, more than several hundred individual reefs are recorded over a distance of 14 km, at mean depths of 300 m, where parts of the reefs reach as high as 30 m up into the water (Fosså, Mortensen, and Furevik 2002; Freiwald et al. 2002). A photo of a *Lophelia pertusa* colony is presented in Figure 3.2a. The Røst reef southwest of Lofoten Archipelago in northern Norway is the largest recorded *Lophelia pertusa* reef and is ten times bigger than the reef on the Sula Ridge (Fosså, Lindberg, et al. 2005).

Fishermen's statements provide anecdotal evidence that corals are vital to fisheries, reporting a decline in fish in areas where trawling has destroyed reefs (Fosså, Mortensen, and Furevik 2002). Fosså, Mortensen, and Furevik 2002 estimated that between 30 and 50 % of the reefs are destroyed or impacted by trawling.

3.2.2.1 Cold-water coral reef in the Hola trough

Another biodiversity area and hot spot for the cold-water coral reef *Lophelia pertusa* is in the Hola trough, where 414 reefs have been located at depths between 150 and 250 m. The reefs are 32 to 334 m long and 27 to 114 m wide, varying between 4 and 17 m in height (Fosså, Kutti, et al. 2015; Osterloff et al. 2019). The reefs grow mainly on the north-eastern side of the trough, where the tidal current comes from the coast towards the shelf edge (Fosså, Kutti, et al. 2015) as well as the geostrophic current systems (the NCC and NwAC) (Bøe et al. 2016). The study by Osterloff et al. 2019 showed that diurnal variations and tidal currents impacted polyp activity by controlling the food supply to the reefs. The coral reefs' location can be seen in Figure 3.2b.

3.3 Internal waves

Internal waves and water movement are crucial components on the continental shelf in shaping the environment, e.g., affecting sediment resuspension and deposition (R. Bøe et al. 2009). Observations of this interaction have been seen, e.g., on the Scotian shelf (Sandstrom and Elliott 1984), the New English shelf (MacKinnon and Gregg 2003), and the Portuguese mid-shelf (Quaresma et al. 2007). Understanding these dynamic processes is fundamental to comprehending the intricate nature of the marine environment (L. Buhl-Mortensen et al. 2012).

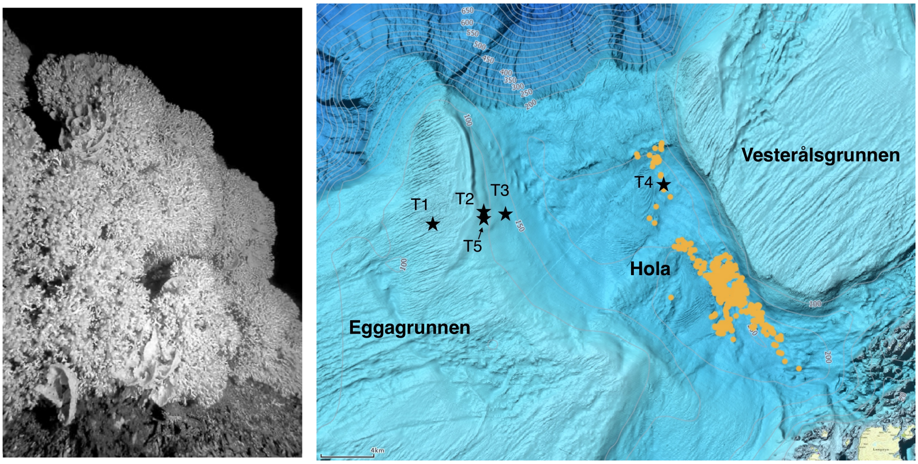

(a) (b)

Figure 3.2: (a) Colony of *Lophelia pertusa* located at 40 m depth in Trondheimsfjorden, Norway. Image from Fosså, Mortensen, and Furevik 2002, reproduced with permission from Springer Nature. (b) Hola trough in between Vesterålgrunnen and Eggagrunnen. The orange dots are the location of previously observed *Lophelia pertusa* reefs. The stars provide the location of the stations in 2021 and 2022, and the text indicates which station (see Section 3.4 for more information). The white lines and numbers display the contour lines of the water depth. The image is created in fiskeri direktoratet (www.portal.fiskeridir.no, publicly available). The scale in the left corner is 4 km.

3.3.1 Internal wave observations in the Lofoten-Vesterålen-Tromsø area

Dokken et al. 2001 conducted a study to identify and characterize internal waves in synthetic aperture radar (SAR) (see Section 1.3.2) images along the Norwegian coast. The study included 2600 SAR images from 1991 to 2000. The results indicate that internal waves occur during almost the whole year. However, the frequency of waves is dominant from May to September/October, with the highest frequency in the late summer when the thermal stratification is most pronounced. Dokken et al. 2001 found four areas along the Norwegian coast with high internal wave activity: Egga, Moskenes, Vøring Plateau, and along the Norwegian Trench in the southern part of Norway (see their Figure 5). The three first locations are in the Lofoten-Vesterålen area. In the Egga area, where we can find the Hola trough, several internal wave trains were estimated to propagate with a speed of ~ 0.5 m s^{-1} almost parallel to the coastline in a south/southwest direction. More than one tidal cycle was frequently observed in the SAR images.

Figure 3.3 provides an example of internal waves observed by Sentinel-1 SAR on 29 August 2019 outside Vesterålen, displaying propagating internal waves over the Hola trough. A total of 16 wave groups can be seen in the figure, appearing on the seasonal pycnocline. Most of the wave groups travel in a south/southwest direction before abruptly shifting orientation to the west, towards the deep ocean. The distance between the wave groups is often seen to be caused by the frequency of the tides, where the $K1$ current is seen to be dominating Moe, Ommundsen, and Gjevik 2002. In addition, a smaller set of internal wave groups are seen to originate from the coast.

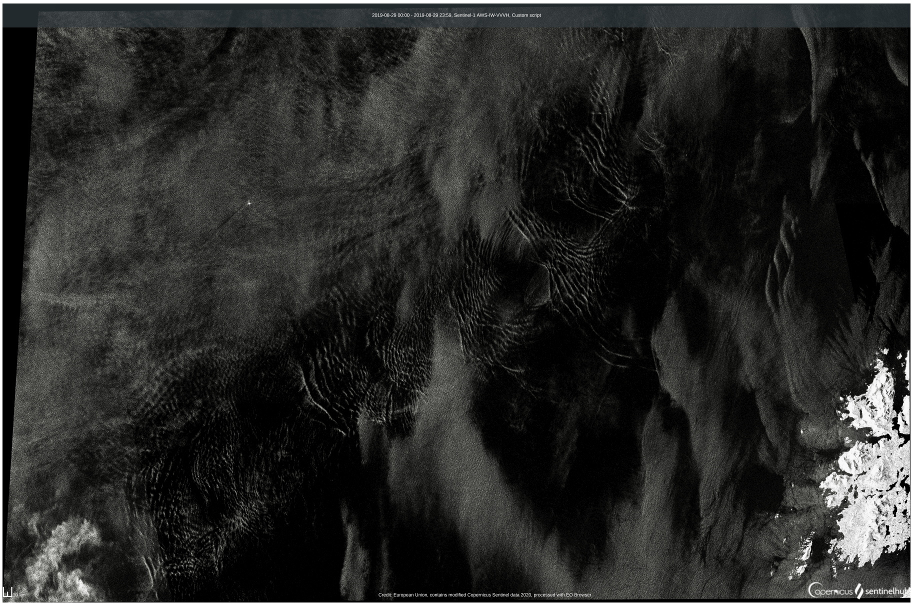

Figure 3.3: Microwave backscatter intensity of internal wave groups in Vesterålen, Norway, observed by Sentinel-1 SAR on 29 August 2019 at 16:31 UTC.

3.3.2 Tide-topography interaction - general basis

When the water is stratified and the barotropic tide encounters topographic features, vertical displacement of the pycnocline occurs, generating internal waves of tidal period (Alford et al. 2012; Sandstrom and Oakey 1995). Accordingly, the baroclinic tide initiates internal waves on the pycnocline (C. R. Jackson, Da Silva, and Jeans 2012). Numerous mechanisms involve tidal flows, e.g., see the works by D. Farmer, Q. Li, and Park 2009; Maxworthy 1979; Nash and Moum 2005. The induced linear internal waves are often sinusoidal, propagating away from the generation zone. However, with sufficient energy input, the waves grow, become steeper, and eventually develop into nonlinear internal waves (C. R. Jackson, Da Silva, and Jeans 2012).

3.4 Ecopulse field campaign

During the Ecopulse project 2020-2023, we have been able to conduct two field expeditions at the Norwegian continental shelf, more specifically at the Hola trough located in Vesterålen, Norway (see Figure 3.2b). The choice of location of investigation is motivated in previous sections; however, a summary is as follows: i) this area is one of four locations identified where there exists high internal wave activity along the Norwegian continental shelf (Dokken et al. 2001), and ii) cold-water coral reefs are located in the Hola trough (R. Bøe et al. 2009).

The aims of the field expeditions have been to i) quantify internal waves at this specific location, ii) determine how often internal waves occur, iii) quantify the internal wave-induced instabilities close to the bottom, and iv) quantify vertical exchange throughout the water column. So far, the processing of all the field data is ongoing, as the extent of complete analysis is out of the scope of this dissertation. The sections below cover the moorings' location, timeline, and equipment used during the expeditions. One observation of an internal wave train from 2021 will be shown in Section 3.4.3, and a summary and an outlook regarding the field work will be provided at the end.

3.4.1 Location and timeline

The field expeditions were conducted on the Norwegian continental shelf at the Hola trough, outside Lofoten in Vesterålen, Norway in 2021 and 2022. The expeditions were conducted with R/V *Kristine Bonnevie*, where moorings were deployed in June and retrieved in September both years. The data was collected from 30 June until 11 September 2021 and from 1 July until 16 September 2022. Five through-water-column moorings, further referred to as stations, were set out in 2021 and four in 2022. Table 3.1 provides the specific locations and the mean depth at the given site for the respective stations. The stations' specific locations are also marked in Figure 3.2b: one station is located in the valley ($T4$), up to three on the slope ($T2$, $T3$, $T5$), and one on the bank to the southwest ($T1$).

The distance between stations $T1$ and $T2$ and stations $T2$ and $T3$ are approximately 4.04 km and 1.30 km, respectively. The slope between stations $T2$ and $T3$ is ~ 1.7 degrees. This is considered to be a relatively gentle slope.

3.4.2 Equipment used in the field

The equipment used during the field expeditions includes temperature probes, conductivity-temperature-depth (CTD), and acoustic Doppler current profilers (ADCPs) to measure the temperature, conductivity, and velocity field, respectively. In addition, chlorophyll-a, oxygen, and turbidity were measured at the station in the valley ($T4$).

On stations $T1$, $T2$, and $T3$, ten temperature probes, three CTDs, and one 250 kHz ADCP were mounted per station in both years. See Figures 3.4a to 3.4c for the configuration in 2021. The temperature probes and the CTDs

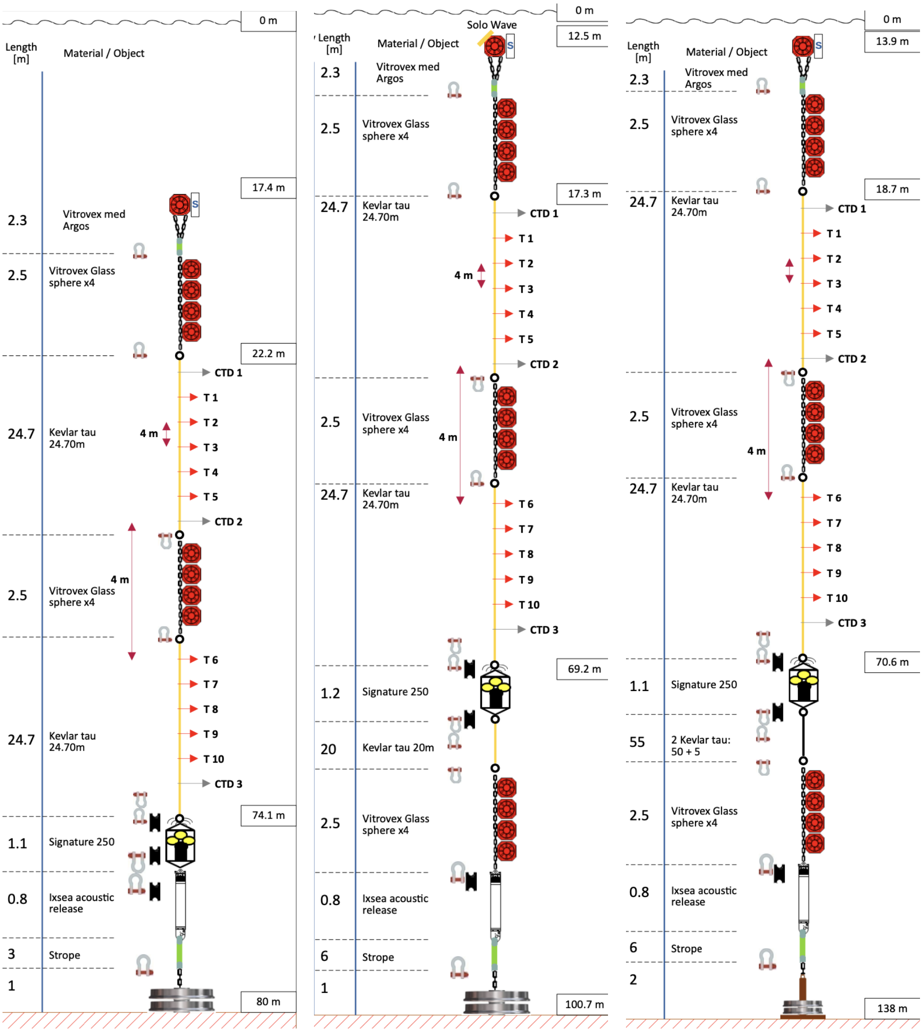

(a) Station $T1$ (b) Station $T2$ (c) Station $T3$

Figure 3.4: The configuration of the stations in 2021 with ten temperature probes (labeled T1-T10), three CTDs and one ADCP 250 kHz mounted on per station. (a) Displays the setup at station $T1$, local mean water depth of 80 m, (b) provides the setup at station $T2$, local mean water depth of 100.7 m, and (c) shows the setup at station $T3$, local mean water depth of 138 m. The schematics are created by the Norwegian Institute of Marine Research, Bergen, Norway.

Year	Station	Latitude	Longitude	Local mean depth (m)
2021 + 2022	$T1$	N68°57.944	E13°50.146	80
2021 + 2022	$T2$	N68°58.282	E13°56.109	100.7
2021 + 2022	$T3$	N68°58.398	E13°58.041	138
2021 + 2022	$T4$	N68°59.400	E14°15.828	241
2021	$T5$	N68°58.197	E013°56.030	99.8

Table 3.1: The latitude and longitude locations for the given stations and the respective local mean water depth for 2021 and 2022.

are stationary with a measuring frequency of 10 Hz and a vertical distance between them of 4 m. On station $T1$, where the local water depth is 80 m, the uppermost CTD is approximately 57.3 m above bottom, and the lowest CTD is approximately 9.3 m above bottom. On station $T2$, where the local water depth is 100.7 m, the uppermost CTD is approximately 78 m above bottom, and the lowest CTD is approximately 30 m above bottom. On station $T3$, where the local water depth of 138 m, the uppermost CTD is approximately 118.8 m above bottom, and the lowest CTD is approximately 70.8 m above bottom.

The velocity of the water throughout the vertical was measured with 250 kHz and 500 kHz ADCPs. The 250 kHz ADCP is a 4-beam Nortek Signature250 ADCP and is a medium-range current profiler. It provides horizontal velocity data throughout the water column. The 250 kHz ADCP was configured to sample average horizontal currents from the slanted beams in 2 m vertical bins and with measuring frequency of 0.14 Hz. The 250 kHz ADCPs are situated close to the bottom in an upward-looking position. A 1000 kHz ADCP was mounted close to the bottom to measure the turbulence close to the sea floor. In 2021, one 500 kHz and one 1000 kHz were mounted on station $T5$. In 2021, the 1000 kHz ADCP was mounted on station $T1$. For the specific data acquisition settings of the 500 kHz and 1000 kHz ADCPs see Appendix B

On station $T4$, a wire walker was deployed with a CTD and systems to measure chlorophyll-a, oxygen, and turbidity. The wire walker moves vertically up and down along a wire. On its way up, buoyancy regulates the speed and is typically around 0.5 m s^{-1}. In order to climb down, it relies upon surface waves. It conducts three profiles every hour over a certain time interval, where the instruments have samplings frequencies of 10 Hz.

3.4.3 Observation from 2021

3.4.3.1 Horizontal velocity

The horizontal velocity plane (u, v) corresponding to the timeline in Figure 3.7 is presented in Figure 3.5. The velocity field is measured by the 250 kHz ADCP at station $T2$. The velocity components sampled are the horizontal velocity component u in the east-west direction and the horizontal velocity component

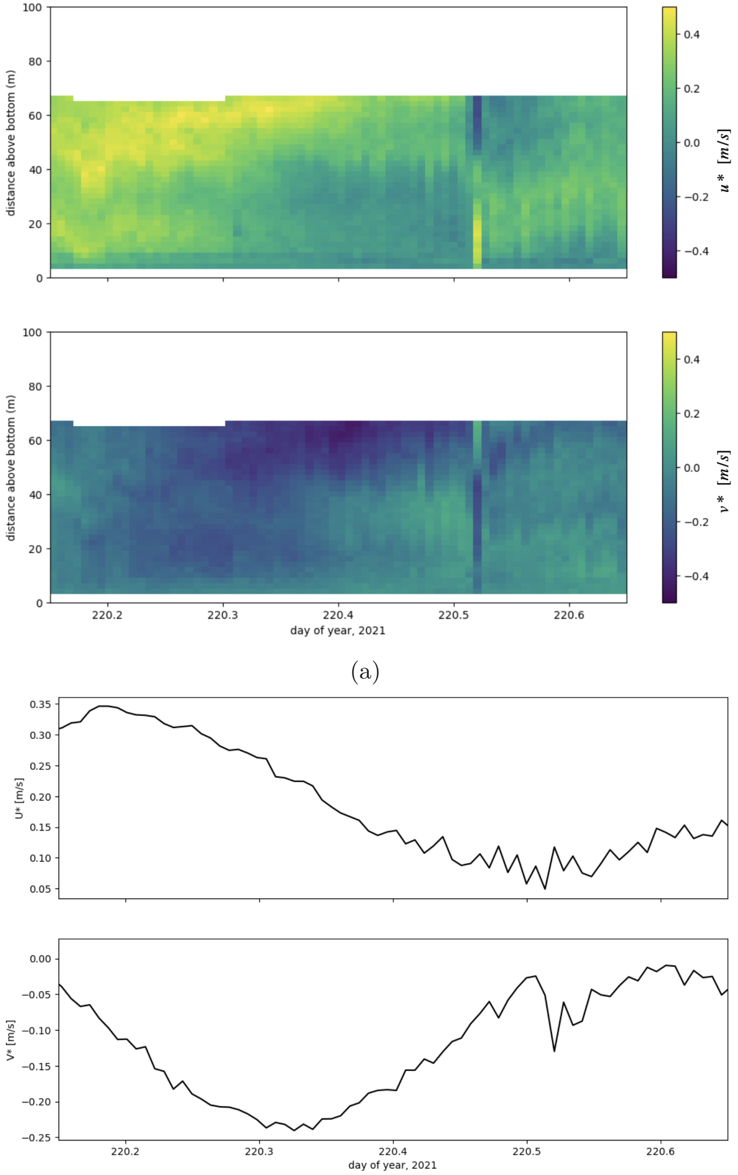

(a)

(b)

Figure 3.5: Horizontal plane velocities. Measurements from the 250 kHz ADCP at station $T2$. (a) Horizontal velocity component u^* parallel to the internal wave propagation (upper panel) and horizontal velocity component v^* perpendicular to the internal wave propagation (lower panel). (b) The vertical averaged horizontal velocities U^* and V^*. View of the timeline day of year 220.15 to 220.65, corresponding to 8 August 2021 03:36:00 to 15:36:00 UTC.

v in the north-south direction. The velocity field (u, v) is further rotated to the principal propagation direction of the internal wave, providing (u^*, v^*). Accordingly, the horizontal velocity components u^* and v^* are parallel and perpendicular to the internal wave propagation direction, respectively. The upper and lower panels in Figure 3.5a show u^* and v^*, respectively, throughout the vertical measured column. Taking a vertical average of (u^*, v^*), we get (U^*, V^*), shown in Figure 3.5b in the upper and lower panels, respectively. The absolute velocity becomes $U^*_{tot} = \overline{\sqrt{U^{*2} + V^{*2}}} = 0.23$ m s^{-1}. Here $\overline{(\cdot)}$ denotes a time-averaged over 12 hours. Only focusing on the current in the parallel direction, we get $\overline{U^*} = 0.19$ m s^{-1}.

3.4.3.2 Temperature profiles

For an optimal sampling of internal waves, it is recommended to employ a vertical array of density measurements with close spacing through the water column (Moulton, 2022). Utilizing time series data on density can be beneficial in approximating parameters such as stratification, wave amplitude, and frequency. However, in our study site, the temperature gradient is more significant than the density gradient, and thus, the preliminary result shown here will be of the temperature measurements from stations $T1$, $T2$, and $T3$ from 2021.

Figures 3.6a to 3.6c display the whole time series of the temperature measurements taken at stations $T3$, $T2$, and $T1$, respectively, over the entire measured field. The color bar shows the temperature range in degrees Celcius $(°C)$. The vertical axis is the depth presented in meters above bottom, and the horizontal axis is day of year, where day of year 0.5 is chosen to be 1 January at noon. The red lines indicate the timeline presented in Figure 3.7. Please note that the vertical field of view in the subfigures is about 50 m. However, it is important to remember that the measuring location above the bottom and the local water depth differ in all three subfigures. This means that the z-axis range varies.

Downward vertical excursions of higher temperatures can be seen in all three subfigures throughout the entire measurement period. Various factors, such as wind and storms, mesoscale eddies, and internal waves, could be responsible, but further investigation is needed to determine the exact causes for each vertical excursion seen. Here, we only focus on one observed internal wave train. In some areas, the isotherm's vertical excursion within the water column can extend beyond half the total water depth. This vertical excursion can cause noteworthy implications, for instance, particles are regularly transported and mixed throughout the water column because of the forces resulting in the isotherm's vertical movement.

3.4.3.3 Passage of one internal wave train

Multiple internal wave trains can be detected when closely examining and analyzing the temperature field. One example of an observed internal wave train will be presented below.

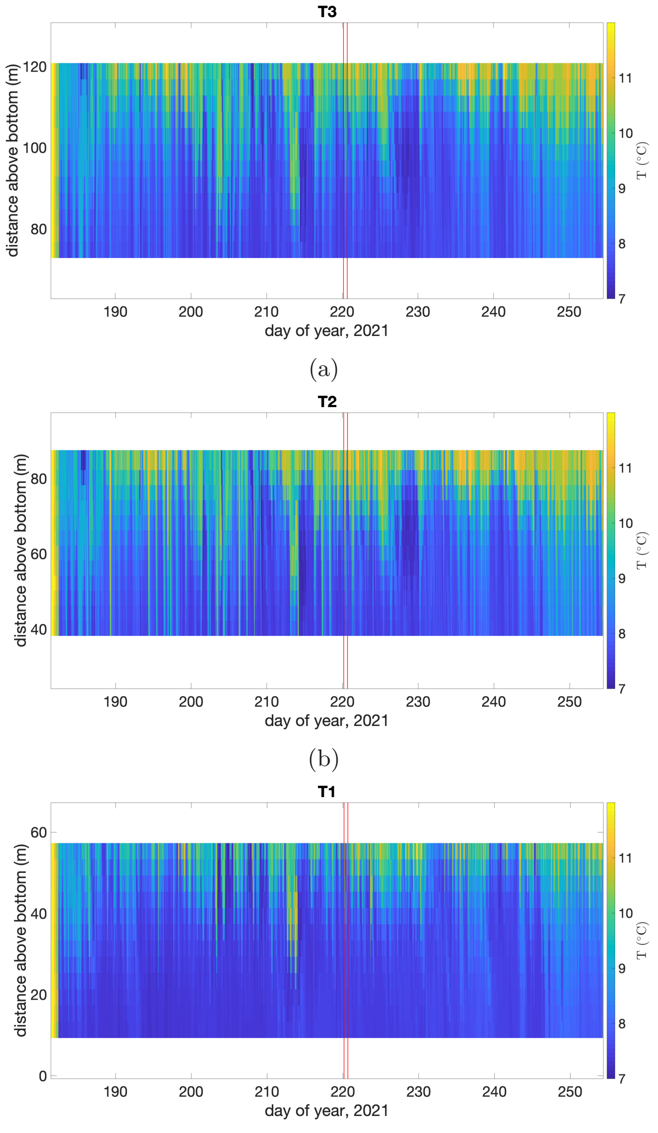

(a)

(b)

(c)

Figure 3.6: The figures display the whole time series of the temperature field measured throughout the vertical water column at stations (a) $T3$, (b) $T2$, and (c) $T1$. The measuring period lasted from 30 June 2021 12:00:00 UTC until 11 September 2021 11:14:40 UTC. The vertical field of view in the figures is approximately 50 m, but the local mean depth differ from each station. Hence, the z-axis varies since the local mean depth at (a) station $T3$ is 138 m, (b) station $T2$ is 100.7 m, and (a) station $T1$ is 80 m. The red lines indicate the timeline in Figure 3.7.

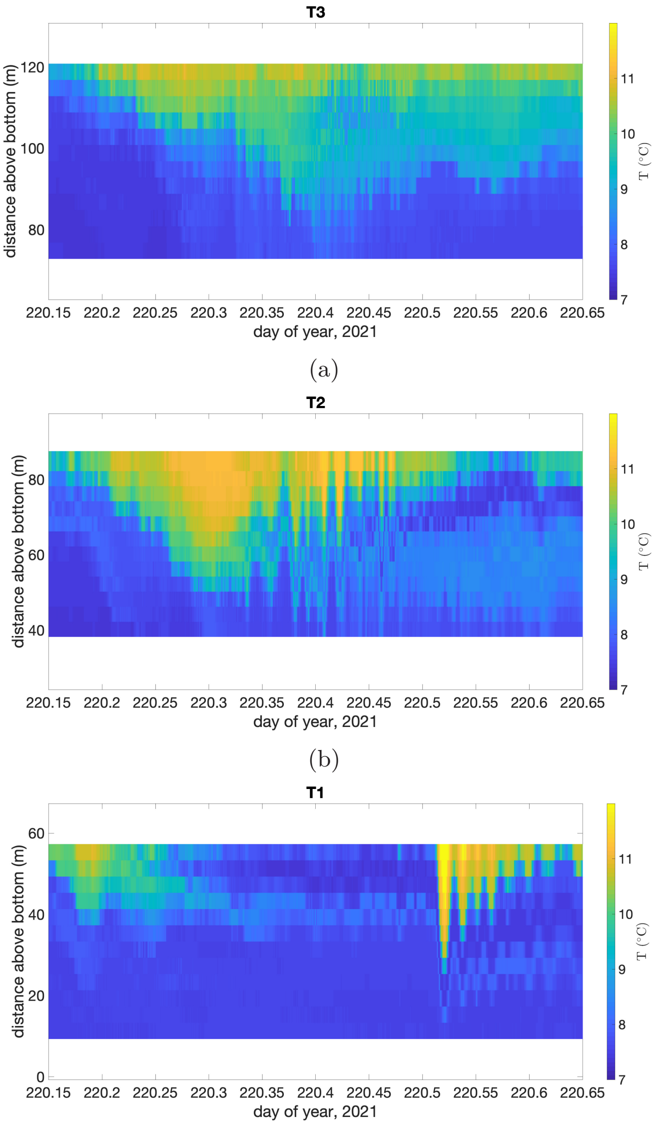

(a)

(b)

(c)

Figure 3.7: Observation of generation of an internal wave train. Same as Figure 3.6, but now a closer view of the timeline day of year 220.15 to 220.65 which correspond to 8 August 2021 03:36:00 to 15:36:00 UTC.

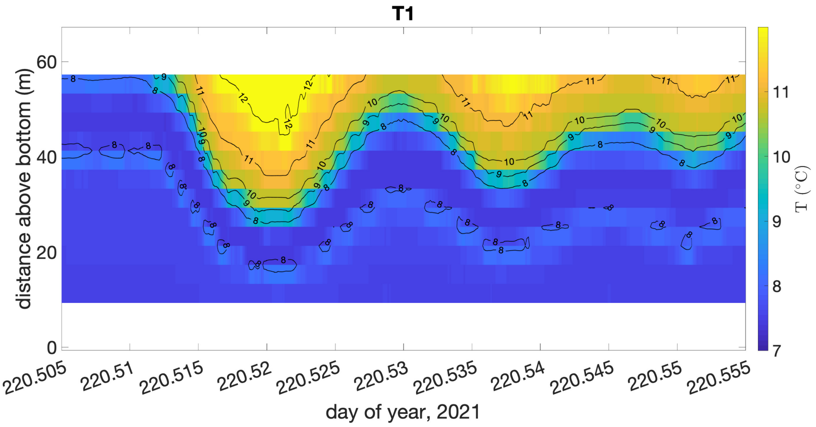

Figure 3.8: Same as Figure 3.7c, but now a closer view of the timeline day of year 220.505 to 220.555 to display the internal wave train. Black lines of temperature contours with step size of 1 degree Celsius with corresponding numbers.

Figure 3.7 provides a closer look at the temperature field from Figure 3.6, between day of year 220.15 to 220.65, which is precisely 8 August from 03:36:00 until 15:36:00 UTC.

When the tide flows over Eggagrunnen towards Hola, a depression of warmer water starts to evolve downstream. This can be seen in Figure 3.7a, at station $T3$, where warm water accumulates. Remember that station $T3$ is located on the lower part of the slope between Hola and Eggagrunnen. Slightly further up the slope, at station $T2$ (Figure 3.7b), it is more evident that warm water is accumulating, and a leading front is starting to evolve. The depression of warm water is growing and increasing its speed, where, at one point, it remains almost stationary against the tide. Then, most likely, the velocity of the tide starts to decrease, and/or the depression has gained a higher speed than the tide, resulting in an upstream propagation, evolving into a sequence of internal waves. It is more evident at station $T1$ that an internal wave group has formed, as shown in Figure 3.7c with one leading wave and subsequent smaller ones behind.

The internal wave train seen in Figure 3.7c is further presented in Figure 3.8 with added temperature contour lines. A proxy of the leading wave amplitude is extracted from the vertical excursion of one isotherm ($8°C$) and is found to be at 32 ± 2 m depth. The nondimensional amplitude becomes $a/H \approx 0.4$. The thickness of the pycnocline is estimated to be 16 m. The local middle depth of the pycnocline is 15 m.

It is approximately 5.3 h between the leading front at station $T2$ and the leading wave at station $T1$. An estimate of the nonlinear internal wave speed is $c \approx 0.21$ m s^{-1}. The wave period is estimated to be 22 minutes. A total horizontal velocity becomes $c + U^*_{tot} = 0.44$ m s^{-1}. An estimate of the wavelength λ based on the total local horizontal velocity is 581 m.

3.4.4 Summary & outlook

One of the future issue points raised in Lamb 2014 states: "*Recent field work has made it clear that the internal wave field on the continental shelf/slope is complicated. Theoretical work, numerical simulations, and laboratory experiments have necessarily focused on simple geometries and on isolated processes. There is clearly a need for studies using more realistic stratifications and more complicated geometries (e.g., canyons) as well as studies on concurrent physical processes (e.g., shoaling internal waves in the presence of barotropic tides). Such studies present many challenges for future investigations*". This statement highlights the importance of continuing to execute in-situ measurements along the Norwegian continental shelf, which is of utmost importance for gaining a comprehensive understanding of the region. Further, one of the future issue points raised in Woodson 2018 states: "*The role internal waves play in vulnerable coastal ecosystems relative to other processes need to be better understood.* Consequently, it is imperative that we meticulously analyze and interpret all the data we have gathered during our field studies in 2021 and 2022. The aims of the field expeditions mentioned in the beginning were i) quantify and qualify internal waves at this specific location, ii) determine how often internal waves occur, iii) quantify and qualify the internal wave-induced instabilities close to the bottom, and iv) estimate particle mixing and transport. Hence, all of these aims should be answered in the future.

Based on the preliminary results, internal waves occur regularly at the Hola trough. Due to their nonlinearity, one can hypothesize that they affect and induce instabilities at the bottom, which will transport sediments and nutrients (Boegman and Stastna 2019). In addition, instability in the pycnocline will lead to strong mixing in the upper part of the water column. To fully analyze the instability in the lower layer, we must examine the vertical velocities collected from the 1000 kHz ADCP. By utilizing this equipment, we may be able to detect structured patterns on the ocean floor through the vertical velocity field and backscatter, such as seen in the field work by Zulberti, N. L. Jones, and G. N. Ivey 2020. In addition, correlating the respective tide with the internal waves and examining the corresponding induced instability at the bottom should be of priority (Zulberti, N. L. Jones, and G. N. Ivey 2020).

When analyzing the field data, it is crucial to look for more than just internal waves. Steep fronts, eddies, and other potential mechanisms should also be thoroughly examined and considered.

Further calculations should include for instance shear and bed stress, turbulent kinetic energy, and diapycnal diffusivity (G. N. Ivey, Bluteau, and N. Jones 2018).

Scrutinizing the horizontal velocity field throughout the water column will provide a picture of whether the current is barotropic or baroclinic, in addition to, e.g., whether we, at times, may have inertia waves materializing. In addition, identify the additional mechanisms through the velocity field direction and magnitude.

3.4.5 In-situ, remote sensing and ocean model

In addition to processing all the data from our detailed in-situ measurements, it is of interest to connect these results with satellite remote sensing and the operational ocean model NorKyst800 at Metrological Institute (MET), Norway. NorKyst800 is an ocean general circulation model (OGCM) and is an operational setup of the Regional Ocean Modelling System (ROMS) (Albretsen et al. 2011). NorKyst800 has been used to derive parameters of internal waves to compare with SAR images. However, the model has a horizontal resolution of 800 m with 35 vertical layers, so it has limitations in resolving the short internal waves adequately. In addition, NorKyst800 is only a hydrostatic model.

In any case, the model has been constructed to factor in the varying depths of the small seamounts found on the continental shelf, along with the slope of the shelf and the physical conditions present in Norway's coastal areas (Albretsen et al. 2011). These conditions include, for instance, the coastal current, tides, and a range of different wave effects (Röhrs et al. 2023).

Integrating in-situ observations, remote sensing, and NorKyst800 will provide a more comprehensive understanding of this region's intricate processes and mechanisms and their effects on the coastal ecosystem.

3.5 ROV-PV: A new methodology

In this section, we will leave the internal wave topic and move over to the research conducted in Paper III. In Paper III, a new method of measuring the velocity and characteristics of water near a heaving ice floe is presented. The methodology was successfully tested in the Barents Sea and, in addition, validated in the laboratory.

The reader is referred to Chapter 4 and the comments under Author Contribution regarding which part of the research in Paper III was conducted during my master's and which part was achieved during my PhD. It is also important to note that the research group involved in Paper III is a different team than the one working on the Ecopulse project.

3.5.1 Wave-ice interaction

The region where sea ice meets open water, known as marginal ice zone (MIZ), is a highly dynamic environment characterized by interactions between sea ice and waves. The MIZ is composed of various forms of ice, ranging from grease ice to large ice floes and compact, semi-continuous ice sheets, and it spans between fast ice and open ocean (Newyear and Martin 1997; Squire et al. 1995).

Sea ice plays a crucial role in the energy exchange between the air, ice, and ocean of the Earth's climate system (Smedsrud et al. 2013). The complex interaction between ice and waves influences multiple conditions, and many of their aspects are still poorly understood (Squire 2007). The ice will move, bend, or even break into smaller floes when waves from the ocean enter the MIZ. The ice floes may then scatter and dissipate the wave energy, altering wave properties.

Hence, the interaction between waves and sea ice is a crucial mechanism, and investigations into waves propagating through ice-covered water have increased in interest during the past decades.

Working in the Arctic can be a difficult task due to its harsh conditions and inaccessibility. Various in-situ methods have been used to investigate wave propagation in ice-covered water, ice-water characteristics, interaction, energy dissipation, and attenuation. The instruments can rely on various sensors, allowing direct measurements of the water motion, ice motion, and other characteristics for the purpose needed. One of the measurement methods to measure a velocity profile below the ice is to use an ADCP (Løken et al. 2022). Other measurement methods implemented are, e.g., Acoustic Doppler velocimeters (ADVs) (Marchenko, Rabault, et al. 2017), Conductivity-Temperature-Depth (CTD) (Frey et al. 2017), accelerometers (Løken et al. 2022; Wadhams et al. 1988), and Inertial Motion Units (IMUs) (Kohout et al. 2014; Rabault, G. Sutherland, Ward, et al. 2016). There are some limitations to the data collected from these types of instruments. For instance, some only record points along a single profile or a time serie of the velocity at a fixed point. Paper III proposes a new methodology of a field measurement technique (the ROV-PV system) adapted for the Arctic's harsh environment, where we are able to measure the two-dimensional velocity field of the water.

Particle tracking velocimetry (PTV) and particle image velocimetry (PIV) are two non-intrusive optical measurement techniques used to investigate the velocity field of a two-dimensional region within the flow (Jensen et al. 2001; Rabault, Halsne, et al. 2016; Rabault, G. Sutherland, Jensen, et al. 2019). In recent years, PIV and PTV systems have been successfully utilized in situ to investigate turbulence in coastal ocean environments (Smith 2008). A submersible PIV system was implemented at the bottom to measure two-dimensional turbulence in the bottom boundary layer of the coastal ocean by Smith et al. 2002. They used naturally occurring particles, such as plankton and sediments, as tracer particles. Regardless, there is a lack of implementing such measurement technique systems in the polar region to investigate the two-dimensional velocity field near ice-water interaction.

3.5.2 The ROV-PV system

The setup consists of an open-source remotely operated vehicle (ROV), used as the optical instrument recording the two-dimensional velocity field, which was represented by rising air bubbles as tracers. The air bubbles rise approximately in a two-dimensional plane (need to subtract the vertical buoyant bubble velocity to get the vertical velocity of the water). The images (obtained by the ROV of the air bubbles) were analyzed using PIV to obtain the two-dimensional velocity field of water after removing the vertical bubble motion in post-processing. In Paper III, this system is referred to as the 'ROV-PV system' (PV = particle velocity). The methodology allows for studying water kinematics around interactions of water-ice (and ice-ice (Paper IV)) with a temporal and spatial resolution that extends beyond traditional instruments like ADCPs.

3.5.3 Validation in a controlled environment

In a controlled environment, two different laboratory experiments have been conducted to examine the characteristics and behavior of the bubbles.

One study was explicitly directed toward investigating the rising bubbles in stagnant water, specifically analyzing the relationship between the bubbles' terminal velocity and diameter. Thus, a high-speed camera for increased accuracy was used during this investigation, not the ROV. The study was conducted in both fresh and salt water. The study aimed to track each bubble to investigate their terminal velocity and size. A logarithmic curve fit was applied to the terminal velocity results (see Figure 4 in Paper III). The result provides a relationship between the bubble diameter and terminal velocity.

In the second investigation, the air bubbles were under the influence of periodic waves to investigate their response in a wave field. Here, the field of interest was directly below the wave crest in a vertical column, where the vertical velocity of the water is known to be zero (see Figure 7 in Paper III). The tracked bubble velocities are compared to theoretical water velocity from third-order Stokes waves (Newman 2018) in the horizontal direction below the wave crest (see Figures 8 and 9 in Paper III). The results show that the air bubbles were able to reproduce the water velocity with high accuracy. The methodology's potential to accurately measure water velocity is demonstrated. See Paper III for further discussion concerning the uncertainties in the measurements.

3.5.4 Field expedition

The field expedition was conducted on 26 April 2019 in the North-West Barents Sea near Hopen Island (marked by a red dot in Figure 3.9a). The setup was implemented close to an ice floe subjected to wave motion. The setup is shown in Figure 3.9b. For details regarding the ice floe, see Marchenko, Zenkin, et al. 2020, and for water properties measured throughout the water column close to our experiment site, see Fer and Drinkwater 2014.

To obtain the velocity field, PIV was applied to the images to obtain the two-dimensional velocity field in the given field of view within the grid. It is necessary to compensate for the bubbles' vertical buoyancy-driven velocity component to find the water's vertical velocity. The original plan was to use the results from the laboratory experiment (in stagnant water). However, the bubbles' rise velocity in the field was seen to be almost half of what was found in the laboratory. Hence, an on-site calibration under relatively calm conditions was performed. Accordingly, a mean vertical velocity was obtained from a reference image-couple taken under calm conditions where the air bubbles' velocity components were relatively small. The mean vertical velocity was then subtracted from all the vertical velocities from an instantaneous velocity field. The resulting two-dimensional velocity field is visualized as a vector plot in Figure 3.9c.

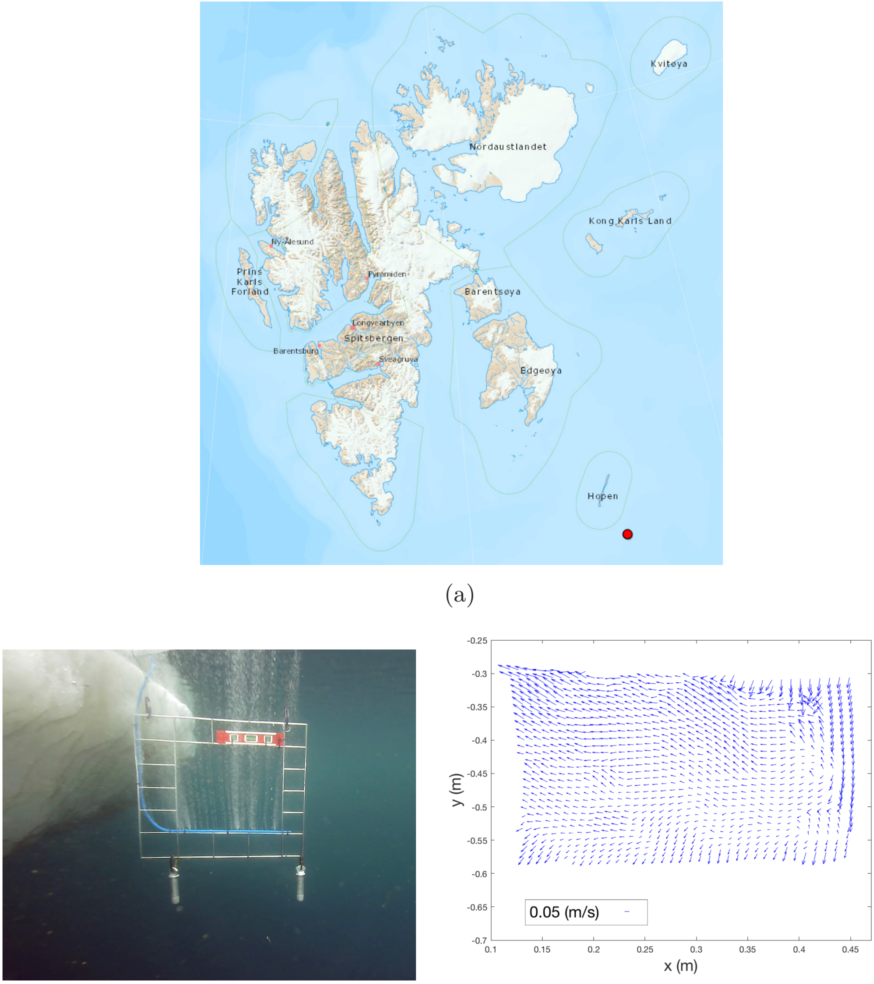

(a)

(b)

(c)

Figure 3.9: (a) An overview of where the field work in Paper III was conducted, where the red dot indicates the specific location. (b) Image from the ROV of the bubble plane and the coordinate grid next to an ice floe. The instantaneous flow field within the grid is presented in (c) as a vector plot. The images are from Paper III.

Chapter 4

Summary of Papers

This chapter presents an overview of the studies published during this thesis. For each paper, a short summary, some main findings, and a comment of my contribution to the papers are outlined. The papers are put into context, and an explanation of how they fit together is provided at the end of the chapter.

Paper I - Calculation of internal-wave-driven instability and vortex shedding along a flat bottom

For decades, researchers have conducted laboratory experiments and numerical simulations to study internal solitary waves propagating over a flat bottom. The investigations have provided valuable insights into the phenomenon of internal waves. However, there are still some (qualitative) discrepancies between laboratory and numerical results.

We investigate nonlinear internal solitary waves of depression propagating over a flat bottom computed by a finite-volume solver in two dimensions. We follow the experimental setup and wave generation as conducted in the laboratory experiments by Carr, Davies, and Shivaram 2008.

Internal solitary waves of depression move horizontally through a stratified fluid, creating an adverse pressure gradient along the bottom behind the wave trough. This causes a separation bubble in the pressure-driven bottom layer, starting from the separation point beneath the wave trough. The fluid near the bottom moves in the direction of the wave, and as the wave amplitude increases, the separation bubble can become unstable and lead to vortex formation. The present work investigates the instability occurring in the separation bubbles. Our computations exhibit two separation bubbles emerging, whereas only one has been previously documented (Aghsaee, Boegman, Diamessis, et al. 2012; Diamessis and Redekopp 2006). One bubble forms in the wave phase behind the trough, while a second forms further downstream. The threshold from the stable to the unstable regime is scrutinized and is found to depend on the depth of the pycnocline. This result was found in previous laboratory experiments and in our numerical computations. The effect of scale is systematically investigated by varying the kinematic viscosity of the water. Hence, our calculations are presented for the wave Reynolds number $Re_w = 1.9 \times 10^4 - 6.5 \times 10^5$.

Our calculations agree very well with the laboratory experiments by Carr, Davies, and Shivaram 2008, where the result presented suggests that the instability observed in their experiments was predominantly two-dimensional. This result has responded to the ongoing discussion regarding laboratory-observed instabilities being primarily three-dimensional.

Author contribution: This is the main work of my PhD thesis. I developed the concept and the methodology together with my supervisor J. Grue. I conducted the model development and configuration, numerical simulations, postprocessing, analysis, and presentation of the results with supervision from J. Grue. I wrote the paper draft. The submitted version was written with guidance and contribution from J. Grue.

Paper II - Tracer particle motion driven by vortex formation in the bottom boundary layer underneath internal solitary waves

Large amplitude internal solitary waves in coastal oceans cause significant horizontal water velocities near the seabed, resulting in bottom boundary layer instabilities and vortex formation. The movement of essential components and organisms facilitated by the induced mechanisms in the bottom boundary can resuspend sediments and, e.g., impact the ecosystem's supply, affecting the balance of marine life.

Using a two-dimensional laminar numerical method, we study the vortex formation and Lagrangian tracer particle motion in the bottom boundary layer. The instability in the bottom boundary layer is induced by nonlinear internal solitary waves of depression, where both the wave field and vortices influence the motion of the tracer particle cloud seeded in the numerical wave tank.

A convergence study on the numerical computations of the vortex formation is performed and documented. We compare the wave-induced vortices with available laboratory observations and obtain a very good match between our numerical calculations and the measurements conducted in the laboratory.

The tracer particles' trajectories, displacements, and vertical positions as a function of time are calculated and illustrated. The vertical positions of the tracer particles are compared to available field observations. Even though the processes at the field scale and our moderate scale may not be directly similar, our computations align fairly well with the observed data.

Author contribution: I developed the concept and the methodology together with the co-authors. I conducted the model development and configuration with contributions from J. Sletten. I conducted the numerical simulations, postprocessing, analysis, and presentation of the results. I wrote the paper draft and submitted version with guidance from J. Grue.

Paper III - Bringing optical fluid motion analysis to the field: a methodology using an open source ROV as a camera system and rising bubbles as tracers

To comprehend the energy exchange between the atmosphere, ice, and the ocean in the Arctic, a thorough understanding of the water movement in the marginal ice zone is crucial. However, very few two-dimensional in-situ observations in the marginal ice zone exist due to the rough and harsh environment.

The research conducted in this paper aimed to develop a setup that could be employed in harsh environments to investigate water kinematics related to mechanisms of wave attenuation in the marginal ice zone. Accordingly, a new field measurement technique is presented. This paper primarily focuses on the methodology and verification of the complete setup.

A remotely operated vehicle (ROV) with open-source software was used as the imaging device and light source. Air bubbles were employed as tracers, allowing typical image processing techniques to be utilized on the data obtained. A thorough investigation was conducted in a controlled environment on the dynamics of the bubbles to determine their suitability as tracers. Examining how the bubbles responded in a wave field was tested in the laboratory and compared with theory. The horizontal velocity component of the bubbles under the influence of periodic waves was measured and found to be within 10% accuracy of reproducing the water velocity. Laboratory test results were also initially intended to estimate the buoyancy-driven vertical bubble velocity to compensate for this during field experiments.

The methodology was successfully employed and tested near a heaving ice floe in the Barents Sea. It was discovered that an on-site calibration was necessary due to varying field conditions, such as temperature and pressure, which altered the bubbles' properties.

Author contribution: I built/assembled the instrumental setup with contributions from the co-authors during my master's. The data used for this paper was collected during my master's.
In the paper: The experiments in the small wave tank (stagnant water, Figure 2) were conducted during my master's. The velocity of the rising bubbles in the stagnant water and their shape were analyzed during my master's (Tables 1 and 2). I conducted additional analysis from this data set for Figure 3 during my PhD. The theory in section 2.3 (Air bubbles as tracers), down to equation 4, originated during my PhD. (hence, it differs from the theory in my master's). I reanalyzed and replotted the data from the stagnant water experiments with the new theory (Figure 4) during my PhD. The experiments in the big wave tank (Figure 5) were conducted during my master's. The theory from the beginning of section 3 (Validation in a wave tank) down to equation 8 is the same as in my master's, but from equation 8 until equation 11 originated during my PhD. I contributed to the analysis of the data set during my PhD. The field work was conducted during my master's (Figures 1 and 11). I reanalyzed and replotted the data (Figures 12 and 13) during my PhD.
I contributed to the paper draft during my PhD.

An integrated view of the papers

Papers I and II utilize a second-order finite-volume solver, Basilisk. Paper II builds on a natural continuation of Paper I. In both papers, internal solitary waves of depression propagating over a flat bottom are studied.

The purpose of the studies in Papers I and II, as well as the field study at the Hola trough (Chapter 3), was to gain a deeper understanding of the hydrodynamics related to internal waves, vertical mixing in the water column, and transport of nutrients. This knowledge may contribute to a more comprehensive understanding of the biophysical relationships between breaking waves and ecosystems' vertical structuring and operation.

One question regarding the internal waves in the Lofoten-Vesterålen region has been how many of the generated internal waves will interact with the ocean bottom to induce instabilities. From the field studies, the internal wave generation site is on the slope between the Hola trough and Eggagrunnen before propagating as an internal wave train over the bank. In Paper I, we found that internal waves induce instabilities at the bottom when having a lower wave amplitude than assumed in previous simulation studies. It is not directly analogous to compare results from flat bottom cases with those cases where we have a slope. Regardless, instabilities occur even earlier over slopes; hence, only sharp fronts or weak internal waves may be necessary to induce bottom instabilities at the slope. Once the internal waves have fully developed, they travel over flatter topography. Even if instability can be set in motion by weak internal waves, the question remains about how much vertical and horizontal movement of particles occurs at this particular site. Paper II demonstrated that the Lagrangian particles seeded in the numerical wave tank were transported out from the bottom boundary layer δ and moved vertically as high as 70δ for simulations having wave Reynolds number $Re_w = 6.5 \times 10^5$ with an internal wave of theoretical maximum amplitude $a/H = 0.3$.

While neutrally buoyant tracer particles have been studied in Paper II, "active" particles have been studied in Paper III, where the field study illustrates the applicability of the measurement technique to measure the dynamics of water motion in the vicinity of ice in harsh environments. Accordingly, Paper III concerns how the fluid velocity is estimated from the motion of bubble tracers, where Paper II examines how internal wave-vortex-induced particle transport behaves.

Chapter 5

Summary and future perspectives

The first part of this chapter gives a summary of this thesis and its contributions, and the second part discusses some possible extensions to the work conducted.

5.1 Summary

This thesis explores numerical simulations of nonlinear internal solitary waves of depression propagating over a flat bottom where Papers I and II centers around this topic. Papers I and II explore the wave-induced instability in the bottom boundary layer and the various occurring mechanisms.

The numerical solver utilized to simulate internal solitary waves is the second-order finite-volume solver Basilisk (www.basilisk.fr), which solves the two-phase incompressible Navier-Stokes equations. The two-dimensional numerical wave tank setup and wave generation method are identical to the physical laboratory experiments conducted by Carr, Davies, and Shivaram 2008.

When the system is set into motion, a nonlinear internal solitary wave of depression is generated, moving horizontally along a stratified fluid. The internal wave-induced velocity field induces an adverse pressure gradient in the bottom boundary layer. In this pressure-driven bottom layer, separation bubbles evolve. Only one separation bubble has been previously documented (Aghsaee, Boegman, Diamessis, et al. 2012; Diamessis and Redekopp 2006; Sakai, Diamessis, and Jacobs 2020). However, in Paper I, it is found that two separation bubbles of anticlockwise vorticity are formed. One separation bubble commences from the separation point beneath the wave trough in the wave phase, and one further upstream outside the wave phase. Accordingly, for large Reynolds numbers, e.g., $Re_w = 5.9 \times 10^5$, the bubbles are seen to separate, whereas for smaller Reynolds numbers, e.g., $Re_w = 5.9 \times 10^4$, they partially overlap. For $Re_w = 2 \times 10^4$, they are seen to merge (Diamessis and Redekopp 2006).

Paper I further scrutinizes the transition from when the separation bubbles go from stable to experiencing instability. Both Paper I and II emphasize convergence, including the resolution of the bottom boundary layer, vortex formation, and other wave parameters. We obtained a very good agreement with the laboratory experiments by Carr, Davies, and Shivaram 2008 for the transition to instability, where long-standing computational attempts have been unsuccessful, as communicated in the conclusion by Boegman and Stastna 2019. They argued that the experiments by Carr, Davies, and Shivaram 2008 did not represent the transition to instability, implying conflicting results.

Paper I discusses the transition to instability and matches the experiments by Carr, Davies, and Shivaram 2008, implying that the instability threshold found in the numerical simulations by Aghsaee, Boegman, Diamessis, et al. 2012 is too strong. Accordingly, the instability occurs much earlier for waves of considerably smaller amplitude than what they predict. In addition, our results indicate that the instability in the three-dimensional wave tank experiments by Carr, Davies, and Shivaram 2008 was predominantly two-dimensional up to a distance of eight water depths behind the wave trough.

As the amplitude a of the wave increases, the separation bubble becomes unstable, leading to the formation of vortices. The formation of vortices causes oscillating bed shear stress, where the strongest stress amplitude materializes during the wave and roll-up phases, emerging over a distance of 1-1.5 water depths, otherwise of less magnitude (Paper I). The shear stress computed in the laminar model and measured in previous field studies has similar non-dimensional values (scaled by $\rho_0 c_0^2/2$) when the non-dimensional amplitude and relative pycnocline depth are equivalent ($a/H \sim 0.3$, $d/H \sim 0.2$).

In oceanic environments, various mechanisms may cause re-suspension of particles at the bottom (Boegman and Stastna 2019). Paper II presents a study of Lagrangian tracer particles and their behavior under the influence of the internal wave-induced velocity field and vortices. Internal waves may supply marine life with essential components and organisms, maintaining the ecosystem (R. Bøe et al. 2009; MacKinnon and Gregg 2003; Quaresma et al. 2007; Sandstrom and Elliott 1984) as discussed in Chapter 3. Nonlinear internal waves are expected to continue being a significant field of research in the future due to their widespread distribution and crucial role in connecting large-scale tides to smaller-scale turbulence (C. R. Jackson, Da Silva, and Jeans 2012).

The well-known measurement techniques particle image velocimetry (PIV) and particle tracking velocimetry (PTV) are commonly used to trace particles in fluids. However, installing instruments in the field to measure the velocity of the water with the measurement techniques PIV and PTV is challenging or even impossible in certain areas. The research in Paper III presents a new method of measuring the velocity and characteristics of water near a heaving ice floe in harsh environments, using an ROV as an imaging device and light source and air bubbles as tracers. Bubbles can rise approximately in a two-dimensional plane, eliminating the need for a light/laser sheet. The main challenge of utilizing bubbles as tracer particles was to generate bubbles of uniform size. Small bubbles are desired as they have a rectilinear rising path (Haberman and Morton 1953) since rise velocity is a function of the bubble diameter and needs to be subtracted from the measured vertical velocity to obtain the water velocity. The methodology allows for investigating the movement of water around interactions between water-ice (and ice-ice discussed in Paper IV) with high temporal and spatial resolution.

As experimental measurements and numerical simulations become more precise, we can observe smaller and smaller scales in dynamical systems. This has allowed us to understand better the flow and motion properties that were previously difficult to quantify.

5.2 Future perspectives

The numerical simulations presented in this thesis focus solely on internal solitary waves of depression propagating over a flat bottom. However, there are numerous different internal waves (as presented in Chapter 1) that could be implemented and their various instabilities studied, such as internal waves of elevation propagating over a flat bottom (Bogucki, Dickey, and Redekopp 1997; Bogucki and Redekopp 1999; Carr and Davies 2010; Diamessis and Redekopp 2006; Stastna and Lamb 2002; Stastna and Lamb 2008), shoaling internal waves of depression and elevation (Klymak and Moum 2003; Sveen et al. 2002; Xu and Stastna 2020) where a sloping bottom is implemented in the numerical wave tank, the wave tank is tilted, or a specific topography is implemented.

Studies could also be conducted where the primary focus is directed toward the pycnocline and instabilities, such as overturning in the upper part of the water column (Carr, Fructus, et al. 2008) and Kelvin-Helmholtz instability in the shear layer (Carr, Franklin, et al. 2017; Fructus, Carr, et al. 2009; Grue, Jensen, et al. 1999; Helfrich and Melville 2006). The stratification in the numerical wave tank during the work of this thesis is the same as in the laboratory experiments by Carr, Davies, and Shivaram 2008. However, this setting can be modified to create a stratified layer close to the bottom, as measured in the field observations by Zulberti, N. L. Jones, and G. N. Ivey 2020, or, for instance, to create a linear stratification in the top layer, as in Carr, Fructus, et al. 2008.

In Paper II, we let the internal wave travel to the end of the wave tank and return to study the motion of the particles after the influence of two internal wave passages. It would have been interesting to model the numerical wave tank with multiple gates to generate multiple waves. Changing the domain size of the wave tank is also a possibility.

The Norwegian continental shelf and field work

In the ocean, understanding the biophysical interaction between breaking internal waves, vertical structuring, and functioning of ecosystems is vital. A summary and future outlook regarding internal waves on the Norwegian continental shelf and the fieldwork conducted in the project were presented in Chapter 3. The goal is to comprehend if there is a connection between the structure and functioning of marine ecosystem communities living in this specific topographically complex setting (at the Hola trough, Vesterålen) and how strongly these communities depend on the interplay between water flow and seafloor relief. Consequently, the main future task is to investigate the wave-induced instabilities both at the sea bottom and in the internal wave and the vertical transport induced by the internal waves present in Vesterålen, particularly understanding the food supply during summer and early autumn, when the coast is depleted for nutrition.

Future studies should connect ideal internal wave models in two dimensions to three-dimensional regional ocean model simulations at Vesterålen and elsewhere along the Norwegian Continental Shelf. For instance, the regional ocean model does not resolve the breaking processes. However, results from Basilisk can reveal how waves would break and how much mixing would occur in terms of intensity and depth for a specific configuration in the regional model. Combining simulations from ideal and regional models can also address the importance of vertical mixing from internal waves compared to other local processes, such as wind-induced mixing, bottom shear flow, and the advection of turbulent kinetic energy.

Bibliography

Aghsaee, P. and Boegman, L. (2015). “Experimental investigation of sediment resuspension beneath internal solitary waves of depression”. In: *Journal of Geophysical Research: Oceans* vol. 120, no. 5, pp. 3301–3314.

Aghsaee, P., Boegman, L., Diamessis, P. J., et al. (2012). “Boundary-layer-separation-driven vortex shedding beneath internal solitary waves of depression”. In: *Journal of Fluid Mechanics* vol. 690, pp. 321–344.

Aghsaee, P., Boegman, L., and Lamb, K. G. (2010). “Breaking of shoaling internal solitary waves”. In: *Journal of Fluid Mechanics* vol. 659, pp. 289–317.

Albretsen, J. et al. (2011). *NorKyst-800 Rapport nr. 1: Brukermanual og tekniske beskrivelser.*

Alford, M. H. et al. (2012). “Internal waves on the Washington continental shelf”. In: *Oceanography* vol. 25, no. 2, pp. 66–79.

Almgren, A., Camassa, R., and Tiron, R. (2012). “Shear instability of internal solitary waves in Euler fluids with thin pycnoclines”. In: *Journal of Fluid Mechanics* vol. 710, pp. 324–361.

Amick, C. J. and Turner, R. E. L. (1986). “A global theory of internal solitary waves in two-fluid systems”. In: *Transactions of the American Mathematical Society* vol. 298, no. 2, pp. 431–484.

Apel, J. R., Holbrook, J. R., et al. (1985). “The Sulu Sea internal soliton experiment”. In: *Journal of Physical Oceanography* vol. 15, no. 12, pp. 1625–1651.

Apel, J. R., Proni, J. R., et al. (1975). “Near-simultaneous observations of intermittent internal waves on the continental shelf from ship and spacecraft”. In: *Geophysical Research Letters* vol. 2, no. 4, pp. 128–131.

Arthur, R. S. and Fringer, O. B. (2014). “The dynamics of breaking internal solitary waves on slopes”. In: *Journal of fluid mechanics* vol. 761, pp. 360–398.

Barad, M. F. and Fringer, O. B. (2010). “Simulations of shear instabilities in interfacial gravity waves”. In: *Journal of Fluid Mechanics* vol. 644, pp. 61–95.

Bell, J. B., Colella, P., and Glaz, H. M. (1989). “A second-order projection method for the incompressible Navier-Stokes equations”. In: *Journal of Computational Physics* vol. 85, no. 2, pp. 257–283.

Benney, D. J. (1966). “Long non-linear waves in fluid flows”. In: *Journal of Mathematics and Physics* vol. 45, no. 1-4, pp. 52–63.

Boegman, L., Imberger, J., et al. (2003). “High-frequency internal waves in large stratified lakes”. In: *Limnology and oceanography* vol. 48, no. 2, pp. 895–919.

Boegman, L. and Ivey, G. N (2009). “Flow separation and resuspension beneath shoaling nonlinear internal waves”. In: *Journal of Geophysical Research: Oceans* vol. 114, no. C2.

Boegman, L., Ivey, G. N., and Imberger, J. (2005). “The degeneration of internal waves in lakes with sloping topography”. In: *Limnology and Oceanography* vol. 50, no. 5, pp. 1620–1637.

Boegman, L. and Stastna, M. (2019). “Sediment Resuspension and Transport by Internal Solitary Waves”. In: *Annual Review of Fluid Mechanics* vol. 51, no. 1, pp. 129–154.

Bogucki, D., Dickey, T., and Redekopp, L. G. (1997). “Sediment resuspension and mixing by resonantly generated internal solitary waves”. In: *Journal of Physical Oceanography* vol. 27, no. 7, pp. 1181–1196.

Bogucki, D. and Garrett, C. (1993). “A simple model for the shear-induced decay of an internal solitary wave”. In: *Journal of physical oceanography* vol. 23, no. 8, pp. 1767–1776.

Bogucki, D. and Redekopp, L. G. (1999). “A mechanism for sediment resuspension by internal solitary waves”. In: *Geophysical Research Letters* vol. 26, no. 9, pp. 1317–1320.

Bourgault, D. et al. (2007). “Evolution of a shoaling internal solitary wavetrain”. In: *Geophysical Research Letters* vol. 34, no. 3.

Buhl-Mortensen, L. et al. (2012). “Banks, troughs, and canyons on the continental margin off Lofoten, Vesterålen, and Troms, Norway”. In: *Seafloor Geomorphology as Benthic Habitat.* Elsevier, pp. 703–715.

Bøe, R. et al. (2009). “Giant sandwaves in the Hola glacial trough off Vesterålen, North Norway”. In: *Marine Geology* vol. 267, no. 1-2, pp. 36–54.

Bøe, R et al. (2016). “Cold-water coral reefs in the Hola glacial trough off Vesterålen, North Norway”. In: *Atlas of Submarine Glacial Landforms: Modern, Quaternary and Ancient. Geological Society, London, Memoirs* vol. 46, pp. 309–10.

Camassa, R. et al. (2006). “On the realm of validity of strongly nonlinear asymptotic approximations for internal waves”. In: *Journal of Fluid Mechanics* vol. 549, pp. 1–23.

Carr, M. and Davies, P. A. (2006). “The motion of an internal solitary wave of depression over a fixed bottom boundary in a shallow, two-layer fluid”. In: *Physics of Fluids* vol. 18, no. 1, p. 016601.

— (2010). “Boundary layer flow beneath an internal solitary wave of elevation”. In: *Physics of Fluids* vol. 22, no. 2, p. 026601.

Carr, M., Davies, P. A., and Shivaram, P. (2008). “Experimental evidence of internal solitary wave-induced global instability in shallow water benthic boundary layers”. In: *Physics of Fluids* vol. 20, no. 6, p. 066603.

Carr, M., Franklin, J., et al. (2017). “The characteristics of billows generated by internal solitary waves”. In: *Journal of Fluid Mechanics* vol. 812, pp. 541–577.

Carr, M., Fructus, D., et al. (2008). “Convectively induced shear instability in large amplitude internal solitary waves”. In: *Physics of Fluids* vol. 20, no. 12.

Chomaz, J.-M. (2005). “Global instabilities in spatially developing flows: Non-Normality and Nonlinearity”. In: *Annual Review of Fluid Mechanics* vol. 37, no. 1, pp. 357–392.

Christie, D. R. (1989). “Long Nonlinear Waves in the Lower Atmosphere”. In: *Journal of Atmospheric Sciences* vol. 46, no. 11, pp. 1462–1491.

Christie, D. R. and White, R. (1992). "The morning glory of the Gulf of Carpentaria". In: *Aust. Meteorol. Mag* vol. 41, pp. 21–60.

Diamessis, P. J. and Redekopp, L. G. (May 2006). "Numerical Investigation of Solitary Internal Wave-Induced Global Instability in Shallow Water Benthic Boundary Layers". In: *Journal of Physical Oceanography* vol. 36, no. 5, pp. 784–812.

Dokken, S. T. et al. (2001). "Identification and characterization of internal waves in SAR images along the coast of Norway". In: *Geophysical research letters* vol. 28, no. 14, pp. 2803–2806.

Duda, T. F. et al. (2004). "Internal tide and nonlinear internal wave behavior at the continental slope in the northern South China Sea". In: *IEEE Journal of Oceanic Engineering* vol. 29, no. 4, pp. 1105–1130.

Ekman, V. W. (1904). "On dead water: the Norwegian north polar expedition 1893-1896. Scientific Results. Edited by F. Nansen. Ch. CV. A. lW. Brogger". In:

Ellevold, T. J. and Grue, J. (2023). "Calculation of internal-wave-driven instability and vortex shedding along a flat bottom". In: *Journal of Fluid Mechanics* vol. 966, A40.

Farmer, D. M. (1978). "Observations of long nonlinear internal waves in a lake". In: *Journal of Physical Oceanography* vol. 8, no. 1, pp. 63–73.

Farmer, D., Li, Q., and Park, J.-H. (2009). "Internal wave observations in the South China Sea: The role of rotation and non-linearity". In: *Atmosphere-Ocean* vol. 47, no. 4, pp. 267–280.

Fer, I. and Drinkwater, K. (2014). "Mixing in the Barents Sea polar front near Hopen in spring". In: *Journal of Marine Systems* vol. 130, pp. 206–218.

Fosså, J. H., Buhl-Mortensen, P., and Furevik, D. M. (2000). *Lophelia-korallrev langs norskekysten: forekomst og tilstand.*

Fosså, J. H., Kutti, T., et al. (2015). *Vurdering av Norske korallrev.*

Fosså, J. H., Lindberg, B., et al. (2005). "Mapping of Lophelia reefs in Norway: experiences and survey methods". In: *Cold-water corals and ecosystems*, pp. 359–391.

Fosså, J. H., Mortensen, P. B., and Furevik, D. M. (2002). "The deep-water coral Lophelia pertusa in Norwegian waters: distribution and fishery impacts". In: *Hydrobiologia* vol. 471, pp. 1–12.

Freiwald, A. et al. (2002). "The Sula reef complex, Norwegian shelf". In: *Facies* vol. 47, pp. 179–200.

Frey, D. I. et al. (2017). "Water structure and currents in the Bear Island trough in July–August 2017". In: *Russian Journal of Earth Sciences* vol. 17, no. 3, pp. 1–5.

Fructus, D., Carr, M., et al. (2009). "Shear-induced breaking of large internal solitary waves". In: *Journal of Fluid Mechanics* vol. 620, pp. 1–29.

Fructus, D. and Grue, J. (2004). "Fully nonlinear solitary waves in a layered stratified fluid". In: *Journal of Fluid Mechanics* vol. 505, pp. 323–347.

Gaster, M. (1967). *The structure and behaviour of laminar separation bubbles.* AGARD CP-4, pp. 813–854.

Grimshaw, R., Pelinovsky, E., and Poloukhina, O. (2002). “Higher-order Korteweg-de Vries models for internal solitary waves in a stratified shear flow with a free surface”. In: *Nonlinear Processes in Geophysics* vol. 9, no. 3/4, pp. 221–235.

Grue, J. (2006). “Very large internal waves in the ocean — observations and nonlinear models”. In: *Waves in Geophysical Fluids: Tsunamis, Rogue Waves, Internal Waves and Internal Tides*. Ed. by Grue, J. and Trulsen, K. Springer Vienna, pp. 205–270.

— (2015). “Nonlinear interfacial wave formation in three dimensions”. In: *Journal of fluid mechanics* vol. 767, pp. 735–762.

Grue, J., Friis, H. A., et al. (1997). “A method for computing unsteady fully nonlinear interfacial waves”. In: *Journal of Fluid Mechanics* vol. 351, pp. 223–252.

Grue, J., Jensen, A., et al. (1999). “Properties of large-amplitude internal waves”. In: *Journal of Fluid Mechanics* vol. 380, pp. 257–278.

— (2000). “Breaking and broadening of internal solitary waves”. In: *Journal of Fluid Mechanics* vol. 413, pp. 181–217.

Grue, J. and Sveen, J. K. (2010). “A scaling law of internal run-up duration”. In: *Ocean Dynamics* vol. 60, no. 4, pp. 993–1006.

Haberman, W. L. and Morton, R. K. (1953). *An experimental investigation of the drag and shape of air bubbles rising in various liquids*. David W. Taylor Model Basin Washington, DC.

Halpern, D. (1971). “Semidiurnal internal tides in Massachusetts Bay”. In: *Journal of Geophysical Research* vol. 76, no. 27, pp. 6573–6584.

Hartharn-Evans, S. G. et al. (2022). “Stratification effects on shoaling internal solitary waves”. In: *Journal of Fluid Mechanics* vol. 933, A19.

Haury, L. R., Briscoe, M. G., and Orr, M. H. (1979). “Tidally generated internal wave packets in Massachusetts Bay”. In: *Nature* vol. 278, no. 5702, pp. 312–317.

Helfrich, K. R. (1992). “Internal solitary wave breaking and run-up on a uniform slope”. In: *Journal of Fluid Mechanics* vol. 243, pp. 133–154.

Helfrich, K. R. and Melville, W. K. (1986). “On long nonlinear internal waves over slope-shelf topography”. In: *Journal of Fluid Mechanics* vol. 167, pp. 285–308.

— (2006). “Long nonlinear internal waves”. In: *Annual Review of Fluid Mechanics* vol. 38, no. 1, pp. 395–425.

Holligan, P. M., Pingree, R. D., and Mardell, G. T. (1985). “Oceanic solitons, nutrient pulses and phytoplankton growth”. In: *Nature* vol. 314, no. 6009, pp. 348–350.

Hsu, M.-K., Liu, A. K., and Liu, C. (2000). “A study of internal waves in the China Seas and Yellow Sea using SAR”. In: *Continental shelf research* vol. 20, no. 4-5, pp. 389–410.

Hunkins, K. and Fliegel, M. (1973). “Internal undular surges in Seneca Lake: A natural occurrence of solitons”. In: *Journal of Geophysical Research* vol. 78, no. 3, pp. 539–548.

Ivey, G. N., Bluteau, C. E., and Jones, N.L. (2018). “Quantifying diapycnal mixing in an energetic ocean”. In: *Journal of Geophysical Research: Oceans* vol. 123, no. 1, pp. 346–357.

Jackson, C. (2007). “Internal wave detection using the moderate resolution imaging spectroradiometer (MODIS)”. In: *Journal of Geophysical Research: Oceans* vol. 112, no. C11.

Jackson, C. R., Da Silva, J. C. B., and Jeans, G. (2012). “The generation of nonlinear internal waves”. In: *Oceanography* vol. 25, no. 2, pp. 108–123.

Jensen, A. et al. (2001). “Accelerations in water waves by extended particle image velocimetry”. In: *Experiments in fluids* vol. 30, no. 5, pp. 500–510.

Kao, T. W., Pan, F.-S., and Renouard, D. (1985). “Internal solitons on the pycnocline: generation, propagation, and shoaling and breaking over a slope”. In: *Journal of Fluid Mechanics* vol. 159, pp. 19–53.

Keulegan, G. H. (1953). *Characteristics of internal solitary waves.*

Klymak, J. M. and Moum, J. N. (2003). “Internal solitary waves of elevation advancing on a shoaling shelf”. In: *Geophysical Research Letters* vol. 30, no. 20.

Knickerbocker, C. J. and Newell, A. C. (1980). “Internal solitary waves near a turning point”. In: *Physics Letters A* vol. 75, no. 5, pp. 326–330.

Kohout, A. L. et al. (2014). “Storm-induced sea-ice breakup and the implications for ice extent”. In: *Nature* vol. 509, no. 7502, pp. 604–607.

Koop, C. G. and Butler, G. (1981). “An investigation of internal solitary waves in a two-fluid system”. In: *Journal of Fluid Mechanics* vol. 112, pp. 225–251.

Lamb, K. G. (2014). “Internal Wave Breaking and Dissipation Mechanisms on the Continental Slope/Shelf”. In: *Annual Review of Fluid Mechanics* vol. 46, no. 1, pp. 231–254.

Lamb, K. G. and Farmer, D. (2011). “Instabilities in an Internal Solitary-like Wave on the Oregon Shelf”. In: *Journal of Physical Oceanography* vol. 41, no. 1, pp. 67–87.

Lee, C.-Y. and Beardsley, R. C. (1974). “The generation of long nonlinear internal waves in a weakly stratified shear flow”. In: *Journal of Geophysical Research (1896-1977)* vol. 79, no. 3, pp. 453–462.

Long, R. R. (1956). “Solitary Waves in the One- and Two-Fluid Systems”. In: *Tellus* vol. 8, no. 4, pp. 460–471.

López-Herrera, J.-M., Popinet, S., and Castrejón-Pita, A.-A. (2019). “An adaptive solver for viscoelastic incompressible two-phase problems applied to the study of the splashing of weakly viscoelastic droplets”. In: *Journal of Non-Newtonian Fluid Mechanics* vol. 264, pp. 144–158.

Løken, T. K. et al. (2022). “Experiments on turbulence from colliding ice floes”. In: *Physics of Fluids* vol. 34, no. 6.

MacKinnon, J. A. and Gregg, M. C. (2003). “Mixing on the late-summer New England shelf—Solibores, shear, and stratification”. In: *Journal of Physical Oceanography* vol. 33, no. 7, pp. 1476–1492.

MacKinnon, J. A., Zhao, Z., et al. (2017). “Climate process team on internal wave–driven ocean mixing”. In: *Bulletin of the American Meteorological Society* vol. 98, no. 11, pp. 2429–2454.

Marchenko, A., Rabault, J., et al. (2017). “Field observations and preliminary investigations of a wave event in solid drift ice in the Barents Sea”. In: *Proceedings-International Conference on Port and Ocean Engineering under Arctic Conditions.* Port and Ocean Engineering under Arctic Conditions.

Marchenko, A., Zenkin, A., et al. (2020). “Monitoring of 3D motion of drifting iceberg with an ice tracker equipped with accelerometers”. In: *Proc. 25th IAHR Int. Symp. on Ice.* IAHR.

Mathur, M. and Peacock, T. (2009). “Internal wave beam propagation in non-uniform stratifications”. In: *Journal of Fluid Mechanics* vol. 639, pp. 133–152.

Maxworthy, T. (1979). “A note on the internal solitary waves produced by tidal flow over a three-dimensional ridge”. In: *Journal of Geophysical Research: Oceans* vol. 84, no. C1, pp. 338–346.

Michallet, H. and Barthelémy, E. (1998). “Experimental study of interfacial solitary waves”. In: *Journal of Fluid Mechanics* vol. 366, pp. 159–177.

Michallet, H. and Ivey, G. N. (1999). “Experiments on mixing due to internal solitary waves breaking on uniform slopes”. In: *Journal of Geophysical Research: Oceans* vol. 104, no. C6, pp. 13467–13477.

Miles, J. W. (1961). “On the stability of heterogeneous shear flows”. In: *Journal of Fluid Mechanics* vol. 10, no. 4, pp. 496–508.

— (1981). “On internal solitary waves. II”. In: *Tellus* vol. 33, no. 4, pp. 397–401.

Moe, H., Ommundsen, A., and Gjevik, B. (2002). “A high resolution tidal model for the area around The Lofoten Islands, northern Norway”. In: *Continental Shelf Research* vol. 22, no. 3, pp. 485–504.

Moum, J. N. et al. (2003). “Structure and generation of turbulence at interfaces strained by internal solitary waves propagating shoreward over the continental shelf”. In: *Journal of Physical Oceanography* vol. 33, no. 10, pp. 2093–2112.

Nakayama, K. et al. (2019). “Classification of internal solitary wave breaking over a slope”. In: *Physical Review Fluids* vol. 4, no. 1, p. 014801.

Nansen, F. (1897). *Fridtjof Nansen's" Farthest North.": Being the Record of a Voyage of Exploration of the Ship Fram, 1893-96 and of a Fifteen Months' Sleigh Journey by Dr. Nansen and Lieut, Johansen.* Vol. 2. Macmillan and Company, Limited.

Nash, J. D. and Moum, J. N. (2005). “River plumes as a source of large-amplitude internal waves in the coastal ocean”. In: *Nature* vol. 437, no. 7057, pp. 400–403.

Newman, J. N. (2018). *Marine hydrodynamics.* The MIT press.

Newyear, K. and Martin, S. (1997). “A comparison of theory and laboratory measurements of wave propagation and attenuation in grease ice”. In: *Journal of Geophysical Research: Oceans* vol. 102, no. C11, pp. 25091–25099.

Osterloff, J. et al. (2019). “Computer vision enables short-and long-term analysis of Lophelia pertusa polyp behaviour and colour from an underwater observatory”. In: *Scientific reports* vol. 9, no. 1, p. 6578.

Ostrovsky, L. A. and Stepanyants, Y. A. (1989). “Do internal solitions exist in the ocean?” In: *Reviews of Geophysics* vol. 27, no. 3, pp. 293–310.

Pauley, L. L., Moin, P., and Reynolds, W. C. (1990). “The structure of two-dimensional separation”. In: *Journal of Fluid Mechanics* vol. 220, pp. 397–411.

Perry, R. B. and Schimke, G. R. (1965). “Large-amplitude internal waves observed off the northwest coast of Sumatra”. In: *Journal of Geophysical Research* vol. 70, no. 10, pp. 2319–2324.

Popinet, S. (2003). “Gerris: a tree-based adaptive solver for the incompressible Euler equations in complex geometries”. In: *Journal of Computational Physics* vol. 190, no. 2, pp. 572–600.

— (2009). “An accurate adaptive solver for surface-tension-driven interfacial flows”. In: *Journal of Computational Physics* vol. 228, no. 16, pp. 5838–5866.

— (2011). “Quadtree-adaptive tsunami modelling”. In: *Ocean Dynamics* vol. 61, no. 9, pp. 1261–1285.

— (2015). “A quadtree-adaptive multigrid solver for the Serre–Green–Naghdi equations”. In: *Journal of Computational Physics* vol. 302, pp. 336–358.

Popinet, S. and collaborators (2013–2023). *Basilisk. http://basilisk.fr.* [Accessed: 18.10.2021].

Quaresma, L. S. et al. (2007). “Evidence of sediment resuspension by nonlinear internal waves on the western Portuguese mid-shelf”. In: *Marine geology* vol. 246, no. 2-4, pp. 123–143.

Rabault, J., Halsne, T., et al. (2016). “PTV investigation of the mean drift currents under water waves”. In: *Proceedings of the 18th Int. Lisb. Symp.*

Rabault, J., Sutherland, G., Jensen, A., et al. (2019). “Experiments on wave propagation in grease ice: combined wave gauges and particle image velocimetry measurements”. In: *Journal of Fluid Mechanics* vol. 864, pp. 876–898.

Rabault, J., Sutherland, G., Ward, B., et al. (2016). “Measurements of waves in landfast ice using inertial motion units”. In: *IEEE Transactions on Geoscience and Remote Sensing* vol. 54, no. 11, pp. 6399–6408.

Roberts, S. and Hirshfield, M. (2004). “Deep-sea corals: out of sight, but no longer out of mind”. In: *Frontiers in Ecology and the Environment* vol. 2, no. 3, pp. 123–130.

Röhrs, J. et al. (2023). “Surface currents in operational oceanography: Key applications, mechanisms, and methods”. In: *Journal of Operational Oceanography* vol. 16, no. 1, pp. 60–88.

Sakai, T., Diamessis, P. J., and Jacobs, G. B. (2020). “Self-sustained instability, transition, and turbulence induced by a long separation bubble in the footprint of an internal solitary wave. I. Flow topology”. In: *Physical Review Fluids* vol. 5, no. 10, p. 103801.

Sanderse, B. and Veldman, A. E. P. (2019). “Constraint-consistent Runge–Kutta methods for one-dimensional incompressible multiphase flow”. In: *Journal of Computational Physics* vol. 384, pp. 170–199.

Sandstrom, H. and Elliott, J. A. (1984). “Internal tide and solitons on the Scotian Shelf: A nutrient pump at work”. In: *Journal of Geophysical Research: Oceans* vol. 89, no. C4, pp. 6415–6426.

Sandstrom, H. and Oakey, N. S. (1995). “Dissipation in Internal Tides and Solitary Waves”. In: *Journal of Physical Oceanography* vol. 25, no. 4, pp. 604–614.

Scotti, A. and Pineda, J. (2004). “Observation of very large and steep internal waves of elevation near the Massachusetts coast”. In: *Geophysical Research Letters* vol. 31, no. 22.

Silva, E. et al. (2021). “Twenty-one years of phytoplankton bloom phenology in the Barents, Norwegian, and north seas”. In: *Frontiers in Marine Science* vol. 8, p. 746327.

Smedsrud, L. H. et al. (2013). “The role of the Barents Sea in the Arctic climate system”. In: *Reviews of Geophysics* vol. 51, no. 3, pp. 415–449.

Smith, W. N. (2008). “A submersible three-dimensional particle tracking velocimetry system for flow visualization in the coastal ocean”. In: *Limnology and Oceanography: Methods* vol. 6, no. 2, pp. 96–104.

Smith, W. N. et al. (2002). “PIV measurements in the bottom boundary layer of the coastal ocean”. In: *Experiments in Fluids* vol. 33, pp. 962–971.

Sperrevik, A. K., Christensen, K. H., and Röhrs, J. (2015). “Constraining energetic slope currents through assimilation of high-frequency radar observations”. In: *Ocean Science* vol. 11, no. 2, pp. 237–249.

Squire, V. A. (2007). “Of ocean waves and sea-ice revisited”. In: *Cold Regions Science and Technology* vol. 49, no. 2, pp. 110–133.

Squire, V. A. et al. (1995). “Of ocean waves and sea ice”. In: *Annual Review of Fluid Mechanics* vol. 27, no. 1, pp. 115–168.

Stanton, T. P. and Ostrovsky, L. A. (1998). “Observations of highly nonlinear internal solitons over the continental shelf”. In: *Geophysical Research Letters* vol. 25, no. 14, pp. 2695–2698.

Stastna, M. and Lamb, K. G. (2002). “Vortex shedding and sediment resuspension associated with the interaction of an internal solitary wave and the bottom boundary layer”. In: *Geophysical research letters* vol. 29, no. 11, pp. 7–1.

— (2008). “Sediment resuspension mechanisms associated with internal waves in coastal waters”. In: *Journal of Geophysical Research: Oceans* vol. 113, no. C10.

Sutherland, B. R., Barrett, K. J., and Ivey, G. N. (2013). “Shoaling internal solitary waves”. In: *Journal of Geophysical Research: Oceans* vol. 118, no. 9, pp. 4111–4124.

Sveen, J. K. et al. (2002). “On the breaking of internal solitary waves at a ridge”. In: *Journal of Fluid Mechanics* vol. 469, pp. 161–188.

Sverdrup, H. U. (1953). “On conditions for the vernal blooming of phytoplankton”. In: *J. Cons. Int. Explor. Mer* vol. 18, no. 3, pp. 287–295.

Sætre, R. (2007). *The Norwegian coastal current: oceanography and climate.* Fagbokforlaget.

Thiem, Ø. et al. (2011). “Numerical simulation of internal solitary wave—induced reverse flow and associated vortices in a shallow, two-layer fluid benthic boundary layer”. In: *Ocean dynamics* vol. 61, pp. 857–872.

Thorpe, S. A. (1971). “Asymmetry of the internal seiche in Loch Ness”. In: *Nature* vol. 231, no. 5301, pp. 306–308.

Troy, C. D. and Koseff, J. R. (2005). “The instability and breaking of long internal waves”. In: *Journal of Fluid Mechanics* vol. 543, pp. 107–136.

van Hooft, J. A. et al. (2018). “Towards Adaptive Grids for Atmospheric Boundary-Layer Simulations”. In: *Boundary-Layer Meteorology* vol. 167, no. 3, pp. 421–443.

Vlasenko, V. and Hutter, K. (2002). “Numerical experiments on the breaking of solitary internal waves over a slope–shelf topography”. In: *Journal of Physical Oceanography* vol. 32, no. 6, pp. 1779–1793.

Wadhams, P. et al. (1988). “The attenuation rates of ocean waves in the marginal ice zone”. In: *Journal of Geophysical Research: Oceans* vol. 93, no. C6, pp. 6799–6818.

Wang, B. J. and Redekopp, L. G. (2001). “Long internal waves in shear flows: topographic resonance and wave-induced global instability”. In: *Dynamics of Atmospheres and Oceans* vol. 33, no. 4, pp. 263–302.

Weber, J. E. H. and Isachsen, P. E. (2023). “Energy transfer from sub-inertial Kelvin waves to continental shelf waves at a transverse bottom escarpment”. In: *Continental Shelf Research* vol. 258, p. 104985.

Woodson, C. B. (2018). “The fate and impact of internal waves in nearshore ecosystems”. In: *Annual review of marine science* vol. 10, pp. 421–441.

Xu, C. and Stastna, M. (2020). “Instability and cross-boundary-layer transport by shoaling internal waves over realistic slopes”. In: *Journal of Fluid Mechanics* vol. 895, R6.

Zahedi, S., Aghsaee, P., and Boegman, L. (2021). “Internal solitary wave bottom boundary layer dissipation”. In: *Physical Review Fluids* vol. 6, no. 7, p. 074802.

Zhao, Z. and Alford, M. H. (2009). “New altimetric estimates of mode-1 M 2 internal tides in the central North Pacific Ocean”. In: *Journal of Physical Oceanography* vol. 39, no. 7, pp. 1669–1684.

Ziegenbein, J. (1969). “Short internal waves in the Strait of Gibraltar”. In: *Deep Sea Research and Oceanographic Abstracts.* Vol. 16. 5. Elsevier, pp. 479–487.

— (1970). “Spatial observations of short internal waves in the Strait of Gibraltar”. In: *Deep Sea Research and Oceanographic Abstracts.* Vol. 17. 5. Elsevier, pp. 867–875.

Zulberti, A., Jones, N. L., and Ivey, G. N. (2020). “Observations of enhanced sediment transport by nonlinear internal waves”. In: *Geophysical Research Letters* vol. 47, no. 19, e2020GL088499.

Papers

Paper I

Calculation of internal-wave-driven instability and vortex shedding along a flat bottom

Thea Josefine Ellevold, John Grue

Published in *Journal of Fluid Mechanics*, July 2023, volume 966, pp. A40. DOI: doi:10.1017/jfm.2023.476.

J. Fluid Mech. (2023), *vol.* 966, A40, doi:10.1017/jfm.2023.476

Calculation of internal-wave-driven instability and vortex shedding along a flat bottom

Thea J. Ellevold[1] **and John Grue**[1],†

[1]Section for Mechanics, Department of Mathematics, University of Oslo, Oslo, Norway

(Received 26 August 2022; revised 6 June 2023; accepted 6 June 2023)

The instability and vortex shedding in the bottom boundary layer caused by internal solitary waves of depression propagating along a shallow pycnocline of a fluid are computed by finite-volume code in two dimensions. The calculated transition to instability agrees very well with laboratory experiments (Carr *et al.*, *Phys. Fluids*, vol. 20, issue 6, 2008, 06603) but disagrees with existing computations that give a very conservative instability threshold. The instability boundary expressed by the amplitude depends on the depth d of the pycnocline divided by the water depth H, and decays by a factor of 2.2 when d/H is 0.21, and by a factor of 1.6 when d/H is 0.16, and the stratification Reynolds number increases by a factor of 32. The instability occurs at moderate amplitude at large scale. The calculated oscillatory bed shear stress is strong in the wave phase and increases with the scale. Its non-dimensional magnitude at stratification Reynolds number 650 000 is comparable to the turbulent stress that can be extracted from field measurements of internal solitary waves of similar nonlinearity, moving along a pycnocline of similar relative depth.

Key words: internal waves, boundary layer stability, vortex shedding

1. Introduction

Internal solitary waves are a naturally occurring phenomenon in stratified oceans. Typically, the waves are driven by the tide or wind (e.g. Helfrich & Melville 2006). In this paper, we study internal solitary waves of depression and the instability that they cause in the bottom boundary layer. The processes occur in the wave phase behind the trough where the pressure gradient is adverse. A separation bubble develops and becomes unstable, and vortices are formed downstream of the wave when the amplitude is large enough (e.g. Diamessis & Redekopp 2006; Carr, Davies & Shivaram 2008; Aghsaee *et al.* 2012; Verschaeve & Pedersen 2014). Sakai, Diamessis & Jacobs (2020) performed

---

† Email address for correspondence: johng@math.uio.no

three-dimensional large-eddy simulation of the instability, vortex formation and break-up into turbulence.

Internal solitary waves of elevation also induce this kind of instability, where a background current is necessary for the instability to occur. The adverse pressure gradient, separation bubble and unsteadiness develop then in the wave phase ahead of the crest (e.g. Bogucki & Redekopp 1999; Stastna & Lamb 2002*b*, 2008; Carr & Davies 2010). The wave-driven instability of the boundary layer at the bottom causes strong variations of the shear stress and thus contributes to re-suspension of particles (e.g. Bogucki, Dickey & Redekopp 1997; Bogucki & Redekopp 1999; Bourgault *et al.* 2007; Quaresma *et al.* 2007; Boegman & Stastna 2019; Zulberti, Jones & Ivey 2020). Waves of depression interacting with a weak slope may, beyond the turning point where the layer depths are equal, break up into a series of elevation waves, and in turn cause instabilities at the bottom (e.g. Xu & Stastna 2020). Adverse pressure gradients, separation bubbles and their instability are investigated in aerodynamic flows (e.g. Gaster 1967; Pauley, Moin & Reynolds 1990; Reed & Saric 1996). Depending on the forcing and the Reynolds number, the instability may become global (e.g. Hammond & Redekopp 1998; Diamessis & Redekopp 2006); see also Huerre & Monkewitz (1990), Schmid & Henningson (2001) and Chomaz (2005).

1.1. *Review of internal-wave-driven instability in the bottom boundary layer*

Motivated by observations of re-suspension of particles at the bottom beneath internal solitary waves (Bogucki *et al.* 1997), Bogucki & Redekopp (1999) investigated the boundary layer instability made by a sheared current interacting with a weakly nonlinear internal solitary wave of elevation moving along a shallow bottom layer of a stratified fluid. Above a threshold amplitude, the boundary layer separated in the adverse pressure gradient region, in the front part of the wave. Vortices were formed in the centre below the wave. Advecting with the flow, the vortex dynamics posed an excess bottom shear stress. Stastna & Lamb (2002*b*) performed fully nonlinear simulations of the scenario described by Bogucki and Redekopp, and showed that it is the wave's velocity field interacting with the boundary layer vorticity of an opposing current that leads to a vortex shedding instability beneath the wave. Neither a separation bubble nor a wave with a recirculating region was required for vortex shedding to occur. Co-propagating waves and current did not lead to instability. In a follow-up paper, Stastna & Lamb (2008) found that the current-driven vorticity in the boundary layer was advected into the footprint of the elevation wave. In its front part, a separation bubble formed, grew and subsequently broke up. When the Reynolds number was too low or the current too weak, no instability occurred. By laboratory experiments, Carr & Davies (2010) measured internal solitary waves of elevation propagating in an unsheared two-layer stably stratified fluid. The amplitude was up to theoretical maximum. No boundary layer separation or vortices beneath the front half of the wave were found. No instabilities were measured. Velocity reversal near the bottom in the deceleration phase of the wave where the pressure gradient is favourable was measured.

In the case of internal solitary waves of depression moving along a (moderately) shallow pycnocline, the pressure gradient behind the wave trough is adverse. By direct numerical simulations of the Navier–Stokes equations combined with weakly nonlinear Korteweg–de Vries (KdV) theory of the internal solitary waves, Diamessis & Redekopp (2006) found that global instability emerged in the boundary layer below the wave. The downstream vortices were created at the bottom and ascended into the water column. The stratification Reynolds number was $Re_w = 2 \times 10^4$ (Re_w is defined properly in § 1.2). A jet at the bottom along the wave propagating direction corresponding to the lower part of the calculated separation bubble was measured experimentally for the same Re_w by Carr & Davies (2006). No instability was found in the laboratory wave tank. However, Thiem *et al.* (2011) performed a numerical re-calculation of one of the physical measurements. Instability was found when the amplitude was increased by 14 %. Carr *et al.* (2008) performed a new set of laboratory experiments at higher Reynolds number. They found that the flow separation beneath the wave occurred at essentially lower amplitudes than calculated by the weakly nonlinear KdV theory in combination with the Navier–Stokes equations (Diamessis & Redekopp 2006). Aghsaee *et al.* (2012) solved the Navier–Stokes equations in combination with a fully nonlinear internal wave formulation. They proposed a universal criterion of the internal-solitary-wave-driven instability of the boundary layer, for the cases of either a flat bottom or a slope. Their very conservative stability boundary does not fit the experiments by Carr *et al.* (2008) or the numerical simulations by Thiem *et al.* (2011).

Local instability made by internal solitary waves interacting with a variable bottom topography may exhibit jet-like roll-up of vorticity near the crest of the topography, as calculated in two and three dimensions at moderate Reynolds number by Harnanan, Soontiens & Stastna (2015) and Harnanan, Stastna & Soontiens (2017). Re-suspension or entrainment of internal solitary waves interacting with a bottom topography was modelled numerically by Olsthoorn & Stastna (2014), and Soontiens, Stastna & Waite (2015) calculated the viscous bottom boundary layer effects on the generation of internal solitary waves at topography and the related instabilities in the case of a background current.

The three-dimensional large-eddy simulation by Sakai *et al.* (2020) showed three regimes of the flow in the boundary layer, where below the wave phase, global instability and transition occurred. Vortex break-up and formation of turbulent clouds, and development of a turbulent boundary layer, took place downstream of the wave. Two-dimensional laminar simulations were compared to the turbulent calculations. A similar, essentially two-dimensional, vortex formation was taking place in the two computations, in a distance of five water depths, corresponding to two wavelengths behind the trough. The unstable simulations by Sakai *et al.* (2020) were performed with a wave of large amplitude interacting with a strong counter-current. They found that two- or three-dimensional simulations with a sufficient resolution of the near-bed scales and no background current could not spontaneously generate any vortex shedding. We note that Sakai *et al.* (2020, p. 9) write that the shed vortices appear to be initially two-dimensional. In the abstract of the paper, they write: ‘In the separation bubble, there exists a three-dimensional global oscillator, which is primarily excited by the two-dimensional absolute instability of the separated shear layer.’

1.2. *Motivation of the paper*

Using laboratory experiments, Carr *et al.* (2008) investigated the flow separation and vortex formation induced in the bottom boundary layer by an internal solitary wave of depression moving along a flat bottom. The amplitude of the wave was varied from a large value where instability occurred, to a small value where the instability disappeared. The threshold wave amplitude where instability emerged was measured. Aghsaee *et al.* (2012) performed numerical simulations in two dimensions of the wave-driven instability along flat and sloping bottoms. Adopting the procedure of Pauley *et al.* (1990), they expressed the inception of the instability in terms of the pressure gradient and the momentum thickness Reynolds number of the boundary layer. However, Aghsaee *et al.* (2012) were not able to reproduce the threshold of instability for the case of a flat bottom, which occurred much earlier in the laboratory experiments by Carr *et al.* (2008). Aghsaee *et al.*

(2012) suggested possible reasons for the discrepancy between their computations and the experiments by Carr *et al.* (2008): (a) the laboratory-observed instabilities are primarily three-dimensional; (b) errors in the estimation of the horizontal velocity below the wave and the wavelength; (c) lack of finite-amplitude perturbations in the numerical solution from which instabilities will grow through the phenomenon of subcritical transition; and (d) existence of an oscillatory background barotropic flow in laboratory experiments generated during the gate release, which may have influenced vortex generation. The discrepancy between experiments and model calculations was repeated in the review by Boegman & Stastna (2019). The conflicting results are addressed here.

By finite-volume solver, we simulate the experiments of Carr *et al.* (2008). The method is detailed in § 2.1. We obtain very good agreement with the measurements. We also obtain that the threshold for instability really depends on the depth of the pycnocline. The pressure gradient and the Reynolds number of the boundary layer are evaluated and compared to the transition proposed by Aghsaee *et al.* (2012). We find an essential mismatch. This is detailed in §§ 3.2 and § 3.3.

The effect of scale is investigated systematically where the kinematic viscosity ν is varied in the range $10^{-5.5}$–10^{-7} $m^2\ s^{-1}$, where $\nu = 10^{-6}\ m^2\ s^{-1}$ for fresh water at 20 °C. The variables ν, the linear internal long-wave speed of the stratified fluid c_0 (defined properly in § 2.2) and the water depth H form a stratification Reynolds number $Re_w = c_0H/\nu$. This quantity is denoted by the wave Reynolds number by Diamessis & Redekopp (2006), Carr *et al.* (2008) and Aghsaee *et al.* (2012), and by the Reynolds number based on the water column height by Sakai *et al.* (2020). Our computations are presented for Re_w in the range 1.9×10^4–6.5×10^5, while the experiments by Carr *et al.* were performed for $Re_w \sim 5.8 \times 10^4$–$6.6 \times 10^4$.

The computations exhibit two separation bubbles, one in the wave phase behind the trough and a second well behind the wave phase. In contrast, one separation bubble has been found in previous computations of the flat bottom case (e.g. Diamessis & Redekopp 2006; Aghsaee *et al.* 2012; Sakai *et al.* 2020). Note that Xu & Stastna (2020) have found that a separation bubble below waves of elevation interacting with a slope eventually breaks down into two parts. In the present calculations, the instability develops in separation bubble one.

The vortex formation that emerges in the wave phase gives rise to powerful oscillations of the bottom shear stress. We use a Froude number scaling of the velocity field outside the boundary layer. The shear stress scaled by c_0^2 times the fluid density is investigated in the range of the Reynolds number. A similar scaling was employed by Boegman & Ivey (2009) and Xu & Stastna (2020). The velocities of the boundary layer in the field are turbulent. The non-dimensional shear stress in a few available measurements (Quaresma *et al.* 2007; Zulberti *et al.* 2020) is obtained just as well and compared to the laminar calculations. The internal solitary waves in the model and the field are of similar nonlinearity and move along similar relative pycnocline depth.

The calculated internal solitary waves are fully nonlinear and dispersive, and agree very well with exact interfacial methods (e.g. Michallet & Barthélemy 1998; Grue *et al.* 1999, 2000; Camassa *et al.* 2006; Fructus *et al.* 2009) and solutions of the continuously stratified case (e.g. Turkington, Eydeland & Wang 1991; Stastna & Lamb 2002*a*; Dunphy, Subich & Stastna 2011) (results are not shown). The Navier–Stokes equations resolve the Stokes bottom boundary layer below the wave phase.

Section 2 describes the method, the numerical wave tank and the resolution. The stratification of the fluid and the procedure of the wave generation are introduced. The noise of the solver is discussed. The Stokes boundary layer thickness is presented.

The results section (§ 3) includes comparison to the experiments by Carr *et al.* (2008) and calculation of the stability border in the range of the Reynolds number (§ 3.1), evaluation of the pressure gradient, the Reynolds number of the bottom boundary layer, and comparison to the results by Aghsaee *et al.* (2012) (§ 3.2). Proposed reasons for the discrepancy between computed and measured instability are discussed (§ 3.3). The separation bubbles, instability and vortex rolls are calculated (§ 3.4). The non-dimensional bed shear stress is compared to a few results extracted from field measurements, at the turbulent scale (§ 3.5). We draw some conclusions in § 4.

2. Method

2.1. *Numerical wave tank*

We present direct numerical simulations of internal-solitary-wave-driven instability and vortex roll formation in the bottom boundary layer along a flat bottom. The two-phase incompressible Navier–Stokes equations are solved in two dimensions by the low-order finite-volume solver Basilisk (basilisk.fr); see Popinet (2003, 2009) and Lagrée, Staron & Popinet (2011). Details of the elliptic solve are given in Popinet (2003, 2015) (where in Popinet (2015) the elliptic problem is different to the one studied here but the method used is the same). Details of the finite-volume approach and the advection scheme can be found in Lagrée *et al.* (2011). The advection equation is integrated by second-order upwind scheme (the parabolic scheme of Bell, Colella & Glaz (1989); Popinet 2003. The spatial discretisation uses a quadtree scheme (Popinet 2009; van Hooft *et al.* 2018). Basilisk uses the volume-of-fluid method to describe variable-density two-phase flows where the interfaces are immiscible. The Basilisk multi-phase flow library has been validated by several recent papers in *Journal of Fluid Mechanics*, e.g. Mostert, Popinet & Deike (2022) (breaking waves), Alventosa, Cimpeanu & Harris (2023) (droplet impact), Riviére *et al.* (2021) (turbulent bubble break-up), Mostert & Deike (2020) (dissipation in waves) and Innocenti *et al.* (2021) (bubble-induced turbulence). The noise of the solver is estimated in § 2.3.

The numerical wave tank has length L and depth H. The grid is composed of square finite-volume cells. The size of a cell is Δx along the horizontal, and Δz along the vertical, where $\Delta x = \Delta z = \varDelta_N = L/2^N$. Integer N gives the resolution. The thin boundary layer along the bottom and its effects are resolved. A coarse grid with $\varDelta_{N_1}$ well above the boundary layer is refined sequentially according to the tree-grid structure of Basilisk, with $\varDelta_{N_1}$ above $\varDelta_{N_1+1}$, above $\varDelta_{N_1+2}$, and so on, until a finest resolution of $\varDelta_{N_2}$ near the bottom ($N_2 > N_1$). The combined grid is termed N_1–N_2. The fine grid ($\varDelta_{N_2}$) is used up to 0.015 water depths above the bottom, and up to 0.02 water depths in the runs with kinematic viscosity $\nu = 10^{-5.5}\ \mathrm{m^2\ s^{-1}}$. In terms of the boundary layer thickness δ (defined in § 2.4), the finest resolution is $\varDelta_{N_2}/\delta = 0.06$ (see table 3 in § 3).

The simulations were run in parallel using shared memory (OpenMP) on the Norwegian Research and Education Cloud (NREC) with eight or sixteen cores and eight or sixteen threads. The CPU time varied between 12 and 16 h for $N = 12$, between 96 and 216 h for $N = 13$, between 12 and 60 h for N_1–$N_2 = 12$–14 (sixteen cores and threads), between 84 and 96 h for N_1–$N_2 = 12$–15 (sixteen cores and threads), and between 48 and 168 h for N_1–$N_2 = 11$–16 (sixteen cores and threads).

Horizontal and vertical coordinates (x, z) are introduced, with $x = 0$ at the position of the gate used for the wave generation (§ 2.2), and $z = 0$ at the bottom. A rigid lid is placed at $z = H$. There is no motion for $z > H$. The viscous boundary layer is modelled along

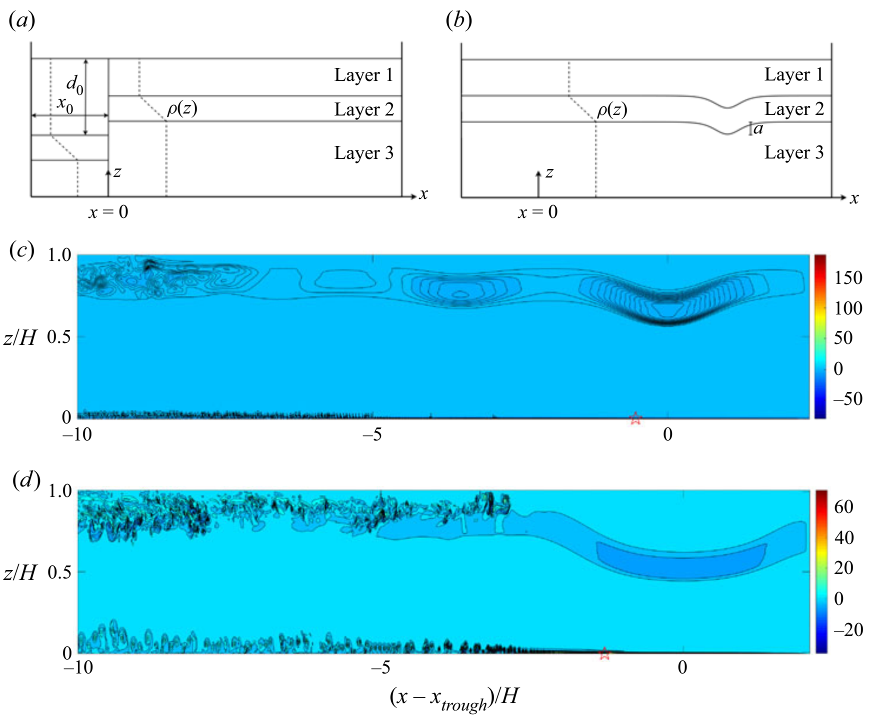

Figure 1. Sketches of the wave tank: (*a*) initial condition, and (*b*) with generated wave. (*c*) Calculated internal solitary wave at $tc_0/H = 6.42$, $a/H = 0.189$, $\nu = 10^{-7}\ \mathrm{m^2\ s^{-1}}$. (*d*) Same as (*c*) with $a/H = 0.325$, $\nu = 10^{-6}\ \mathrm{m^2\ s^{-1}}$. Separation point indicated by the red star. Vorticity $\omega/(c_0/H)$ in colour scale. Contour lines (black) of $\omega/(c_0/H)$.

the bottom where the no-slip condition applies. The free-slip condition is applied at the upper boundary ($z = H$), at the vertical end walls of the tank and at the gate used for wave generation.

2.2. *Generation*

The fluid is stratified with a pycnocline of thickness h_2. This is sandwiched between an upper layer of depth h_1 and density ρ_1, and a lower layer of depth h_3 and density ρ_3. The continuous density varies linearly within the pycnocline. The physical length 6.4 m and depth 0.38 m of the numerical tank ($L/H = 16.84$), and the stratification and the wave generation process, are the same as in the experiments by Carr *et al.* (2008). The gate is located 0.6 m from the left tank wall (figure 1*a*).

Three different stratifications used in the experiments by Carr *et al.* are also used in the present computations. We denote these by Strat.1, Strat.2 and Strat.3 (table 1). Stratification 1 has middle depth $d \simeq 0.16H$ and a thin pycnocline with $h_2 \simeq 0.07H$, where $d = h_1 + (1/2)h_2$. Stratification 2 has the same middle depth but is twice as thick ($0.14H$). The third pycnocline is relatively deeper ($d = 0.21H$) and of thickness $0.12H$.

Upon release of an added volume ($x_0 \times (d_0 - h_1)$) of the light fluid trapped by the gate, a leading nonlinear internal solitary wave is generated. The amplitude a is defined by the maximum excursion of the interface separating layers 2 and 3 (figure 1*b*). The two-layer

No.	Date	Strat.	$h_3/h_2/h_1$ (cm)	a_L (cm)	a_C (cm)	a_C/H	L	C	θ_{sep}/δ	$Re_{\theta_{sep}}$	$-P_{x_{sep}}$
1a	050207		30.2/2.7/5.2	10.4	10.17	0.268	Yes	Yes	0.107	29.1	0.109
1b	140207	Strat.1	30.8/2.5/4.7	10.1	10.00	0.263	No	Yes	0.108	25.9	0.109
1c			30.8/2.5/4.7	—	9.41	0.248		Yes	0.112	23.8	0.102
1d			30.8/2.5/4.7	—	9.14	0.241		Yes	0.111	21.7	0.094
1e			30.8/2.5/4.7	—	8.63	0.220		No	0.113	19.8	0.087
2*	080207	Strat.2	29.3/5.2/3.5	11.0	11.4	0.300	Yes	Yes	0.108	39.2	0.129
2a	060307		29.0/5.2/3.8	9.5	9.41	0.248	Yes	Yes	0.109	25.7	0.104
2b	090207		29.2/5.3/3.7	9.2	9.24	0.243	No	Yes	0.113	24.2	0.102
2c			29.3/5.2/3.5	—	8.94	0.235		Yes	0.114	22.9	0.098
2d			29.3/5.2/3.5	—	8.47	0.223		No	0.116	20.6	0.091
3a	210207		27.6/5.3/5.0	8.6	8.59	0.226	Yes	Yes	0.115	25.7	0.090
3b	230207	Strat.3	28.0/4.7/5.5	8.3	8.29	0.218	No	Yes	0.118	23.8	0.087
3c			28.0/4.7/5.5	—	7.81	0.206		No	0.121	21.5	0.079

Table 1. Experiment number and date in Carr *et al.* (2008, table 1), stratification (Strat.), and amplitude measured in laboratory (a_L) or computed (a_C). Instability in laboratory (L) or computation (C). Numerical values of θ_{sep}/δ, $Re_{\theta_{sep}}$, $P_{x_{sep}}$ defined in the text. Resolution $N = 12$–14, and $Re_w = 5.9 \times 10^4$.

approximation of the linear internal long-wave speed, used by Carr *et al.* (2008), is also used here as reference speed: $c_0 = [g'd(H-d)/H]^{1/2}$, where $g' = g(\rho_3 - \rho_1)/\rho_3$, and g denotes the acceleration due to gravity. The fully nonlinear wave speed c, obtained in the experiment or simulation, is used to connect time and propagation distance.

In each physical or numerical experiment, a leading depression wave of mode one is generated (figure 1*c*). Two smaller disturbances also of mode one propagate behind the main wave. Strong vorticity on small-scale results from the velocity shear during the generation and disperse along the pycnocline behind a slower wave of mode two found at approximately nine water depths behind the main trough, a feature of the wave-making procedure. Note that the main wave and the subsequent small mode one waves exhibit neither shear instability nor mixing of the pycnocline in this case. The wave amplitude is right above the threshold for vortex generation in the bottom boundary layer. Figure 1(*d*) shows a stronger internal solitary wave with $a/H = 0.325$. The wave causes both instability and vortex generation in the boundary layer, as well as breaking due to shear instability in the pycnocline (e.g. Fructus *et al.* 2009; Lamb 2014).

2.3. *Noise of the solver*

The truncation error of the solver is the only perturbation that creates instability in the computations. The noise is computed from the vertical velocity variable $w(x_i, z = 0.402H) = w_i$, where x_i are all of the horizontal evaluation points. We evaluate the locally averaged variable $f_i = [\sum_{j=i-n_1}^{j=i+n_1} w_i]/(2n_1+1)$, where $n_1 = 1$ or 2, and the relative error $\mathrm{err} = \|w-f\|_2/\|w\|_2 = \text{const.} \times 10^{-5}$ (here, $\|\cdot\|_2$ is the 2-norm). The const. equals 1.3 ($n_1 = 1, N_1 = N_2 = 13$), 1.8 ($n_1 = 2, N_1 = N_2 = 13$) or 2.0 ($n_1 = 1, N_1 = N_2 = 12$), and shows that the growth of the unstable modes arises from the truncation error of the solver at the fifth decimal place.

2.4. *Boundary layer thickness*

The Stokes boundary layer at the bottom below the wave phase is characterised by the thickness δ, the kinematic viscosity ν, and the frequency of the wave ω_0, where

$$\delta = (2\nu/\omega_0)^{1/2}. \tag{2.1}$$

The frequency is estimated by $\omega_0 = c_0/L_w$, with the wave speed c_0 defined in § 2.2. The wavelength is defined by the integral $L_w = (1/a)\int_{-\infty}^{\infty} \eta_{23}\,\mathrm{d}x$, where η_{23} is the vertical excursion of the isoline separating layers two and three.

3. Results

3.1. *Stability border*

Carr *et al.* (2008) investigated transition to instability at Reynolds number $Re_w = 5.8 \times 10^4$–6.6×10^4. Seven measurements are referred to by date in table 1, column 2. The transition expressed in terms of the measured amplitude is found between rows 1a,b (stratification 1), rows 2a,b (stratification 2) and rows 3a,b (stratification 3). The computations show instability at a somewhat smaller amplitude, indicated in rows 1d,e of the table (stratification 1), rows 2c,d (stratification 2) and rows 3b,c (stratification 3). The comparison is quite good. The highest stable experimental wave and the lowest unstable computed wave in row 3b (stratification 3) are matching ($a = 8.3$ cm). The similar amplitudes are $a = 9.2$ cm (experiment) and $a = 8.94$ cm (computation) for stratification 2 (rows 2b,c), and $a = 10.1$ cm (experiment) and $a = 9.14$ cm (computation) for stratification 1 (rows 1b,d).

The kinematic viscosity in the computations is varied in the range $\nu = 10^{-n}\ \mathrm{m^2\ s^{-1}}$ with $5.5 < n < 7$. The extended Reynolds number range is $Re_w \sim 1.9 \times 10^4$–$6.5 \times 10^5$. Unstable waves with the lowest possible amplitude, and stable waves with the largest possible amplitude, are searched by trial and error for the four values $n = 5.5$, 6, 6.5 and 7. Unstable waves are judged by the presence of small unstable disturbances in the computations. Two separation bubbles and the onset of instability are discussed and visualised in § 3.4 and figures 4–6 below. A linear fit to a logarithmic relationship of the eight calculated amplitudes of the transition obtains

$$\log_{10} a = \log_{10} a_{0,C} - m_1 \log_{10}(Re_w/Re_{w,0}), \tag{3.1}$$

with results presented in figures 2(*a–c*). Here, $a_{0,C}$ estimates the computed threshold amplitude of instability for $Re_{w,0} = c_0 H/\nu_0$, with $\nu_0 = 10^{-6}\ \mathrm{m^2\ s^{-1}}$ (fresh water at 20 °C) such as in the Carr *et al.* experiments. The computed $a_{0,C}/H$ (table 2, column 2) and experimental $a_{0,L}/H$ (table 2, column 1) – obtained by an average between the experimental waves right above and below instability – show very good agreement. The relative difference between computation and experiment is less than 1 % for stratifications 2 and 3, and 8 % for the thin pycnocline of stratification 1, while Carr *et al.* have suggested an accuracy of 2 % of the experimental amplitude measurement. The threshold decreases according to $Re_w^{-m_1}$, where exponent $m_1 \simeq 0.13$ in practice is the same for stratifications 1 and 2, which are of the same middle depth. The deeper pycnocline of stratification 3 has a greater decay exponent, $m_1 = 0.23$. The computed threshold amplitude decreases by a factor of 1.6 for stratifications 1 and 2, and by a factor of 2.2 for the deeper stratification 3, when Re_w increases by a factor of $10^{1.5} \simeq 31.6$.

The experimental runs of a previous paper by Carr & Davies (2006) with a smaller Reynolds number $Re_w \sim 2.4 - 3.4 \times 10^4$ showed no instability in the bottom

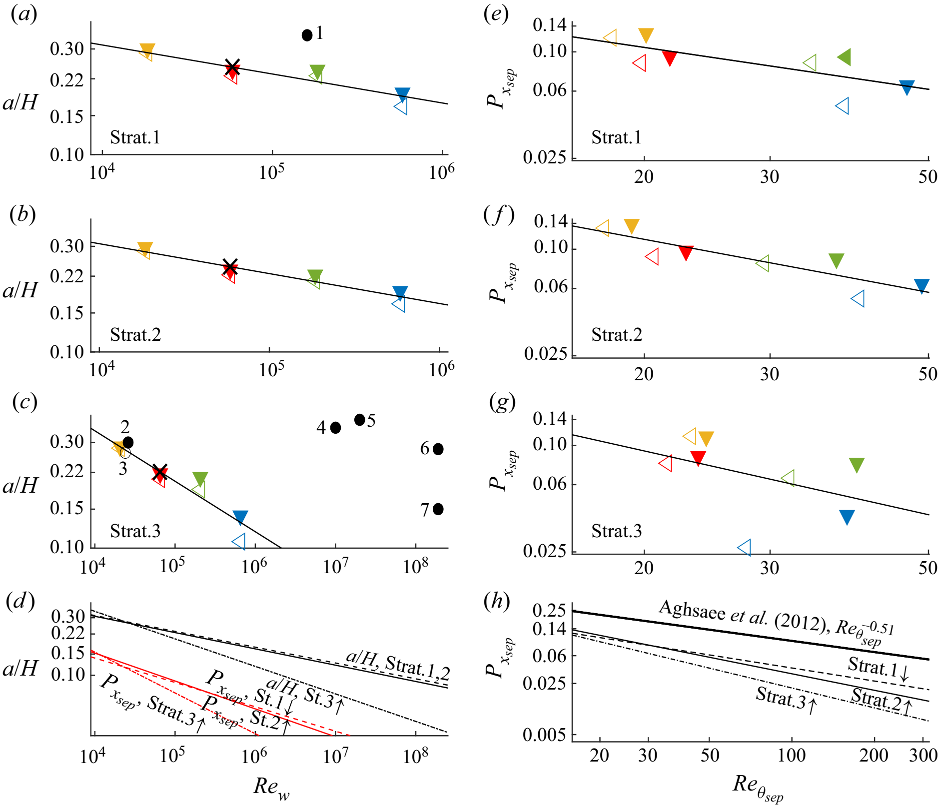

Figure 2. Threshold of instability. (*a–c*) Plots of a/H versus Re_w (both log scale). Solid line shows fit to (3.1). (*d*) Plots of $a_0(Re_w/Re_{w,0})^{-m_1}$ (black lines) and $C_0(Re_w/Re_{w,0})^{-m_3}$ (red lines) versus n. (*e–h*) Plots of $P_{x_{sep}}$ versus $Re_{\theta_{sep}}$ (both log scale). Solid line shows fit to $B_0(Re_{\theta_{sep}})^{-m_2}$. In (*h*), Aghsaee *et al.* (2012), $Re_{\theta_{sep}}^{-0.51}$ (thick solid line). Present computations for Strat.1 (dashed), Strat.2 (thin solid), Strat.3 (dash-dotted). Symbols in colour with $\nu = 10^{-n}\ \mathrm{m^2\ s^{-1}}$: $n = 5.5$ (yellow), 6 (red), 6.5 (green), 7 (blue); unstable shown filled, stable shown open, × threshold for instability measured by C08. In (*a*) and (*c*), unstable (●) and stable (○) observations: 1 (Sakai *et al.* 2020), 2 (Thiem *et al.* 2011), 3 (Carr & Davies 2006), 4 (Bourgault *et al.* 2007), 5 (Quaresma *et al.* 2007), 6 and 7 (Zulberti *et al.* 2020).

boundary layer. In a re-computation of one of the experiments (labelled 20538), Thiem *et al.* (2011) increased the amplitude by 14 % and obtained instability. The parameters of the unstable wave were $a/H = 0.30$, $d/H = 0.2$, $Re_w = 2.6 \times 10^4$, while the stable wave measured in the experiments had $a/H = 0.27$, $d/H = 0.2$, $Re_w = 2.4 \times 10^4$ fitting at each side of the predicted stability border of stratification 3 (figure 2*c*).

The amplitude and Reynolds number of unstable calculations (Thiem *et al.* 2011; Sakai *et al.* 2020), field observations (Bourgault *et al.* 2007; Quaresma *et al.* 2007; Zulberti *et al.* 2020) and stable measurements (Carr & Davies 2006) are included in figures 2(*a*,*c*).

3.2. *The pressure gradient and Reynolds number of the bottom boundary layer*

Aghsaee *et al.* (2012) have discussed the threshold of instability in terms of the pressure gradient and the momentum thickness Reynolds number of the boundary layer beneath the wave. They were motivated by studies in aerodynamic flows (e.g. Gaster 1967;

$a_{0,L}/H$	$a_{0,C}/H$	m_1	B_0	m_2	C_0	m_3	Stratification	d/H	h_2/H
0.269	0.249	0.131	0.629	0.595	0.098	0.202	Strat.1	0.16	0.07
0.245	0.243	0.135	1.082	0.752	0.102	0.231	Strat.2	0.16	0.14
0.222	0.221	0.228	1.400	0.906	0.083	0.338	Strat.3	0.21	0.12

Table 2. Wave variables at threshold for instability. Amplitude $a_{0,L}/H$ obtained from the Carr *et al.* experiments, $a_{0,C}/H$ calculated from the fit (3.1), exponent m_1 from (3.1), B_0 and m_2 from fit to $P_{x_{sep}} = B_0(Re_{\theta_{sep}})^{-m_2}$, C_0 and m_3 from fit to $P_{x_{sep}} = C_0(Re_w/Re_{w,0})^{-m_3}$. Stratifications 1–3 with $d = h_1 + h_2/2$.

Pauley *et al.* 1990). Both quantities were evaluated at the separation point of the separation bubble, at x_{sep} at the bottom. It appears from their paper that only one separation bubble was calculated. The present evaluation of x_{sep} refers to the separation point of bubble one.

The pressure gradient is expressed in non-dimensional form by $P_{x_{sep}} = (1/\rho_0 g')(\partial p/\partial x)|_{x_{sep}}$, where p denotes pressure. The momentum thickness of the boundary layer is evaluated by $\theta_{sep} = \int_0^{Z_\infty} u(U_\infty - u)|_{x_{sep}}\,\mathrm{d}z/U_\infty^2$, where U_∞ is the horizontal velocity, and Z_∞ is the vertical coordinate outside of the boundary layer at the position of x_{sep}. The momentum thickness Reynolds number at x_{sep} is calculated by $Re_{\theta_{sep}} = U_\infty \theta_{sep}/\nu$.

The boundary layer is resolved by fine grid resolution obtaining convergence. Section 2.1 describes the discretisation of the numerical wave tank and the bottom boundary layer. The resolution varies from $N_1 = 13$ and N_1–$N_2 = 12$–14 for the thickest boundary layer ($\nu = 10^{-5.5}\ \mathrm{m^2\ s^{-1}}$) to N_1–$N_2 = 12$–15 and N_1–$N_2 = 11$–16 for the thinnest ($\nu = 10^{-7}\ \mathrm{m^2\ s^{-1}}$). The finest resolution of the boundary layer of $\Delta x = \Delta z = \varDelta_{N_2} \simeq 0.06\delta$ is used up to $z = 0.015H$ (up to $0.02H$ for $\nu = 10^{-5.5}\ \mathrm{m^2\ s^{-1}}$).

The variables x_{sep}, u/U_∞, θ_{sep}, $Re_{\theta_{sep}}$ and $P_{x_{sep}}$ are calculated. The functions u/U_∞ and $u(U_\infty - u)/U_\infty^2$ for the marginally unstable cases are illustrated in figure 3 for each $\nu = 10^{-n}\ \mathrm{m^2\ s^{-1}}$ $(5.5 < n < 7)$ with the two different resolutions. Values of $Re_{\theta_{sep}}$ have relative discrepancies 6.9 % ($n = 5.5$), 3 % ($n = 6$), 1.9 % ($n = 6.5$) and 0.8 % ($n = 7$) (see table 3). Calculations of the other variables are convergent. Note from tables 1 and 3 that $\theta_{sep} \simeq (0.11 \pm 0.01)\delta$ in all cases. Note further that $Re_{\theta_{sep}} = 0.11 U_\infty \delta/\nu \simeq 0.16 U_\infty/(\nu\omega_0)$, where U_∞ and ω_0 both depend on the relative depth of the pycnocline; see § 3.3.1. This questions the assertion that $P_{x_{sep}}$ is function of just $Re_{\theta_{sep}}$. The present calculations document that this is not a valid assumption for the case of the bottom boundary layer beneath internal solitary waves of depression.

The lowest possible unstable wave and the greatest possible stable wave are computed for $n = 5.5$, 6, 6.5 and 7. The results fitted to $P_{x_{sep}} = B_0(Re_{\theta_{sep}})^{-m_2}$ show that coefficient B_0 and exponent m_2 both depend on depth and thickness of the pycnocline; see figures 2(*e–h*) and table 2, columns 4 and 5. A lower threshold is observed for the deeper pycnocline or for the thicker pycnocline (figure 2*h*). The figure also plots the function $P_{x_{sep}} = (Re_{\theta_{sep}})^{-0.51}$ as proposed by Aghsaee *et al.* (2012). This is insensitive to the depth and thickness of the pycnocline, and suggests a very conservative threshold in terms of a large amplitude.

Their proposed universal stability criterion is contrary to the experiments by Carr *et al.* and the present computations. A corresponding fit to $P_{x_{sep}} = C_0(Re_w/Re_{w,0})^{-m_3}$ suggests that C_0 and m_3 both depend on the depth of the pycnocline. The instability threshold is only weakly sensitive to the thickness h_2/H of the pycnocline (figure 2*d*). The calculated $Re_{\theta_{sep}}$

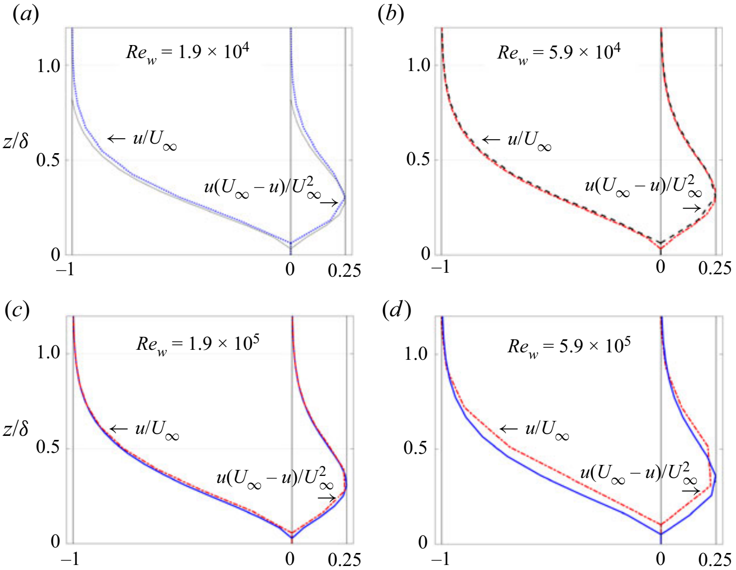

Figure 3. Horizontal velocity u/U_∞ and $u(U_\infty - u)/U_\infty^2$ in the boundary layer, for the runs in table 3. Blue dotted line shows $N = 13$, black dashed line shows N_1–$N_2 = 12-14$, red dashed line shows N_1–$N_2 = 12-15$, and blue solid line shows N_1–$N_2 = 11-16$. Evaluation at x_{sep}.

N_1–N_2	Δ_{N_2}/δ	a_C/H	x_{sep}/H	θ_{sep}/δ	$Re_{\theta_{sep}}$	$-P_{x_{sep}}$	n	Re_w
13–13	0.120	0.298	−0.713	0.101	20.5	0.128	5.5	1.9×10^4
12–14	0.060	0.297	−0.716	0.096	19.2	0.139	5.5	1.9×10^4
12–14	0.122	0.235	−0.568	0.114	22.9	0.098	6.0	5.9×10^4
12–15	0.061	0.235	−0.561	0.116	23.6	0.097	6.0	5.9×10^4
12–15	0.111	0.223	−0.526	0.114	37.2	0.088	6.5	1.9×10^5
11–16	0.055	0.223	−0.571	0.117	36.7	0.090	6.5	1.9×10^5
12–15	0.204	0.186	−0.461	0.113	48.5	0.062	7.0	5.9×10^5
11–16	0.102	0.188	−0.561	0.123	48.9	0.063	7.0	5.9×10^5

Table 3. Computed waves, right above the instability threshold, as function of Re_w and grid refinement (N_1–N_2), for Strat.2, with $\nu = 10^{-n}$ m^2 s^{-1}.

increases according to $Re_{\theta_{sep}} \sim Re_w^{0.231}$ (stratification 1), $Re_{\theta_{sep}} \sim Re_w^{0.256}$ (stratification 2) and $Re_{\theta_{sep}} \sim Re_w^{0.095}$ (stratification 3), at the threshold of instability. Present calculations disagree with Aghsaee *et al.* (2012, their eq. (5.2)), which suggests that $Re_{\theta_{sep}} \sim Re_w^{1/2}$.

3.3. *Computed versus measured instability*

Aghsaee *et al.* (2012) were not able to reproduce the threshold of instability as measured by Carr *et al.* (2008) for the case of a flat bottom and $Re_w \sim 5.8 \times 10^4$–$6.6 \times 10^4$. They proposed several reasons for the discrepancy: (a) the laboratory-observed instabilities are primarily three-dimensional; (b) errors in the estimation of the horizontal velocity below the wave and the wavelength; (c) lack of finite-amplitude perturbations in the numerical solution from which instabilities will grow through the phenomenon of subcritical transition; and (d) existence of an oscillatory background barotropic flow in laboratory experiments generated during the gate release, which may have influenced vortex generation.

In response to the possible reasons suggested by Aghsaee *et al.* (2012), we note that present calculations: (a) are two-dimensional; (b) solve the full Navier–Stokes equations, and include convergent estimates of the wave-induced velocities and wavelength; (c) do not, however, include finite-amplitude perturbations; and (d) mimic the wave generation procedure of the laboratory experiments by Carr *et al.* (2008). At the threshold of the vortex formation, the computations document that there is no vorticity at the position of the wave resulting from the generation (figure 1*c*).

Our calculations obtain very accurately the threshold that was measured by Carr *et al.* (2008), and suggest that the onset of instability in the wave tank was predominantly two-dimensional. The calculated instability appears because of the truncation error of the solver. This suggests that the instability may appear spontaneously because of small perturbations of the experimental waves. Note that Sakai *et al.* (2020) calculated this kind of instability by large eddy-simulation in three dimensions. They found that the shed vortices were initially two-dimensional.

The instability threshold depends on the depth of the pycnocline and is found in both experiment and computation. The instability threshold is here computed for a wider Reynolds number range. The computed internal solitary waves of finite amplitude have been tested with excellent fit to the exact two- and three-layer models by Michallet & Barthélemy (1998), Grue *et al.* (1999, 2000), Camassa *et al.* (2006) and Fructus *et al.* (2009) (results not shown). Our calculations document that the instability criterion proposed by Aghsaee *et al.* (2012) is not universal.

3.3.1. *Instability threshold dependence of the pycnocline depth*

The horizontal velocity below the trough ($U_{\infty,0}$) depends on the depth of the pycnocline. The dependency may be illustrated at large Reynolds number where the instability threshold depends on the weakly nonlinear amplitude. The KdV theory is then a valid approximation. The velocity becomes $U^{KdV}_{\infty,0}/c_0 \simeq a/(H-d)$. The velocity scale of the bottom boundary layer is $\delta\omega_0$, with $\omega_0 = c_0/L_w$. The wavelength estimated by the KdV approximation obtains $L^{KdV}_w/d = 2(3a/4H)^{-1/2}[1-d^2/(H-d)^2]^{-1/2}$ $(\Delta\rho/\rho \ll 1)$ (e.g. Grue *et al.* 1999). The dimensionless velocity estimated by $U^{KdV}_{\infty,0}/(\delta\omega_0)$ is thus a function of the depth of the pycnocline d/H and the amplitude a/H. Moreover, the Reynolds number evaluated at the separation point is a function of d/H since $Re_{\theta_{sep}} \simeq 0.11 U_\infty \delta/\nu$ (table 3), where U_∞ and δ are functions of d/H and a/H. Similar results for waves with a/H outside the KdV range are computed.

3.4. *Separation bubbles and instability*

Two separation bubbles of anticlockwise vorticity form in the boundary layer behind the wave trough. The first is located in the wave phase, and the second is found downstream of the wave. They are calculated at the onset of instability in figure 4. The bubbles separate for the larger $Re_w = 5.9 \times 10^5$, and partially overlap for $Re_w = 5.9 \times 10^4$, but merge for the smaller $Re_w = 2 \times 10^4$ (Diamessis & Redekopp 2006). Bubble one has width $2.2H$–$3.5H$, and bubble two has width $10H$. The height of bubble one is slightly less than half of the

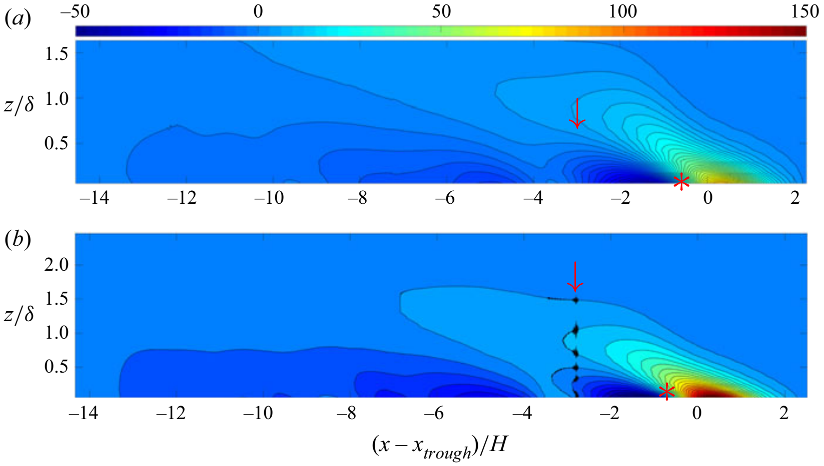

Figure 4. Vorticity plot of separation bubbles, with $\omega(c_0/H)$ in colour scale. Amplitude right above threshold of instability in Strat.2. Instability shown by red arrow, separation point of bubble one shown by red $*$. (*a*) Run 2c, $a/H = 0.235$, $Re_w = 5.9 \times 10^4$; (*b*) $a/H = 0.188$, $Re_w = 5.9 \times 10^5$.

w_1/H	β_1/δ	w_2/H	β_2/δ	a/H	Re_w
3.50	0.43	10.4	0.78	0.235	5.9×10^4
2.20	0.46	10.1	0.78	0.165	5.9×10^5

Table 4. Width w and height β of the separation bubbles one (index 1) and two (index 2) calculated right above the threshold of instability, for amplitude a/H and Reynolds number Re_w, in stratification 2.

$\alpha_i l_0$	l_0/δ	λ_0/δ	$\lambda_{v,0}/\delta$	Re_δ	Re_w	Stratification
5.2	80	5.3	5.4	490	5.9×10^4	Run 2*
6.6	80	4.2	3.5	1630	5.9×10^5	Strat.2
5.7	80	5.1	5.1	1650	6.5×10^5	Strat.3

Table 5. Initial instability: growth rate times distance of growth ($\alpha_i l_0$), distance of growth (l_0/δ), wavelength during growth (λ_0/δ), separation length between initial rolls ($\lambda_{v,0}/\delta$), Re_δ, Re_w and stratifications 2 and 3 for unstable waves of amplitude $a/H = 0.30$.

boundary layer thickness, and the height of bubble two is 0.78 times the boundary layer thickness. The heights do not depend on the scale (table 4). Flow reversal occurs closer to the bottom and decreases in strength when the Reynolds number increases.

The instability emerges in the back part of bubble one and moves to the front part when the amplitude increases. A wavelength (λ_0) of the dominant unstable mode is defined (table 5). The amplitude increases approximately exponentially according to the rate α_i, and takes place over a short distance l_0, where $l_0/\delta \simeq 80$ is independent of the scale (figure 5). The large vertical velocity is confined mainly to the wave phase when Re_w grows. A series of vortex rolls of separation length $\lambda_{v,0} \simeq \lambda_0$ forms. The growth then slows down, and the instability saturates. The distance between the downstream vortices

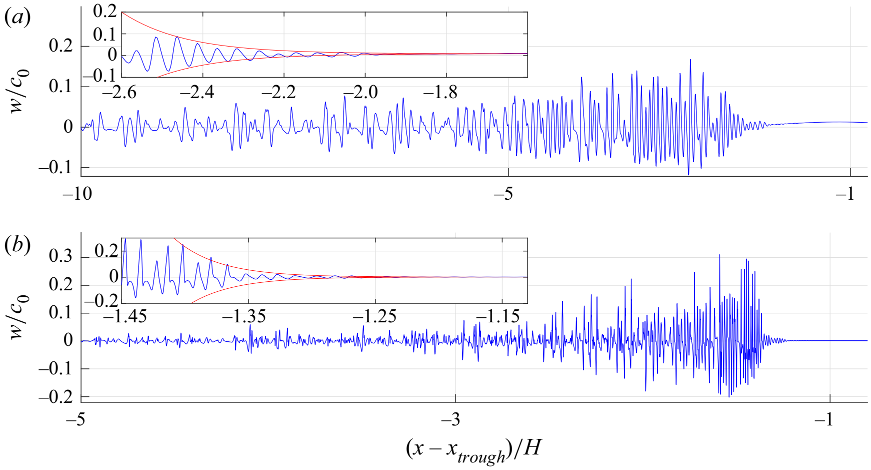

Figure 5. Vertical velocity w/c_0 versus horizontal position, with $a/H = 0.30$ in Strat.2, where inserts show estimated amplitude of exponential growth (red line): (*a*) $z/H = 0.0226$, $Re_w = 5.9 \times 10^4$, run 2*; (*b*) $z/H = 0.00218$, $Re_w = 5.9 \times 10^5$.

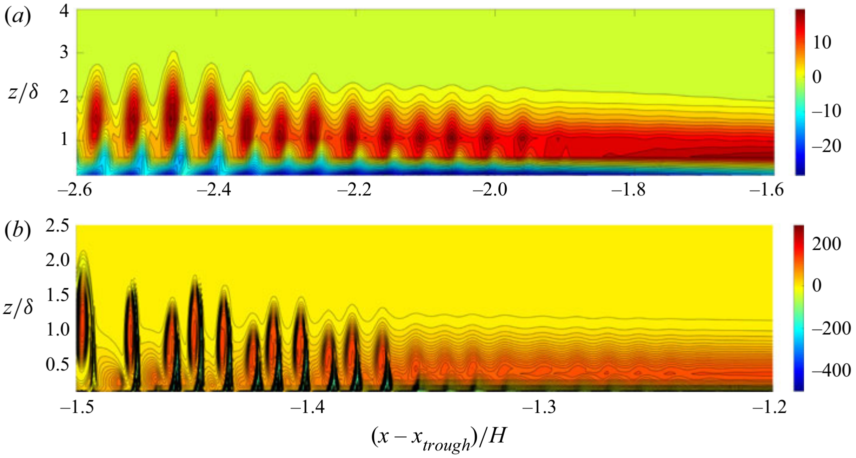

Figure 6. Vorticity $\omega/(c_0/H)$ (colour scale), with $a/H = 0.30$ in Strat.2: (*a*) $Re_w = 5.9 \times 10^4$, run 2*; (*b*) $Re_w = 5.9 \times 10^5$.

increases. Figure 6 illustrates the instability and the vortex roll-up. The vortex rolls ascend vertically beyond the boundary layer. The vorticity strength reduces with the downstream position. No new instability occurs in bubble two.

3.5. *Bed shear stress*

The calculated bed shear stress τ is of the form $\tau/(\rho c_0^2/2) \simeq A_0 \sin[k_{v,0}(x - \hat{x})]$ and oscillates according to the wavenumber $k_{v,0} = 2\pi/\lambda_{v,0}$ of the vortex rolls, where $\hat{x}$ denotes the forward position of the oscillation (figure 7). In the sense of Froude number scaling,

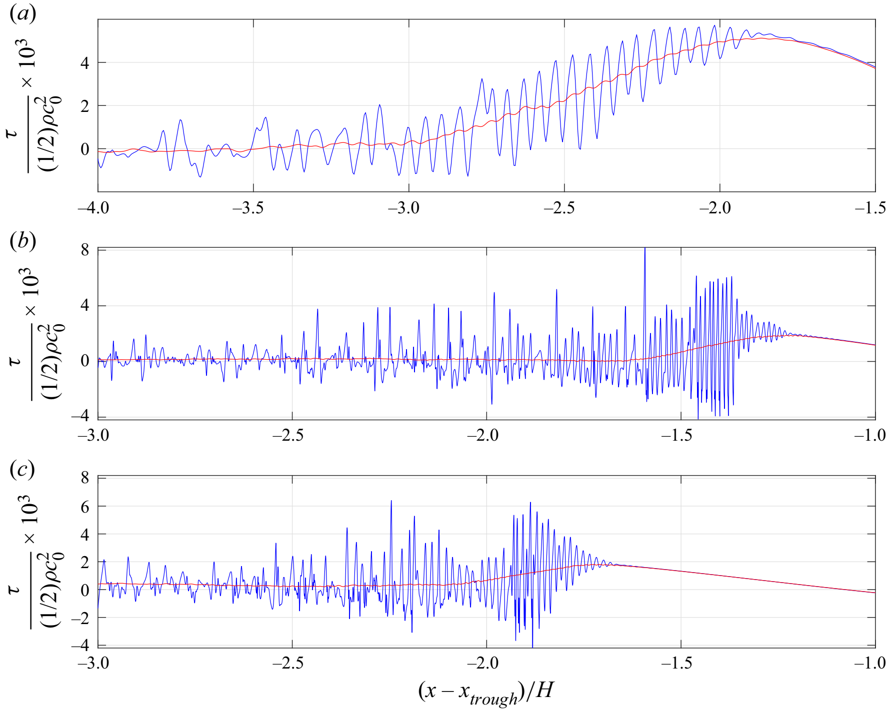

Figure 7. Shear stress τ (blue line) at the bottom versus horizontal position, with $a/H = 0.30$, and averaged τ (red line): (*a*) $Re_w = 5.9 \times 10^4$, Strat.2, run 2*; (*b*) $Re_w = 5.9 \times 10^5$, Strat.2; (*c*) $Re_w = 6.5 \times 10^5$, Strat.3.

the linear long-wave speed is used to scale the stress (e.g. Boegman & Ivey 2009; Xu & Stastna 2020). The stress amplitude is strong in the wave phase and during the vortex roll-up phase, and occurs over a distance of 1–1.5 water depths but is weak otherwise. The maximum strength A_0 is $\simeq 1.5 \times 10^{-3}$ for the smaller Re_w, and $\simeq 5 \times 10^{-3}$ for the higher Re_w. The fluctuating stress has a root-mean-square estimate $A_0/\sqrt{2}$. The strength and oscillation frequency of the stress both increase when the scale increases. A similar growth of the bed shear stress amplitude with the scale has been found in the case of internal waves of elevation interacting with a weak slope; see Xu & Stastna (2020). The Re_w value was 1.5–6 $\times 10^4$ in their calculations.

3.5.1. *Field observations*

The bed shear stress has been estimated in field measurements by the Reynolds stress method and the quadratic drag method using acoustic doppler velocimetry. Both methods assume that a log layer exists and extends to the measurement height above the bottom. Measurements on the Australian North West Shelf by Zulberti *et al.* (2020) showed enhanced turbulent shear stress below nonlinear internal solitary waves, and maximum stress 1 Pa. A non-dimensional shear stress becomes 1 Pa$/(\rho c_0^2/2) \simeq 3 \times 10^{-3}$, where $c_0 \simeq 0.77$ m s^{-1} and $Re_w = 1.9 \times 10^8$ are computed from Zulberti *et al.* (2020). Measurements on the northern shelf of Portugal by Quaresma *et al.* (2007) found maximum bed shear stress 0.2 Pa below the strong internal waves. A non-dimensional shear stress becomes 0.2 Pa/$(\rho c_0^2/2) \simeq 4 \times 10^{-3}$, where $c_0 \simeq 0.34$ m s^{-1} and $Re_w = 2 \times 10^7$ are calculated from Quaresma *et al.* (2007). The strong shear stress measured in the field occurs in the wave phase. The calculated laminar shear stress also occurs below the wave, in the vortex roll-up phase. The relative wave amplitude and pycnocline depth of the field measurements and the model waves are similar ($a/H \simeq 0.3$, $d/H \simeq 0.2$). The non-dimensional shear stress is also similar.

4. Conclusions

Instability and vortex shedding in the bottom boundary layer beneath internal solitary waves of depression have been calculated by finite-volume code Basilisk in two dimensions. The modelled waves compare very well to exact solutions. The range of the stratification Reynolds number is $Re_w = c_0H/\nu \sim 1.9 \times 10^4$–$6.5 \times 10^5$.

Our calculations obtain very accurately the threshold of instability that was measured by Carr *et al.* (2008). The very good agreement suggests that the instability in their wave tank experiments was predominantly two-dimensional. The calculated instability is caused spontaneously by the truncation error of the solver. This suggests that small perturbations caused the instability in the wave tank experiments. Note that Sakai *et al.* (2020) calculated this kind of instability by large-eddy simulation in three dimensions. They found that the shed vortices were initially two-dimensional.

We have computed the instability threshold and vortex formation for a wider Reynolds number range. The instability is found to depend on the depth of the pycnocline, and has a stronger decay with Re_w for a deeper pycnocline than for a shallower pycnocline. For example, the threshold amplitude decays according to $(Re_w)^{-m_1}$, where $m_1 = 0.23$ when $d = 0.21H$, and $m_1 = 0.13$ when $d = 0.16H$. The instability criterion proposed by Aghsaee *et al.* (2012) is re-calculated. Their criterion is not universal and is also very conservative in the sense that only waves of very large amplitude are unstable.

The computations show two separation bubbles. The first is located in the wave phase behind the trough. The second is found well behind the wave phase. The instability emerges as a tiny short-wave disturbance in the back part of bubble one, and moves to the front part when the amplitude increases. Instability and vortex rolls appear in the wave phase behind the trough. No new instability occurs in bubble two.

The vortex formation causes an oscillating bed shear stress. The stress amplitude is strong in the wave phase and during the roll-up phase, and occurs over a distance of 1–1.5 water depths but is weak otherwise. The strong shear stress measured in the field also occurs in the wave phase (Quaresma *et al.* 2007; Zulberti *et al.* 2020). The shear stress computed in the laminar model and measured in the field has similar non-dimensional value (scaled by $\rho c_0^2/2$) when the non-dimensional amplitude and relative pycnocline depth are similar ($a/H \simeq 0.3$, $d/H \simeq 0.2$).

Acknowledgements. The critical comments and suggestions by three anonymous referees helped to improve the paper. Professor M.S. Floater is acknowledged for help in improving the language.

Funding. Funding by the Research Council of Norway (Ecopulse, NFR300329) is gratefully acknowledged. The computations were performed on the Norwegian Research and Education Cloud (NREC), using resources provided by the University of Bergen and the University of Oslo (http://www.nrec.no/).

Declaration of interests. The authors report no conflict of interest.

Author ORCIDs.

John Grue https://orcid.org/0000-0001-6560-4970.

References

Aghsaee, P., Boegman, L., Diamessis, P.J. & Lamb, K.G. 2012 Boundary-layer-separation-driven vortex shedding beneath internal solitary waves of depression. *J. Fluid Mech.* **690**, 321–344.

Alventosa, L.F.L., Cimpeanu, R. & Harris, D.M. 2023 Inertio-capillary rebound of a droplet impacting a fluid bath. *J. Fluid Mech.* **958**, A24.

Bell, J.B., Colella, P. & Glaz, M.G. 1989 A second-order projection method for the incompressible Navier–Stokes equations. *J. Comput. Phys.* **85** (2), 257–283.

Boegman, L. & Ivey, G. 2009 Flow separation and resuspension beneath shoaling nonlinear internal waves. *J. Geophys. Res.* **114**, C02018.

Boegman, L. & Stastna, M. 2019 Sediment resuspension and transport by internal solitary waves. *Annu. Rev. Fluid Mech.* **51** (1), 129–154.

Bogucki, D., Dickey, T. & Redekopp, L.G. 1997 Sediment resuspension and mixing by resonantly generated internal solitary waves. *J. Phys. Oceanogr.* **27** (7), 1181–1196.

Bogucki, D.J. & Redekopp, L.G. 1999 A mechanism for sediment resuspension by internal solitary waves. *Geophys. Res. Lett.* **26** (9), 1317–1320.

Bourgault, D., Blokhina, M.D., Mirshak, R. & Kelley, D.E. 2007 Evolution of a shoaling internal solitary wave train. *Geophys. Res. Lett.* **34**, L03601.

Camassa, R., Choi, W., Michallet, H., Rusås, P.-O. & Sveen, J.K. 2006 On the realm of validity of strongly nonlinear asymptotic approximations for internal waves. *J. Fluid Mech.* **549**, 1–23.

Carr, M. & Davies, P.A. 2006 The motion of an internal solitary wave of depression over a fixed bottom boundary in a shallow, two-layer fluid. *Phys. Fluids* **18** (1), 016601.

Carr, M. & Davies, P.A. 2010 Boundary layer flow beneath an internal solitary wave of elevation. *Phys. Fluids* **22** (1), 026601.

Carr, M., Davies, P.A. & Shivaram, P. 2008 Experimental evidence of internal solitary wave-induced global instability in shallow water benthic boundary layers. *Phys. Fluids* **20** (6), 066603.

Chomaz, J.-M. 2005 Global instabilities in spatially developing flows: non-normality and nonlinearity. *Annu. Rev. Fluid Mech.* **37** (1), 357–392.

Diamessis, P.J. & Redekopp, L.G. 2006 Numerical investigation of solitary internal wave-induced global instability in shallow water benthic boundary layers. *J. Phys. Oceanogr.* **36** (5), 784–812.

Dunphy, M., Subich, C. & Stastna, M. 2011 Spectral methods for internal waves: indistinguishable density profiles and double-humped solitary waves. *Nonlinear Process. Geophys.* **18**, 351–358.

Fructus, D., Carr, M., Grue, J., Jensen, A. & Davies, P.A. 2009 Shear-induced breaking of large internal solitary waves. *J. Fluid Mech.* **620**, 1–29.

Gaster, M. 1967 *The Structure and Behaviour of Laminar Separation Bubbles*. AGARD CP-4.

Grue, J., Jensen, A., Rusås, P.-O. & Sveen, J.K. 1999 Properties of large-amplitude internal waves. *J. Fluid Mech.* **380**, 257–278.

Grue, J., Jensen, A., Rusås, P.-O. & Sveen, J.K. 2000 Breaking and broadening of internal solitary waves. *J. Fluid Mech.* **413**, 181–217.

Hammond, D.A. & Redekopp, L.G. 1998 Local and global instability properties of separation bubbles. *Eur. J. Mech.* (*B/Fluids*) **17**, 145–164.

Harnanan, S., Soontiens, N. & Stastna, M. 2015 Internal wave boundary layer interaction: a novel instability over broad topography. *Phys. Fluids* **27**, 016605.

Harnanan, S., Stastna, M. & Soontiens, N. 2017 The effects of near-bottom stratification on internal wave induced instabilities in the boundary layer. *Phys. Fluids* **29**, 016602.

Helfrich, K.R. & Melville, W.K. 2006 Long nonlinear internal waves. *Annu. Rev. Fluid Mech.* **38**, 395–425.

van Hooft, J.A., Popinet, S., van Heerwaarden, C.C., van der Linden, S.J.A., de Roode, S.R. & van de Wiel, B.J.H. 2018 Towards adaptive grids for atmospheric boundary-layer simulations. *Boundary-Layer Meteorol.* **167** (3), 421–443.

Huerre, P. & Monkewitz, P.A. 1990 Local and global instabilities in spatially developing flows. *Annu. Rev. Fluid Mech.* **22**, 473–537.

Innocenti, A., Jaccod, A., Popinet, S. & Chibbaro, S. 2021 Direct numerical simulation of bubble-induced turbulence. *J. Fluid Mech.* **918**, A23.

Lagrée, P.-Y., Staron, L. & Popinet, S. 2011 The granular column collapse as a continuum: validity of a two-dimensional Navier–Stokes model with a $\mu(I)$-rheology. *J. Fluid Mech.* **686**, 378–408.

Lamb, K.G. 2014 Internal wave breaking and dissipation mechanisms on the continental slope/shelf. *Annu. Rev. Fluid Mech.* **46** (1), 231–254.

Michallet, H. & Barthélemy, E. 1998 Experimental study of interfacial solitary waves. *J. Fluid Mech.* **366**, 159–177.

MOSTERT, W. & DEIKE, L. 2020 Inertial energy dissipation in shallow-water breaking waves. *J. Fluid Mech.* **890**, A12.

MOSTERT, W., POPINET, S. & DEIKE, L. 2022 High-resolution direct simulation of deep water breaking waves: transition to turbulence, bubbles and droplets production. *J. Fluid Mech.* **942**, A27.

OLSTHOORN, J. & STASTNA, M. 2014 Numerical investigation of internal wave-induced sediment motion: resuspension versus entrainment. *Geophys. Res. Lett.* **41**, 2876–2882.

PAULEY, L.L., MOIN, P. & REYNOLDS, W.C. 1990 The structure of two-dimensional separation. *J. Fluid Mech.* **220**, 397–411.

POPINET, S. 2003 Gerris: a tree-based adaptive solver for the incompressible Euler equations in complex geometries. *J. Comput. Phys.* **190** (2), 572–600.

POPINET, S. 2009 An accurate adaptive solver for surface-tension-driven interfacial flows. *J. Comput. Phys.* **228** (16), 5838–5866.

POPINET, S. 2015 A quadtree-adaptive multigrid solver for the Serre–Green–Naghdi equations. *J. Comput. Phys.* **302**, 336–358.

QUARESMA, L.S., VITORINO, J., OLIVEIRA, A. & DA SILVA, J. 2007 Evidence of sediment resuspension by nonlinear internal waves on the western Portuguese mid-shelf. *Mar. Geol.* **246** (2), 123–143.

REED, H.L. & SARIC, W.S. 1996 Linear stability theory applied to boundary layers. *Annu. Rev. Fluid Mech.* **28**, 389–428.

RIVIÉRE, A., MOSTERT, W., PERRARD, S. & DEIKE, L. 2021 Sub-Hinze scale bubble production in turbulent bubble break-up. *J. Fluid Mech.* **917**, A40.

SAKAI, T., DIAMESSIS, P.J. & JACOBS, G.B. 2020 Self-sustained instability, transition, and turbulence induced by a long separation bubble in the footprint of an internal solitary wave. I. Flow topology. *Phys. Rev. Fluids* **5**, 103801.

SCHMID, P.J. & HENNINGSON, D.S. 2001 *Stability and Transition in Shear Flows*. Springer.

SOONTIENS, N., STASTNA, M. & WAITE, M.L. 2015 Topographically generated internal waves and boundary layer instabilities. *Phys. Fluids* **27**, 086602.

STASTNA, M. & LAMB, K.G. 2002*a* Large fully nonlinear internal solitary waves: the effect of a background current. *Phys. Fluids* **14**, 2987–2999.

STASTNA, M. & LAMB, K.G. 2002*b* Vortex shedding and sediment resuspension associated with the interaction of an internal solitary wave and the bottom boundary layer. *Geophys. Res. Lett.* **29** (11), 7.

STASTNA, M. & LAMB, K.G. 2008 Sediment resuspension mechanisms associated with internal waves in coastal waters. *J. Geophys. Res.* **113**, C10016.

THIEM, Ø., CARR, M., BERNTSEN, J. & DAVIES, P.A. 2011 Numerical simulation of internal solitary wave-induced reverse flow and associated vortices in a shallow, two-layer fluid benthic boundary layer. *Ocean Dyn.* **61**, 857–872.

TURKINGTON, B., EYDELAND, A. & WANG, S. 1991 A computational method for solitary internal waves in a continuously stratified fluid. *Stud. Appl. Maths* **85**, 93–127.

VERSCHAEVE, J.C.G. & PEDERSEN, G.K. 2014 Linear stability of boundary layers under solitary waves. *J. Fluid Mech.* **761**, 62–104.

XU, C. & STASTNA, M. 2020 Instability and cross-boundary-layer transport by shoaling internal waves over realistic slopes. *J. Fluid Mech.* **895**, R6.

ZULBERTI, A., JONES, N.L. & IVEY, G.N. 2020 Observations of enhanced sediment transport by nonlinear internal waves. *Geophys. Res. Lett.* **47**, 1–11.

Paper II

Tracer particle motion driven by vortex formation in the bottom boundary layer underneath internal solitary waves

Thea Josefine Ellevold, John Grue, Joakim Soløy Sletten

Published in *Frontiers in Marine Science*, August 2023, volume 10, pp. 1155270
DOI: doi:10.3389/fmars.2023.1155270.

frontiers

Tracer particle motion driven by vortex formation in the bottom boundary layer underneath internal solitary waves

Thea Josefine Ellevold [1,*], **John Grue** [1] **and Joakim Soløy Sletten** [1]

[1] *Department of Mathematics, University of Oslo, Oslo, Norway*

Correspondence*:
Thea Josefine Ellevold
theajel@math.uio.no

ABSTRACT

Internal solitary waves (ISWs) of large amplitude moving in the coastal ocean induce sizeable horizontal velocities above the sea bed. In turn, these give rise to instability and vortex formation in the bottom boundary layer (BBL), and sediment resuspension and concentration maintenance in the water column. We present two-dimensional laminar simulations in a numerical tank suitable for internal wave motion, including the processes of the BBL. The combined wave and vorticity field encounters a cloud of tracer particles near the bottom. The tracer particles are moved vertically because of the vorticity field during a first encounter. The reflected wave intercepts a second time with the tracer particles, which are then moved further vertically. Numerical experiments with a kinematic viscosity of $1/100$ cm^{2}s^{-1} or $1/1000$ cm^{2}s^{-1} are used to manipulate the scale of the Reynolds number at a moderate and great laboratory scale. The final vertical position of the tracer particles is found below a vertical level of approximately 0.23 times the water depth (H) after the second passage. The result is independent of the scale. This vertical position matches available field measurements of a summer benthic nepheloid layer reaching a height of $0.19H$. The laminar model predictions compare very well to the ISW-driven vortex formation measured in a three-dimensional laboratory wave tank. Convergence of the calculated vortex formation is documented.

Keywords: Internal waves, vortex formation, Lagrangian tracer particle trajectories, probability distribution, upscaling to field dimension

Number of words: ∼6300. Number of figures and tables: 10 figures and 2 tables.

1 INTRODUCTION

Internal solitary waves (ISWs) are commonly observed in the coastal ocean and are generally driven by the wind or the tide (Helfrich and Melville, 2006). The ISWs are driven by the acceleration of gravity ($g = 9.81$ ms^{-2}) and may move along the pycnocline of the ocean located at a middle depth d, which is small compared to the local water depth H, implying the dimensionless ratio d/H. The density jump across the pycnocline ($\Delta\rho$) relative to the density of the water below the pycnocline (ρ_3) is typically small, with a dimensionless value of $\Delta\rho/\rho_3 << 1$. In practice, $\Delta\rho/\rho_3$ is $1/1000$. The wave motion and the velocity field are functions of the wave amplitude a, obtaining another dimensionless variable a/H. The wave-driven velocities scale according to a reference velocity c_0. This is proportional to $\sqrt{dg\Delta\rho/\rho_3}$ times a function of

d/H. As regards the bottom boundary layer effect, it is commonly characterized by the Reynolds number based on the total water depth, the wave speed c_0, and the kinematic viscosity ν, obtaining $Re_w = c_0 H/\nu$.

ISWs are often highly nonlinear. The theories, like weakly nonlinear Korteweg–de Vries (KdV) -type theories, have played a primary role in explaining the essential features of the observed wave, even though those theories do not always provide accurate quantitative details. Grue et al. (1999) conducted laboratory experiments of solitary waves propagating in a two-layer fluid. They compared the weakly nonlinear KdV theory and a fully nonlinear interface model towards the experimental results. Having a small amplitude, both theory and model compared excellently. However, above a certain amplitude threshold, the weakly nonlinear theory exhibits systematic deviation from the experiments where the fully nonlinear model still compared excellently for all quantities measured.

Above the pycnocline, the velocities have a dominant horizontal component, a substantial fraction of the wave propagation velocity. Below the pycnocline, the horizontal velocity is opposite of the wave propagation and is also a substantial fraction of the wave propagation speed. The vertically integrated horizontal velocity is zero and satisfies the mass balance. There are also vertical velocities. These are proportional to the horizontal gradient of the displaced pycnocline along the wave propagation times the wave speed.

The wave-induced boundary layer underneath an ISW of depression separates in the adverse pressure gradient region behind the trough. Strong enough instability may give rise to the spontaneous onset of vortex shedding (e.g., Diamessis and Redekopp, 2006; Carr et al., 2008; Aghsaee et al., 2012; Sakai et al., 2020). The vortex structures are formed behind the wave trough, ascend vertically into the water column, and then propagate downstream in the same direction as the mother wave but with a much slower speed (Carr et al., 2008). The instabilities in the bottom boundary layer may contribute to the resuspension of particles due to, e.g., substantial variation of the shear stress (e.g., Bogucki and Redekopp, 1999; Boegman and Stastna, 2019). The ability of nonlinear internal waves to move sediments on the bottom vertically in the water column has been observed by Bogucki et al. (1997), and has been further studied model-wise by, e.g., Bogucki and Redekopp (1999), and in field observations, e.g., Bourgault et al. (2007), Quaresma et al. (2007), Zulberti et al. (2020), see also the review by Boegman and Stastna (2019).

Large eddy simulations (LES) in three dimensions (3D) of the ISW-driven separated boundary layer and its development were carried out by Sakai et al. (2020) for a Reynolds number similar to our ($Re_w = 1.6 \cdot 10^5$). A strong wave of $a/H = 0.35$ was moving on a counter-current of the same magnitude as the wave propagation speed, implying that the excitation is stronger than in our cases. The LES computations were compared to two-dimensional direct numerical simulations finding that the vortex generation was essentially two-dimensional down to a distance of six water depths behind the wave trough. Further downstream, vortex breakup and degeneration into turbulent clouds, and relaxation to a spatially developing turbulent boundary layer were found to take place.

In this research, we investigate the ISW-driven vortex formation and tracer particle displacements in the bottom boundary layer. We conduct laminar two-dimensional numerical simulations of a set of laboratory experiments by Carr et al. (2008) where this kind of physical effect has been measured. Several questions are addressed, including:

1. As regards the two-dimensional laminar method: How well can the model reproduce the laboratory measurements conducted in a three-dimensional (3D) wave tank? In particular, how well can the model calculations reproduce the measured vortices at the bottom behind the wave?
2. As regards accuracy: How close are prediction and measurement?

3. As regards flow and motion properties: How can the model be used to evaluate quantities which have not been measured in the laboratory?
4. As regards the tracer particle motion: The wave- and boundary-layer-induced tracer particle motion is of interest to study and visualize. This motion was not measured in the laboratory experiments, even though the experimental visual tracking method is based on neutrally buoyant tracer particles added to the fluid.
5. As regards the vertical tracer particle displacements: In the shallow ocean, the particles at the sea bed contain organic matter that is important to the marine production taking place in the euphotic zone in the upper part of the water column. By the present model calculations, we investigate how high up in the water column the tracer particles may be transported. The wave may intercept a cloud of tracer particles once and twice.
6. Finally, we compare the simulated results with available field observations.

In section 2, we present the numerical wave tank, wave generation, wave characteristics, and the Stokes boundary layer thickness. Further, details of the two-dimensional numerical solver are described. The grid resolution and information regarding the Lagrangian tracer particles used in this study are provided. Section 3 presents the obtained results, including answers to the research questions posed. In section 3.1, similarities between the vortex formation in simulation and experiment at $Re_w = 5.9 \cdot 10^4$ are presented. A convergence study of the calculated vortex separation distance and the vortex strength is performed. In section 3.2, we present the Lagrangian tracer particle displacements and paths. The vertical tracer particle distribution is calculated. The results are briefly compared to available field measurements in section 3.3, and conclusions are given in section 4.

2 METHOD

This article presents numerical simulations of non-linear internal solitary waves (ISWs) of large amplitude, as visualized in figure 1b, where the wave travels from left to right with a speed c. The wave-induced velocity field beneath the wave interacts with the bottom, initiating instabilities in the viscous bottom boundary layer (BBL) (e.g., Diamessis and Redekopp, 2006; Carr and Davies, 2006; Aghsaee et al., 2012; Sakai et al., 2020). Tracer particles are implemented close to the bottom in order to investigate their motion in the fluid induced by the wave (Boegman and Stastna, 2019).

2.1 The numerical wave tank

We are following the same setup of the wave tank and the wave generation procedure as conducted in the laboratory experiments by Carr et al. (2008). The numerical wave tank is filled with a stratified fluid. The upper layer has a depth of h_1 and a density of ρ_1. The pycnocline has a thickness of h_2 and density $\rho(z)$, which varies as a linear function of z. The lower layer has thickness h_3 and density ρ_3. The density is continuous throughout the vertical. The total water depth is $H = h_1 + h_2 + h_3$. Figure 1a is a sketch of the wave tank. The amplitude a is defined as the maximum excursion of the isoline separating layers two and three. The middle depth of the pycnocline is defined by $d = h_1 + h_2/2$. In the present investigation, two different stratifications are studied, where stratification one, denoted by Strat. 1, has $d/H = 0.16$, and stratification two, denoted by Strat. 2, has $d/H = 0.21$. These two stratifications correspond to two of the pycnocline depths studied by Carr et al. (2008). In present calculations, the thickness of the pycnocline is $h_2 \sim 0.12H - 0.14H$, and the wave amplitude $a/d \sim 1.45 - 1.87$.

The physical dimensions of the 2D numerical wave tank are the same as those used in the laboratory setup by Carr et al. (2008). The length $L = 6.4$ m and depth $H = 0.38$ m provide a non-dimensional length of $L/H = 16.84$.

2.2 Generation and wave characteristics

To generate ISWs in the tank (physical or numerical), the trapped volume method is applied where a large volume V, given by $(x_0 \times (d_0 - h_1))$ of density ρ_1, is added behind a gate. The gate is located at a distance of $\Delta x_0 = 0.6$ m from the left tank wall. Its horizontal position defines $x = 0$, where the horizontal x-axis is along the bottom. The total volume can be modified by varying the depth d_0, generating ISWs with different amplitudes, by releasing the volume. In the laboratory, the gate is removed by quickly lifting it upwards. In the numerical simulations, the gate is imposed before time zero, and after time zero, we assume it is instantaneously removed. A leading wave of mode 1 is generated in each experiment (physical or numerical).

The wave frequency is defined by $\tilde{\omega} = c_0/L_w$, where c_0 is the linear long wave speed given by the two-layer approximation

$$c_0 = \sqrt{\frac{g(h_3 + h_2/2)(h_1 + h_2/2)(\rho_3 - \rho_1)}{\rho_1(h_3 + h_2/2) + \rho_3(h_1 + h_2/2)}} \cong \sqrt{\frac{g' d(H - d)}{H}}, \tag{1}$$

where $g' = g(\rho_3 - \rho_1)/\rho_3$ and $\Delta\rho/\rho_3 \ll 1$. The wavelength of the ISW is defined by

$$L_w = \frac{1}{a} \int_{-\infty}^{\infty} \eta(x) dx, \tag{2}$$

where η denotes the vertical displacement of the isoline separating layers two and three, and the amplitude a is defined above.

The Reynolds number based on the water depth, alternatively denoted the wave Reynolds number, is a helpful quantity used by a group of researchers studying the combined wave and boundary layer effects (e.g., Diamessis and Redekopp, 2006; Carr et al., 2008; Aghsaee et al., 2012; Sakai et al., 2020). The quantity is defined by $Re_w = c_0 H/\nu$ where ν is the kinematic viscosity of the water. In the laboratory experiments by Carr et al. (2008), the Re_w was approximately 60 000. In the field scale, Re_w is 10^8 (e.g., Zulberti et al., 2020). The present calculations are carried out with Re_w between 60 000 and 600 000. The calculations at $Re_w = 60\ 000$ are carried out with $\nu = 1/100\ \mathrm{cm^2 s^{-1}}$ for fresh water at 20 $°C$. In the calculations at $Re_w = 600\ 000$, the ν is manipulated with a value put to $\nu = 1/1000\ \mathrm{cm^2 s^{-1}}$. Alternatively, the water depth may be increased to $\tilde{H} = 10^{2/3} H$, $\tilde{c_0} = 10^{1/3} c_0$, and $\nu = 1/100\ \mathrm{cm^2 s^{-1}}$ producing $Re_w = 600\ 000$. Additionally, we define a boundary layer Reynolds number, $Re_\delta = \delta U_{\infty,0}/\nu$, where $U_{\infty,0}$ is the free stream horizontal velocity underneath the wave trough, right above the bottom, and δ is the boundary layer thickness, defined in section 2.3 below.

The wave travels along the pycnocline from left to right. The nonlinear celerity is $c = \Delta x/\Delta t$. There is no background current. A snapshot of an ISW at time $tc_0/H = 6.4$ is visualized by its nondimensional vorticity field in figure 1b (corresponding to run 1 in table 1). The simulation is run with a kinematic viscosity of $\nu = 1/100\ \mathrm{cm^2 s^{-1}}$. The wave drives the instability and vortex formation in the BBL, in addition to the shear instability in the pycnocline (e.g., Fructus et al., 2009; Lamb, 2014). As the volume is released, a local mixing of the fluid taking place across the gate position is confined to a small volume (physical or numerical). This is set into horizontal motion along the pycnocline, generating a short and slower wave of mode 2, observed at approximately nine water depths behind the main wave. Such a wave is measured by Sveen et al. (2002, their figure 17) and more recently studied by Carr et al. (2019).

The ISW propagating at small speed c, proportional to $(\Delta\rho/\rho_3)^{1/2}$, implies that the effect on the free surface elevation is small. The vertical velocity is approximately zero at the free surface. The small free surface elevation may be calculated a posteriori from the Bernoulli equation giving $\eta = (1/2g)(c^2 - u^2)$, where u is the horizontal speed driven by the ISW at the free surface (e.g., Fructus and Grue, 2004). On the laboratory scale, the wave speed is 0.26 ms^{-1}, $u/c << 1$ for the waves of large amplitude (and the wavelength is approximately 1 m). This obtains a surface elevation of 0.3 cm while the internal wave amplitude is 11 cm. Corresponding estimates of ISWs in the coastal ocean are: wave speed of 0.5 ms^{-1}, a surface elevation of 1 cm, while the internal wave amplitude is typically 30 m. The internal waves are 500 m to 1000 m long.

2.3 Boundary layer thickness

The Stokes boundary layer thickness at the bottom beneath the wave phase is characterized by $\delta = \sqrt{(2\nu/\tilde{\omega})}$, where $\tilde{\omega}$ is defined in § 2.2.

2.4 Finite Volume Solver

We present numerical simulations of ISWs, utilizing the open-source software Basilisk (Popinet and collaborators, 2013–2023). The important part of the calculation is to resolve the wave-driven viscous boundary layer effect at the bottom of the fluid domain. Basilisk is a second-order finite volume solver, where the two-phase incompressible Navier-Stokes equations are solved and is the successor of Gerris (Popinet, 2003, 2009). Basilisk provides ready-to-use finite volume solvers for fluid dynamics and has been widely used in calculations and simulations of several problems, i.e., tsunamies (e.g., Popinet, 2015), shallow water, wave breaking and surface flows (e.g., Popinet, 2011; Mostert and Deike, 2020; Popinet, 2020), incompressible two-phase flow (e.g., López-Herrera et al., 2019), and atmospheric turbulent boundary layer (e.g., van Hooft et al., 2018).

In this two-dimensional (2D) study, the incompressible, non-hydrostatic equations in a Cartesian reference frame become,

$$\frac{\partial \mathbf{u}}{\partial t} + (\mathbf{u}\cdot\nabla)\mathbf{u} = -\frac{1}{\rho}\nabla p + \nu\nabla^2\mathbf{u} + \rho\mathbf{a}, \tag{3}$$

$$\frac{\partial \rho}{\partial t} + \nabla\cdot(\rho\mathbf{u}) = 0, \tag{4}$$

$$\nabla\cdot\mathbf{u} = 0, \tag{5}$$

where ρ, $\mathbf{u} = (u, w)$, p and ν are the density, velocity vector, pressure and kinematic viscosity, respectively. The vector $\mathbf{a} = -g\mathbf{k} = g(0, -1)$, where g is the acceleration due to gravity. Further, t is time, and (x, z) are the (horizontal, vertical) coordinates. The Navier-Stokes equations determine the pressure and the velocity field driven by the wave where mass conservation is included, additionally to set the effect of viscosity in the viscous boundary layer at the bottom.

The field equations are solved by means of a multilevel Poisson solver. The Bell-Colella-Glaz (Bell et al., 1989) advection scheme integrates the momentum equation. The viscous terms are treated implicitly. The solver employs a geometric volume of fluid method (VOF) to reconstruct the interfaces by the continuous change of the fluid properties; density and viscosity. The cells that include an interface are treated by introducing the volume fraction of the two fluids, $f(x, z, t)$. The implementation of the numerical scheme is briefly described below. The time integration (supplied in Appendix A.1) adheres to the standard Basilisk setup, with a slight modification where the dynamic viscosity is harmonically averaged. For more details, see the Basilisk web page (basilisk.fr), Popinet (2003, 2009), and references therein.

2.5 The domain

By default, Basilisk defines a computational domain with sides L. Our numerical wave tank is defined as a part of this spatial domain, with horizontal length L and vertical height H $(< L)$. At $z = H$ ($z = 0$ at the tank bottom, see figure 1a), a rigid lid is placed, implying no motion in the domain $z > H$. The effect of viscosity is taken into account within the fluid and at the bottom. This means that the no-slip condition is applied at the lower boundary. Free-slip conditions are used at the upper boundary, vertical end walls, and gate. The depth provides the physical length scale in the calculations. The time and velocity scales are $\sqrt{H/g}$ and $\sqrt{gH}$, respectively.

2.6 Discretization and grid resolution

The discretization of the computational domain utilizes a quad-tree scheme (Popinet, 2003; van Hooft et al., 2018) where the user can choose to run the scheme with either a non-adaptive mesh or an adaptive mesh, further referred to as ”refine” and ”adapt”, respectively.

The size of a cell is characterized by its level N where it is located. The cells are square finite volume cells, providing equal subdivisions vertically and horizontally, creating $\Delta_N = \Delta_x = \Delta_z$. Hence, the grid size of the cell at a given level is $\Delta_N = L/2^N$.

The grid resolution is discussed relative to the boundary layer thickness, i.e., Δ_N/δ. A fine discretization with $\Delta_{N_+} = L/2^{N_+}$ is developed near the bottom for $0 < z < 0.015H$, where the finest resolution becomes $\Delta_{N_+}/\delta = 0.022$ (run 3, table 1). Hence, $N_+ > N$. This is to ensure grid independence of the results.

Adaptive meshing is widely used and is known to significantly reduce the computation cost. We will utilize adapting meshing when exploring convergence properties of our numerical scheme. When the mesh is adapted, the refinement criterion is based on the discretization error of the velocities u and w, and the criterion for refinement of the volume fraction f is based upon a wavelet algorithm. The threshold values are set to $\epsilon_u^{th} = \epsilon_w^{th} = 3 \times 10^{-4}$ and $\epsilon_f^{th} = 3 \times 10^{-2}$. Further details are provided in the Appendix A.2.

van Hooft et al. (2018), their figure 8, have compared the numerical dissipation in the ”refine” and ”adapt” versions of Basilisk, finding that small discrepancies on the order of 5% were present between the runs with the fixed uniform grid and the adaptive grid, where this discrepancy decreased with increasing refinement. Numerical tests diagnosed with a lower dissipation rate were associated with lower kinetic energy, indicating that a small part of the dissipation was of numerical/non-physical origin.

The advantage of the Basilisk framework is that it includes OpenMP/MPI parallelism capability. The simulations were run in parallel using shared memory (OpenMP), and the computations were performed on the Norwegian Research and Education Cloud (NREC).

2.7 Lagrangian tracer particles

Tracking of Lagrangian tracer particles is performed using a two-stage Runge-Kutta (RK2) scheme. The seeded neutrally buoyant tracer particles are purely Lagrangian tracers, and their settling velocity, added mass, history effects, etc., are ignored (Necker et al., 2005; Stastna and Lamb, 2008).

The tracer particles are seeded close to the bottom in a two-dimensional rectangular grid. More precisely, 160×160 tracer particles are equally distributed horizontally between $x_p - H < x < x_p + H$ and vertically between $z_1 < z_p < z_2$ before time zero. Table 1 provides the x_p/H values. The tracer particle positions are presented relative to the total water depth H and the boundary layer's height δ (§2.3). The vertical extent is $z_p/H \sim 0.0037 - 0.0283$. However, the boundary layer thickness, δ, is a better vertical scale of the tracer particle vertical motion, providing vertical extension between $0.31 < z_p/\delta < 2.93$ for $Re_w = 5.9 \cdot 10^4$ and $6.5 \cdot 10^4$, and $0.96 < z_p/\delta < 8.82$ for $Re_w = 5.9 \cdot 10^5$ and $6.5 \cdot 10^5$.

The tracer particles displacement $\mathbf{r}_p = (x_p, z_p)$ and the path driven by the wave-induced instabilities are calculated by integrating:

$$\frac{dx_p}{dt} = u(x_p, z_p, t), \tag{6}$$

$$\frac{dz_p}{dt} = w(x_p, z_p, t), \tag{7}$$

obtaining

$$x_p = x_{p,0} + \int_{t_0}^{t} u(x_p, z_p, t)dt, \tag{8}$$

$$z_p = z_{p,0} + \int_{t_0}^{t} w(x_p, z_p, t)dt. \tag{9}$$

The RK2 scheme employs

$$\mathbf{r}_{p,n+1} = \mathbf{r}_{p,n} + \Delta t(b_1 k_1 + b_2 k_2), \tag{10}$$

$$k_1 = \mathbf{u}(\mathbf{r}_{p,n}, t_n), \tag{11}$$

$$k_2 = \mathbf{u}(\mathbf{r}_{p,n} + c_2 k_1, t_n + \Delta t\alpha), \tag{12}$$

where $c_2 = \alpha$, $b_1 = 1 - \frac{1}{2\alpha}$ and $b_2 = \frac{1}{2\alpha}$, and $b_1 + b_2 = 1$, $b_2 c_2 = 1/2$, and $b_2\alpha = 1/2$ (Sanderse and Veldman, 2019). The tracer particles paths are visualized both in a fixed frame of reference and a frame of reference following the wave.

3 RESULTS

3.1 Vortex formation

3.1.1 Simulation of the laboratory experiments by Carr et al. (2008)

In this section, a numerical simulation of the wave-induced instability is presented. We simulate one of the laboratory experiments by Carr et al. (2008), their experiment dated 080207, and directly compare our results. The parameters of the numerical simulation corresponding to the experiment are provided in table 1, denoted by Run 1. In the table, a/H is the non-dimensionalized amplitude and is similar in the computation and experiment ($a/H = 0.30$).

The created wave, numerically and physically, is strong enough to induce instability and vortices. Figure 2a shows the instability and vortex ejection from the boundary layer due to the wave illustrated in figure 1b. The horizontal axis is $(x - x_{trough})/H$, where x_{trough} denotes the position of the wave trough. The instability grows exponentially between $(x - x_{trough})/H = -1.7$ and -2.5, whereafter the vortices are formed. The series of vortex rolls in the instability growth area have a shorter separation length than the vortices found further downstream. The vortex formation goes on continuously, producing the vortex wake. Specifically, we compare to the experiment in which Carr et al. (2008) presented the vertical velocity corresponding to the vortices, their figure 13, reproduced here in figure 2c.

The separation distance λ_v between the vortices located in the vortex wake is set to be the center-to-center distance between the vortices. The computational result (figure 2b) shows five vortices, the same number as in the experiment for the similar horizontal extension (figure 2c). In the experiment, the separation distance between the vortices is between $0.069H$ and $0.122H$, with an average of $\lambda_v \sim 0.103H$. The similar average distance in the computation is $\lambda_v \sim 0.103H$, which is exactly the same result. The maximum vertical extent of the vortices was 8.7% of the water depth in the laboratory and 6.6% in the simulation. The results in figure 2 were simulated with $N = 12$ and $N_+ = 14$, see section 2.6.

3.1.2 Convergence of the separation distance, vorticity, amplitude and wave speed

We now discuss research question two of the introduction: how close are prediction and measurement?

Two different numerical representations are included in Basilisk, as described in section 2.6. Calculations using both representations are presented.

The resolution level is in the range of $N = 10 - 12$. When running with ”refine”, there is no additional refinement close to the bottom. The minimum and maximum refinement levels in ”adapt” are set to $N_{min} = N - 1$ and $N_{max} = N$.

Each simulation was performed ten times with the same settings and executed with and without parallelization. The average values and standard deviations of the variables: distance, vorticity, amplitude, and speed were calculated over the ten runs with the same settings. Hence, a total of 120 simulations were run.

The vortices measured in Carr et al. (2008) (figure 2c) exhibit an individual distance that slightly varies. Figure 3 illustrates the respective computational distance, calculated over the same area, further referred to as the local area, as a function of the resolution level N. The distance is further explored over a broader range in the wave tank where $-13.3 < (x - x_{trough})/H < -4.3$ (results are not shown). The simulations converge for increasing resolution level. A small anomaly for $N = 12$ ”adapt” in the result presented in figure 3 is observed. However, if we increase the respective local area three times, its average distance reduces from $0.134H$ to $0.108H$ (marked by a green circle in the figure). When simulating with the lowest resolution, the vortex formation formed is the main difference between ”refine” and ”adapt”. However, this discrepancy decreases with increasing resolution. For our purposes, the advantages of utilizing ”adapt” instead of ”refine” are minor.

An additional convergence check is conducted where the results are analyzed after a downscaling of the resolution in the post-processing procedure. Hence, the simulations are executed with ”refine” and $N = 11$ and 12. In the post-processing procedure, the simulations conducted with $N = 11$ are downscaled to level

$N = 10$, and the simulations performed with $N = 12$ are downscaled to level $N = 11$. The results are plotted in figures 3 and 4c with black $*$ and are marked with an asterisk in the figure legend.

The measured average amplitude a and wave speed c are visualized in figures 4a and 4b, respectively. The amplitude in the simulation is $\sim 3.3\%$ higher than the amplitude measured in the laboratory experiments by Carr et al. (2008). The average wave speed in the computations converges to 0.262 ms^{-1}, corresponding to the upper limit of the wave speed measured in the laboratory of 0.242 ± 0.022 ms^{-1}.

The vorticity in the numerical simulations is obtained by evaluating the circulation integral in each grid cell, divided by the area A enclosed by the integration contour obtaining $\omega(x, z) = \left[\oint(u, w) \cdot d\mathbf{l}\right]/A$. Here $d\mathbf{l}$ is the vector length along the side of the grid cell. An average of the non-dimensional maximum vorticity $\omega^* = \overline{\omega}_{max}/(c_0/H)$ is calculated over the vortices located in the local area and in the global area $-13.3 < (x - x_{trough})/H < -4.3$. The results of averaging over the broader range are illustrated in figure 4c. The respective standard deviation of ω^* is found to be 1% ($N = 10, 11$), "refine" and adapt", 2% ($N = 12$), "refine", and 3% ($N = 12$), "adapt".

3.1.3 Proximity between prediction and measurement

The comparison between the computations and the laboratory experiments by Carr et al. (2008), presented in § 3.1.1, is also included in figure 3. The simulation conducted with $N = 12, N_+ = 14$ is marked in the figure by 14_+.

This subsection illustrates that the model very well reproduces the laboratory experiment in the 3D wave tank by Carr et al. (2008). The predictions and measurements are very close. Moreover, the 2D laminar calculations illustrate that the dominant processes in the laboratory experiments are dominated by 2D processes. The processes investigated by Carr et al. (2008) are indeed dominated by two-dimensionality. This correspondence lasts up to a distance of eight water depths behind the wave trough.

The computations in this section illustrate the convergence of the method where the vorticity and the distance between the vortices are evaluated. The computed and measured averaged separation distance at 7.8 ± 0.2 water depths behind the trough correspond. The vorticity strength is computed, where this motion property was not measured in the laboratory. The calculated amplitude and wave speed were both converged. These findings respond to research points $1 - 3$ of the introduction.

3.2 Tracer particles

3.2.1 Trajectories

As seen in section 3.1.1, the wave-induced velocity field interacts with the bottom, and vortices are being ejected from the bottom boundary layer (BBL). In this section we explore how the wave-induced velocity field moves a cloud of tracer particles, initially found in the BBL, upstream of the ISW. The tracer particles are located approximately between $x/H = 6.4$ and 8.4 before time zero, and the simulations are conducted with wave Reynolds number in the range $Re_w \sim 5.9 \cdot 10^4 - 6.5 \cdot 10^5$ (table 1).

In our numerical simulations, we can only generate one wave and not a train of waves as may be observed in the coastal ocean (e.g., Quaresma et al., 2007; Zulberti et al., 2020). We let the wave intercept the tracer particle cloud twice, first during the propagation along the undisturbed fluid and second as a reflected wave from the right end of the tank. When the wave becomes a reflected wave, the horizontal velocity changes the sign, while the vertical velocity maintains the sign. During wave passage one, the time runs from 0 to $tc_0/H \simeq 19.6$ and 21.0 for Strat.1 and Strat.2, respectively, and is defined as the transit until the wave encounters the right end wall. Then the wave passage two stage starts and endures until $tc_0/H \simeq 40.7$ and 44.7 for Strat.1 and Strat.2, respectively.

The wave propagating from left to right induces a velocity of the lower fluid layer in the opposite direction of the wave propagation, pushing the fluid backward. The vertical velocity in the forward part of the wave is also negative, pushing the fluid downward. When the wave encounters the cloud of tracer particles, the tracer particles are first driven backward, approximately a horizontal distance of $1H$ for Strat. 1 (visualized in figures 5 and 6) and $1.5H$ for Strat. 2 (results are not shown). The figures display the traces of 12 random tracer particles out of the $25\,600$ tracer particles implemented. The colors are constant according to the vertical position of tracer particles before time zero.

The trajectory of the tracer particles has the same shape as the wave displacement before the vortices intercept the tracer particles' movement. The tracer particles are then displaced vertically. The vortices intercept the cloud of the leftmost tracer particles when the wave trough is at approximately $x_{trough}/H \simeq 7.7$ when $Re_w = 5.9 \cdot 10^4$, see figures 5a and 5b. The integration illustrates how the displacements and paths depend on the location of the tracer particle before time zero.

Figures 5b and 5d illustrate the trajectories in a reference frame that follows the wave. The time period illustrated lies between $ct/H = -10$ to -69. In the figures, the black vertical line indicates when the wave trough is at $x_{trough}/H = 7.6$. The solid red line is a time $tc_0/H = 6.4$ later and shows the position x_{trough}/H at this time. The dashed red line indicates x_{trough}/H when the wave begins its encounter with the wall.

The trajectories at the beginning are almost horizontal, with some small fluctuations. The vortices behind the trough intercept the tracer particles, where the tracers acquire an oscillatory behavior of a range of wavelengths. They are in the range from $0.3H$ (Run 4) up to $16H$ (Run 1). The shortest wavelengths are in the same order of magnitude as the separation distance of the vortices generated behind the trough when the instability saturates. Run 4 exhibits very short wavelengths and a wavelength of $10H$.

The wave propagates to the end of the tank and returns. The wave intercepts again with the group of tracer particles, visualized in figures 5 and 6, plots c and d. During the second passage, the tracer particles are moved further upward. The vertical position, relative to the boundary layer δ, depends on the Reynolds number. In figure 6c, the uppermost position after wave passage one is $z/\delta \simeq 13$ and $z/\delta \simeq 55$ after wave passage two.

Figures 7 and 8 show paths due to 128 tracer particles. Plots a and c display that the downstream vortices transport the tracer particles upwards and out of the boundary layer. In plots b and d, the second wave encounter and its induced instabilities move the tracer particles even higher.

3.2.2 Displacements

The terminal position of a number of $25\,600$ particles are then discussed (figure 9). The 50th (median) and 90th percentile of the vertical tracer particle position are evaluated. For the 90th percentile, the vertical height increases by a factor of three between passage one and passage two. The vertical displacement of the 50th percentile is similar, although there are some large variations at the moderate Re_w (table 2). For the same percentile, the height relative to δ increases by a factor of 2.4, approximately, when the wave Reynolds number increases by a factor of 10. The horizontal position of the tracer particle cloud is negative during the first passage and positive during the second passage due to the reflected wave. The net horizontal displacement of the tracer particle cloud is approximately zero. The red lines in the figure indicate the tracer particles' left and right most horizontal seeded position before time zero.

The probability density function (PDF) of the tracer particles' vertical position as a function of time is illustrated in figure 10. The black line indicates the initial uppermost vertical position of the tracer particles. The blue line indicates the tracer particle distribution after wave passage one. The red line provides the tracer particle distribution when the wave has intercepted the cloud of tracer particles for the second time. After passage one, tracer particle distribution is below 20δ, and after passage two, below 65δ for the large $Re_w \sim 5.9 - 6.5 \cdot 10^5$. The similar numbers for the smaller $Re_w \sim 5.9 - 6.5 \cdot 10^4$ are 10δ and 25δ, respectively.

The results imply that the particles are found below a vertical level of approximately $0.23H$ after the second passage for both Reynolds numbers.

3.3 Comparison to field measurements

Quaresma et al. (2007) conducted a field study of internal waves propagating over the northern shelf of Portugal over a canyon head. The local water depth was measured to be ~ 80 m with a middle depth of the pycnocline of $d/H = 0.19$. The wave amplitudes were in the range $a/H = 0.13 - 0.38$. The measured local sediment concentration mainly consists of sandy sediments ($\sim 93\%$) of a settling velocity of 2 cms^{-1}. The remaining sediments, silt and clay components with diameters in the range $\sim 1 - 20$ μm were found to remain suspended. Their measurements showed that only the strongest waves were capable of suspending the sediments, contributing to a summer bottom nepheloid layer (BNL) of $10 - 15$ m thickness, corresponding to $0.13 - 0.19H$.

We note that the vertical height of the tracer particles after wave passage two was found to be approximately $0.23H$ in our numerical computations and was insensitive to the Re_w. This tracer particle height is in correspondence with the height of the BNL measured by Quaresma et al. (2007).

Quaresma et al. (2007) also measured a strong local sediment concentration up to a height of $0.56H$ below the leading wave. Our present computation does not exhibit such an effect.

Zulberti et al. (2020) conducted field observations of nonlinear internal waves over a low-gradient topography on Australia's Northwest Shelf. They observed that large-amplitude internal waves of depression greatly enhanced the sediment transport. From sediment grab samples, they deduced that the bed sediment was of typical silt. The settling velocity of silt particles of density $\rho_s = 1350$ kgm^{-3} and diameter of 30 μm, may be calculated to be $U = 0.014$ cms^{-1}. They measured sediment resuspension to exceed 20 m ($0.08H$) beneath the leading wave of amplitude $a/H = 0.3$. However, they measured a density gradient at this level, limiting the advancement of bottom sediments. A direct correspondence between the measurements and the present computations are not realistic because we have not included a weak stratification layer at the bottom. One of the factors driving the resuspension mechanism in the measurement of Zulberti et al. (2020), was a vertical pumping mechanism associated with the compression underneath the wave trough followed by a subsequent expansion of the mixing-layer at the bottom. This effect is included in our simulations, however.

Finally, the subjects discussed in these result sections 3.2 and 3.3 include the tracer particles, the vertical tracer particle displacement during the wave encounters, as well as comparison to observations in the field, and response to the research subject 4, 5, and 6 as presented in the introduction.

4 CONCLUSIONS

By a 2D laminar method, the vortex formation and the tracer particle motion in the bottom boundary layer of the water column of a fluid layer, driven by large internal solitary waves of depression, are calculated. The motion in a numerical wave tank for internal waves is simulated. Comparison is made to a set of available laboratory observations, and a very good match between the model and the laboratory measurements is found. Convergence of the numerical calculation of the vortex formation is documented.

A cloud of tracer particles in the bottom boundary layer obtains vertical displacements because of the wave-driven vortices. The paths exhibit the following properties: when the wave approaches the tracer particle cloud, the tracer particles are first moved horizontally in the opposite direction of the wave. Behind the wave trough, the tracer particles are transported vertically in the water column. The wave is reflected and returns to the tracer particle cloud. At the second passage, the tracer particles are moved in the opposite direction of the wave propagation. The vortices behind the trough transport the tracer particles further vertically. The tracer particles are found below a vertical level of approximately $0.23H$ after the second passage, for the Reynolds number in the range $Re_w \sim 5.9 \cdot 10^4 - 6.5 \cdot 10^5$. The net horizontal transport of the tracer particle cloud is approximately zero.

We have compared the results to available field observations by Quaresma et al. (2007), obtained at the northern shelf of Portugal, where the local depth was 80 m. The wave amplitude was in the range $a/H = 0.13 - 0.38$, and a summer bottom nepheloid layer was measured to be $10 - 15$ m, corresponding to $0.13 - 0.19H$. Our computational results are in a fair match with that observation. We note that the processes in the computations at the moderate scale and the processes at the field scale may not be directly similar, however. In another field measurement by Zulberti et al. (2020), large amplitude internal waves of depression were found to resuspend the sediments at the sea bed greatly. In their measurements, a density gradient at 20 m ($0.08H$) above the sea bottom was found to limit the vertical advancement of the bottom sediments. Direct correspondence to the present computations is not realistic.

CONFLICT OF INTEREST STATEMENT

The authors declare that the research was conducted in the absence of any commercial or financial relationships that could be construed as a potential conflict of interest.

FUNDING

The funding by the Research Council of Norway (Ecopulse, NFR300329) is gratefully acknowledged.

ACKNOWLEDGMENTS

The discussions with Dr. Johannes Röhrs are acknowledged. The computations were performed on the Norwegian Research and Education Cloud (NREC), using resources provided by the University of Bergen and the University of Oslo. http://www.nrec.no/. The authors would like to acknowledge the referees for helpful comments.

AUTHOR CONTRIBUTIONS

TE, JG, and JS contributed to the conception and methodology of the study. TE and JS wrote the code. TE performed the processing of the data. Visualization by TE and JG. TE wrote the first draft of the manuscript.

TE and JG wrote the submitted manuscript. All authors contributed to the manuscript revision, read, and approved the submitted version.

DATA AVAILABILITY STATEMENT

The raw data supporting the conclusions of this article will be made available by the authors, without undue reservation.

REFERENCES

Aghsaee, P., Boegman, L., Diamessis, P. J., and Lamb, K. G. (2012). Boundary-layer-separation-driven vortex shedding beneath internal solitary waves of depression. *J. Fluid Mech.* 690, 321–344. doi:10.1017/jfm.2011.432

Bell, J. B., Colella, P., and Glaz, M. G. (1989). A second-order projection method for the incompressible Navier-Stokes equations. *J. Comp. Phys.* 85, 257–283. doi:10.1016/0021-9991(89)90151-4

Boegman, L. and Stastna, M. (2019). Sediment Resuspension and Transport by Internal Solitary Waves. *Annu. Rev. Fluid Mech.* 51, 129–154. doi:10.1146/annurev-fluid-122316-045049

Bogucki, D., Dickey, T., and Redekopp, L. G. (1997). Sediment Resuspension and Mixing by Resonantly Generated Internal Solitary Waves. *J. Phys. Oceanogr.* 27, 1181 –1196. doi:10.1175/1520-0485(1997)027⟨1181:SRAMBR⟩2.0.CO;2

Bogucki, D. J. and Redekopp, L. G. (1999). A mechanism for sediment resuspension by internal solitary waves. *Geophys. Res. Lett.* 26, 1317–1320. doi:10.1029/1999GL900234

Bourgault, D., Blokhina, M. D., Mirshak, R., and Kelley, D. E. (2007). Evolution of a shoaling internal solitary wave train. *Geophys. Res. Lett.* 34, L03601–1–5. doi:10.1029/2006GL028462

Carr, M. and Davies, P. A. (2006). The motion of an internal solitary wave of depression over a fixed bottom boundary in a shallow, two-layer fluid. *Phys. Fluids* 18, 016601. doi:10.1063/1.2162033

Carr, M., Davies, P. A., and Shivaram, P. (2008). Experimental evidence of internal solitary wave-induced global instability in shallow water benthic boundary layers. *Phys. Fluids* 20, 066603. doi:10.1063/1.2931693

Carr, M., Stastna, M., Davies, P. A., and van de Wal, K. J. (2019). Shoaling mode-2 internal solitary-like waves. *Journal of Fluid Mechanics* 879, 604–632. doi:10.1017/jfm.2019.671

Chorin, A. (1968). Numerical solution of the Navier-Stokes equations. *Math. Comp.* 22, 745–762

Diamessis, P. J. and Redekopp, L. G. (2006). Numerical Investigation of Solitary Internal Wave-Induced Global Instability in Shallow Water Benthic Boundary Layers. *J. Phys. Oceanogr.* 36, 784–812. doi:10.1175/JPO2900.1

Fructus, D., Carr, M., Grue, J., Jensen, A., and Davies, P. A. (2009). Shear-induced breaking of large internal solitary waves. *J. Fluid Mech.* 620, 1–29. doi:10.1017/S0022112008004898

Fructus, D. and Grue, J. (2004). Fully nonlinear solitary waves in a layered stratified fluid. *Journal of Fluid Mechanics* 505, 323—-347. doi:10.1017/S0022112004008596

Grue, J., Jensen, A., Rusås, P.-O., and Sveen, J. K. (1999). Properties of large-amplitude internal waves. *J. Fluid Mech.* 380, 257–278. doi:10.1017/S0022112098003528

Helfrich, K. R. and Melville, W. K. (2006). Long nonlinear internal waves. *Annu. Rev. Fluid Mech.* 38, 395–425. doi:10.1146/annurev.fluid.38.050304.092129

Lamb, K. G. (2014). Internal Wave Breaking and Dissipation Mechanisms on the Continental Slope/Shelf. *Annu. Rev. Fluid Mech.* 46, 231–254. doi:10.1146/annurev-fluid-011212-140701

López-Herrera, J. M., Popinet, S., and Castrejón-Pita, A. A. (2019). An adaptive solver for viscoelastic incompressible two-phase problems applied to the study of the splashing of weakly viscoelastic droplets. *J. Non-Newtonian Fluid Mech.* 264, 144–158. doi:10.1016/j.jnnfm.2018.10.012

Mostert, W. and Deike, L. (2020). Inertial energy dissipation in shallow-water breaking waves. *Journal of Fluid Mechanics* 890, A12. doi:10.1017/jfm.2020.83

Necker, F., Härtel, C., Kleiser, L., and Meiburg, E. (2005). Mixing and dissipation in particle-driven gravity currents. *Journal of Fluid Mechanics* 545, 339–372. doi:10.1017/S0022112005006932

Popinet, S. (2003). Gerris: a tree-based adaptive solver for the incompressible Euler equations in complex geometries. *J. Comp. Phys.* 190, 572–600. doi:10.1016/S0021-9991(03)00298-5

Popinet, S. (2009). An accurate adaptive solver for surface-tension-driven interfacial flows. *J. Comp. Phys.* 228, 5838–5866. doi:10.1016/j.jcp.2009.04.042

Popinet, S. (2011). Quadtree-adaptive tsunami modelling. *Ocean Dyn.* 61, 1261–1285. doi:10.1007/s10236-011-0438-z

Popinet, S. (2015). A quadtree-adaptive multigrid solver for the Serre-Green-Naghdi equations. *J. Comp. Phys.* 302, 336–358. doi:10.1016/j.jcp.2015.09.009

Popinet, S. (2020). A vertically-Lagrangian, non-hydrostatic, multilayer model for multiscale free-surface flows. *J. Comp. Phys.* 418, 109609. doi:10.1016/j.jcp.2020.109609

Popinet, S. and collaborators (2013–2023). Basilisk. http://basilisk.fr [Accessed: 18.10.2021]

Quaresma, L. S., Vitorino, J., Oliveira, A., and da Silva, J. (2007). Evidence of sediment resuspension by nonlinear internal waves on the western Portuguese mid-shelf. *Mar. Geol.* 246, 123–143. doi:10.1016/j.margeo.2007.04.019

Sakai, T., Diamessis, P. J., and Jacobs, G. B. (2020). Self-sustained instability, transition, and turbulence induced by a long separation bubble in the footprint of an internal solitary wave. I. Flow topology. *Phys. Rev. Fluids* 5, 103801. doi:10.1103/PhysRevFluids.5.103801

Sanderse, B. and Veldman, A. (2019). Constraint-consistent Runge–Kutta methods for one-dimensional incompressible multiphase flow. *Journal of Computational Physics* 384, 170–199. doi:https://doi.org/10.1016/j.jcp.2019.02.001

Stastna, M. and Lamb, K. G. (2008). Sediment resuspension mechanisms associated with internal waves in coastal waters. *J. Geophys. Res.* 113, C10016–1–19. doi:10.1029/2007JC004711

Sveen, J. K., Guo, Y., Davies, P. A., and Grue, J. (2002). On the breaking of internal solitary waves at a ridge. *J. Fluid Mech.* 469, 161–188. doi:10.1017/S0022112002001556

van Hooft, J. A., Popinet, S., van Heerwaarden, C. C., van der Linden, S. J. A., de Roode, S. R., and van de Wiel, B. J. H. (2018). Towards Adaptive Grids for Atmospheric Boundary-Layer Simulations. *Boundary-Layer Meteorol.* 167, 421–443. doi:10.1007/s10546-018-0335-9

Zulberti, A., Jones, N. L., and Ivey, G. N. (2020). Observations of enhanced sediment transport by nonlinear internal waves. *Geophys. Res. Lett.* 47, 1–11. doi:10.1029/2020GL088499

FIGURE CAPTIONS

APPENDIX A: FINITE VOLUME SOLVER

A.1 Time integration

The discretization in time is staggered and second-order accurate. The advection term is calculated using the Bell-Colella-Glaz scheme (Bell et al., 1989). The unsplit, upwind scheme reads:

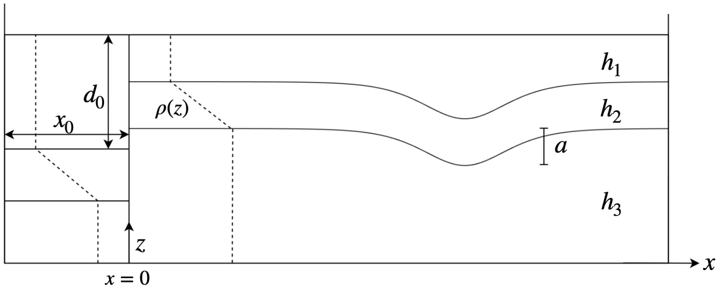

Figure 1a.

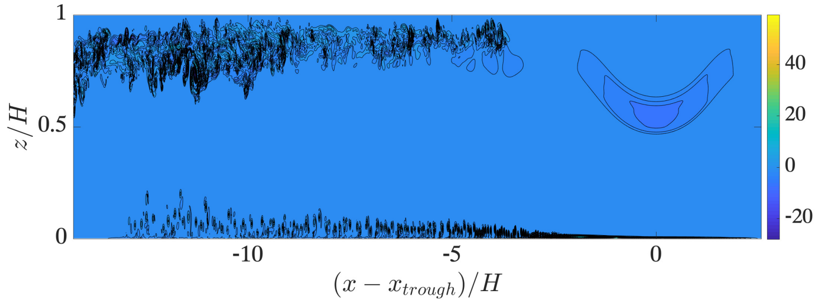

Figure 1b.

Figure 1. **(A)** Sketch of the wave tank. **(B)** Vorticity field $\omega/(c_0/H)$ (color scale, black contour lines of ω) due to ISW travelling to the right at $tc_0/H = 6.4$ with $a/H = 0.30$ and $Re_w = 5.9 \cdot 10^4$.

$$\rho_{n+\frac{1}{2}}\left[\frac{\mathbf{u}_{n+1}-\mathbf{u}_n}{\Delta t}+\mathbf{u}_{n+\frac{1}{2}}\cdot\nabla\mathbf{u}_{n+\frac{1}{2}}\right]=-\nabla p_{n+\frac{1}{2}}+\nabla\cdot\left[\mu_{n+\frac{1}{2}}(\mathbb{D}_n+\mathbb{D}_{n+1})\right]+\rho_{n+\frac{1}{2}}\mathbf{a}_{n+\frac{1}{2}}, \tag{13}$$

$$\frac{f_{n+\frac{1}{2}}-f_{n-\frac{1}{2}}}{\Delta t}+\nabla\cdot(f_n\mathbf{u}_n)=0, \tag{14}$$

$$\nabla\cdot\mathbf{u}_n=0, \tag{15}$$

where $\mathbb{D} = (\nabla\mathbf{u} + (\nabla\mathbf{u})^T)/2$ is the strain rate tensor, where $()^T$ denotes transpose. The index n indicates time t_n, and likewise for $n+1$, $n+\frac{1}{2}$, $n-1$, etc.

An equivalent advection equation of the volume fraction replaces the advection equation of the density. The density and viscosity are defined using the averages $\rho(\tilde{f}) = \tilde{f}(\rho_1 - \rho_2) + \rho_2$ and $\mu(\tilde{f}) = [\tilde{f}(1/\mu_1 - 1/\mu_2) + 1/\mu_2]^{-1}$, where ρ_1, μ_1, and ρ_2, μ_2 are the densities and dynamic viscosities of the upper and lower fluid layers, respectively. The field $\tilde{f}$ is constructed by applying a smoothing spatial filter to f. This is accomplished by averaging the four corner values of f obtained from the cell-centered values by bilinear interpolation. The fluid properties are updated by:

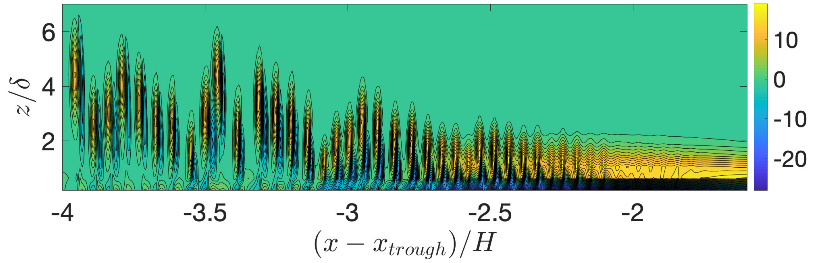

Figure 2a.

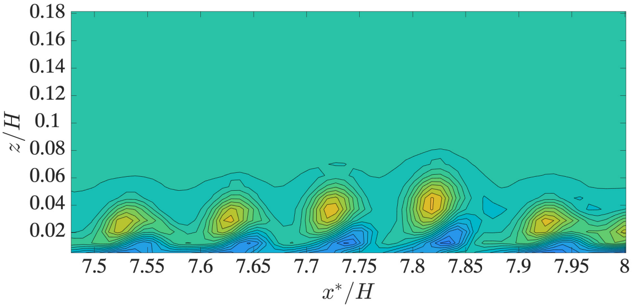

Figure 2b.

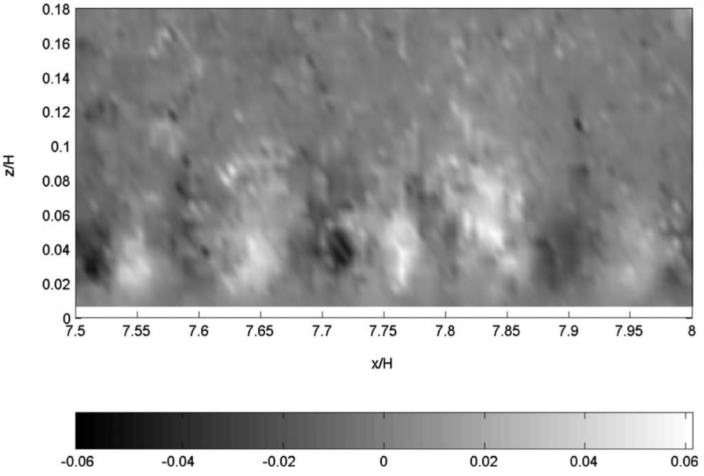

Figure 2c.

Figure 2. **(A)** Vorticity field $\omega/(c_0/H)$ (color scale, black contour lines of ω) vs. horizontal position. **(B)** $\omega/(c_0/H)$ with horizontal position $x^*/H = ct/H + constant$ corresponding to the measurement area in c). **(C)** Image adapted from (Carr et al., 2008). Vortices displayed by their vertical velocity at time $tc_0/H = 6.4$.

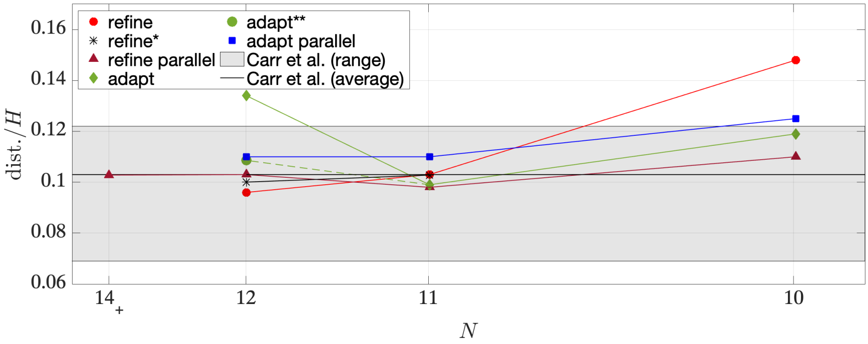

Figure 3. Vortex separation distance (dist.) over the local area versus the resolution level N. The result from the simulation with $N = 12, N_+ = 14$ is marked by $N = 14_+$. The black line corresponds to the experimental average local distance. The grey-shaded area corresponds to the measured individual separation distance in figure 2c. Simulations without parallelization: refine ○, refine* $*$, adapt ◊ and adapt** ○.Simulations with parallelization: refine △ and adapt □.

$$\rho_{n+\frac{1}{2}} = \tilde{f}_{n+\frac{1}{2}}(\rho_1 - \rho_2) + \rho_2, \tag{16}$$

$$\mu_{n+\frac{1}{2}} = [\tilde{f}_{n+\frac{1}{2}}(1/\mu_1 - 1/\mu_2) + 1/\mu_2]^{-1}. \tag{17}$$

By using a classical time-splitting projection method (Chorin, 1968), the system is further simplified:

$$\rho_{n+\frac{1}{2}} \left[\frac{\mathbf{u}_* - \mathbf{u}_n}{\Delta t} + \mathbf{u}_{n+\frac{1}{2}} \cdot \nabla \mathbf{u}_{n+\frac{1}{2}} \right] = \nabla \cdot \left[\mu_{n+\frac{1}{2}} (\mathbb{D}_n + \mathbb{D}_*) \right] + \rho_{n+\frac{1}{2}} \mathbf{a}_{n+\frac{1}{2}}, \tag{18}$$

$$\frac{f_{n+\frac{1}{2}} - f_{n-\frac{1}{2}}}{\Delta t} + \nabla \cdot (f_n \mathbf{u}_n) = 0. \tag{19}$$

The velocity at the new time is found by combining equations (13) and (18). Hence,

$$\mathbf{u}_{n+1} = \mathbf{u}_* - \frac{\Delta t \nabla p_{n+\frac{1}{2}}}{\rho_{n+\frac{1}{2}}}. \tag{20}$$

The equation for the pressure is found by requiring

$$\nabla \cdot \mathbf{u}_{n+1} = 0. \tag{21}$$

This leads to a Poisson equation for the pressure

$$\nabla \cdot \left[\frac{\Delta t \nabla p_{n+\frac{1}{2}}}{\rho_{n+\frac{1}{2}}} \right] = \nabla \cdot \mathbf{u}_*. \tag{22}$$

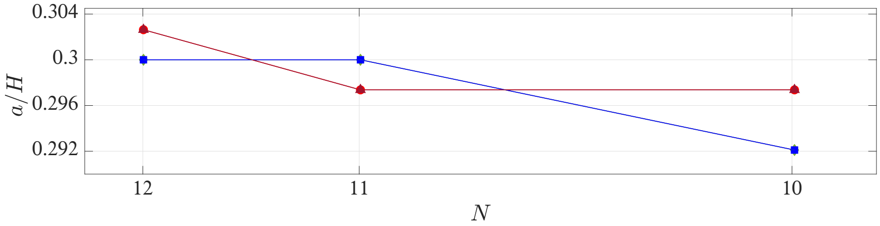

Figure 4a.

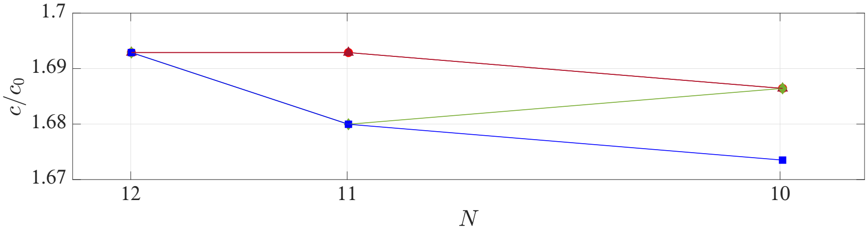

Figure 4b.

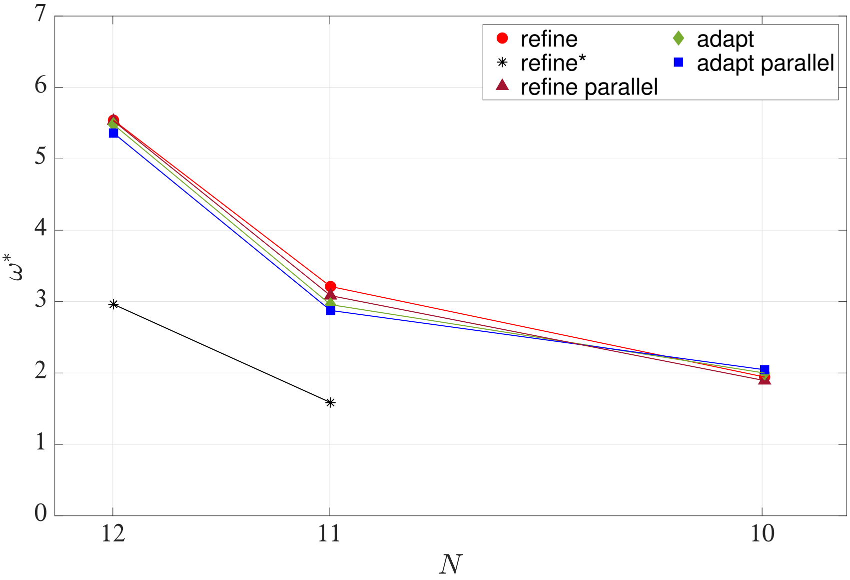

Figure 4c.

Figure 4. **(A)** Wave amplitude a/H, **(B)** speed c/c_0 and **(C)** maximum vorticity $\omega^* = \tilde{\omega}_{max}/(c_0/H))$ versus resolution level N. Simulations without parallelization: refine ○, refine* $*$, and adapt ◇. Simulations with parallelization: refine △ and adapt □.

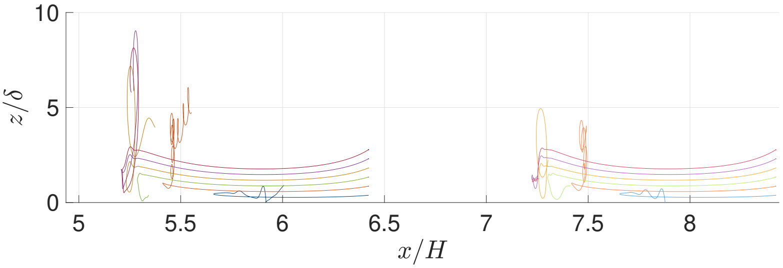

Figure 5a.

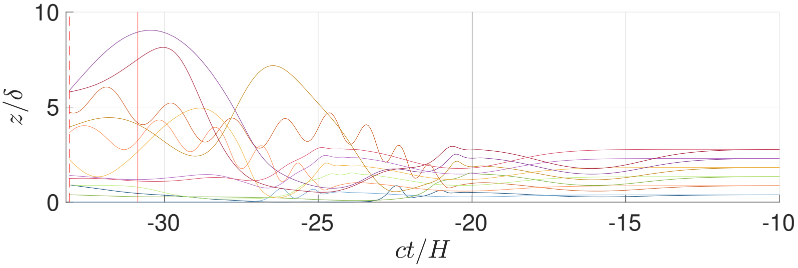

Figure 5b.

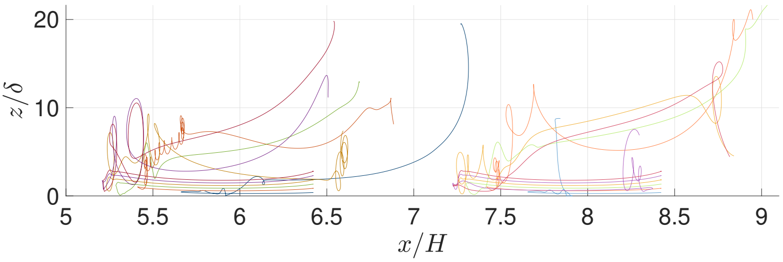

Figure 5c.

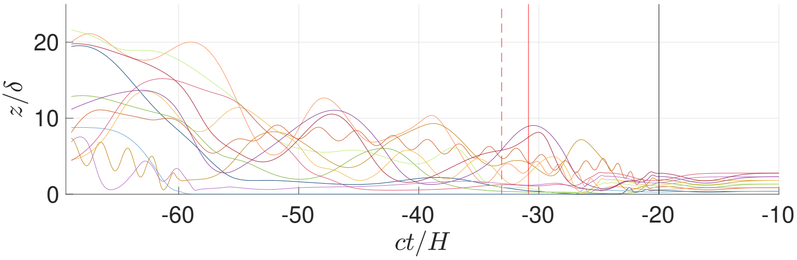

Figure 5d.

Figure 5. Tracer particle trajectories for $Re_w = 5.9 \cdot 10^4$. **(A)** and **(C)** Fixed frame of reference. **(B)** and **(D)** Frame of reference following the wave. In **(A)**-**(B)** wave passage one, $tc_0/H = 0 - 19.6$. In **(C)**-**(D)** wave passage two, $tc_0/H = 0 - 40.7$.

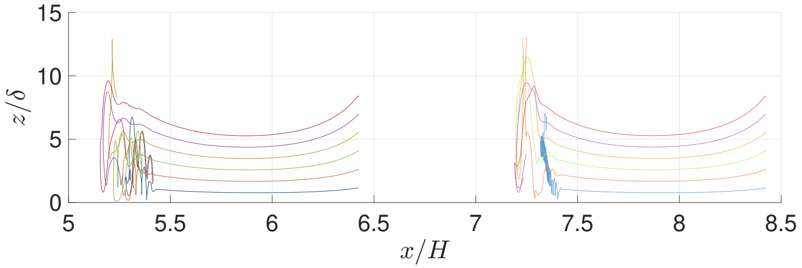

Figure 6a.

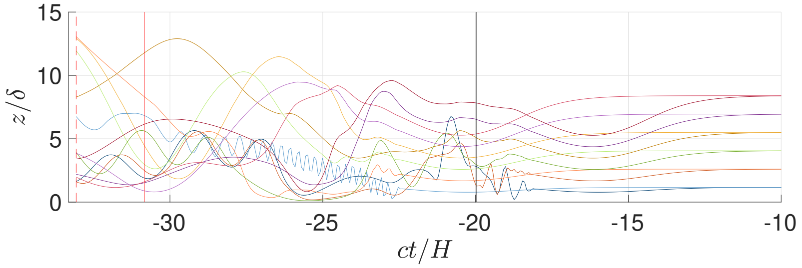

Figure 6b.

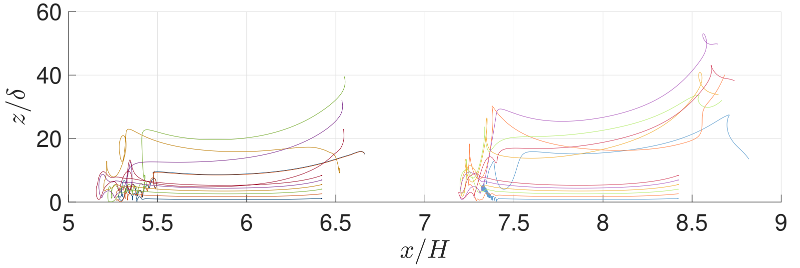

Figure 6c.

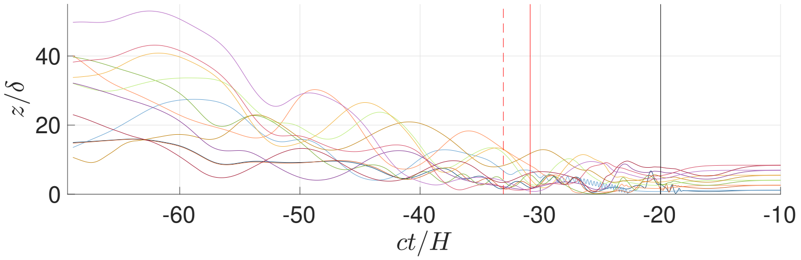

Figure 6d.

Figure 6. Same as figure 5 but with $Re_w = 5.9 \cdot 10^5$.

The time step in each iteration is controlled by the Courant-Friedrich-Levy (CFL) condition.

A.2 Spatial discretization

The quadtree structure can be seen as a family tree. An important parameter is the level N of a given cell of the tree. The *root* cell is that corresponding to $N = 0$, from which the cells at the next level hang down. A *parent* cell (at level N) can have zero or four *children* cells, where the children are at level $N + 1$. If the cell has no *children* it is called a *leaf* cell. The size of a cell is characterized by its level N, where it is located. Hence, the grid size of the cells at that level is $\Delta_N = L/2^N$. The cells are square finite volume cells, providing $\Delta_N = \Delta x = \Delta z$, where (x, z) are the horizontal and vertical coordinates.

Further, a few restrictions apply. For example, the maximum difference of the level between two neighbouring *leaf* cells is one; each cell has a direct neighbour at the same level; the level increases by one for each successive generation; the grid can be refined and coarsened dynamically (adapted) as the simulation proceeds, where this occurs at an affordable computational cost. We have used two central representations of the numerical grid, a non-adaptive (static grid) mesh and an adaptive mesh.

1. "Refine":

Refine (static grid refinement) is referred to when the simulation is run with the same level of refinement in the mesh hierarchy.

2. "Adapt":

The adaptive mesh hierarchy enables increase/decrease of the grid resolution where necessary. Such an approach can significantly reduce the memory required to obtain a given level of accuracy. The algorithm is based on the estimation of the numerical errors in the representation of the spatially discretized fields. This analysis is used to determine which grid cells require refinement, and wherein the domain cells can be coarsened. Following van Hooft et al. (2018) and López-Herrera et al. (2019), a scalar field g_N discretized at grid level N, can be coarsened one level down utilizing a downsampling operation denoted by $restriction$, $g_{N-1} = restriction(g_N)$. Next, the upsampled (or prolongated) operator, which upsamples the coarser field distribution, g_{N-1}, to the original level, $g_N^0 = prolongation(g_{N-1})$, is defined. The prolongation procedure is second-order accurate. Noting that in general $g_N \neq g_N^0$, a comparison provides an estimation of the absolute discretization error, $\zeta_N = |g_N - g_N^0|$. A particular cell i with level N in which the error is ζ_N^i, will be,

- refined if $\zeta_N^i > \zeta$,
- coarsened if $\zeta_N^i < 2\zeta/3$,
- remain unchanged otherwise,

where ζ is called the refinement criterion and is the error threshold set in the numerical scheme. The "refine" and "adapt" procedures are used in the present study. Further details of the algorithm can be found in Popinet (2003) and van Hooft et al. (2018).

Near the resolution boundaries, ghost cells are generated as virtual cells. This allows for simple Cartesian stencil operations, for the typically uneven grid at the boundary. The ghost cells have neighbours with the same refinement level N, whereas their values are defined by interpolating the original field values.

Table 1. Layer depths, stratification (Strat.), calculated amplitude a, numerical values for $U_{\infty,0}/c_0$, δ, Re_δ, Re_w, and x_p/H. Resolution $N = 12, N_+ = 14$ for Run 1 and 3, and $N = 11, N_+ = 16$ for Run 2 and 4.

Run	$h_3/h_2/h_1$ (m)	Strat.	a/H	$U_{\infty,0}/c_0$	$\delta \cdot 10^{-3}$ (m)	Re_δ	Re_w	x_p/H
1	$0.293/0.052/0.035$	1	0.300	0.863	3.68	490	$5.9 \cdot 10^4$	7.42
3	$0.280/0.047/0.055$	2	0.300	0.833	4.44	631	$6.5 \cdot 10^4$	7.43
2	$0.293/0.052/0.035$	1	0.297	0.858	1.22	1620	$5.9 \cdot 10^5$	7.42
4	$0.280/0.047/0.055$	2	0.301	0.835	1.46	2080	$6.5 \cdot 10^5$	7.43

Table 2. The vertical location z/δ corresponding to the 50th and 90th percentiles of the tracer particle density field for wave passage one and two. Boundary layer thickness, Re_δ, Re_w. Runs $1 - 4$.

	Passage one		Passage two				
Run	50%	90%	50%	90%	$\delta \cdot 10^{-3}$ (m)	Re_δ	Re_w
1	4.5	8.3	7.1	15.6	3.68	490	$5.9 \cdot 10^4$
3	1.4	4.7	9.2	20.4	4.44	631	$6.5 \cdot 10^4$
2	7.4	15.1	23.0	42.0	1.22	1620	$5.9 \cdot 10^5$
4	8.9	16.2	23.5	46.4	1.46	2080	$6.5 \cdot 10^5$

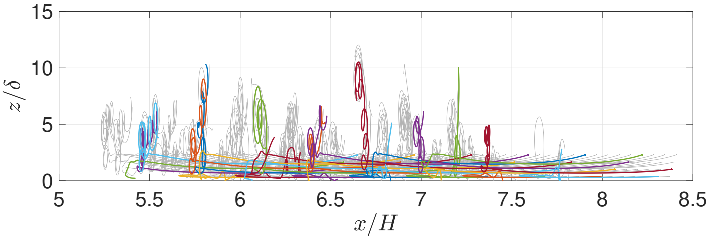

Figure 7a.

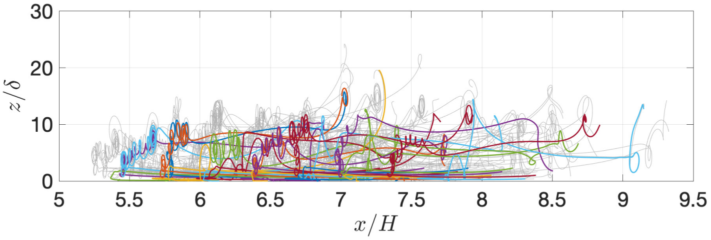

Figure 7b.

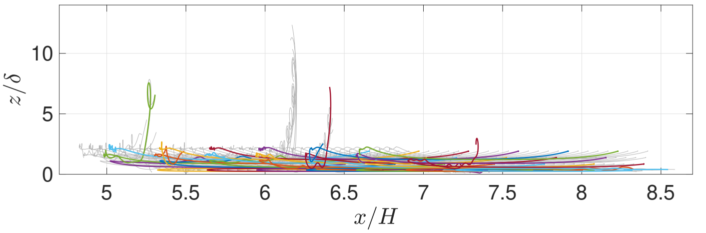

Figure 7c.

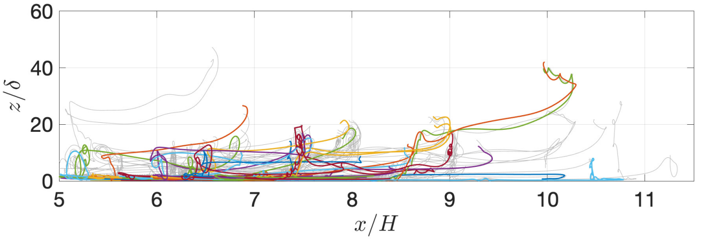

Figure 7d.

Figure 7. Tracer particle trajectories of 128 particles. **(A)** $Re_w = 5.9 \cdot 10^4$. Wave passage one, $tc_0/H = 0 - 19.6$. **(B)** $Re_w = 5.9 \cdot 10^4$. Wave passage two, $tc_0/H = 0 - 40.7$. **(C)** $Re_w = 6.5 \cdot 10^4$. Wave passage one, $tc_0/H = 0 - 21.0$. **(D)** $Re_w = 6.5 \cdot 10^4$. Wave passage two, $tc_0/H = 0 - 44.7$.

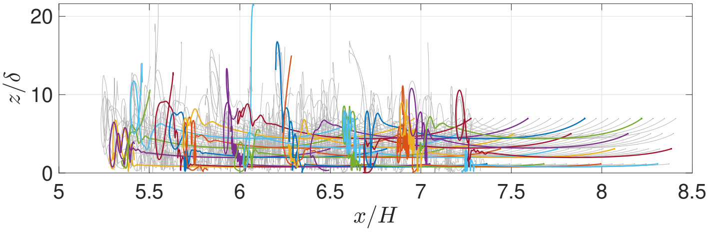

Figure 8a.

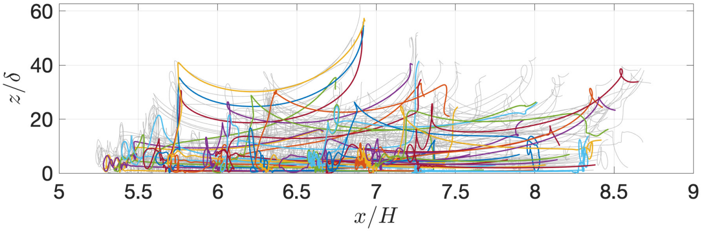

Figure 8b.

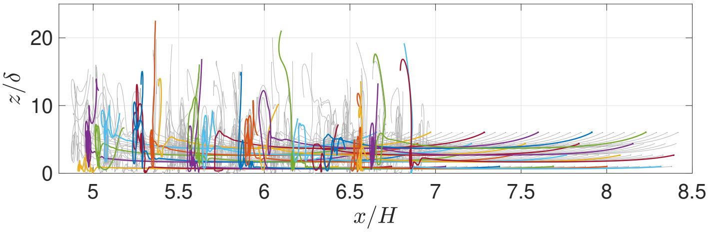

Figure 8c.

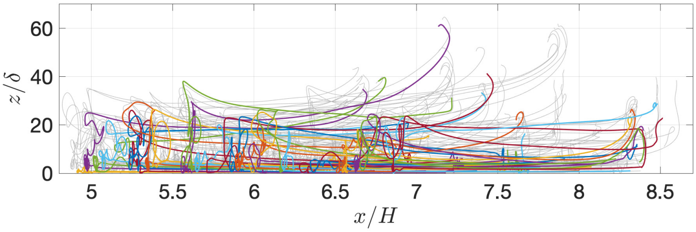

Figure 8d.

Figure 8. Same as figure 7 but with **(A)** and **(B)** $Re_w = 5.9 \cdot 10^5$. **(C)** and **(D)** $Re_w = 6.5 \cdot 10^5$.

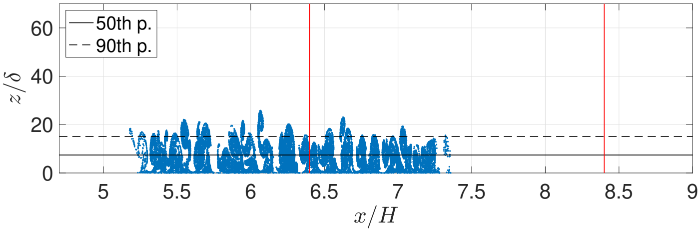

Figure 9a.

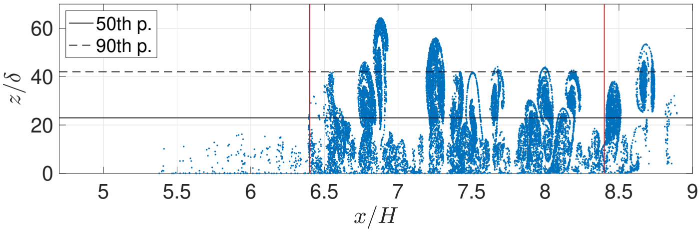

Figure 9b.

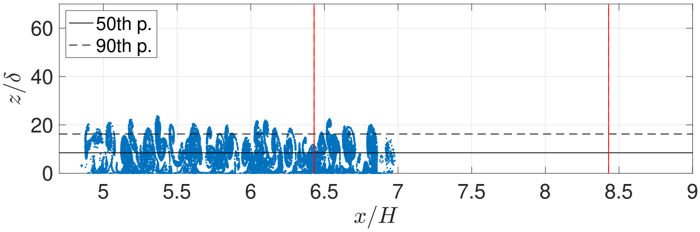

Figure 9c.

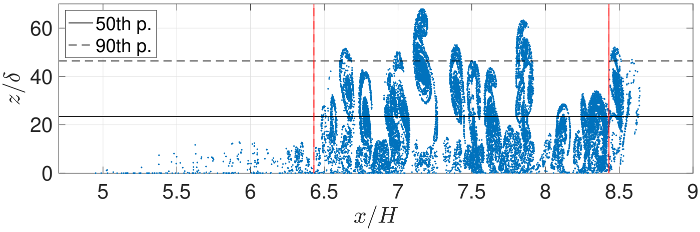

Figure 9d.

Figure 9. Snapshots of the Lagrangian tracer particle density field. The black solid line indicates the 50th percentile (median depth) of the tracer particles vertical height and the black dashed line indicates the layer containing up to 90% of all of the tracer particles. The red lines indicate the tracer particles' left and right most horizontal seeded position before time zero. **(A)** $Re_w = 5.9 \cdot 10^5$. Wave passage one, $tc_0/H = 19.6$. **(B)** $Re_w = 5.9 \cdot 10^5$. Wave passage two, $tc_0/H = 40.7$. **(C)** $Re_w = 6.5 \cdot 10^5$. Wave passage one, $tc_0/H = 21.0$. **(D)** $Re_w = 6.5 \cdot 10^5$. Wave passage two, $tc_0/H = 44.7$.

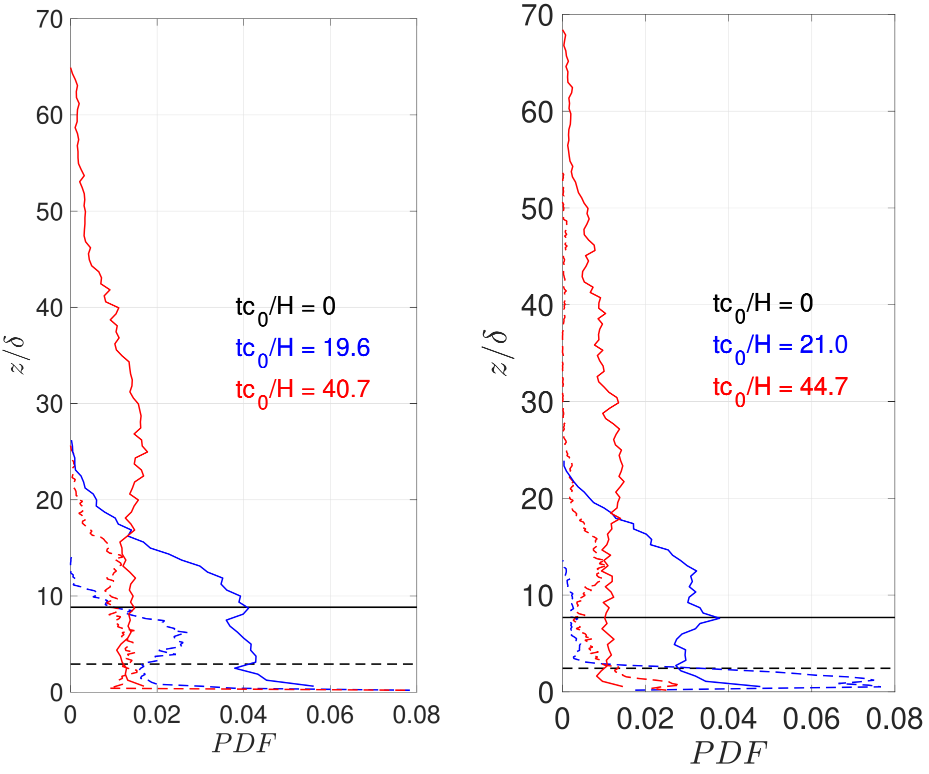

Figure 10a. **Figure 10b.**

Figure 10. Probability distribution function of the vertical position of the tracer particles relative to the boundary layer thickness δ. **(A)** $Re_w = 5.9 \cdot 10^4$ (dashed lines) and $5.9 \cdot 10^5$ (solid lines). Black line, $tc_0/H = 0$; blue line, $tc_0/H = 19.6$ (wave passage one); red line, $tc_0/H = 40.7$ (wave passage two). **(B)** $Re_w = 6.5 \cdot 10^4$ (dashed lines) and $6.5 \cdot 10^5$ (solid lines). Black line, $tc_0/H = 0$; blue line, $tc_0/H = 21.0$ (wave passage one); red line, $tc_0/H = 44.7$ (wave passage two).

Paper III

Bringing optical fluid motion analysis to the field: a methodology using an open source ROV as a camera system and rising bubbles as tracers

Trygve Kvåle Løken, Thea Josefine Ellevold, Reyna G Ramirez de la Torre, Jean Rabault, Atle Jensen

Published in *Measurement Science and Technology*, June 2021, volume 32, no. 9, pp. 095302 DOI: doi: 10.1088/1361-6501/abf09d.

Appendices

Appendix A

Mathematical calculations

In this section, we will provide a step-by-step calculation outline for the Korteweg-de Vries (KdV) theory provided in Section 1.2.1. The present equations are collected from the review written by Grue 2006.

A.1 The Korteweg-de Vries equation

Continuous stratification

The development of weakly nonlinear theory of internal waves in continuously stratified fluids that led to the Korteweg-de Vries equation and its higher-order extensions started with Benney 1966.

A coordinate system is introduced where the x is directed along the horizontal axis, and z is the vertical axis. The internal wave motion occurs in the fluid layer between two horizontal rigid walls at $z = 0$ and $z = -H$. Thus, the free surface is replaced by a rigid lid. When there is no motion in the fluid, the density field is determined by $\bar{\rho}(z)$. We are considering a two-dimensional motion with velocity field perturbations $\mathbf{w}(x, z, t) = (u(x, z, t), w(x, z, t))$ and density field perturbation $\rho(x, z, t)$ which makes the total density field $\rho_d = \bar{\rho} + \rho$.
Mass conservation:

$$\rho_{dt} + \nabla \cdot (\rho \mathbf{w}) = 0 \tag{A.1}$$

Momentum conservations:

$$\rho_d \mathbf{w}_t + \rho_d \mathbf{w} \cdot \nabla \mathbf{w} = -\nabla p + \rho_d g(-\mathbf{k}) \tag{A.2}$$

Incompressibility condition:

$$\nabla \cdot \mathbf{w} = 0 \tag{A.3}$$

where p denotes pressure and g acceleration of gravity. By using Equation (A.1) with Equation (A.3), the mass conservation becomes:

$$\rho_{dt} + u\rho_{dx} + w\rho_{dz} = 0 \tag{A.4}$$

To eliminate the pressure term in the momentum equation, we take the vorticity of the momentum equation, i.e. $\nabla\times$ (Equation (A.2)):

$$[\rho_d u_t + \rho_d(uu_x + wu_z)]_z = -p_{xz} \tag{A.5}$$

$$[\rho_d w_t + \rho_d(uw_x + ww_z)]_x = -p_{xz} - \rho_{dx} g \tag{A.6}$$

and subtract Equation (A.5) from Equation (A.6):

$$[\rho_d u_t + \rho_d(uu_x + wu_z)]_z - [\rho_d w_t + \rho_d(uw_x + ww_z)]_x - \rho_{dx} g = 0 \tag{A.7}$$

Scaling the equations: The wave amplitude is defined by the parameter a, the wavelength by λ, and the wave frequency by ω. Further, we introduce the scaling parameters:

Horizontal length [m]:	λ
Vertical length [m]:	H
Time [s]:	ω^{-1}
Horizontal velocity [m/s]:	U
Vertical velocity [m/s]:	W

and dimensionless, primed variables:

$$\begin{aligned}
x' &= x/\lambda, \\
z' &= z/H, \\
p' &= p/(\rho_0 g H), \\
t' &= t\omega, \\
u' &= u/U = O(\epsilon) \rightarrow u' = u'\epsilon, \\
w' &= w/W = O(\epsilon) \rightarrow w' = w'\epsilon, \\
\rho' &= \rho/\rho_0 = O(\epsilon) \rightarrow \rho' = \rho'\epsilon,
\end{aligned}$$

where ρ_0 is the reference density. Additionally, two small non-dimensional parameters are defined: $\epsilon = a/H$ and $\mu = H^2/\lambda^2$ where ϵ gives a number on the nonlinearity of the problem and μ a number for the dispersive effects. We look for a balance between the nonlinear and dispersive effects, i.e., ϵ and μ are of the same order of magnitude. From the incompressibility condition, the balance UH = Wλ and the balance U = $\omega\lambda$ are chosen. Further, we introduce the inverse Froude number G = gh/U^2 and a stream function $\psi'(x, z, t)$. Since the fluid is assumed irrotational, we also achieve the relationship $(u', w') = (\psi'_z$,-$\psi'_x)$. The differentiations becomes now:

$$\begin{aligned}
\frac{\partial}{\partial t} &= \omega \frac{\partial}{\partial t'} \\
\frac{\partial}{\partial x} &= \frac{1}{\lambda} \frac{\partial}{\partial x'} \\
\frac{\partial}{\partial z} &= \frac{1}{H} \frac{\partial}{\partial z'}
\end{aligned}$$

Pertubations analysis: Rewrite the total density field:

$$\rho_d(x, z, t) = \bar{\rho}(z) + \rho(x, z, t) = \bar{\rho}_0(z) + \rho_1(x, z, t), \tag{A.8}$$

$$= \rho_0 \bar{\rho}(z) + \epsilon \rho_0 \rho'. \tag{A.9}$$

Continue with perturbation analysis on Equation (A.7) first inserting Equation (A.8), then taking term by term:

$$[(\bar{\rho}_0(z) + \rho_1)(u_t + uu_x + wu_z)]_z - [(\bar{\rho}_0(z) + \rho_1)(w_t + uw_x + ww_z)]_x - \rho_{1x} g = 0. \tag{A.10}$$

$$\begin{aligned}[\bar{\rho}_0 u_t]_z &= [\rho_0 \bar{\rho} u_t]_z,\\ &= [\rho_0 \bar{\rho} u'_{t'} \omega U \epsilon]_{z'} \frac{1}{H},\\ &= [\bar{\rho} u'_{t'}]_{z'} \underbrace{\frac{U \rho_0 \omega \epsilon}{H}}_{\mathcal{C}_0}. \qquad \text{(A.11)}\end{aligned}$$

$$\begin{aligned}[\bar{\rho}_0 (u u_x + w u_z)]_z &= [\rho_0 \bar{\rho} (u' u'_{x'} \epsilon^2 \frac{U^2}{\lambda} + w' u'_{z'} \epsilon^2 \frac{WU}{H})]_{z'} \frac{1}{H},\\ &= [\rho_0 \bar{\rho} (u' u'_{x'} \epsilon^2 \frac{U^2}{\lambda} + w' u'_{z'} \epsilon^2 \frac{U^2}{\lambda})]_{z'} \frac{1}{H},\\ &= [\bar{\rho} (u' u'_{x'} + w' u'_{z'})]_{z'} \mathcal{C}_0 \epsilon. \qquad \text{(A.12)}\end{aligned}$$

$$\begin{aligned}[\rho_1 u_t]_z &= [\rho_0 \rho' \epsilon^2 u'_{t'} \omega U]_{z'} \frac{1}{H},\\ &= [\rho' u'_{t'}]_{z'} \mathcal{C}_0 \epsilon. \qquad \text{(A.13)}\end{aligned}$$

$$\begin{aligned}[\rho_1 (u u_x + w u_z)]_z &= [\rho_0 \rho' \epsilon (u' u'_{x'} \epsilon^2 \frac{U^2}{\lambda} + w' u'_{z'} \epsilon^2 \frac{WU}{H})]_{z'} \frac{1}{H},\\ &= [\rho_0 \rho' \epsilon (u' u'_{x'} \epsilon^2 \frac{U^2}{\lambda} + w' u'_{z'} \epsilon^2 \frac{U^2}{\lambda})]_{z'} \frac{1}{H},\\ &= [\rho' (u' u'_{x'} + w' u'_{z'})]_{z'} \mathcal{C}_0 \epsilon^2. \qquad \text{(A.14)}\end{aligned}$$

$$\begin{aligned}[\bar{\rho}_0 w_t]_x &= [\rho_0 \bar{\rho} w'_{t'} \epsilon W \omega]_{x'} \frac{1}{\lambda},\\ &= [\bar{\rho} w'_{t'}]_{x'} \mathcal{C}_0 \mu. \qquad \text{(A.15)}\end{aligned}$$

$$\begin{aligned}[\bar{\rho}_0 (u w_x + w w_z)]_x &= [\rho_0 \bar{\rho} (u' w'_{x'} \epsilon^2 \frac{UW}{\lambda} + w' w'_{z'} \epsilon^2 \frac{W^2}{H}]_{x'} \frac{1}{\lambda},\\ &= [\rho_0 \bar{\rho} (u' w'_{x'} \epsilon^2 \frac{U^2 H}{\lambda^2} + w' w'_{z'} \epsilon^2 \frac{U^2 H}{\lambda^2}]_{x'} \frac{1}{\lambda},\\ &= [\bar{\rho} (u' w'_{x'} + w' w'_{z'})]_{x'} \mathcal{C}_0 \epsilon \mu. \qquad \text{(A.16)}\end{aligned}$$

$$\begin{aligned}[\rho_1 w_t]_x &= [\rho_0 \rho' \epsilon^2 w'_{t'} W \omega]_{x'} \frac{1}{\lambda},\\ &= [\rho' w'_{t'}]_{x'} \mathcal{C}_0 \epsilon \mu. \qquad \text{(A.17)}\end{aligned}$$

$$
\begin{aligned}
[\rho_1(uw_x + ww_z)]_x &= [\rho_0\rho'\epsilon(u'w'_{x'}\epsilon^2\frac{UW}{\lambda} + w'w'_{z'}\epsilon^2\frac{W^2}{H})]_{x'}\frac{1}{\lambda},\\
&= [\rho_0\rho'\epsilon(u'w'_{x'}\epsilon^2\frac{U^2H}{\lambda^2} + w'w'_{z'}\epsilon^2\frac{U^2H}{\lambda^2})]_{x'}\frac{1}{\lambda},\\
&= [\rho'(u'w'_{x'} + w'w'_{z'})]_{x'}\mathcal{C}_0\epsilon^2\mu. \qquad \text{(A.18)}
\end{aligned}
$$

$$
\begin{aligned}
g\rho_{1x} &= g\rho_0\rho'_{x'}\frac{\epsilon}{\lambda},\\
&= \rho'_{x'}g\rho_0\frac{\epsilon}{\lambda}(\frac{UH}{UH}),\\
&= \rho'_{x'}\mathcal{C}_0 G. \qquad \text{(A.19)}
\end{aligned}
$$

From now on we are dropping the primes, and Equation (A.10) now becomes:

$$
\begin{aligned}
&[\bar\rho u_t]_z - \rho_x G + \epsilon[\rho u_t + \bar\rho(uu_x + wu_z)]_z - \mu\bar\rho w_{tx}\\
&\qquad + \epsilon^2[\rho(uu_x + wu_z)]_z - \epsilon\mu[\rho w_t + \bar\rho(uw_x + ww_z)]_x\\
&\qquad\qquad - \epsilon^2\mu[\rho(uw_x + ww_z)]_x = 0. \qquad \text{(A.20)}
\end{aligned}
$$

Doing the same procedure with mass conservation Equation (A.4):

$$
\begin{aligned}
\rho_{dt} + u\rho_{dx} + w\rho_{dz} &= \frac{\partial}{\partial t}(\rho_0\bar\rho + \rho_0\rho'\epsilon) + u\frac{\partial}{\partial x}(\rho_0\bar\rho + \rho_0\rho'\epsilon) + w\frac{\partial}{\partial z}(\rho_0\bar\rho + \rho_0\rho'\epsilon),\\
&= \frac{\partial}{\partial t'}(\rho_0\rho'\epsilon)\omega + u'\epsilon U\frac{\partial}{\partial x'}\frac{\rho_0\rho'\epsilon}{\lambda} + w'\epsilon W\frac{\partial}{\partial z'}\frac{\rho_0\rho'\epsilon}{H} + w'\epsilon W\frac{\partial}{\partial z'}\frac{\rho_0\bar\rho}{H},\\
&= \frac{\rho_0 U\epsilon}{\lambda}(\rho'_{t'} + w'\bar\rho_{z'} + \epsilon(u'\rho'_{x'} + w'\rho'_{z'}) = 0, \qquad \text{(A.21)}
\end{aligned}
$$

providing

$$\rho_t + w\bar\rho_z + \epsilon(u\rho_x + w\rho_z) = 0. \qquad \text{(A.22)}$$

Next step is to include the stream function $(u, w) = (\psi_z, -\psi_x)$. Equation (A.22) and Equation (A.20) becomes:

$$\rho_t - \bar\rho_z\psi_x + \epsilon(\rho_x\psi_z - \rho_z\psi_x) = 0. \qquad \text{(A.23)}$$

$$
\begin{aligned}
&[\bar\rho\psi_{zt}]\psi_z - \rho_x G + \epsilon[\rho\psi_{zt} + \bar\rho(\psi_z\psi_{xz} - \psi_x\psi_{zz})]\psi_z + \mu\bar\rho\psi_{xxt}\\
&\qquad + \epsilon^2[\rho(\psi_z\psi_{xz} - \psi_x\psi_{zz})]\psi_z + \epsilon\mu[\rho\psi_{xt} + \bar\rho(\psi_z\psi_{xx} - \psi_x\psi_{xz})]_x\\
&\qquad\qquad + \epsilon^2\mu[\rho(\psi_z\psi_{xx} - \psi_x\psi_{xz})]_x = 0. \qquad \text{(A.24)}
\end{aligned}
$$

The rigid lid condition $\psi_x = 0$ is applied as the boundary conditions at $z = 0$ and $z = -1$. The next step is to use separation of variables and seek wave solutions by introducing the amplitude function $A(x,t)$ and expand $\rho(x,z,t)$ and $\psi(x,z,t)$ on the following form:

$$\rho(x,z,t) = A\rho(z) + \epsilon A^2\tilde{\rho}(z) + \mu A_{xx}\hat{\rho}(z), \tag{A.25}$$

$$\psi(x,z,t) = A\phi(z) + \epsilon A^2\tilde{\phi}(z) + \mu A_{xx}\hat{\phi}(z). \tag{A.26}$$

Equations (A.25) and (A.26) are introduced into Equations (A.23) and (A.24), giving to leading order in nonlinearity and dispersion:

$$A_t + cA_x + \epsilon\alpha_0 AA_x + \mu\beta_0 A_{xxx} = 0. \tag{A.27}$$

Further, we are going to look at the linear terms and up to leading order of ϵ and μ separately.

Linear terms

We are starting by looking at the linear terms in Equations (A.23) and (A.24) first.

$$\rho_t - \bar{\rho}_z\psi_x = 0, \tag{A.28}$$

$$[\bar{\rho}\psi_{zt}]\psi_z - \rho_x G = 0. \tag{A.29}$$

Taking $\partial/\partial x$ of Equation (A.28)

$$\begin{aligned} \rho_{xt} - \bar{\rho}_z\psi_{xx} &= 0,\\ \rho_{xt} &= \bar{\rho}_z\psi_{xx}, \end{aligned} \tag{A.30}$$

and $\partial/\partial t$ of Equation (A.29)

$$\begin{aligned} [\bar{\rho}\psi_{ztt}]\psi_z - G\rho_{xt} &= 0,\\ [\bar{\rho}\psi_{ztt}]\psi_z - G\bar{\rho}_z\psi_{xx} &= 0,\\ [\bar{\rho}A_{tt}\phi_z]\psi_z - G\bar{\rho}_y A_{xx}\phi &= 0,\\ [\bar{\rho}\phi_z]\psi_z - \frac{G\bar{\rho}_y A_{xx}\phi}{A_{tt}} &= 0,\\ [\bar{\rho}\phi_z]\psi_z - \frac{G\bar{\rho}_z\phi}{c^2} &= 0, \end{aligned} \tag{A.31}$$

with the boundary conditions $\phi(0) = \phi(-1) = 0$. Additionally, we assume a linear wave amplitude on the form $A(x-ct)$, providing the relation $A_t = -cA_x$, where c is the phase speed. The eigenvalue problem has an infinite set of eigenvalues $c_0 > c_1 > c_2 > ... > 0$ with corresponding eigenfunctions $\phi_0(z), \phi_1(z), \phi_2(z), ...$. The eigenvalues and eigenfunctions represent the wave speed and vertical structure of the n-th mode linear, hydrostatic internal wave motion. Further, we are only interested in the lowest mode corresponding to c_0 and ϕ_0. These quantities are determined from Equation (A.31) with the boundary conditions.

Up to leading order ϵ

Second step is to include terms up to order ϵ in Equations (A.23) and (A.24). We have now the relation:

$$A_t + cA_x + \epsilon\alpha_0 AA_x = 0. \tag{A.32}$$

Further, Equations (A.23) and (A.24) becomes

$$\rho_t - \bar{\rho}_z\psi_x + \epsilon(\rho_x\psi_z - \rho_z\psi_x) = 0, \tag{A.33}$$

$$[\bar{\rho}\psi_{zt}]\psi_z - \rho_x G + \epsilon[\rho\psi_{zt} + \bar{\rho}(\psi_z\psi_{xz} - \psi_x\psi_{zz})]\psi_z = 0. \tag{A.34}$$

Mass, term by term:

$$\begin{aligned} \rho_t &= A_t\rho + 2\epsilon AA_t\tilde{\rho}, \\ &= A_x[-c\rho] + \epsilon AA_x[-\alpha_0\rho - 2c\tilde{\rho}]. \end{aligned} \tag{A.35}$$

$$-\bar{\rho}_z\psi_x = A_x[-\bar{\rho}_z\phi] - \epsilon AA_x[-2\bar{\rho}_z\tilde{\phi}]. \tag{A.36}$$

$$\begin{aligned} \epsilon(\rho_x\psi_z - \rho_z\psi_x) &= \epsilon(A_x\rho A\phi_z - A\rho_y A_x\phi), \\ &= \epsilon AA_x[\rho\phi_z - \rho_z\phi]. \end{aligned} \tag{A.37}$$

Then Equation (A.33) becomes:

$$A_x \underbrace{[-c\rho - \bar{\rho}_z\phi]}_{\underline{1}} + \epsilon AA_x \underbrace{[-\alpha_0\rho - 2c\tilde{\rho} - 2\bar{\rho}_z\tilde{\phi} + \rho\phi_z - \rho_z\phi]}_{\underline{2}} = 0 \tag{A.38}$$

Each term in the [ ] needs to be zero. From $\underline{1}$: $\rho = \frac{-\bar{\rho}_z\phi}{c}$. Substitute into $\underline{2}$ and solve for $\tilde{\rho}$

$$\begin{aligned} -\alpha_0\rho - 2c\tilde{\rho} - 2\bar{\rho}_z\tilde{\phi} + \rho\phi_z - \rho_z\phi &= 0, \\ \frac{\alpha_0\bar{\rho}_z\phi}{c} - 2c\tilde{\rho} - 2\bar{\rho}_z\tilde{\phi} - \frac{\bar{\rho}_z\phi_z\phi}{c} + \frac{\bar{\rho}_{zz}\phi\phi}{c} + \frac{\bar{\rho}_z\phi_z\phi}{c} &= 0, \\ \frac{\alpha_0\bar{\rho}_z\phi}{c} - 2c\tilde{\rho} - 2\bar{\rho}_z\tilde{\phi} + \frac{\bar{\rho}_{zz}\phi\phi}{c} &= 0. \end{aligned} \tag{A.39}$$

$$2\tilde{\rho} = \frac{\alpha_0\bar{\rho}_z\phi}{c^2} - \frac{2\bar{\rho}_z\tilde{\phi}}{c} + \frac{\bar{\rho}_{zz}\phi\phi}{c^2}. \tag{A.40}$$

Momentum, term by term:

$$\begin{aligned} [\bar{\rho}\psi_{zt}]\psi_z &= [\bar{\rho}(A_t\phi_z + 2\epsilon AA_t\tilde{\phi}_z)]\psi_z, \\ &= [\bar{\rho}(\phi_z + 2\epsilon A\tilde{\phi}_z)]\psi_z(-cA_x - \epsilon\alpha_0 AA_x), \\ &= [\bar{\rho}(-cA_x\phi_z - \epsilon\alpha_0 AA_x\phi_z - 2\epsilon cAA_x\tilde{\phi}_z)]\psi_z, \end{aligned}$$

$$= A_x[-c\bar\rho\phi_z]\psi_z + \epsilon AA_x[-\alpha_0\bar\rho\phi_z - 2c\bar\rho\tilde\phi_z]\psi_z. \tag{A.41}$$

$$\begin{aligned} -\rho_x G &= A_x[-G\rho] + \epsilon 2AA_x[-G\tilde\rho], \\ &= A_x[\frac{G\bar\rho_z\phi}{c}] + \epsilon AA_x[-\frac{\alpha_0 G\bar\rho_z\phi}{c^2} + \frac{2G\bar\rho_z\tilde\phi}{c} - \frac{G\bar\rho_{zz}\phi\phi}{c^2}]. \end{aligned} \tag{A.42}$$

$$\begin{aligned} \epsilon[\rho\psi_{zt} + \bar\rho(\psi_z\psi_{xz} - \psi_x\psi_{zz})]\psi_z &= \epsilon[\rho\psi_{zt}]\psi_z + \epsilon[\bar\rho(\psi_z\psi_{xz} - \psi_x\psi_{zz})]\psi_z, \\ &= \epsilon[\rho A(A_t\phi_z]\psi_z + \epsilon[\bar\rho(AA_x\phi_z^2 - AA_x\phi\phi_{zz})]\psi_z, \\ &= \epsilon[-c\rho AA_x\phi_z]\psi_z + \epsilon[\bar\rho(AA_x\phi_z^2 - AA_x\phi\phi_{zz})]\psi_z, \\ &= \epsilon AA_x[-c\rho\phi_z]\psi_z + \epsilon AA_x[\bar\rho(\phi_z^2 - \phi\phi_z)]\psi_z, \\ &= \epsilon AA_x[\bar\rho_z\phi\phi_z + \bar\rho(\phi_z^2 - \phi\phi_{zz})]\psi_z. \end{aligned} \tag{A.43}$$

Then Equation (A.34) becomes:

$$\begin{aligned} &A_x\underbrace{[-c(\bar\rho\phi_z)\psi_z + \frac{G\bar\rho_z\phi}{c}]}_{\underline{3}}+ \\ &\qquad \epsilon AA_x[-\alpha_0(\bar\rho\phi_z)\psi_z - 2c(\bar\rho\tilde\phi_z)\psi_z - \frac{\alpha_0 G\bar\rho_z\phi}{c^2}+ \\ &\qquad \underbrace{\frac{2G\bar\rho_z\tilde\phi}{c} - \frac{G\bar\rho_{zz}\phi\phi}{c^2} + (\bar\rho_z\phi\phi_z + \bar\rho(\phi_z^2 - \phi\phi_{zz}))\psi_z]}_{\underline{4}} = 0 \end{aligned} \tag{A.44}$$

Each term in the [ ] needs to be zero. From $\underline{3}$: $(\bar\rho\phi_z)\psi_z = \frac{G\bar\rho_z\phi}{c^2}$. Substitute into $\underline{4}$ and solve for $\tilde\phi$:

$$\begin{aligned} &-\frac{\alpha_0 G\bar\rho_z\phi}{c^2} - 2c(\bar\rho\tilde\phi_z)\psi_z - \frac{\alpha_0 G\bar\rho_z\phi}{c^2}+ \\ &\qquad \frac{2G\bar\rho_z\tilde\phi}{c} - \frac{G\bar\rho_{zz}\phi\phi}{c^2} + (\bar\rho_z\phi\phi_z + \bar\rho(\phi_z^2 - \phi\phi_{zz}))\psi_z = 0. \end{aligned} \tag{A.45}$$

$$\begin{aligned} &-\frac{2\alpha_0 G\bar\rho_z\phi}{c^2} - 2c(\bar\rho\tilde\phi_z)\psi_z + \frac{2G\bar\rho_z\tilde\phi}{c}- \\ &\qquad \frac{G\bar\rho_{zz}\phi\phi}{c^2} + (\bar\rho_z\phi\phi_z + \bar\rho(\phi_z^2 - \phi\phi_{zz}))\psi_z = 0. \end{aligned} \tag{A.46}$$

$$(\bar\rho\tilde\phi_z)\psi_z - \frac{G\bar\rho_z\tilde\phi}{c^2} = -\frac{\alpha_0 G\bar\rho_z\phi}{c^3} - \frac{G\bar\rho_{zz}\phi^2}{2c^3} + \frac{(\bar\rho_z\phi\phi_z)\psi_z}{2c} + \frac{(\bar\rho(\phi_z^2 - \phi\phi_{zz}))\psi_z}{2c}. \tag{A.47}$$

Up to leading order μ

Third step is to include terms up to order μ in Equations (A.23) and (A.24). We have now the relation:

$$A_t + cA_x + \mu\beta_0 A_{xxx} = 0. \tag{A.48}$$

Further, Equations (A.23) and (A.24) becomes

$$\rho_t - \bar{\rho}_z\psi_x = 0, \tag{A.49}$$

$$(\bar{\rho}\psi_{zt})\psi_z - G\rho_x + \mu\bar{\rho}\psi_{xxt} = 0. \tag{A.50}$$

Mass, term by term:

$$\begin{aligned}\rho_t &= \rho A_t + \mu A_{xxt}\hat{\rho},\\ &= -c\rho A_x - \mu\beta_0\rho A_{xxx} - \mu c A_{xxx}\hat{\rho},\\ &= A_x[-c\rho] + \mu A_{xxx}[-\beta_0\rho - c\hat{\rho}].\end{aligned} \tag{A.51}$$

$$\begin{aligned}-\bar{\rho}_z\psi_x &= -\bar{\rho}_y A_x\phi - \mu\bar{\rho}_y A_{xxx}\hat{\phi},\\ &= A_x[-\bar{\rho}_z\phi] + \mu A_{xxx}[-\bar{\rho}_z\hat{\phi}].\end{aligned} \tag{A.52}$$

Then Equation (A.49) becomes:

$$A_x\underbrace{[-c\rho - \bar{\rho}_z\phi]}_{\underline{5}} + \mu A_{xxx}\underbrace{[-\beta_0\rho - c\hat{\rho} - \bar{\rho}_z\hat{\phi}]}_{\underline{6}} = 0. \tag{A.53}$$

Each term in the [ ] needs to be zero. From $\underline{5}$: $\rho = -\frac{\bar{\rho}_z\phi}{c}$. Substitute into $\underline{6}$ and solve for $\hat{\rho}$:

$$\begin{aligned}-\beta_0\rho - c\hat{\rho} - \bar{\rho}_z\hat{\phi} &= 0\\ \frac{\beta_0\bar{\rho}_z\phi}{c} - c\hat{\rho} - \bar{\rho}_z\hat{\phi} &= 0.\end{aligned} \tag{A.54}$$

$$\hat{\rho} = \frac{\beta_0\bar{\rho}_z\phi}{c^2} - \frac{\bar{\rho}_z\hat{\phi}}{c}. \tag{A.55}$$

Momentum, term by term:

$$\begin{aligned}(\bar{\rho}\psi_{zt})\psi_z =&(\bar{\rho}(A_t\phi_z + \mu A_{xxt}\hat{\phi}_z))\psi_z,\\ &= (-cA_x\bar{\rho}\phi_z - \mu\beta_0 A_{xxx}\bar{\rho}\phi_z - \mu c A_{xxx}\bar{\rho}\hat{\phi}_z)\psi_z.\end{aligned} \tag{A.56}$$

$$\begin{aligned}-G\rho_x &= -GA_x\rho - \mu G A_{xxx}\hat{\rho},\\ &= \frac{GA_x\bar{\rho}_z\phi}{c} - \mu G A_{xxx}\hat{\rho}.\end{aligned} \tag{A.57}$$

$$\begin{aligned}\mu\bar{\rho}\psi_{xxt} &= \mu\bar{\rho}(A_{xxt}\phi),\\ &= -\mu c A_{xxx}\bar{\rho}\phi. \end{aligned} \tag{A.58}$$

Then Equation (A.50) becomes:

$$\begin{aligned} &A_x \underbrace{[-c(\bar{\rho}\phi_z)\psi_z + \frac{G\bar{\rho}_z\phi}{c}]}_{\underline{7}} + \\ &\qquad \mu A_{xxx} \underbrace{[-\beta_0(\bar{\rho}\phi_z)\psi_z - c(\bar{\rho}\hat{\phi}_z)\psi_z - \frac{\beta_0 G\bar{\rho}_z\phi}{c^2} + \frac{G\bar{\rho}_z\hat{\phi}}{c} - c\bar{\rho}\phi]}_{\underline{8}}. \end{aligned} \tag{A.59}$$

Each term in the [ ] needs to be zero. From $\underline{7}$: $(\bar{\rho}\phi_z)\psi_z = \frac{G\bar{\rho}_z\phi}{c^2}$. Substitute into $\underline{8}$ and solve for $\hat{\phi}$:

$$\begin{aligned} -\beta_0(\bar{\rho}\phi_z)\psi_z - c(\bar{\rho}\hat{\phi}_z)\psi_z - \frac{\beta_0 G\bar{\rho}_z\phi}{c^2} + \frac{G\bar{\rho}_z\hat{\phi}}{c} - c\bar{\rho}\phi &= 0,\\ -\frac{\beta_0 G\bar{\rho}_z\phi}{c^2} - \frac{\beta_0 G\bar{\rho}_z\phi}{c^2} - c(\bar{\rho}\hat{\phi}_z)\psi_z + \frac{G\bar{\rho}_z\hat{\phi}}{c} - c\bar{\rho}\phi &= 0,\\ -\frac{2\beta_0 G\bar{\rho}_z\phi}{c^2} - c(\bar{\rho}\hat{\phi}_z)\psi_z + \frac{G\bar{\rho}_z\hat{\phi}}{c} - c\bar{\rho}\phi &= 0. && \text{(A.60)}\\ & && \text{(A.61)} \end{aligned}$$

$$(\bar{\rho}\hat{\phi}_z)\psi_z - \frac{G\bar{\rho}_z\hat{\phi}}{c^2} = -\frac{2\beta_0 G\bar{\rho}_z\phi}{c^3} - \bar{\rho}\phi. \tag{A.62}$$

Determine the constants α_0, β_0

To determine the constants α_0 and β_0 in $A_t + cA_x + \epsilon\alpha_0 AA_x + \mu\beta_0 A_{xxx} = 0$, we use the boundary value problems for $\tilde{\phi}(z)$ (Equation (A.47)) and $\hat{\phi}(z)$ (Equation (A.62)). Additionally we have $\tilde{\phi}(0) = \tilde{\phi}(-1) = 0$ and $\hat{\phi}(0) = \hat{\phi}(-1) = 0$. The boundary value problems have unique solutions provided that the coefficients α_0 and β_0 have values such that:

$$\int_{-1}^{0} \phi[(\bar{\rho}\tilde{\phi}_z)\psi_z - \frac{G\bar{\rho}_z\tilde{\phi}}{c^2}]dz = 0, \tag{A.63}$$

$$\int_{-1}^{0} \phi[(\bar{\rho}\hat{\phi}_z)\psi_z - \frac{G\bar{\rho}_z\hat{\phi}}{c^2}]dz = 0. \tag{A.64}$$

In Equation (A.63) and Equation (A.64), we insert the respective r.h.s from Equations (A.47) and (A.62), and solve for α_0 and β_0, respectively. Starting with Equation (A.63):

$$\int_{-1}^{0}\phi[\underbrace{-\frac{\alpha_0 G\bar{\rho}_z\phi}{c^3}}_{\underline{9}}\underbrace{-\frac{G\bar{\rho}_{zz}\phi^2}{2c^3}}_{\underline{10}}\underbrace{+\frac{(\bar{\rho}_z\phi\phi_z)\psi_z}{2c}}_{\underline{11}}\underbrace{+\frac{(\bar{\rho}(\phi_z^2-\phi\phi_{zz}))\psi_z}{2c}}_{\underline{12}}]dz = 0. \quad (A.65)$$

<u>*Term by term*</u>:

<u>9</u>:

$$-\frac{\alpha_0 G}{c^3}\int_{-1}^{0}\bar{\rho}_z\phi^2 dz = -\frac{\alpha_0}{c}\int_{-1}^{0}\phi(\bar{\rho}\phi_z)\psi_z,$$
$$= \frac{\alpha_0}{c}\int_{-1}^{0}\bar{\rho}\phi_z^2 dz. \quad (A.66)$$

<u>10</u>:

$$-\frac{G}{2c^3}\int_{-1}^{0}\bar{\rho}_{zz}\phi^3 dz = \frac{3G}{2c^3}\int_{-1}^{0}\bar{\rho}_z\phi^2\phi_z dz,$$
$$= \frac{3}{2c}\int_{-1}^{0}(\bar{\rho}\phi_z)\psi_z\phi\phi_z dz,$$
$$= -\frac{3}{2c}\int_{-1}^{0}\bar{\rho}(\phi_z^3+\phi\phi_z\phi_{zz})dz. \quad (A.67)$$

<u>11</u>:

$$\frac{1}{2c}\int_{-1}^{0}\phi(\bar{\rho}_z\phi\phi_z)\psi_z dz = -\frac{1}{2c}\int_{-1}^{0}\bar{\rho}_z\phi\phi_z^2 dz,$$
$$= \frac{1}{2c}\int_{-1}^{0}\bar{\rho}(\phi_z^3+2\phi\phi_z\phi_{zz})dz. \quad (A.68)$$

<u>12</u>:

$$\frac{1}{2c}\int_{-1}^{0}\phi(\bar{\rho}(\phi_z^2-\phi\phi_{zz}))\psi_z dz = -\frac{1}{2c}\int_{-1}^{0}\bar{\rho}(\phi_z^2-\phi\phi_{zz})\phi_z dz,$$
$$= -\frac{1}{2c}\int_{-1}^{0}\bar{\rho}(\phi_z^3-\phi\phi_z\phi_{zz})dz. \quad (A.69)$$

Insert back:

$$\frac{\alpha_0}{c}\int_{-1}^{0}\bar{\rho}\phi_z^2 dz - \frac{3}{2c}\int_{-1}^{0}\bar{\rho}(\phi_z^3+\phi\phi_z\phi_{zz})dz +$$

$$\frac{1}{2c}\int_{-1}^{0}\bar{\rho}(\phi_z^3 + 2\phi\phi_z\phi_{zz})dz - \frac{1}{2c}\int_{-1}^{0}\bar{\rho}(\phi_z^3 - \phi\phi_z\phi_{zz})dz = 0. \tag{A.70}$$

$$\frac{\alpha_0}{c}\int_{-1}^{0}\bar{\rho}\phi_z^2 dz - \frac{3}{2c}\int_{-1}^{0}\bar{\rho}\phi_z^3 dz = 0, \tag{A.71}$$

providing that α_0 becomes:

$$\alpha_0 = \frac{3}{2}\frac{\int_{-1}^{0}\bar{\rho}\phi_z^3 dz}{\int_{-1}^{0}\bar{\rho}\phi_z^2 dz}. \tag{A.72}$$

Inserting the respective r.h.s. into Equation (A.64), solving for β_0:

$$\begin{aligned}\int_{-1}^{0}\phi(-\frac{2\beta_0 G\bar{\rho}_z\phi}{c^3} - \bar{\rho}\phi)dz &= -\frac{2\beta_0}{c_0}\int_{-1}^{0}\phi(\frac{G\bar{\rho}_z\phi}{c_0^2})dz - \int_{-1}^{0}\bar{\rho}\phi^2 dz,\\ &= -\frac{2\beta_0}{c_0}\int_{-1}^{0}(\bar{\rho}\phi_z)psi_z\phi dz - \int_{-1}^{0}\bar{\rho}\phi^2 dz,\\ &= \frac{2\beta_0}{c_0}\int_{-1}^{0}\bar{\rho}\phi_z^2\phi dz - \int_{-1}^{0}\bar{\rho}\phi^2 dz = 0, \end{aligned}\tag{A.73}$$

providing that β_0 becomes:

$$\beta_0 = \frac{c_0}{2}\frac{\int_{-1}^{0}\bar{\rho}\phi^2 dz}{\int_{-1}^{0}\bar{\rho}\phi_z^2\phi dz}. \tag{A.74}$$

A.1.1 Vector Group Velocity

Some additional calculations: Assume no boundaries, just seeking wave solutions. Additionally, assume $\bar{\rho}_z$ is constant, and from Boussinesq $\Delta\rho/\rho \ll 1$. The linear equations of momentum, Equation (A.2), in an approximate form due to Boussinesq becomes

$$\rho u_t = -p_x, \tag{A.75}$$
$$\rho w_t = -p_z - \rho g, \tag{A.76}$$

Taking $\partial^2/(\partial t \partial z)$ of Equation (A.75) and $\partial^2/(\partial t \partial x)$ of Equation (A.76) and subtracting them from each other, eliminates the pressure and we get

$$\rho(u_z - w_x)_{tt} = \rho_{xt} g. \tag{A.77}$$

From earlier, we have $\rho_{xt} = -\bar{\rho}_z \psi_{xx}$ (Equation (A.30)). Inserting this we get:

$$\begin{aligned}
(u_z - w_x)_{tt} + \frac{\bar{\rho}_z}{\rho} w_x g &= 0, \\
(\psi_{zz} + \psi_{xx})_{tt} - \psi_{xx} \frac{\bar{\rho}_z g}{\rho} &= 0, \\
(\psi_{zz} + \psi_{xx})_{tt} + N^2 \psi_{xx} &= 0.
\end{aligned} \tag{A.78}$$

Here $N^2 = -\bar{\rho}_z g/\rho$ is the buoyancy frequency, also called the Brunt-Väisala frequency. We are setting the buoyancy frequency to be constant, and thereby possesses a plane-wave solution of the the form $\psi = e^{i\chi}$ where $\chi = \bar{\mathbf{k}} \cdot \mathbf{x} - \omega t$. Here $\bar{\mathbf{k}} = k_x \mathbf{i} + k_z \mathbf{k}$ is the wave number vector , and $k = |\bar{\mathbf{k}}| = \sqrt{k_x^2 + k_z^2}$.

$$\Big(\frac{\partial^2}{\partial t^2}\Big[\frac{\partial^2}{\partial z^2} + \frac{\partial^2}{\partial x^2}\Big] + N^2 \frac{\partial^2}{\partial x^2}\Big)\psi = 0. \tag{A.79}$$

Plug in for ψ:

$$\begin{aligned}
\big((i\omega)^2(-k_x^2 - k_z^2) - N^2 k_x^2\big) e^{i\chi} &= 0, \\
\omega^2(k_x^2 + k_z^2) - N^2 k_x^2 &= 0.
\end{aligned} \tag{A.80}$$

Solve for ω:

$$\begin{aligned}
\omega^2(k_x^2 + k_z^2) &= N^2 k_x^2, \\
\omega^2 &= \frac{N^2 k_x^2}{k_x^2 + k_z^2}, \\
\omega &= \pm \frac{N k_x}{k}.
\end{aligned} \tag{A.81}$$

The vector group velocity is characterized by $\mathbb{C}_g = \nabla_{\bar{\mathbf{k}}}\omega = (\frac{\partial \omega}{\partial k_x}, \frac{\partial \omega}{\partial k_z})$. Inserting $\omega+$:

$$\mathbb{C}_g = \Big(\frac{N}{k} - \frac{N k_x^2}{k^3}, -\frac{N k_x k_z}{k^3}\Big). \tag{A.82}$$

If we take $\overline{\mathbf{k}} \cdot \mathbb{C}_g$:

$$\begin{aligned}
\overline{\mathbf{k}} \cdot \mathbb{C}_g &= \frac{Nk_x}{k} - \frac{Nk_x^3}{k^3} - \frac{Nk_x k_z^2}{k^3}, && \text{(A.83)}\\
&= \frac{Nk_x}{k}\left(\frac{k^2 - k_x^2 - k_z^2}{k^2}\right), && \text{(A.84)}\\
&= 0, && \text{(A.85)}
\end{aligned}$$

we see that the wave number vector $\overline{\mathbf{k}}$ stands perpendicular on the group velocity.

Appendix B

Equipment used in field

In 2021, a 5-beam Nortek Signature1000 (kHz) broadband ADCP was utilized to measure the water's velocity near the bottom topography ($T5$). Hence, the 1000 kHz ADCP was as well mounted close to the bottom, approximately 14 m above bottom, but in a downward position. The measuring frequency was set to 8 Hz and a vertical resolution of 0.5 m. In addition, a 5-beam Nortek Signature500 (kHz) broadband ADCP was mounted approximately 61.9 m above bottom in an upward-looking position. The 500 kHz ADCP was configured to sample average horizontal currents from the slanted beams in 0.5 m vertical bins and a measuring frequency of 8 Hz. See Figure B.1 for the specific configuration.

In 2022, the ADCP 1000 kHz was mounted on station $T1$, approximately 20 m above bottom in a down-looking position. The measuring frequency was now set to 16 Hz.

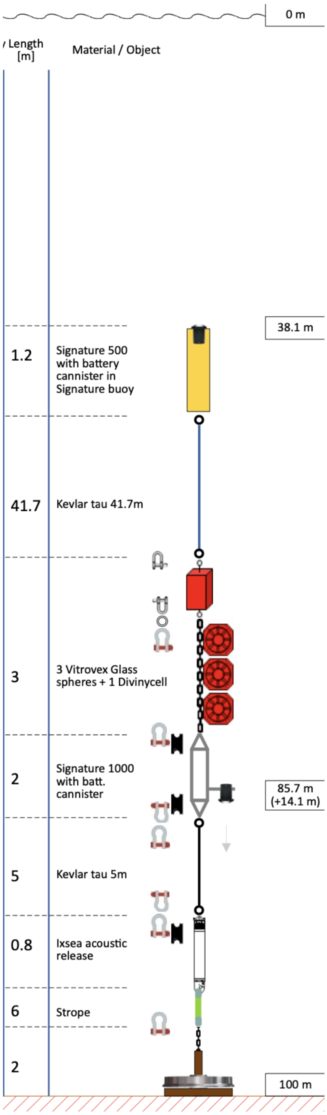

Figure B.1: The configuration of station $T5$ in 2021 with one ADCP 1000 kHz measuring the vertical velocity field near the topography and one ADCP 500 kHz measuring the velocity in the upper part of the water column. Local mean water depth of 100 m. The schematics are created by the Norwegian Institute of Marine Research, Bergen, Norway.